

Synthesis gas production via CO conversion with in-situ CO₂ removal for e-fuels synthesis

Zur Erlangung des akademischen Grades einer

DOKTORIN DER INGENIEURWISSENSCHAFTEN

von der KIT-Fakultät für Chemieingenieurwesen und Verfahrenstechnik des

Karlsruher Instituts für Technologie (KIT)

genehmigte

DISSERTATION

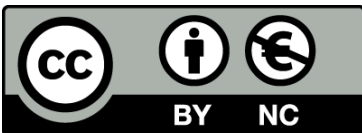
von

Tabea J. Stadler

Tag der mündlichen Prüfung: 03.07.2024

Erstgutachter: Prof. Dr.-Ing. Peter Pfeifer

Zweitgutachter: Prof. Dr. Jan-Dierk Grunwaldt



This document - unless otherwise stated - is licensed under a Creative Commons Attribution-NonCommercial 4.0 International License (CC BY-NC 4.0):
<https://creativecommons.org/licenses/by-nc/4.0/deed.en>

DOI: 10.5445/IR/1000174128

Preface

The research presented in this thesis was conducted at the Institute for Micro Process Engineering (IMVT) at Karlsruhe Institute of Technology (KIT) in Eggenstein-Leopoldshafen between October 2018 and March 2022.

This work is part of the European project Kerogreen, which has received funding from the European Union's Horizon 2020 research and innovation programme under grant agreement no. 763909.

I would like to express my sincere gratitude to my supervisor, Prof. Dr.-Ing. Peter Pfeifer, for his continuous support and guidance, and for providing me with trust and opportunities to develop my ideas and approaches.

I would like to extend my appreciation to Prof. Dr. Jan-Dierk Grunwaldt for serving as the second reviewer of this work.

I would like to thank the students who supported this work. Your involvement has contributed a vital part to the success of this work.

Many thanks to my dear colleagues at IMVT and beyond for insightful discussions (about everything), expertise in the laboratory, and active support in the container work.

I deeply thank my friends for taking my mind off work whenever needed.

Mein größter Dank geht an meine geliebte Familie und an Simon: ihr alle macht mein Leben bunt und prägt meine Entscheidungen. Eure vielfältige und unermüdliche Unterstützung ermöglicht es mir, meine Ziele mit ganzer Kraft zu verfolgen und nicht aus den Augen zu verlieren.

Und zu guter Letzt: danke, meine kleine Ida Paula, für deine große Geduld während der Schreibphase dieses Manuskripts.

Friesenheim, 28.02.2024

Tabea J. Stadler

Danke • Gracias • Obrigada • Merci
Faleminderit • Teşekkürler • متشکرم
Bedankt • Takk • 謝謝
Thank you!

Abstract

Climate change is an urgent global issue that has been caused mainly by the extensive use of fossil fuels. Fossil fuels combustion leads to increasing concentrations of the greenhouse gas CO₂, ultimately resulting in rising average global temperatures. The effects of climate change are far-reaching, impacting not only the environment but also social and economic systems.

The aviation sector is a major contributor to CO₂ emissions, with estimates predicting an increase from 1 Gt in 2018 to up to 1.9 Gt of CO₂ by 2050. These data highlight the necessity to move away from fossil fuels and shift towards sustainable alternatives. Synthetic e-fuels are among the discussed options to serve as sustainable fossil fuel substitutes in the aviation sector. E-fuels are typically produced in Power-to-Liquid (PtL) processes using renewable electricity, CO₂, and water as feedstocks. By capturing the emitted CO₂ from the air and reusing it for the production of e-fuels, a closed carbon cycle is achieved and e-fuels can be considered to be carbon neutral.

A novel PtL route based on the Fischer-Tropsch pathway was developed in the EU project *Kerogreen*. Unlike conventional Fischer-Tropsch-based PtL processes, this route does not employ energy-intensive electrolysis. Instead, captured CO₂ is dissociated into CO and O₂ using microwave plasma technology. The crucial step of synthesis gas production is realized by means of CO conversion via the Water-Gas Shift (WGS) reaction with in-situ CO₂ removal. The synthesis gas is chemically converted into a range of hydrocarbons using the Fischer-Tropsch reaction. A synthetic hydrocarbon product is obtained that can potentially be used as synthetic jet fuel by cracking heavy hydrocarbons into the kerosene range. This thesis explores the possibilities of the synthesis gas production step and its influence on the subsequent kerosene synthesis. Furthermore, the thesis provides a technical solution for this process step in a pilot plant.

Based on engineering and economic considerations, the Sorption-Enhanced Water-Gas Shift (SEWGS) technology was employed for synthesis gas production. In a packed-bed reactor, a WGS catalyst mixed with a material that adsorbs CO₂ enables the WGS reaction with simultaneous CO₂ separation in a single unit operation. As the sorbent is saturated with CO₂ at some point, cyclic operation with reactive adsorption and subsequent desorption phases for regeneration is inevitable.

The choice of SEWGS materials, sorption parameters, and reactor configurations was examined in characterization tests and lab-scale experiments. A Cu/ZnO-Al₂O₃ catalyst showed the best activity and stability. Calcination of commercial hydrotalcite at 400 °C led to the desired CO₂-adsorbing mixed oxide structure and potassium impregnation improved the CO₂ adsorption capacity of this material. Experiments recording the breakthrough curves of CO₂ in a packed-bed microchannel reactor revealed that the sorption properties were influenced by the prevailing water content during the reactive adsorption as well as the desorption phase length. Furthermore, the reactor packing configuration was found to affect the sorption performance. The presence of catalyst-free zones at the reactor outlet enhanced the CO₂ uptake significantly.

In addition to these experimental studies, numerical simulations were carried out to investigate the SEWGS performance using dynamic reactor modeling. A novel graphical simulation approach was created in Matlab Simulink to optimize cyclic process operation and automated plant control. The model allowed for automatic adjustment of cyclic switching times from reactive adsorption to regeneration phases during runtime based on pre-defined parameters. The simulation results highlighted the potential benefits of combining carefully selected operating parameters and process configurations.

The experimental and simulation results were used to develop a compact SEWGS module for the *Kerogreen* pilot plant. This first-of-its-kind demonstration plant aims to feature the full process chain from CO₂ to a crude form of synthetic kerosene. Simulation-driven process design was applied to optimize the intended operation procedures of the SEWGS reactor. Therefore, the Simulink model on system scale was employed to quantify the influence of design configurations and key operating parameters.

Finally, an experimental study elucidated the impact of possibly remaining CO₂ from the SEWGS step on consecutive steps in the *Kerogreen* process chain. Different synthesis gas compositions with and without CO₂ were used to simulate a possible malfunction of the SEWGS module and investigate the influence of CO₂-rich synthesis gas feeds on the product distribution of a Fischer-Tropsch reactor with a subsequent hydrocracking reactor cascade. The experimental results demonstrated that Fischer-Tropsch syncrude upgrade by means of direct hydrocracking is not remarkably influenced by the CO₂ content in the synthesis gas feed. However, it was concluded that the diluting effect has to be considered in the reactor design and the process parameters.

Both, the experimental as well as the simulation results, confirmed that the SEWGS technology investigated in this thesis has the necessary potential and technical feasibility for the production of synthesis gas from pure CO. This development marks a significant step in the *Kerogreen* PtL process chain, towards new possibilities for replacing fossil kerosene and lowering CO₂ emissions from the aviation sector.

Kurzzusammenfassung

Der Klimawandel ist ein akutes globales Problem, das hauptsächlich durch die intensive Nutzung fossiler Energieträger verursacht wird. Die Verbrennung fossiler Rohstoffe führt zu steigenden CO₂-Treibhausgaskonzentrationen und damit zu einem Anstieg der weltweiten Durchschnittstemperatur. Die Auswirkungen des Klimawandels sind weitreichend und wirken sich nicht nur auf die Umwelt, sondern auch auf die sozialen und wirtschaftlichen Strukturen aus.

Der Luftfahrtsektor trägt einen signifikanten Teil zu den CO₂-Emissionen bei. Schätzungen zufolge werden die Emissionen aus der Luftfahrt von etwa 1 Gt im Jahr 2018 auf bis zu 1.9 Gt CO₂ im Jahr 2050 ansteigen. Diese Zahlen verdeutlichen die Notwendigkeit, auf fossile Energieträger zu verzichten und zu nachhaltigen Alternativen überzugehen. Eine mögliche Alternative zu fossilen Kraftstoffen im Luftverkehrssektor sind synthetische Kraftstoffe, sogenannte e-Fuels. E-Fuels werden typischerweise in Power-to-Liquid (PtL)-Prozessen unter Verwendung von erneuerbarem Strom, CO₂ und Wasser hergestellt. Durch die Abtrennung des emittierten CO₂ aus der Luft und dessen Rückgewinnung für die Herstellung von e-Fuels wird der Kohlenstoffkreislauf geschlossen und e-Fuels können als kohlenstoffneutral betrachtet werden.

Im Rahmen des EU-Projekts *Kerogreen* wurde eine neuartige PtL-Route auf der Grundlage des Fischer-Tropsch-Prozesses entwickelt. Im Gegensatz zu bekannten PtL-Prozessen auf Fischer-Tropsch-Basis kommt hierbei keine energieintensive Elektrolyse zum Einsatz. Stattdessen wird das abgetrennte CO₂ mittels Mikrowellenplasmatechnologie in CO und O₂ aufgespalten. Der entscheidende Schritt der Synthesegaserzeugung erfolgt mittels CO-Konvertierung über die Wasser-Gas-Konvertierungsreaktion (WGS) mit in-situ-CO₂-Abtrennung. Das Synthesegas wird über die Fischer-Tropsch-Reaktion in ein breites Spektrum von Kohlenwasserstoffen umgewandelt. Durch Spaltung der langkettigen Komponenten in den Kerosinbereich entsteht ein Gemisch synthetischer Kohlenwasserstoffe, welches als Flugzeugtreibstoff verwendet werden kann. In dieser Arbeit wird der Prozessschritt der Synthesegaserzeugung und dessen Einfluss auf die anschließende Kerosinsynthese untersucht. Außerdem wird eine technische Lösung für diesen Prozessschritt in einer Pilotanlage vorgestellt.

Auf der Grundlage technischer und wirtschaftlicher Erwägungen wurde die Sorptionsunterstützte Wasser-Gas-Konvertierungstechnologie (SEWGS) für die Synthesegaserzeu-

gung ausgewählt. Hierbei wird in einem Festbettreaktor ein WGS-Katalysator mit einem Material gemischt, das CO_2 adsorbiert, um die WGS-Reaktion mit gleichzeitiger CO_2 -Abtrennung in einer einzigen Verfahrensstufe durchzuführen. Da das Sorptionsmittel ab einem gewissen Punkt mit CO_2 gesättigt ist, ist ein zyklischer Betrieb mit reaktiven Adsorptions- und anschließenden Desorptionsphasen zur Regeneration erforderlich.

Die Auswahl der Materialien, Sorptionsparameter und Reaktorkonfigurationen wurde in Charakterisierungstests und Experimenten im Labormaßstab untersucht. Ein Cu/ZnO- Al_2O_3 -Katalysator zeigte die beste Aktivität und Stabilität. Die Kalzinierung von kommerziellem Hydrotalcit bei $400\text{ }^\circ\text{C}$ führte zu der gewünschten Mischoxidstruktur, die die Adsorption von CO_2 ermöglicht. Die Imprägnierung mit Kalium verbesserte die CO_2 -Adsorptionskapazität dieses Materials. Experimente, bei denen die Durchbruchkurven von CO_2 in einem Festbett-Mikrokanalreaktor aufgezeichnet wurden, zeigten, dass die Sorptionseigenschaften vom vorherrschenden Wassergehalt während der reaktiven Adsorption sowie von der Länge der Desorptionsphase beeinflusst werden. Außerdem wurde festgestellt, dass die Reaktorkonfiguration die Sorptionsleistung verändert. Das Anwesenheit von katalysatorfreien Zonen am Reaktorausgang verbesserte die CO_2 -Aufnahme erheblich.

Zusätzlich zu diesen experimentellen Studien wurden numerische Simulationen durchgeführt, um das Verhalten des SEWGS-Prozesses mit Hilfe dynamischer Reaktormodelle zu untersuchen. In Matlab Simulink wurde ein neuartiger grafischer Simulationsansatz entwickelt, mit dem der zyklische Prozessbetrieb und die automatische Anlagensteuerung optimiert werden können. Das Modell ermöglicht die automatische Anpassung der zyklischen Umschaltzeiten von reaktiven Adsorptions- zu Regenerationsphasen während der Laufzeit basierend auf vordefinierten Parametern. Die Simulationsergebnisse haben die potenziellen Vorteile einer sorgfältigen Kombination ausgewählter Betriebsparameter und Prozesskonfigurationen aufgezeigt.

Die Versuchs- und Simulationsergebnisse wurden zur Entwicklung eines kompakten SEWGS-Moduls für die *Kerogreen* Pilotanlage verwendet. Diese Demonstrationsanlage ist die erste ihrer Art und soll die gesamte Prozesskette von CO_2 bis zu einer Rohform von synthetischem Kerosin abbilden. Die angestrebte Betriebsweise des SEWGS-Reaktors wurde mittels simulationsgestütztem Prozessdesign optimiert. Hierzu wurde das entwickelte Simulink-Modell zur Quantifizierung des Einflusses von Designkonfigurationen und wichtigen Betriebsparametern herangezogen.

In einer experimentellen Studie wurden schließlich die Auswirkungen von möglicherweise verbleibendem CO_2 aus dem SEWGS-Schritt auf die nachfolgenden Schritte in der *Kerogreen*-Prozesskette betrachtet. Mit unterschiedlichen Synthesegaszusammensetzungen (mit und ohne CO_2) wurde eine mögliche Fehlfunktion des SEWGS-Moduls simuliert, um den Einfluss von CO_2 -reichem Synthesegas auf die Produktverteilung

des Fischer-Tropsch-Reaktors und der darauffolgenden Hydrocracking-Reaktorkaskade zu untersuchen. Die experimentellen Ergebnisse zeigten, dass die Aufbereitung von Fischer-Tropsch-Produkten durch direktes Hydrocracken nicht nennenswert von dem CO₂-Gehalt im Synthesegas beeinträchtigt wird. Allerdings zeigte sich, dass der auftretende Verdünnungseffekt bei der Reaktorauslegung und der Auswahl der Prozessparameter berücksichtigt werden muss.

Sowohl die experimentellen Ergebnisse als auch die Simulationsergebnisse haben gezeigt, dass die in dieser Arbeit untersuchte SEWGS-Technologie das notwendige Potenzial und die technische Machbarkeit für die Herstellung von Synthesegas aus reinem CO besitzt. Diese Entwicklung stellt einen wichtigen Schritt in der *Kerogreen* PtL-Prozesskette dar, die neue Möglichkeiten zur Substitution von fossilem Kerosin und damit zur Reduktion der CO₂ Emissionen des Luftverkehrs eröffnet.

List of Publications

Peer-reviewed Publications

The thesis is based on the following peer-reviewed publications which are referred to in the text as [P1–P4].

- [P1] T.J. Stadler, P. Barbig, J. Kiehl, R. Schulz, T. Klövekorn, P. Pfeifer. "Sorption-Enhanced Water-Gas Shift Reaction for Synthesis Gas Production from Pure CO: Investigation of Sorption Parameters and Reactor Configurations". *Energies* 14.2 (2021). <https://doi.org/10.3390/en14020355>
- [P2] T.J. Stadler, J.-H. Knoop, S. Decker, P. Pfeifer. "Numerical Simulation Approach for a Dynamically Operated Sorption-Enhanced Water-Gas Shift Reactor". *Processes* 10.6 (2022). <https://doi.org/10.3390/pr10061160>
- [P3] T.J. Stadler, L.J. Bender, P. Pfeifer. "Dynamic simulation of a compact sorption-enhanced water-gas shift reactor". *Frontiers in Chemical Engineering* 4 (2022). <https://doi.org/10.3389/fceng.2022.1000064>
- [P4] T.J. Stadler, B. Bertin-Mente, R. Dittmeyer, L.T. Brübach, T. Böltken, P. Pfeifer. "Influence of CO₂-Rich Syngas on the Selectivity to C₁₀-C₁₄ in a Coupled Fischer-Tropsch/Hydrocracking Process". *Chemie Ingenieur Technik* 94.3 (2022). <https://doi.org/10.1002/cite.202100172>

Non peer-reviewed Publication

The author has published the following non-peer-reviewed publication.

T.J. Stadler, P. Pfeifer. "Innovative Synthesegas-Gewinnung zur Herstellung CO₂-neutraler Flugtreibstoffe". *ENERGIEWIRTSCHAFTLICHE TAGESFRAGEN* 2021, 71. Jg, Heft 1/2.

Conference and Symposia Contributions

The author has presented her research at the following events.

T.J. Stadler, P. Pfeifer. "Syngas Production in the Kerogreen Process Chain: Development of a compact Sorption-Enhanced Water-Gas Shift Reactor". Oral presentation at *Future directions in research on Power-to-X for sustainable chemicals and fuels*, online, 10.02 – 11.02.2022. **1st prize best oral presentation.**

T.J. Stadler, L.J. Bender, J.-H. Knoop, P. Pfeifer. "Sorption-enhanced water gas shift reaction for synthesis gas production from pure CO: Dynamic model development for cyclic process operation". Oral presentation at *13th European Congress of Chemical Engineering (ECCE)*, online, 20.09 – 23.09.2021.

T.J. Stadler, P. Barbig, J. Kiehl, P. Pfeifer. "Sorption-enhanced water-gas shift reaction for synthesis gas production from pure CO: Investigation of sorption parameters and reactor configurations". Poster presentation at *Annual Meeting on Reaction Engineering 2021 (REAKT)*, online, 10.05 – 12.05.2021.

T.J. Stadler, P. Barbig, J. Kiehl, P. Pfeifer. "Experimental investigation of the sorption-enhanced water-gas shift reaction for continuous syngas production in jet fuel synthesis". Poster presentation at *Jahrestreffen der ProcessNet-Fachgruppe Energieverfahrenstechnik (EVT)*, online, 03.03. – 04.03.2021.

T.J. Stadler, P. Barbig, J. Kiehl, P. Pfeifer. "Experimental investigation of the sorption-enhanced water-gas shift reaction for continuous syngas production in jet fuel synthesis". Poster presentation at *International Workshop on CO₂ Capture and Utilization*, online, 16.02. – 17.02.2021.

T.J. Stadler. "Sustainable Aviation Fuels - or: How to enable air traffic with a clear conscience?". Contribution to the competition of ideas launched by "Stiftung Energie und Klimaschutz": *Energie und Umwelt - Meine Idee für morgen*, Stuttgart, Germany, 20.11.2020. **1st prize best contribution.**

T.J. Stadler, A. da Silva Moreira, R. Schulz, F. Vidal Vázquez, P. Pfeifer. "Water-gas shift reaction with in-situ CO₂ removal for syngas production in jet fuel synthesis". Poster presentation at *Jahrestreffen der ProcessNet-Fachgruppe Energieverfahrenstechnik (EVT)*, Frankfurt am Main, Germany, 04.03 – 05.03.2020.

T.J. Stadler, F. Vidal Vázquez, P. Pfeifer. "Advanced Microreactors for the Water Gas Shift Reaction in the Jet Fuel Production from Plasma Splitting of CO₂". Poster presentation at *17th International Conference on Carbon Dioxide Utilization (ICCDU)*, Aachen, Germany, 23.07 – 27.07.2019.

T.J. Stadler, F. Vidal Vázquez, P. Pfeifer, H. Leibold, L. Bünger, D. Stapf. "Advanced Microreactors for the Water Gas Shift Reaction in the Jet Fuel Production from Plasma Splitting of CO₂. Poster presentation at *14th International Conference on Catalysis in Membrane Reactors (ICCMR)*, Eindhoven, The Netherlands, 8.07 – 11.07.2019.

Contents

Preface	i
Abstract	iii
Kurzzusammenfassung	v
List of Publications	ix
1 Introduction	1
1.1 Do we need Sustainable Aviation Fuels?	1
1.2 Framework of this Work	3
1.3 Scope of this Work	5
1.4 Aims and Outline	6
2 Theoretical Background	9
2.1 Power-to-Liquid Processes	9
2.2 Synthesis Gas Production: SEWGS	12
2.2.1 Water-Gas Shift Reaction	12
2.2.2 Adsorption of CO ₂ on Solid Sorbents	16
2.2.3 State-of-the-Art: SEWGS	21
2.3 Hydrocarbon Synthesis and Upgrade	22
2.3.1 Fischer-Tropsch Reaction	22
2.3.2 Hydrocracking	24
3 Methods	27
3.1 SEWGS Experimental Setup	27
3.2 SEWGS Model Development	30
3.3 FT-HC Experimental Setup	33
4 Findings	37
4.1 Choice of Materials, Sorption Parameters and Reactor Configurations	37
4.1.1 Catalyst and Sorbent Characterization	37
4.1.2 Sorption Parameters	40
4.1.3 Reactor Configurations	43
4.2 Numerical Simulation Approaches	44

4.2.1	Conventional Methods: Method-of-Lines and Matlab [®] 's built-in Solver <i>pdepe</i>	44
4.2.2	Novel graphical Implementation in Matlab [®] Simulink	46
4.3	Dynamic Reactor Modeling	49
4.3.1	Pilot Plant Reactor Model	49
4.3.2	Base Case Simulation Results	52
4.4	Impact on subsequent Process Steps	56
4.4.1	Experimental FT-HC Coupling	56
4.4.2	Hydrocarbon Products	57
4.4.3	Carbonaceous Species in the Water Phase	59
5	Scale-Up: SEWGS Module in the <i>Kerogreen</i> Pilot Plant	61
5.1	SEWGS Reactor: Design, Construction and Operating Strategies	61
5.2	SEWGS Module: Planning, Construction and Implementation	65
6	Conclusions and Outlook	69
	Symbols and Abbreviations	73
	Bibliography	77
	Publications	91
P I	Choice of Materials, Sorption Parameters and Reactor Configurations	93
P II	Numerical Simulation Approaches	121
P III	Dynamic Reactor Modeling	143
P IV	Impact on subsequent Process Steps	163

1.1 Do we need Sustainable Aviation Fuels?¹

Human kind needs energy in many forms – yesterday, today, and tomorrow. The important question is: Is the way we are consuming energy today still justifiable tomorrow with the knowledge of what happened yesterday? This question is particularly relevant in the context of climate change. The extensive use of fossil fuels as energy carriers in the past decades has caused an increase in atmospheric greenhouse gas concentrations, especially CO₂. Hence, global average temperature is still rising [1]. To mitigate this effect of human-caused climate change accompanied by massive environmental impact in the future, the above-mentioned question must be rethought.

Therefore, we have to clarify on the one hand if the existing energy resources are being used for the "right purpose", and on the other hand if they are used in the "right way". The first issue, the definition of the "right purpose", is mainly a matter of social needs and aims. Depending on the point of view, it may be difficult to distinguish between more or less important energy consuming sectors. For instance: Is it more important to provide energy for home heating use to ensure peoples' health or for industrial applications to ensure society's wealth? The second issue, the "right way" of using available energy resources, might be easier to evaluate as specific risks and measurable consequences can be attributed to the use of specific technologies and energy carriers, and energy efficiencies can be determined for technical energy conversion processes. These social ("purpose") and technical ("way") issues related to nowadays energy consumption are highly interconnected via political decisions and measures. A political milestone that has been signed by almost 200 signatories is the UN Paris Agreement on Climate Change. The participating parties agreed to restrict the "increase in the global average temperature to well below 2 °C above pre-industrial levels and pursuing efforts to limit the temperature increase to 1.5 °C above pre-industrial levels" [2]. To reach this ambitious goal, especially major contributors to greenhouse gas emissions must undergo drastic changes [3].

A substantial emitter is the international aviation industry, which released about 1 Gt CO₂ to the atmosphere in 2018 [4]. Forecasts for the coming decades suggest a further increase to about 1.2-1.9 Gt CO₂ in 2050 [5]. The projections from 2005 to 2050 are depicted in Figure 1.1 and include assumed improvements in technology, operations, and infrastructure use. Although those predictions were made before the pandemic, they are still of utmost relevance as pre-COVID levels are being reached again rapidly [6]. Even

¹Parts of this section are taken from the author's contribution to the PhD competition launched by "Stiftung Energie und Klimaschutz": *Energie und Umwelt - Meine Idee für morgen*.

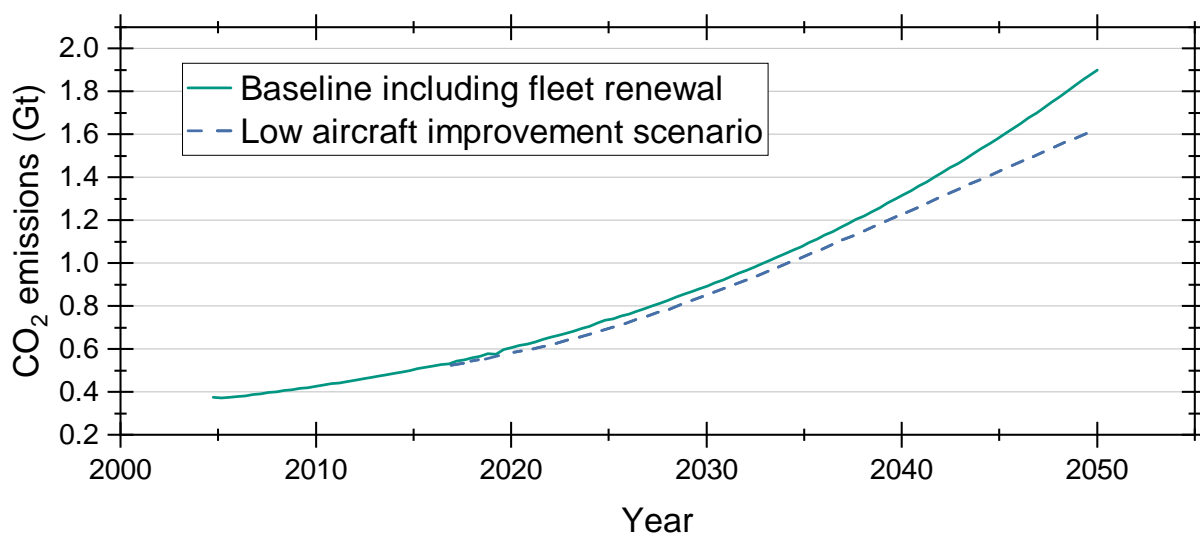


Fig. 1.1: Projections of CO₂ emissions for international aviation in the upcoming decades. Data from [5, 8]. Note: Projections were made prior to the COVID-19 pandemic.

the massive reduction of international air travel as one effect of the COVID-pandemic is expected to have only a short-term impact until about 2024 [7].

This emphasizes that also the aviation sector has to undergo a transition away from fossil fuels until 2050 to still achieve the Paris climate goals [8]. The decarbonization of this sector is particularly difficult due to long technology development and fleet turnover times. However, hydrogen or full-electric powered airplanes can not be envisaged as short- to mid-term solution due to the radical aircraft design changes required for those technologies. Although liquid hydrogen has a three times higher energy density per unit mass than fossil kerosene, its low energy density per unit volume in combination with the need for thick insulation substantially increases the space requirements for this technology. Batteries for full-electric propulsion exhibit a low energy density per unit mass. The heavy machinery limits the use of battery-propelled aircraft to extremely short distance flights of around 80-320 km [9].

This is where Sustainable Aviation Fuels (SAFs) come into play, as these fossil fuel substitutes can be applied using existing infrastructure and propulsion technologies. SAF are synthetic hydrocarbon fuels that physically and chemically resemble conventional jet fuel. These so-called "synthetic jet fuels" can either be produced from biogenic raw material ("biofuels") or from renewable energy and CO₂ ("e-fuels"). By capturing released carbon from the atmosphere, a closed carbon cycle in line with the circular economy principle is realized. Apart from their carbon neutrality, SAF are beneficial to the climate because they largely prevent the formation of soot particles known from the combustion of fossil fuels. Reduced soot emissions decrease the fuels' contribution to cloud formation, which, in turn, would also contribute to global warming [10]. Biofuels are already employed on small scale in aviation, but their market share is limited

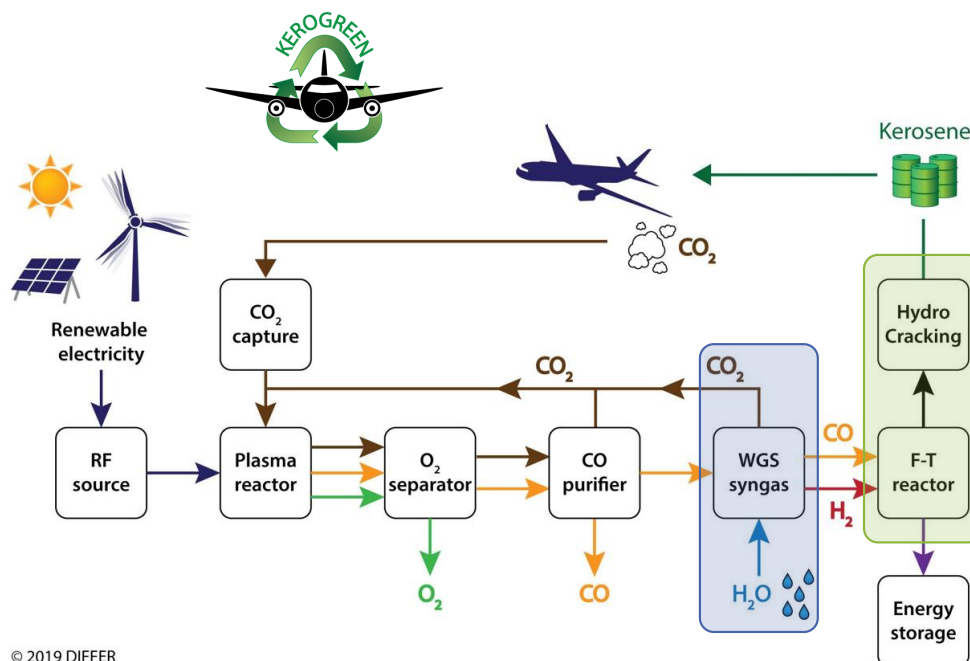
by natural and ethical constraints. In 2024, aviation biofuel production could reach 2.8×10^9 L which corresponds to less than 1 % of the anticipated aviation fuel demand [11]. Currently, their price is three to five times higher than that of fossil-based jet fuel [12]. E-fuel production is realized in so-called Power-to-Liquid (PtL) processes, technologies that are just about to become available on the market. In 2021, the world's first e-kerosene production plant opened in Werlte, Germany [13]. The most significant drawbacks of PtL technologies are the availability and cost of renewable energy and CO₂. CO₂ can be captured directly from the atmosphere (Direct Air Capture (DAC)), a promising technology that still has some challenges ahead of it [8, 14], or from point sources, such as industrial plants that emit large quantities of concentrated CO₂. The significant demand for renewable electricity results in higher prices for e-fuels compared to conventional fuels [15–18]. Unlike biofuels, the production of e-fuels does not require arable land, so they are preferable from an environmental and social point of view [16].

Recognizing the emerging challenges, the EU has committed to ensure the mobility needs of people and goods ("purpose") by means of a low-carbon, circular economy [19]. Their strategy comprises the exploration of synthetic fuels as one "way" of providing energy "for sectors that could remain at least partially dependent on liquid fuels, such as aviation" [19]. For this reason, the title question "Do we need SAFs?" can be answered with "yes". Therefore, the European Commission facilitates research projects such as the Horizon 2020 project *Kerogreen*. This project aims to demonstrate an innovative process chain for sustainable kerosene production and will be presented in more detail in the next section.

1.2 Framework of this Work

Synthetic e-fuels are typically produced in PtL process routes from renewable electricity, air-captured CO₂, and water. Two pathways are currently under discussion: the Fischer-Tropsch (FT) pathway and the methanol pathway [16]. The FT pathway is based on synthesis gas (CO + H₂) (syngas) as feedstock. Syngas can be obtained by means of water electrolysis combined with reverse water-gas shift reaction for reducing CO₂ to CO [20] or by co-electrolysis of steam and CO₂ [21]. It is chemically converted via the FT reaction into a wide range of hydrocarbons. Further upgrading steps, such as heavy hydrocarbons Hydrocracking (HC), are required to produce synthetic hydrocarbon products that are potentially usable as synthetic jet fuel. In the methanol pathway, CO and CO₂ can be taken as carbon source. Together with H₂, they react to the commodity methanol. Methanol can further be processed by oligomerization processes into desired middle distillate hydrocarbons. In both pathways, the required H₂ is typically generated by electrolysis powered by renewable electricity.

In the *Kerogreen* project, however, a novel PtL route based on the FT pathway is investigated that avoids energy-intensive electrolysis (Figure 1.2): the crucial step of CO production is realized using plasma-driven dissociation of CO₂ using renewable electricity. In the plasma reactor, CO₂ is split into CO and O₂ employing microwave plasma technology. O₂ is electrochemically separated through solid oxide membranes. The remaining CO/CO₂ mixture is fed into a Pressure Swing Adsorption (PSA) unit to obtain pure CO. CO partly reacts with H₂O to generate syngas with a H₂:CO ratio of 2 via the Water-Gas Shift (WGS) reaction with in-situ CO₂ removal. Syngas is then used as feed for the kerosene synthesis in the FT reactor with subsequent HC. In this process, carbon-neutrality is achieved as air-captured CO₂ serves as feedstock, and separated CO₂ recovered in the PSA and the WGS unit is recirculated to the plasma reactor. Hence, CO₂ emitted upon fuel usage and CO₂ used in the e-fuel production process form a closed carbon cycle. The overall *Kerogreen* technology is modular, scalable and optimized for decentralized operation in remote areas, for example close to off-shore wind turbine parks. The project aims to design, construct and operate a container-sized demonstration plant located at the Institute for Micro Process Engineering (IMVT) at Karlsruhe Institute of Technology (KIT) to produce 0.1 kg h⁻¹ of synthetic kerosene. The *Kerogreen* consortium consists of six partners from academia and industry from four countries. The project is coordinated by the Dutch Institute for Fundamental Energy Research DIFFER (NL) and carried out in collaboration with the Karlsruhe Institute of Technology KIT (Germany), the Flemish Institute for Technology Research VITO (Belgium), and industry partners: HyGear (Netherlands), Cerpotech (Norway), INERATEC (Germany).



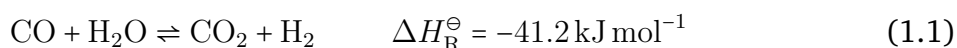
© 2019 DIFFER

Fig. 1.2: *Kerogreen* process chain for carbon-neutral kerosene production from renewable energy, captured CO₂ and water. Marked in blue: syngas production from CO and H₂O via WGS reaction with simultaneous CO₂ separation, and in green: coupled FT-HC reaction for kerosene production from syngas. Adapted figure from [22].

1.3 Scope of this Work

This work deals with the syngas production via WGS (marked in blue in Figure 1.2) and the impacts of this process step on the subsequent kerosene synthesis steps (marked in green in Figure 1.2). For the syngas production step, various WGS and CO₂ separation combinations in one unit operation were theoretically assessed. Three main routes are depicted schematically in Figure 1.3: A) a WGS membrane reactor with a H₂ selective membrane, B) a WGS membrane reactor with a CO₂ selective membrane, and C) a Sorption-Enhanced Water-Gas Shift (SEWGS) reactor.

In all routes, the thermodynamic equilibrium of the WGS reaction (Equation 1.1) is shifted towards the product side by selectively removing one of the product components. Hence, full conversion of CO is likely and the required H₂:CO ratio could be adjusted with a CO bypass flow.



Both membrane-based routes theoretically enable continuous operation, while the SEWGS reactor requires complex operating strategies consisting of cyclic adsorption-

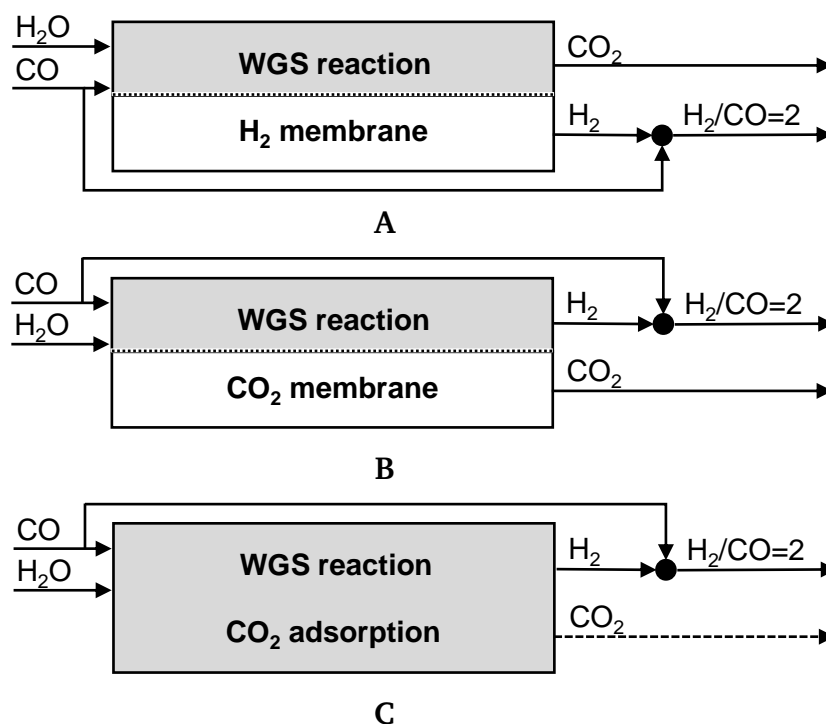


Fig. 1.3: Basic concepts for syngas generation from pure CO and H₂O via WGS with integrated CO₂ separation in one operation unit. A) WGS membrane reactor with a H₂ selective membrane, B) WGS membrane reactor with a CO₂ selective membrane, and C) SEWGS reactor. Full conversion of CO is assumed due to the selective removal of one product component and the required H₂:CO ratio is adjusted with a CO bypass flow.

and regeneration phases. However, the membrane-based routes were discarded. Simulation results as well as literature studies regarding available membrane materials suggested that these routes are less efficient and suitable compared to the SEWGS route. The SEWGS route exhibited superior properties regarding the overall *Kerogreen* integration requirements. Therefore, the SEWGS technology was chosen for this work to be integrated in the *Kerogreen* process chain due to technical and economical reasons.

1.4 Aims and Outline

The main aim of this thesis is to gain insight into the synthesis gas production step from H_2O and CO with simultaneous CO_2 separation via adsorption and to provide a technical solution for performing this unit operation in the *Kerogreen* pilot plant.

For this purpose, the following aspects have been investigated in detail:

- **SEWGS: Lab Scale Experiments** (Section 4.1)
Different sorbent and catalyst materials were characterized to find suitable candidates for SEWGS. A laboratory SEWGS setup was designed and built for further investigations regarding their applicability in a SEWGS reactor system. A beneficial reactor configuration was deduced from experiments in this setup.
- **SEWGS: Modeling and Simulation** (Section 4.2 and Section 4.3)
A time- and space-resolved SEWGS model was developed. It accounts for simultaneous CO_2 adsorption and WGS reaction as well as subsequent desorption. Essential kinetic parameters were determined based on experimental data. The model was solved numerically. A complex system-level model was derived from a single reaction chamber model and enabled simulation with automated switching time adjustment during runtime.
- **SEWGS: Pilot Plant Module** (Section 4.3 and Chapter 5)
A compact SEWGS pilot plant module for decentralized use was designed and built. Simulation-driven guidelines for practical application in the real pilot plant were established and implemented in the automated plant control.
- **FT-HC: Impact of CO_2** (Section 4.4)
The impact of remaining CO_2 from the SEWGS step or omitting the sorption process (solely WGS) on consecutive steps in the *Kerogreen* process chain was elucidated. Experiments with different feeds for combined FT synthesis with subsequent HC were conducted and revealed the importance of the feed gas composition.

The correlation of these aspects is depicted in Figure 1.4.

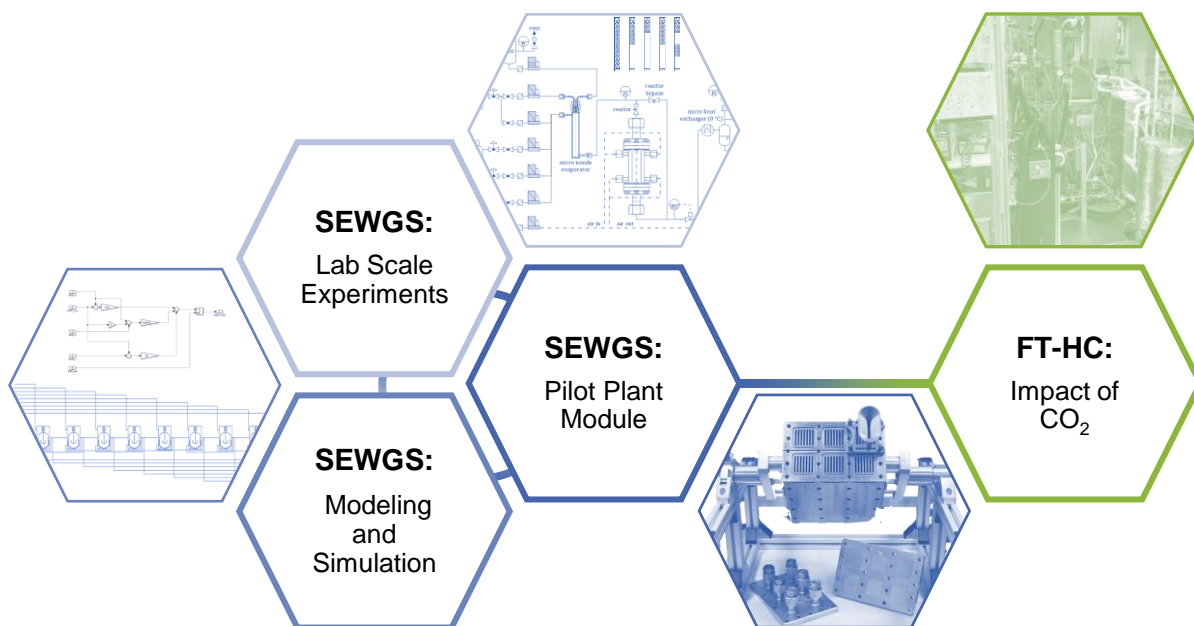


Fig. 1.4: Overview of the main fields of investigations of this thesis. Detailed information regarding *SEWGS: Lab Scale Experiments* can be found in Section 4.1, *SEWGS: Modeling and Simulation* in Section 4.2 and Section 4.3, *SEWGS: Pilot Plant Module* in Section 4.3 and Chapter 5, and *FT-HC: Impact of CO₂* in Section 4.4.

This work is based on four peer-reviewed publications, which are attached in full length at the end of this thesis (Chapter Publications). The following chapters summarize the main findings obtained in those publications. **Chapter 2: Theoretical Background** contains all relevant theoretical background information on the scientific topics covered in this thesis. The experimental setups and basic modeling methods used are briefly discussed in **Chapter 3: Methods**. **Chapter 4: Findings** provides an overview of the main results of each publication. The outcomes of all experimental and theoretical investigations were put into practice in a larger-scale container-sized pilot plant SEWGS module. The design and construction of this module contributed a vital part to this work and is presented in **Chapter 5: Scale-Up: SEWGS Module in the Kerogreen Pilot Plant**. Finally, the main results are summarized in **Chapter 6: Conclusions and Outlook** with suggestions for future investigations.

This chapter gives a concise overview of the currently discussed and researched PtL processes, with a specific focus on the technologies investigated in this thesis: syngas production through the WGS reaction with simultaneous CO₂ removal via selective adsorption on a solid sorbent, a process known as SEWGS; and the subsequent hydrocarbon product synthesis via the FT route with synthetic crude (syncrude) upgrade by means of heavy hydrocarbons HC.

2.1 Power-to-Liquid Processes

PtL processes utilize energy from renewable power generation to convert CO₂ and water into liquid fuels. The significantly higher energy densities of PtL products, in both weight and volume, compared to Li-ion batteries or Power-to-Gas (PtG) products like H₂ and CH₄, make them especially appealing for hard-to-decarbonize industries such as aviation, shipping, and heavy transportation [23]. Various PtL pathways are currently the subject of research and development. The most commonly discussed processes are depicted in Figure 2.1 and shortly described in the following section.

Sustainable Feedstock

Besides the requirement of electricity from renewable sources, such as solar, wind, geothermal or hydro power, all PtL pathways require the provision of water for H₂ generation, and CO₂ as carbon source.

The water demand for PtL fuel is mainly defined by the reaction stoichiometry of the fuel synthesis and accounts to about 1700 m³ water for 1 kt PtL fuel. Despite the fact that the water demand for PtL is relatively low compared to the water demand for biofuel production (up to 15 000 times lower), considerations of local water availability and supply options are still important. These aspects need to be evaluated in local environmental impact assessments when seeking approval for PtL plants [16].

CO₂ can either be obtained from point sources, such as industrial sites or biomass-based applications, or directly captured from the air. Although the CO₂ concentration in the atmosphere is significantly lower compared to point sources (0.04 % and >10 %, respectively [24]), the first commercial DAC plant powered by geothermal energy recently started operating in Hellisheidi, Island. Climeworks' *Orca* is said to be the world's first and largest DAC and storage plant with an annual capture capacity of 4000 t CO₂ [25]. A plant with an even higher capacity of 36 000 t, *Mammoth*, is currently under construction [26].

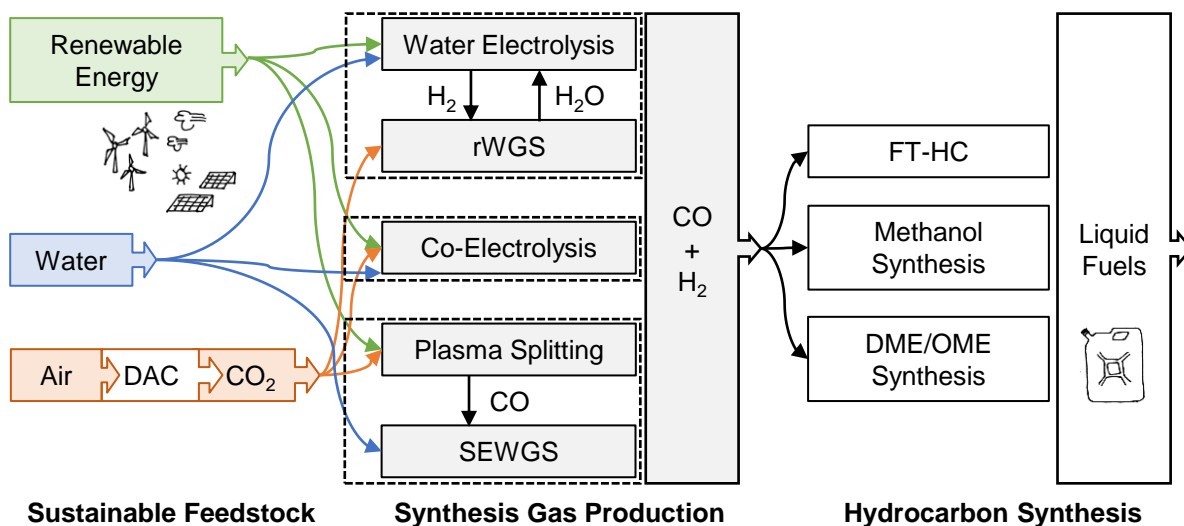


Fig. 2.1: Overview of commonly discussed PtL pathways. Electricity from renewable sources, water and air-captured CO₂ are used to produce sustainable hydrocarbon fuels.

If the renewable electricity is additionally generated (and not withdrawn from other purposes), DAC-based PtL processes result in a closed carbon cycle. They facilitate carbon neutrality of the entire process chain from CO₂ capture to synthetic fuel combustion.

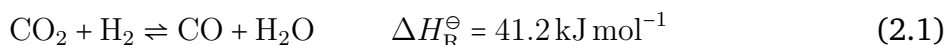
Synthesis Gas Production

As direct CO₂ activation is still in its early stages of research and development [27], the majority of PtL processes require the production of syngas as intermediate product for subsequent hydrocarbon synthesis. Syngas, as defined in this work, is composed of CO and H₂. Unlike traditional industrial syngas production routes, such as gasification, steam reforming or partial oxidation of fossil resources, alternative routes are developed and improved in the frame of sustainable PtL processes.

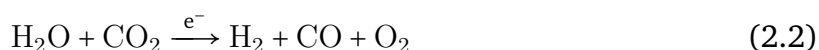
The current state-of-the-art to provide syngas for PtL comprises water electrolysis powered by renewable energy for H₂ generation in combination with the so-called reverse Water-Gas Shift (rWGS) reaction. Water electrolysis can be performed at low temperatures (50 °C to 80 °C) in an Alkaline Electrolyzer (AEL) or Polymer Electrolyte Membrane Electrolyzer (PEM-EL). At high temperatures (600 °C to 900 °C), water steam can be electrolyzed in a Solid-Oxide Electrolysis Cell (SOEC) [16, 23, 28]. In all systems, water (or steam) is electrochemically split into H₂ and O₂.

The current industrial standard of electrolyzers is based on the AEL technology. This technology operates with low current density and is less suitable for dynamic applications due to its low load-flexibility. PEM-EL are available in small and medium scale and enable higher current densities. They can operate under pressure and provide higher operational flexibility than AEL. Utilizing high-temperature electrolysis (SOEC) can substantially decrease electricity requirements compared to low-temperature electrolysis, resulting

in an overall system-level advantage when appropriate heat sources, like heat from the exothermic FT synthesis, can be used for steam generation. Additionally, SOEC systems can perform with higher efficiencies of >80 % (low-temperature AEL or PEM-EL: 60 % to 70 %). However, the SOEC technology is (currently still) less developed and provides disadvantages in terms of system costs and long-term durability [23]. As illustrated in Figure 2.1, a portion of the H₂ stream produced by water electrolysis reacts via rWGS reaction (Equation 2.1) with captured CO₂ to produce CO under external heat supply.



Recently, progress has been made in the development of SOEC-based co-electrolyzers, which enable the conversion of CO₂ and steam into CO and H₂ in one single step at high temperatures (850 °C, Equation 2.2) [29]. This technology could eliminate the need for separate rWGS and generate more syngas output using the same amount of renewable energy input in comparison to other syngas production pathways [30]. In the frame of the research project *Kopernikus P2X*, the German company Sunfire achieved an output of up to 220 kW with an electrical efficiency of more than 85 % and marked an important step towards the industrial use of the co-electrolysis technology [31].



A novel syngas production route is currently being investigated in the *Kerogreen* project. The concept comprises the dissociation of CO₂ into CO and O₂ through a plasma generated with microwave radiation in a plasmolysis unit with subsequent O₂ removal in an advanced solid oxide membrane. The remaining CO/CO₂ mixture is separated in a PSA unit to obtain pure CO. CO is then converted into H₂ by means of the WGS reaction (Equation 1.1) with simultaneous separation of the generated CO₂ by adsorption (SEWGS). Detailed information on the SEWGS concept can be found in Section 2.2.

Hydrocarbon Synthesis

The conversion of syngas into hydrocarbons is the next step in PtL process chains. Currently, there are two primary pathways being discussed: the FT pathway and the methanol pathway.

The FT reaction has been applied for decades in industrial scale [32]. It generates a variety of different long-chain hydrocarbons, which can differ based on the process design and operation. This syncrude mixture is further processed through refining steps to produce fuels that have similar chemical properties to conventional fossil fuels, such as diesel, gasoline, and kerosene, or basic chemicals for the chemical industry. These refining steps can be carried out in existing petroleum refineries alongside the processing

of fossil crude oil. The resulting fuels are so-called "drop-in fuels" without the need for modifications to the existing combustion engines or infrastructure used for storing and transporting fuels, and abide by the American Society for Testing and Materials (ASTM) norms. Therefore, the FT pathway is employed in the majority of large-scale PtL projects, and also used in the frame of this work. Detailed information regarding the FT reaction as well as heavy hydrocarbon HC as upgrading step can be found in Section 2.3.

Methanol synthesis is also a well-established large-scale process that operates under moderate conditions and provides very high product purities [32]. As the use of pure methanol as a fuel would require modified combustion engines, methanol is rather used as a blending component in today's combustion engines at concentrations of up to 3%. Alternatively, methanol or its dehydrated form, Dimethyl Ether (DME), are further processed to C₂-C₄ olefins (Methanol-to-Olefins (MTO) or Dimethyl Ether-to-Olefins (DTO), respectively) with subsequent oligomerization to hydrocarbons in the gasoline and jet fuel range [33].

State-of-the-Art: PtL in Germany

As a result of the German "Energiewende" envisioned by policymakers and society, PtL processes are becoming up-scaled for market rollout of e-fuels [34]. A selection of the most recently announced PtL projects in Germany based on the FT pathway is listed in Table 2.1.

2.2 Synthesis Gas Production: SEWGS

The following section discusses the WGS reaction as well as the adsorption of CO₂ on solid sorbent materials, and gives insight into the combination of both processes by means of the SEWGS reaction.

2.2.1 Water-Gas Shift Reaction

The conversion of CO and H₂O to CO₂ and H₂ is known as WGS reaction (Equation 1.1). The reaction was first described in by Fontana in 1780 [35], and patented by Mond and Langer for fuel cell applications in 1888 [36]. From 1913 on, the WGS reaction was employed in large scale in the frame of the Haber-Bosch process for ammonia production [37]. Until today, the WGS reaction plays an important role in industrial processes involving or producing H₂ [38]. WGS is typically employed to decrease the CO content in feed gases of fuel cell applications, or to increase the hydrogen yield in reforming processes.

Tab. 2.1: Overview of selected large-scale PtL projects in Germany based on the FT pathway.

Stakeholder	Project	Location	Technology	Capacity	Year	Ref.
atmosfair	FairFuel	Werlte	Biomass/DAC + PEM-EL/rWGS + FT	350 t/a	2021	[39]
DLR	TPP (DS)	not yet announced	Biomass + Electrolysis (EL)/rWGS + FT	10000 t/a	~2026	[40, 41]
KIT	Energy Lab2.0	Eggenstein-Leopoldshafen	DAC + PEM-EL/rWGS + FT	200 l/d	2019	[42–44]
INERATEC		Frankfurt-Höchst	Biomass + industrial H ₂ /rWGS + FT	2500 t/a ¹	~2024	[45, 46]
H&R		Hamburg	Biomass + PEM-EL/rWGS + FT	350 t/a ¹	2022	[47]

¹ This plant has been announced to become the "world's largest PtL pioneering plant" [45].

Thermodynamic Considerations

The WGS reaction is a moderately exothermic equilibrium reaction. As can be seen in Figure 2.2A and from the widely used Equation 2.3 [48], the equilibrium constant decreases with increasing temperature.

$$K_{\text{eq}} = \exp\left(\frac{4577.8}{T} - 4.33\right) \quad (2.3)$$

An increase in temperature makes the product formation thermodynamically less favorable, resulting in lower H₂ yields at higher temperatures. At temperatures above 830 °C, the equilibrium constant is <1 and the reverse reaction, rWGS, is favored. However, an increase in temperature leads to a higher reaction rate. Hence, a balance between favorable thermodynamic and kinetic conditions must be found. For that reason, the combination of subsequent High-Temperature (HT) and Low-Temperature (LT) WGS in a multi-stage reactor setup is commonly found in industry to achieve CO contents below 0.5 % [38, 49, 50]. In the HT shift on a Fe-based catalyst (320 °C to 450 °C) in the first stage, CO levels are reduced to 3 % to 5 % at relatively fast reaction rates requiring relatively small catalyst bed volumes. In the LT shift on a Cu-based catalyst (200 °C to 250 °C) in the second stage, higher CO conversion limited by the reaction equilibrium can be achieved and the CO content is reduced to 0.1 % to 0.3 %.

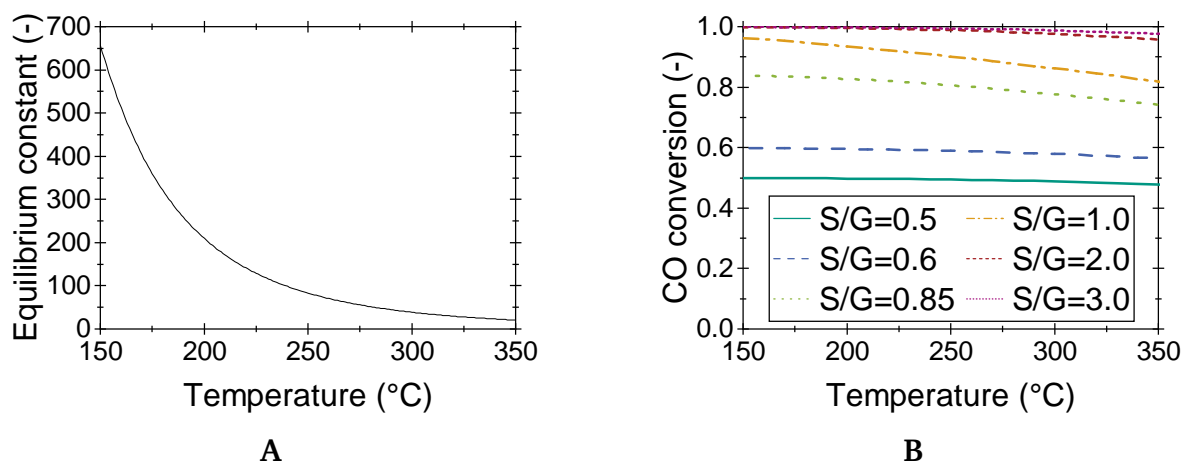


Fig. 2.2: Temperature dependence of A) WGS equilibrium constant (Equation 2.3, and B) CO equilibrium conversion for various steam-to-gas ratios.

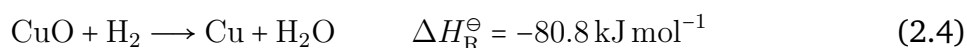
Due to the reversible nature of the WGS reaction, the forward reaction is limited by the presence of the reaction products according to LeChatelier's principle. Vice versa, the removal of CO_2 or the addition of steam promote the achievable CO conversion. Figure 2.2B illustrates the influence of the reactant gas composition: an increasing steam-to-gas ratio ($\text{H}_2\text{O}:\text{CO}$) results in a higher equilibrium CO conversion.

LeChatelier's principle also predicts that the reaction pressure does not affect the thermodynamic WGS equilibrium due to the constant number of moles. However, the total pressure increases the reaction rate on the way to the equilibrium and influences the conversion of CO in a beneficial manner in industrial applications.

Heterogeneous Low-Temperature Water-Gas Shift

Many catalysts were suggested and researched for the heterogeneous LT WGS: non-noble metal based catalysts (Cu, Ni), or noble metal based catalysts (Pt, Ru, Rh, Pd, Au) deposited on partially reducible oxides (CeO_2 , ZrO_2 , TiO_2 , Fe_2O_3 , mixed oxides) [38]. In this study, a conventional $\text{Cu}/\text{ZnO}-\text{Al}_2\text{O}_3$ is utilized, similar to the majority of industrial processes.

The Cu metal crystallites serve as the active species within the catalyst, while ZnO acts as a functional promoter to enhance the catalyst's activity. Al_2O_3 is a primarily inactive structural promoter, it helps dispersing the active sites, to stabilize them against thermal sintering, and minimizing pellet shrinkage to enhance the strength of the catalyst [51]. To obtain active Cu metal crystallites for the WGS operation, CuO needs to be initially reduced in H_2 (Equation 2.4).



As Cu is prone to thermal sintering, temperatures exceeding 300 °C should be avoided during both the catalyst reduction and WGS operation. The lower operating temperature is limited by the dew point of the mixture under industrial conditions. Due to its intolerance to sulphur, halogens, and unsaturated hydrocarbons, the Cu/ZnO-Al₂O₃ catalyst requires protection from these compounds.

Although the WGS reaction being known for over two centuries, the complete understanding of its detailed reaction mechanism has yet to be fully uncovered [38, 50, 51]. Most studies explain the WGS reaction over a metal oxide catalyst with one of the following reaction pathways:

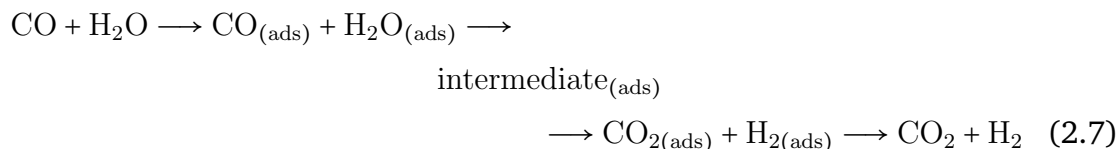
- **Regenerative mechanism (reduction-oxidation cycle)**

The regenerative mechanism is based on the Eley-Rideal model, wherein only one of the reactant molecules adsorbs on the catalyst surface and reacts directly with the other molecule from the gas phase (Figure 2.3A). In this mechanism, H₂O is dissociated on the catalyst surface producing H₂ and oxidizing a vacant reduced active site. The oxidized catalyst site is reduced by CO to form CO₂, leaving again a vacant reduced active site on the catalyst surface to complete the catalytic cycle.



- **Associative mechanism**

The associative mechanism is based on the Langmuir–Hinshelwood model, wherein both reactant molecules adsorb on adjacent active sites on the catalyst surface, and the adsorbed molecules then react in a bimolecular reaction (Figure 2.3B). In this mechanism, H₂O and CO adsorb on the catalyst surface and interact to form an adsorbed intermediate. The intermediate then splits into CO₂ and H₂. Although numerous authors endorse this mechanism, there is still a lack of consensus regarding the nature of the intermediate species. Proposed reaction intermediates include carboxyl- or formate-like species [52, 53].



While the regenerative mechanism is commonly used to describe the HT WGS reaction on Fe-based catalysts, the predominant mechanism in the LT WGS is still controversially discussed in literature [38, 54].

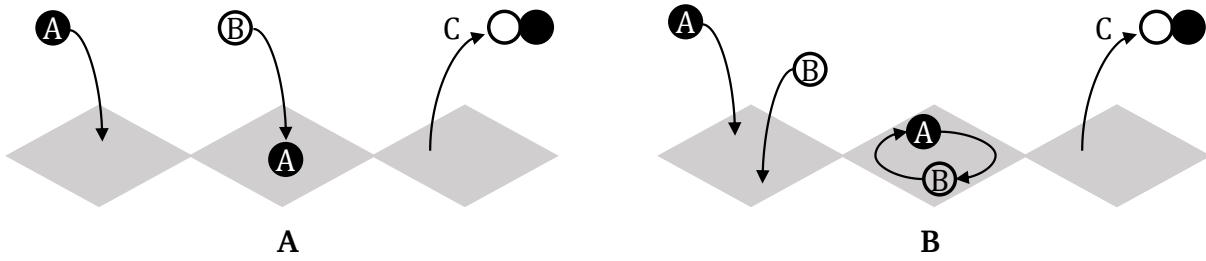


Fig. 2.3: Mechanistic models for describing bimolecular reactions ($A + B \rightarrow C$) in heterogeneous catalysis. A) Eley-Rideal mechanism, and B) Langmuir-Hinshelwood mechanism.

Despite the ongoing discussions regarding the detailed reaction mechanism on LT WGS catalysts, various empirical models have been developed based on experimental results. A comprehensive overview of kinetic rate expressions based on the above mentioned mechanisms is given in the literature [38, 51, 55]. Unlike rate expressions derived from detailed reaction mechanisms and rate-determining steps, the power-law represents a simple empirical rate expression that does not take into account any specific mechanism [50]. Various studies found that the power-law type expression given in Equation 2.8 and Equation 2.9 delivers satisfying descriptions of their experimental observations for the WGS forward reaction rate [56–61]. This approach was also chosen for the transient reactor description in this work. Table 2.2 presents various power-law parameters from different studies for Cu/ZnO-Al₂O₃ catalysts, including the data obtained in this research.

$$r_{\text{WGS}} = k_{\infty} \cdot \exp\left(-\frac{E_a}{R \cdot T}\right) \cdot p_{\text{CO}}^{e1} \cdot p_{\text{H}_2\text{O}}^{e2} \cdot p_{\text{CO}_2}^{e3} \cdot p_{\text{H}_2}^{e4} \cdot (1 - \delta) \quad (2.8)$$

$$\delta = \frac{p_{\text{CO}_2} \cdot p_{\text{H}_2}}{K_{\text{eq}} \cdot p_{\text{CO}} \cdot p_{\text{H}_2\text{O}}} \quad (2.9)$$

Tab. 2.2: Overview of power-law parameters for Cu/ZnO-Al₂O₃ catalysts.

Arrhenius Parameters		Reaction Order				Temperature	Study
k_{∞}	E_a (kJ mol ⁻¹)	$e1$	$e2$	$e3$	$e4$	T (°C)	
2.96×10^5	47.4	1	1	0	0	120 to 250	[56]
3.99×10^5	52.8	1	1	0	0	160 to 250	[57]
-	79.0	0.8	0.8	-0.9	-0.9	190	[58]
-	86.5	1*	1.4	-0.7	-0.9	180 to 200	[59]
$5.37 \times 10^{-7**}$	-	0.45	0.07	0	0	200	[60]
4.9×10^6	47.0	1	1	0	0	123 to 175	[61]
2.01×10^5	51.8	1	1	0	0	250	[P3]

* fixed to unity, ** area related

2.2.2 Adsorption of CO₂ on Solid Sorbents

As discussed above, the selective removal of a product component from the reaction mixture favors the forward reaction according to LeChatelier's principle and hence,

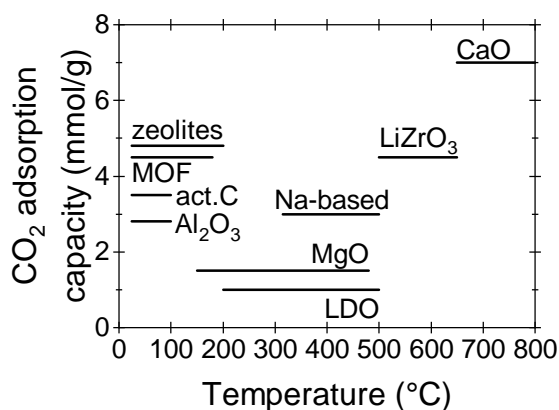


Fig. 2.4: CO₂ adsorption capacities and temperature ranges of selected CO₂ adsorbents [64, 65].

increases the H₂ production and purity. This approach also allows for the separated component to be recycled. For these reasons, an advanced SEWGS system with in-situ CO₂ adsorption was investigated in this work. Therefore, a suitable solid sorbent needed to be mixed with the WGS catalyst to be integrated into the reactor.

Choice of Sorbent Materials

A sorbent suitable for use in SEWGS systems must possess the following characteristics under WGS operating conditions to be technically and economically viable [62, 63]:

- High selectivity towards CO₂
- High adsorption capacity for CO₂
- Fast adsorption and desorption kinetics
- Mechanical stability
- Thermal stability
- Low energy requirement during regeneration
- Stable sorption properties during cyclic operation
- Stable sorption properties in the presence of steam

An overview of selected adsorption capacities as well as temperature ranges of typically employed CO₂ sorbents is given in Figure 2.4. Further information can be found elsewhere [62, 64, 65].

For temperatures below 120 °C, physisorbents such as zeolites [66–68], activated carbons [67, 69, 70], alumina oxide [71], and Metal Organic Frameworks (MOFs) [72–75] have been suggested. The physisorption is generally rather weak and sensitive to temperature and less suitable for SEWGS applications [65]. Chemisorbents, however,

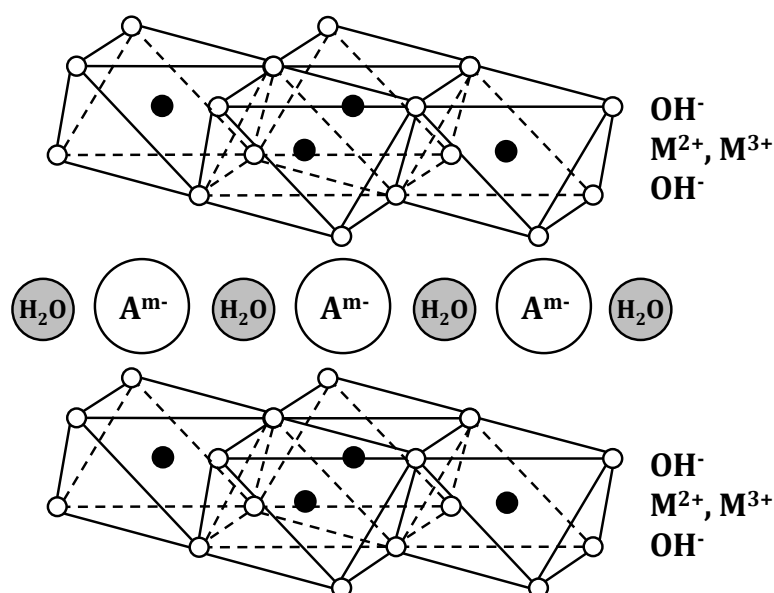


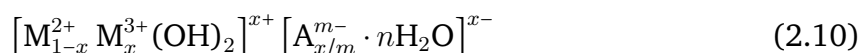
Fig. 2.5: 3D structure of a LDH with two positively charged brucite-like layers and an interlayer region. Adapted figure from [63].

yielded higher adsorption capacities at temperatures above 120 °C. Among the most discussed chemisorbents are magnesium oxide (and MgO-based materials) [76, 77], Layered Double Oxides (LDOs) [78–81], lithium zirconates [82, 83], calcium oxides [84–87], and sodium-based materials [88]. LDOs, derived from Layered Double Hydroxides (LDHs), exhibit a reasonable combination of CO₂ capacity and cyclic stability for SEWGS applications due to their moderate CO₂ adsorption heat. Additionally, they are highly selective towards CO₂, and the presence of steam has been reported to have a positive impact on their capacity [80]. Their cheap price makes them especially interesting for large scale applications. Therefore, various authors suggested LDOs as most promising sorbents for SEWGS processes [62–65, 89]. LDOs, precisely Hydrotalcite-Derived Mixed Oxides (HDMOs), are also employed in this work and will be presented in more detail in the next section.

Hydrotalcite-derived Materials as CO₂ Sorbents

LDHs are classified as anionic clay minerals. They possess a two-dimensional structure consisting of two brucite-like layers with positively charged divalent cations (M²⁺), partially substituted by trivalent cations (M³⁺). These positive ions occupy the center of octahedral sites within hydroxide sheets, while the vertices of these sheets contain hydroxide anions. Always three octahedral cations share one hydroxyl group, which extends towards the interlayer region [90]. The excess charge in the interlayer is balanced by highly disordered anions (A^{m-}) and water molecules [91]. Figure 2.5 depicts the neutral structure of LDHs.

The general chemical formula of LDH is given in Equation 2.10, with x determining the partial substitution of M^{2+} with M^{3+} , typically ranging between 0.17 and 0.33 [91].



Within the naturally occurring mineral LDH, also known as Hydrotalcite (HTC), the divalent metal is Mg^{2+} , the trivalent cation is Al^{3+} , and the compensating anion is CO_3^{2-} . The resulting formula is $\text{Mg}_6\text{Al}_2(\text{OH})_{16}\text{CO}_3 \cdot 4\text{H}_2\text{O}$. In the case of synthetically produced LDHs, it is possible to utilize various combinations of anions and cations, as listed in Table 2.3.

Tab. 2.3: Overview of selected anions and cations used in synthetic LDHs [62, 92].

M^{2+} :	Mg^{2+} , Ca^{2+} , Ni^{2+} , Zn^{2+} , Cu^{2+} , Mn^{2+}
M^{3+} :	Al^{3+} , Fe^{3+} , Cr^{3+} , Co^{3+} , Ga^{3+}
A^{m-} :	CO_3^{2-} , SO_4^{2-} , SO_3^{2-} , NO_3^- , Cl^- , OH^-

As-synthesized LDHs do not possess great CO_2 adsorption capacities, as their interlayers are already saturated with anions, and water molecules prevent the permeation of CO_2 to the Lewis-basic active sites. Their adsorption properties can be enhanced by means of controlled thermal activation (calcination), by changing the nature and ratio of M^{2+}/Mg^{3+} cations as well as the type of interlayer anion, or by doping with alkaline metals.

The adsorption characteristics of as-synthesized LDHs can be improved through calcination in N_2 atmosphere for at least 4 h. Calcination temperatures of up to 400°C enable the release of the interlayer ions and water, resulting in highly amorphous mixed oxide materials with higher surface area and increased Lewis-basicity. During this thermal treatment, LDHs undergo a structural transformation into LDOs, thereby exposing appropriate basic properties for CO_2 adsorption under WGS conditions [93, 94].

The molar ratio of divalent-to-trivalent cations considerably determines the adsorption behavior of LDOs. Typically, the alumina content in HTC is below 50%. With increasing alumina content, the loading of the hydroxide layer as well as the number of surface defects increases, whereas the interlayer distance decreases [80, 95, 96]. These effects controversially influence the adsorption properties, and a balance between stronger sites and lower basic density must be found. Recently, Macedo et al. tested Mg/Al molar ratios up to 20 and suggested an optimum ratio between 4 to 10 [97].

It was also found that the type of charge balancing anion present in the interlayer significantly influences the adsorption capacity of LDOs. In HTC, CO_3^{2-} anions lead to

higher adsorption capacities than OH^- [63], due to their higher loading and greater interlayer spacing (0.756 nm for carbonates compared to 0.755 nm for hydroxides) [91].

Various studies confirm the positive effect of alkaline (e.g. Na, K, Cs, Li) impregnation on the CO_2 adsorption capacity of LDOs [98–103]. Alkali metal ions accumulate on the octahedral structure, increasing the number and strength of the basic adsorption sites [104, 105]. Especially the impregnation of the calcined HTC (HDMO) with potassium (Potassium-impregnated Hydrotalcite-Derived Mixed Oxide (K-HDMO)) enables great potential for improvements and received special attention in the frame of sorption-enhanced reactions [79, 100, 106–108].

Additionally, it has been demonstrated that the presence of water during CO_2 adsorption has a positive impact on the adsorption capacity of LDO. Improvements of up to 10 % associated with enhanced cyclic behaviour on K-HDMO were reported by Ding et al. [106]. Ram Reddy et al. reported an even higher increase of more than 15 % (from 0.61 mmol g^{-1} to 0.71 mmol g^{-1}) in a wet feed compared to a dry feed [109]. Water partially reverses the dehydroxylation achieved during calcination and thus, creates additional adsorption sites. This finding is of utmost importance for SEWGS applications, as the presence of water is inevitable during the WGS reaction.

Sorption of CO_2 on Hydrotalcite-derived Materials

The process of CO_2 adsorption occurs on active basic sites on the surface of the solid sorbent. While LDHs feature only weak Brønsted-type basic sites, LDOs exhibit different types of Lewis-basic active sites for CO_2 adsorption: O^{2-} (strong basicity), Mg-O (intermediate basicity), and OH^- (low basicity).

Leon et al. showed in infrared spectroscopic studies that CO_2 coordinates weakly on surface OH^- groups to form bicarbonate anions, whereas bidentate carbonates (chelating or bridging) are build on adjacent cationic sites (such as Mg-O pairs), and unidentate carbonate species are formed on O^{2-} sites. Figure 2.6 shows the different binding types. Unidentate species bound on the strongest adsorption sites were identified as the cause of irreversible adsorption, whereas bidentate carbonates and surface bicarbonates contributed to highly reversible adsorption [93].

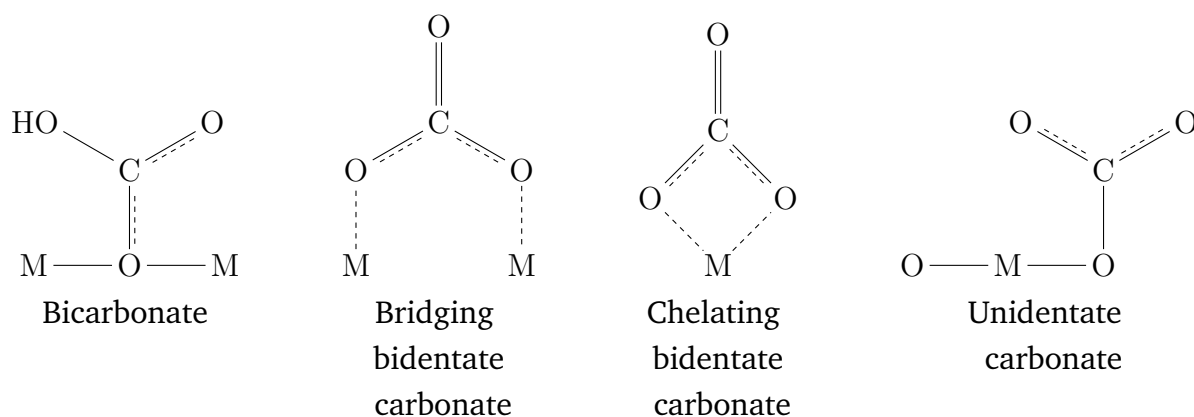


Fig. 2.6: Bicarbonate, bidentate and unidentate carbonate formation.

2.2.3 State-of-the-Art: SEWGS

The principle of combined WGS reaction with simultaneous CO₂ removal by means of adsorption was first patented by Gluud et al. in 1931. The authors presented an invention for H₂ production and explained that "the carbon monoxide and steam being brought to react with each other in such manner that the carbon dioxide formed is removed at once from the reaction phase" [110]. By combining an active WGS catalyst with a selective CO₂ sorbent in a packed bed reactor, an increase in CO conversion can be achieved by displacing the thermodynamic equilibrium towards the H₂ and CO₂ production side according to LeChatelier's principle.

Hence, the yield and purity of the desired product, H₂, can be improved, and CO₂ is separated and can potentially be reused. In a SEWGS system, the previously separate steps of H₂ production and CO₂ removal are combined into a single unit operation. This simplification has the potential to save costs and improve the overall energy efficiency [111, 112]. However, as the sorbent must be regenerated regularly to ensure continuous operation, the design of the reactor becomes more complex [113]. At least two reactors that run alternately in reactive adsorption or regeneration mode are needed for continuous H₂ production. Gazzani et al. proposed an optimal range of six to nine reactor units for cyclic operation, considering factors such as efficiency and economic considerations [114]. A cycle typically consists of a reactive adsorption, depressurization, regeneration, and pressurization step. Regeneration can be initiated through temperature or pressure variations to release the adsorbate from the sorbent. Usually, PSA concepts are employed in SEWGS systems, accompanied using purge gas to further implement a concentration change and to reduce the partial pressure [65].

In the last decades, there has been a growing scientific interest in the topic of sorption-enhanced reactions within the context of hydrogen economy and fuel cell applications. Various studies have suggested that sorption-enhanced hydrogen production is not only a viable option for WGS reaction [115–118], but also for methane steam reforming [119–

122], steam gasification of biomass [123], glycerol steam reforming [124], ethanol steam reforming [125], and dimethyl ether [126–128]. In the case of SEWGS, research focused on the development of advanced sorbent materials with suitable sorption properties and regenerability in the presence of a WGS catalyst [94, 97, 103]. Furthermore, significant effort has been made in modeling the SEWGS process to obtain optimized process strategies and ideal operating conditions by means of simulative parameter studies [115, 129–133].

Although the sorption-enhanced concept has been known for almost a century for the WGS reaction, the SEWGS technology has not been implemented on an industrial scale yet and only a few large-scale pilot plants were presented so far. In 2013, Jansen et al. declared that the "SEWGS Technology is Now Ready for Scale-up!". Based on experimental and theoretical investigations in the *CAESAR* project, they concluded that the SEWGS technology can be classified at Technology Readiness Level (TRL) 5-6 [134]. The developed technology was subsequently up-scaled in the *STEPWISE* project to demonstrate its feasibility in an industrial setting. A full scale pilot plant at TRL 6 was constructed near a steel manufacturing site in Luleå, Sweden, with a capacity of $1500 \text{ t d}^{-1} \text{ CO}_2$ [135]. More recently, Sebastiani et al. published modeling results for the cyclic operation in five out of six available columns in this plant. Each vessel had a diameter of 0.038 m and a height of 6 m [136]. Their study demonstrated the feasibility of describing the experimentally observed phenomena and adequately capturing the periodic fluctuations of the nominal hydrogen flow (15 L min^{-1}). However, this thesis deals with a rather unconventional approach for decentralized SEWGS operation in remote areas. It presents the design and construction of a compact SEWGS reactor consisting of six individually fed reaction chambers.

2.3 Hydrocarbon Synthesis and Upgrade

2.3.1 Fischer-Tropsch Reaction

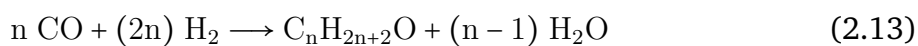
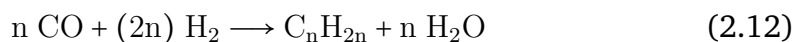
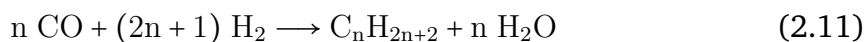
The FT synthesis was first patented by Fischer and Tropsch in 1925 [137]. It chemically converts syngas into a mixture of hydrocarbons and water. The reaction is highly exothermic, whereby the reaction heat depends on the produced hydrocarbon species. The product range includes hydrocarbons with one carbon atom (CH_4) up to more than 100 carbon atoms. The composition of hydrocarbons, whether linear or branched, saturated or unsaturated, and oxygen-containing species, depends on the reaction conditions (pressure, temperature, residence time, $\text{H}_2:\text{CO}$ ratio), and the catalyst employed [138].

Potential metal catalysts for the heterogeneously catalyzed FT are iron, cobalt, nickel, and ruthenium. Co exhibits a high degree of selectivity in synthesizing linear saturated hydrocarbons with a suitable average chain length for the production of synthetic

kerosene at low temperatures (200 °C to 250 °C). Therefore, a Co-based catalyst was employed in this work.

The FT synthesis is a polymerization-type reaction and proceeds in three macroscopic steps: 1) chain initiation, 2) chain propagation and 3) chain termination. The detailed reaction network has not been fully elucidated yet, but the following three mechanisms are predominantly being discussed: 1) carbide mechanism, 2) enol-based mechanism, and 3) CO insertion mechanism [139]. The differences in those mechanisms primarily arise from the suggested monomer on the catalyst surface and the type of chain growth. All mechanisms serve to explain the synthesis of different FT products through various chain termination steps. However, none of the mechanisms is capable to describe the formation of all FT products. Therefore, a combination of different mechanisms is typically assumed.

The main reaction products on Co-based catalysts at low temperatures include linear alkanes (Equation 2.11), alpha-alkenes (Equation 2.12), and minor quantities of oxygenates, such as alcohols (Equation 2.13) [139]. According to Equation 2.11, a molar H₂:CO ratio of two is required for the desired alkene production.



The simplified distribution of FT product species can be described using the Anderson-Schulz-Flory (ASF) model. Equation 2.14 calculates the weight fraction of a product species with *n* carbon atoms for a given chain growth probability *α*. The chain growth probability is influenced by both the reaction conditions and the catalyst employed. Figure 2.7A depicts the accumulative weight fractions of lumped product groups as a function of the chain growth probability. The lumps are classified as follows: C₁-C₄: gases, C₅-C₉: naphtha, C₁₀-C₁₄: kerosene, C₁₅-C₂₂: gas oil, C₂₂₊: waxes. It can be deduced that the fraction of long-chain hydrocarbons increases with increasing chain growth probability, and the primary selectivity towards kerosene is mathematically limited to a theoretical maximum of 23 % for *α* = 0.84 according to the ASF model. In Co-based FT processes, typical chain growth probability values from 0.88 to 0.95 are reported [140]. The ASF distribution for *α* = 0.9 is shown in Figure 2.7B. The maximum fraction is found for species with around 10 carbon atoms.

$$w_{ASF} = n_C (1 - \alpha)^2 \alpha^{(n_C - 1)} \quad (2.14)$$

As mentioned above, the ASF distribution is more of an approximation and does neither accurately represent the actual composition of products nor provide information about

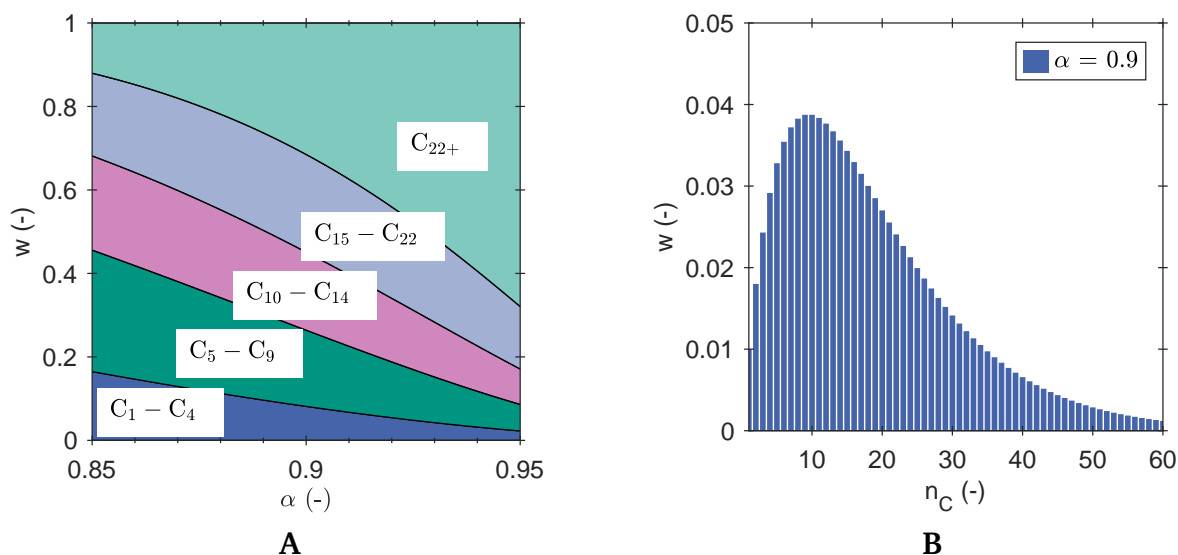


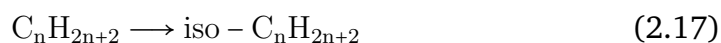
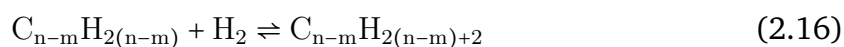
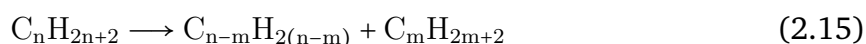
Fig. 2.7: ASF syncrude composition for **A**) lumped product groups (C_1 - C_4 : gases, C_5 - C_9 : naphtha, C_{10} - C_{14} : kerosene, C_{15} - C_{22} : gas oil, C_{22+} : waxes), and **B**) chain growth probability $\alpha = 0.9$. Figure A from [P4].

the type of species formed. The selectivity towards methane is typically higher than predicted by ASF, whereas the C_2 selectivity is lower. Also the amount of long-chain hydrocarbons is often underestimated, as secondary reactions involving previously produced FT products are not considered in the ASF model. Re-adsorption of alkenes may influence the chain propagation and lead to longer product species. Hence, the chain growth probability is not constant and increases slightly with increasing chain length [139].

2.3.2 Hydrocracking

The FT syncrude needs to undergo additional upgrading processes to increase the fraction of the intended target product, e.g. kerosene. Although HC has been largely employed in refineries for decades, its application in combination with FT products is rather new and has raised increasing interest during the last years [141].

HC is a catalytic cracking process used to convert long-chain hydrocarbons into mainly middle distillates. Along with cracking reactions (Equation 2.15), de/hydrogenation of the cracking products (Equation 2.16), and skeletal izomerization of n-alkanes to iso-alkanes (Equation 2.17) take place in the presence of H_2 .



HC is commonly conducted at high pressures (35 bar to 70 bar) and temperatures (325 °C to 375 °C) in refineries. However, when combined directly with FT, a milder form of HC with lower pressure and temperature can be employed due to nearly isothermal conditions and the absence of carbonaceous deposition [139, 142].

Bifunctional catalysts were frequently reported for hydrocracking of the FT product due to their high activity and selectivity to the middle distillate fraction under mild conditions [141]. Bifunctional catalysts enable the cracking and isomerization reactions on Brønsted-type acid sites, and the de/hydrogenation on metal sites. Acid functionality can be provided by amorphous oxides (e.g. Al₂O₃) or zeolites (e.g. ZSM-5). Metals (e.g. molybdenum, wolfram, cobalt, nickel) or noble metals (e.g. palladium, platinum) provide the metal sites.

The catalytic properties of bifunctional catalysts are influenced by the ratio of the functional sites as well as their spatial distribution. In this work, a Pt/H-ZSM-5 catalyst was employed. This catalyst features strong de/hydrogenation properties on the metal sites in combination with the shape selective characteristics of the zeolite. Weitkamp introduced the concept of ideal HC on properly balanced bifunctional catalysts to describe the selective cracking of long-chain n-alkanes into short-chain iso-alkanes [143]. Alkanes are dehydrogenated on the metal sites to form alkenes. These alkenes are protonated on the acid sites into alkyl carbenium ions, which are subject to skeletal rearrangements and carbon-carbon bond rupture through β -scission. In the case of ideal HC, the rate-determining steps in the chemical rearrangement and β -scission of alkyl carbenium ions occur at the acid sites. In contrast, the de/hydrogenation reactions and transport processes are fast and do not impose any rate or mass transfer limitations. Hence, ideal HC does not involve secondary reactions and long-chain hydrocarbons are cracked only once into hydrocarbon products with bell-shaped carbon-number distributions. However, secondary cracking may occur due to mass transfer limitations and strong adsorption affinity in micropores, depending on the catalyst and process conditions employed. The principle of competitive adsorption may thus be used to control selectivity, e.g. in the presence of steam [144].

The following chapter presents the most relevant experimental and modeling methods used in this work. Section 3.1 describes the experimental setup which was built for the SEWGS breakthrough experiments. Section 3.2 deals with the basic SEWGS modeling concept. The setup used for experiments on the combined FT synthesis with HC is shown in Section 3.3.

3.1 SEWGS Experimental Setup¹

The behavior of catalyst and sorption materials, as well as the performance of adsorption and desorption strategies for the intended SEWGS technology, was experimentally investigated [P1]. Additionally, kinetic investigations were performed to derive model parameters [P3].

A laboratory setup with a Packed Bed Microchannel Reactor (PBMR) (manufactured in-house) was designed and built for those investigations. A schematic drawing of the overall setup is given in Figure 3.1. The reaction and dilution gases (CO, CO₂, H₂, and N₂) entered the system through mass flow controllers (Brooks Instrument, USA). Water was supplied by a liquid flow controller (Brooks Instrument, USA) and vaporized in an electrically heated micro nozzle evaporator (manufactured in-house). This sophisticated vaporization instrument enables precise and pulsation-free steam supply in pressurized systems. The feed gas mixture was fed into the PBMR for experiments and the resulting product gas entered the gas analysis systems. Optionally, the feed gas bypassed the reactor and was led directly to the gas analysis systems for feed gas analysis. Temperatures above the boiling point prevented unwanted steam condensation in the tubes and were realized by electrical heating coils. The system pressure was adjusted by an automated regulating valve (Flowserve, USA).

Packed Bed Microchannel Reactor (PBMR)

A detailed illustration of the PBMR is given in Figure 3.2. The stainless steel reactor enabled experiments with isothermal reaction conditions in two identical reaction slits. Five programmable electrical heating cartridges (controlled by type K thermocouples) together with tempering air flow in adjacent microchannels regulated the temperature in the reaction slits. Additional thermocouples were inserted in the stainless steel block and the packed bed for continuous temperature monitoring.

¹This section contains content from [P1], [P2] and [P3].

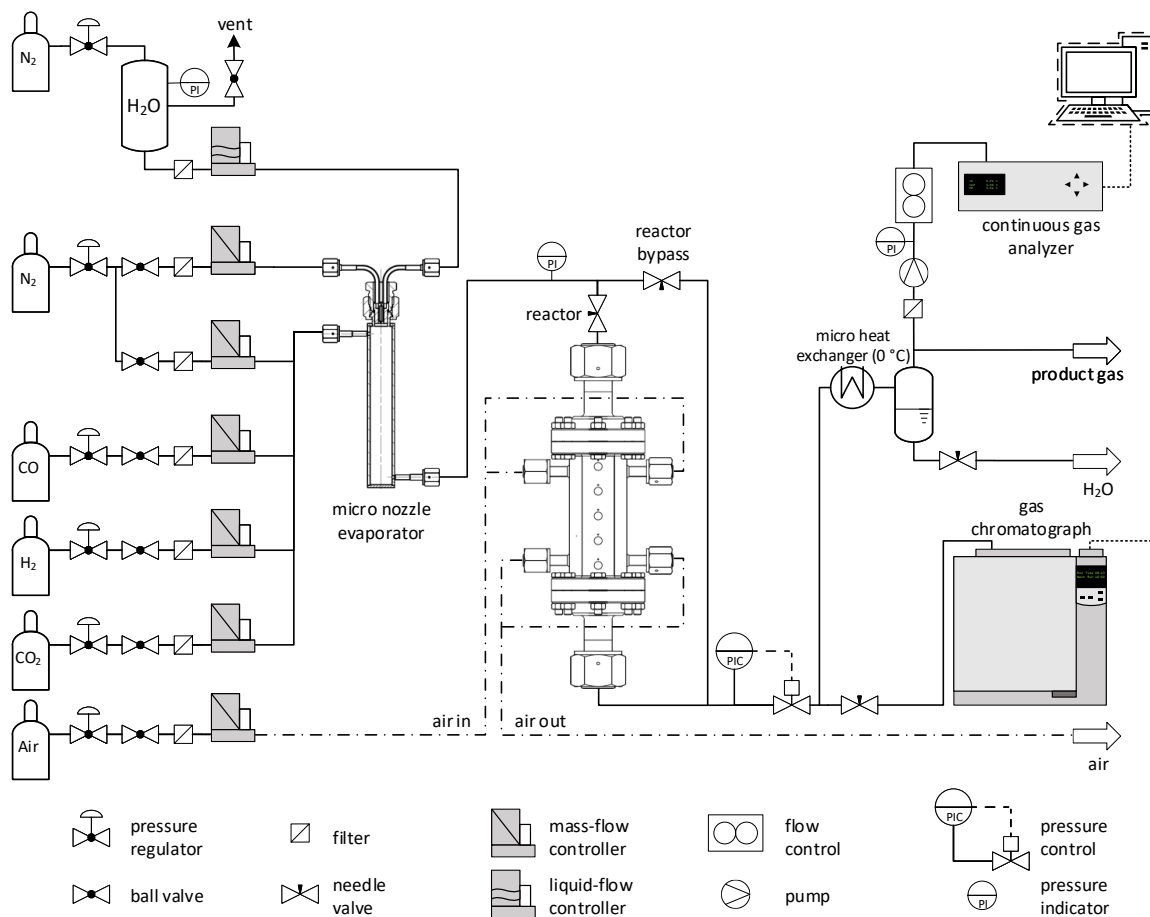


Fig. 3.1: Schematic flow scheme of the designed and built SEWGS laboratory setup. The setup was used for materials tests and sorption experiments. Figure from [P1] and [P3].

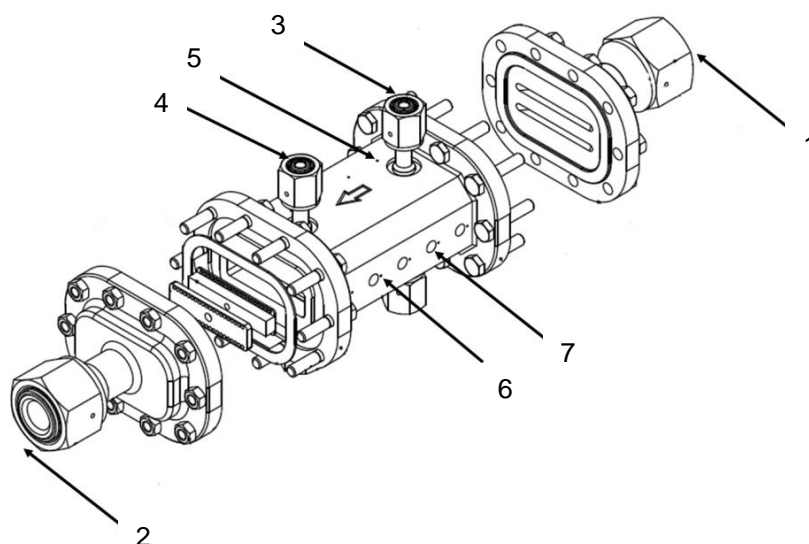


Fig. 3.2: PBMR for SEWGS breakthrough experiments. 1: reaction gas inlet, 2: reaction gas outlet, 3: air inlet, 4: air outlet, 5,6: drilled hole for thermocouple insertion, 7: heating cartridge insertion.

Both reaction slits (each 2 mm × 50 mm × 100 mm) were filled with catalyst (Cu/ZnO-Al₂O₃) and/or sorbent (K-HDMO) particles, depending on the experiment. The diameters of the particles ranged from 100 μm to 300 μm.

Gas Analysis Systems

The wet feed or product gas composition (in steady-state) was analyzed in a Gas Chromatograph (GC) (Agilent 7890A, Agilent Technologies, USA). The GC was equipped with two columns (HP-Plot/Q and HP-Molsieve/5A, Agilent Technologies, USA) and two detectors (Thermal Conductivity Detector (TCD) and Flame Ionization Detector (FID)). N₂ served as internal standard and Ar as carrier gas. GC measurements served to detect possible by-product formation and to investigate blank activity of the materials.

The dry effluent, however, was monitored continuously. The volume fractions of CO, CO₂ and H₂ were recorded in a Process Gas Analyzer (PGA) (X-STREAM Enhanced, Emerson, USA) by infrared-based detectors (CO and CO₂), and by a TCD (H₂). Prior to the PGA, steam was removed in a micro heat exchanger (manufactured inhouse). Countercurrent flow with a cooling liquid near 0 °C ensured full condensation to obtain precise measurement results.

The deviation of both analysis systems, GC and PGA was less than 1 % for the respective gases. Hence, comparability and accuracy was assumed.

Catalyst and Sorbent

The WGS catalyst pellets containing Cu/ZnO-Al₂O₃ were acquired from commercial sources. The pellets underwent crushing and sieving procedures to yield particles within the diameter range of 100 μm to 300 μm. The catalyst was reduced in-situ prior to the experiments in 3 % H₂ flow (balanced in N₂), while the temperature was increased up to 240 °C; and then in pure H₂ up to 250 °C.

A commercially available HTC (Pural MG70 from Sasol GmbH, Germany) was impregnated with potassium and calcined to obtain K-HDMO particles, which were employed as CO₂ sorbent under WGS conditions. The HTC Pural MG70 provided a Al₂O₃:MgO ratio of 30:70. It was loaded with 20 % potassium to form Potassium-impregnated Hydrotalcite (K-HTC) by means of incipient wetness impregnation with potassium carbonate (K₂CO₃, ≥99 %, Sigma-Aldrich, United States). The impregnated samples were then calcined ex-situ prior to the experiments in N₂ atmosphere at 400 °C for 10 h. Finally, the obtained K-HDMO powder was tabletized, crushed and sieved to produce particles ranging in size between 100 μm and 300 μm.

While the materials' preparation for all experiments conducted in the laboratory setup could be performed manually at the IMVT laboratory, the powder treatment had to be

scaled up significantly for the intended pilot plant campaign. Therefore, this task was assigned to an external company. They produced the required amount and quality of K-HDMO from provided K-HTC by calcination in large inertizable ovens (N_2 , $400\text{ }^\circ\text{C}$, 10 h) and powder compaction in a roller compactor. The bulk density of the calcined powder was sufficiently high (1096 kg m^{-3}) after four repetitions in the roller compactor, and the yield of the target fraction ($106\text{ }\mu\text{m}$ to $315\text{ }\mu\text{m}$) accounted to nearly 80 %.

3.2 SEWGS Model Development²

A reactor model was developed to describe time- and (one-dimensional) space resolved theoretical processes on a catalyst-sorbent mixture. The mathematical model describes the simultaneous WGS reaction and CO_2 adsorption followed by the desorption process.

Various numerical approaches were applied to solve the model equations in Programming and numeric computing platform (The MathWorks Inc., USA) (Matlab[®]) [145]. The approaches were assessed regarding their consistency and applicability for dynamic simulations on system-level [P2].

A novel Matlab-based graphical programming environment for modeling, simulating, and analyzing dynamical systems (Simulink) implementation approach was developed and used to model the complex SEWGS system with multiple reaction channels [146]. Due to its hybrid character, this model on system-level enables the investigation of different process configurations and cyclic operating strategies [P3].

Reactor Model Basics

WGS reaction and adsorption as well as consecutive desorption in a packed bed reactor are mathematically described by a set of differential algebraic equations. The packed bed reactor used in this work consists of rectangular slits filled with a homogeneous mixture of uniformly sized K-HTC (sorbent) and Cu/ZnO- Al_2O_3 (catalyst) particles. The reaction takes place on the active sites on the surface of the catalyst, whereas adsorption and desorption occur on the active sites on the surface of the sorbent. Figure 3.3 shows a schematic drawing of particles in a packed bed reactor.

The reactor model developed herein is based on the following assumptions and considerations:

- Uniform gas distribution in the reaction chambers realized by a gas inlet
- Isothermal conditions in the slits due to an advanced temperature control system

²This section contains content from [P2] and [P3].

- Negligible pressure drop in the slits owing to the fluid dynamics' properties of the reactor
- Constant superficial velocity in the slits due to high feed dilution
- No gradients rectangular to flow direction owing to the geometry of the slits in combination with the particle size
- Axial dispersion considered with a calculated axial dispersion coefficient
- External mass transfer limitations neglected (according to Maers-criterion)
- Internal mass transfer limitations considered (according to Weisz-Prater-criterion) and implemented with a linear driving force (LDF) model (according to Glueckauf-criterion)

Reactor Model Equations

Conservation equations formulated for the bulk phase (Equation 3.1), particle void phase (Equation 3.2), and particle solid phase (Equation 3.3) describe the system. For the sake of simplicity, catalyst and sorbent particles are taken together as one particle solid phase and weighted according to their overall weight fraction.

$$\varepsilon_b \frac{\partial c_i}{\partial t} = -u \frac{\partial c_i}{\partial z} + \varepsilon_b D_{ax,i} \frac{\partial^2 c_i}{\partial z^2} + (1 - \varepsilon_b) k_{LDF,i} (\bar{c}_i - c_i) \quad (3.1)$$

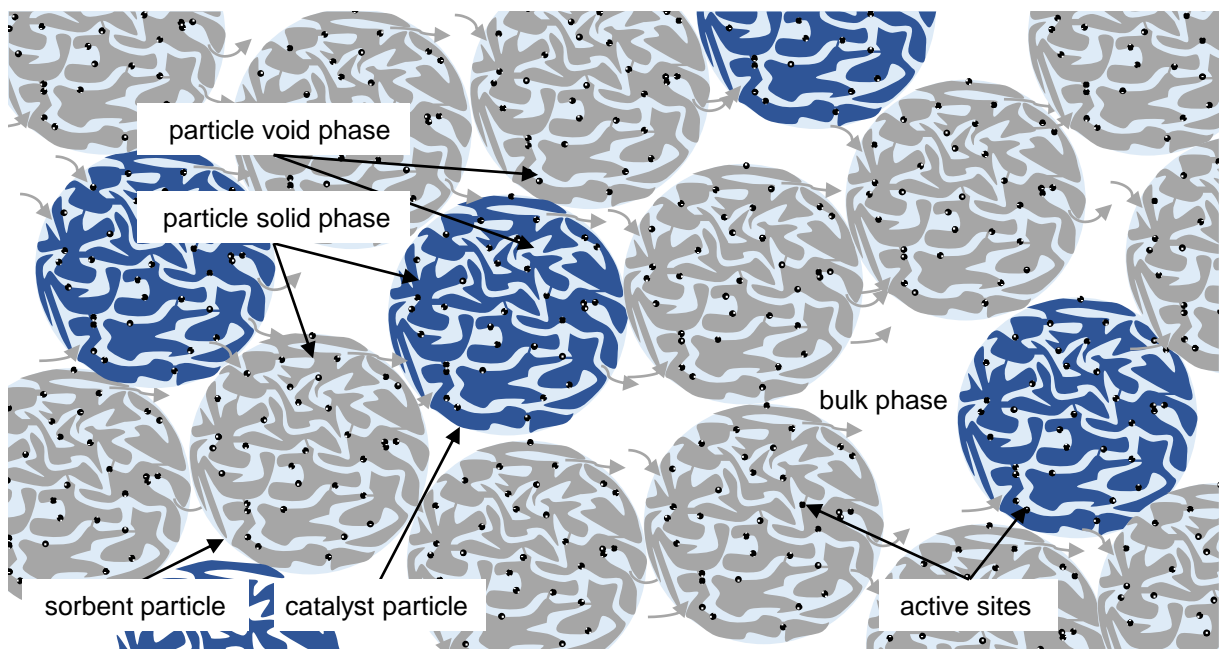


Fig. 3.3: Schematic drawing of catalyst (blue) and sorbent (grey) particles in the SEWGS packed bed reactor model. Conservation equations are formulated for (1) bulk phase, (2) particle void phase, and (3) particle solid phase. Catalyst and sorbent particles are taken together as one particle solid phase according to their weight fractions.

$$\varepsilon_p \frac{\partial \bar{c}_i}{\partial t} = \varepsilon_p k_{\text{LDF},i} (c_i - \bar{c}_i) + w_{\text{cat}} \rho \nu_i r_{\text{WGS}} - (1 - w_{\text{cat}}) \rho a_{\text{ads/des},i} \quad (3.2)$$

$$\frac{\partial q_{\text{CO}_2}}{\partial t} = a_{\text{ads/des},\text{CO}_2} \quad (3.3)$$

$i = \text{CO}, \text{H}_2\text{O}, \text{CO}_2, \text{H}_2, \text{N}_2$

$\nu_i = -1$ for $i = \text{CO}, \text{H}_2\text{O}$; $\nu_i = 1$ for $i = \text{CO}_2, \text{H}_2$; $\nu_i = 0$ for $i = \text{N}_2$

$a_{\text{ads/des},i} = 0$ for $i = \text{CO}, \text{H}_2\text{O}, \text{H}_2, \text{N}_2$; $a_{\text{ads/des},i} = \text{Equation 3.5/ Equation 3.6}$ for $i = \text{CO}_2$

A kinetic rate expression for the WGS reaction is taken from Choi et al. [56] (Equation 3.4). Equation 2.3 gives the correlation for the temperature-dependent equilibrium constant.

$$r_{\text{WGS}} = k_{\infty} \cdot \exp\left(-\frac{E_a}{R \cdot T}\right) \cdot \left(p_{\text{CO}} \cdot p_{\text{H}_2\text{O}} - \frac{p_{\text{CO}_2} \cdot p_{\text{H}_2}}{K_{\text{eq}}}\right) \quad (3.4)$$

Adsorption of CO_2 and H_2O on three different sorption sites is considered according to the model of Coenen et al. [147] (Equation 3.5):

Site A: Only H_2O adsorbs

Site B: Only CO_2 adsorbs

Site C: H_2O and CO_2 adsorb comparatively

The desorption kinetics of H_2O and CO_2 are described based on equilibrium data (Equation 3.6).

$$a_{\text{ads},\text{CO}_2} = k_{\text{ads}} \cdot (q_{\text{CO}_2}^{\text{eq}} - q_{\text{CO}_2}) \quad (3.5)$$

$$a_{\text{des},\text{CO}_2} = k_{\text{des}} \cdot (q_{\text{CO}_2}^{\text{eq}} - q_{\text{CO}_2}) \quad (3.6)$$

The desorption rate coefficient was described by an Arrhenius-type equation with an Elovich-type expression for the activation energy to account for the heterogeneity of the surface (Equation 3.7).

$$k_{\text{des}} = k_{\text{des}}^1 \cdot \exp\left(-\frac{\left(-\beta_{\text{des}} \cdot \frac{q_{\text{CO}_2}}{q_{\text{max}}}\right)}{R \cdot T}\right) \quad (3.7)$$

The CO_2 adsorption equilibrium isotherm on K-HDMO was described using the Freundlich equation for heterogeneous surfaces (Equation 3.8).

$$q_{\text{CO}_2}^{\text{eq}} = m_{\text{Fr}} \cdot p_{\text{CO}_2}^{\frac{1}{n_{\text{Fr}}}} \quad (3.8)$$

Numerical Solution

The SEWGS model was solved using three different numerical simulation approaches. Firstly, the set of combined Partial Differential Equations (PDEs) was solved numerically

with Matlab[®]'s built-in solver for systems of parabolic and elliptic PDEs in Matlab (pdepe) in one dimension. According to the solver's definition, at least one PDE must be parabolic. Thus, for the applicability of this solver, the axial dispersion term in Equation 3.1 is necessary. Secondly, a semi-discretization approach was applied to solve the SEWGS model equations. According to the Method-of-Lines (MoL), algebraic approximations are used to replace spatial derivatives in the PDEs, resulting in a set of Ordinary Differential Equations (ODEs). ODEs can be solved with well-established solving algorithms such as Matlab[®]'s built-in solver for stiff ODEs in Matlab (ode15s). Lastly, the Matlab[®] Simulink programming environment was used for a novel graphical implementation approach. Based on the idea of the MoL, the set of PDEs is implemented with uniform spatial discretization in up to 100 finite differences, and solved with the built-in solver for moderately stiff ODEs in Matlab (ode23t).

3.3 FT-HC Experimental Setup³

The influence of CO₂ in the feed gas on the selectivity to C₁₀-C₁₄ components in a coupled FT-HC process was experimentally investigated [P4]. The experiments were conducted in a micro-structured FT reactor coupled with a HC reactor cascade. Thus, the FT effluent could directly be fed into the HC reactor. A schematic drawing of the overall setup is given in Figure 3.4.

Mass flow controllers (Brooks Instrument, USA) delivered the feed gases H₂, CO, CO₂, and N₂ to the system. A permanent reactor bypass enabled feed gas analysis and control during an experimental run. 5 % of the total inlet flow passed through this bypass in all experiments for optional GC analysis. For the FT synthesis, the rest of the inlet flow was fed into the evaporation-cooled FT reactor (INERATEC GmbH, Germany). The reactor effluent could optionally be analyzed directly after separation (in hot (180 °C) and cold (10 °C) trap) or processed to the subsequent HC reactor cascade. The HC reactor cascade was also followed by a separation unit (hot (180 °C) and cold (10 °C) trap). In the separation units, products from FT or coupled FT-HC, respectively, initially entered the hot trap, where the wax fraction (long-chain hydrocarbons) condensed. In the subsequent cold trap, the oil and water fractions accumulated. The remaining non-condensed gases were finally released to a GC for analysis. Wax, oil and water fraction samples were gathered and analyzed offline. All tubes were wrapped with electrical heating coils to avoid unwanted condensation and wax plugging. The system pressure was regulated by a back-pressure regulating valve (BSH series, Swagelok, USA).

³This section contains content from [P4].

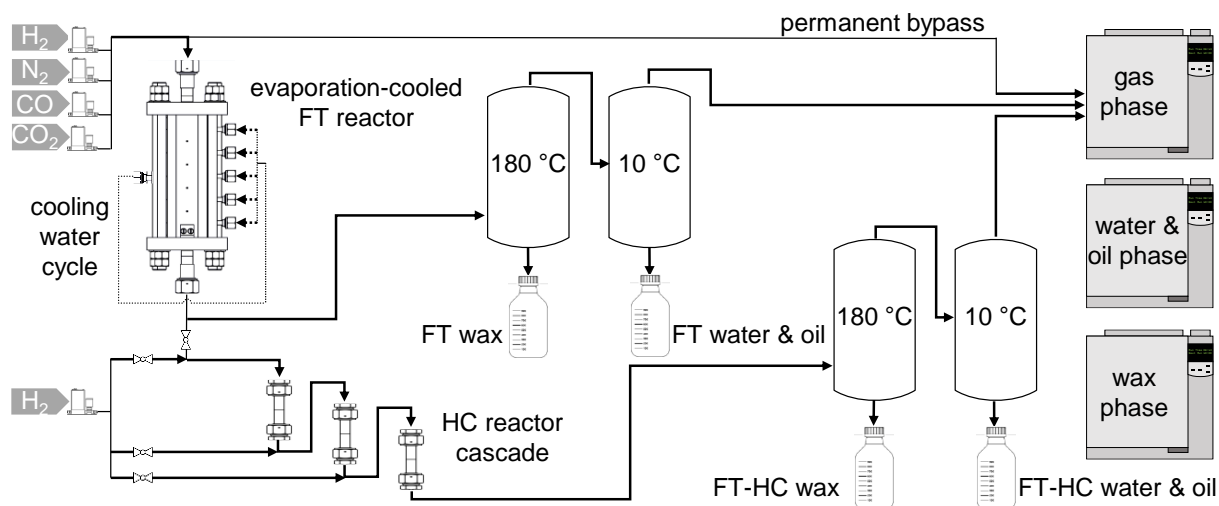


Fig. 3.4: Schematic flow scheme of the combined FT and HC laboratory setup. The setup was used for experiments with a variety of inlet gas compositions. Adapted figure from [P4].

Evaporation Cooled FT Reactor and HC Reactor Cascade

The evaporation cooled FT reactor features a large number of micro-structured reaction channels and adjacent cooling channels for nearly isothermal reaction conditions. The reaction channels were packed with commercial Co-based catalyst spheres (50 μm to 200 μm) for low-temperature FT. The cooling channels contained preheated water that evaporated by consuming the reaction heat from the reaction channels. Hence, the temperature in the reactor could be adjusted by changing the pressure in the cooling channels thus also to change the boiling point. For the start-up of the FT reaction and the compensation of heat losses along the reactor, additional heat needed to be provided. Thus, electrical heating cartridges were mounted. The temperature was monitored at the inlet and outlet of the reactor (in the reaction and cooling channels) as well as at various positions between the channels with type K thermocouples.

The HC reactor cascade consisted of three identical tubular reactors (inner diameter: 14 mm, length: 102 mm) in sequence. They were filled with bifunctional Pt/H-ZSM-5 (0.5 % Pt) catalyst extrudates (1/16" x 3 mm). Heating jackets and type K thermocouples regulated and monitored the temperature in each reactor. The number of operating HC reactors could be defined manually. Gas dosage prior to the HC cascade enabled further operating strategies. Both reactor systems, the evaporation-cooled FT reactor as well as the HC reactor cascade, were placed in boxes filled with insulation material to reduce heat losses.

Gas, Water, Oil, and Wax Phase Analysis

The gaseous components were analyzed online in a GC (7890B, Agilent Technologies, customized by Teckso GmbH, Germany). H_2 , CH_4 , CO , and N_2 were separated on a micropacked HayeSep Q and a mole sieve 5A column and detected by a TCD. CO_2 and

hydrocarbons up to C₇ were separated on a HP-Plot/Q column (all columns: Agilent Technologies, USA) and detected by another TCD and a FID, respectively. N₂ served as internal standard and Ar as carrier gas.

Both phases from the cold trap (water and oil phase) were analyzed offline in a GC (7820A, Agilent Technologies, USA). The carbonaceous components were separated on a Rtx-1 column (Restek, USA) and detected by a FID. The alcohols C₁ to C₅ in the water phase were quantified with Acetonitrile as internal standard. The hydrocarbons C₄ to C₂₇ in the oil phase were quantified with a 100 % method under the assumption of a constant relative response factor.

The wax phase from the hot trap was analyzed offline in a high temperature GC (7890B, Agilent Technologies, USA). The long-chain hydrocarbons C₁₀ to C₆₀ were separated on a MXT-1 column (Restek, USA) and detected by a high temperature FID.

The most significant findings based on the attached peer-reviewed publications are summarized in this chapter. Section 4.1 discusses the selection of materials for producing syngas from pure CO for jet fuel synthesis, along with appropriate SEWGS sorption parameters and reactor configurations. Section 4.2 applies, compares, and evaluates three numerical simulation approaches for a SEWGS reactor model. A novel graphical simulation approach is demonstrated for dynamic reactor operation. The implementation of this approach in a complex system-level model with multiple reaction channels is discussed in detail in Section 4.3. Based on the simulation results, an operating strategy is derived for a pilot plant reactor. Lastly, Section 4.4 provides insight into the subsequent process step in the jet fuel production process chain. It shows the impact of CO₂ in the syngas on the selectivity to the kerosene fraction in a coupled FT-HC process.

4.1 Choice of Materials, Sorption Parameters and Reactor Configurations¹

In this section, the selection of suitable materials, namely a WGS catalyst and a CO₂ sorbent, as well as the choice of appropriate sorption parameters and beneficial reactor configurations are discussed.

4.1.1 Catalyst and Sorbent Characterization

Three different commercial copper-based catalysts were tested under various operating conditions, including gas feed flow rates, feed composition, temperature, and pressure. The experimental results indicated that all of these catalysts were suitable for the WGS reaction at operating temperatures below 300 °C. However, one of the Cu/ZnO-Al₂O₃ catalysts demonstrated superior long-term stability compared to the others and was therefore selected for the SEWGS experiments.

The Electron Probe Micro Analysis (EPMA) (JXA 8530F, Jeol, Japan) coupled with Energy-Dispersive X-Ray Spectroscopy (EDX) was used to determine the elemental composition of this catalyst at fixed probe positions. The average weight fractions of the main components were as follows: Al 3 %, Cu 42 %, and Zn 16 %. Maps displaying the elemental distribution of Cu, Al, Zn, and O are presented in Figure 4.1. These maps, obtained with Wavelength-Dispersive X-Ray Spectroscopy (WDX), demonstrate that the active components are well-distributed. The surface area of the catalyst was

¹This section contains content from [P1].

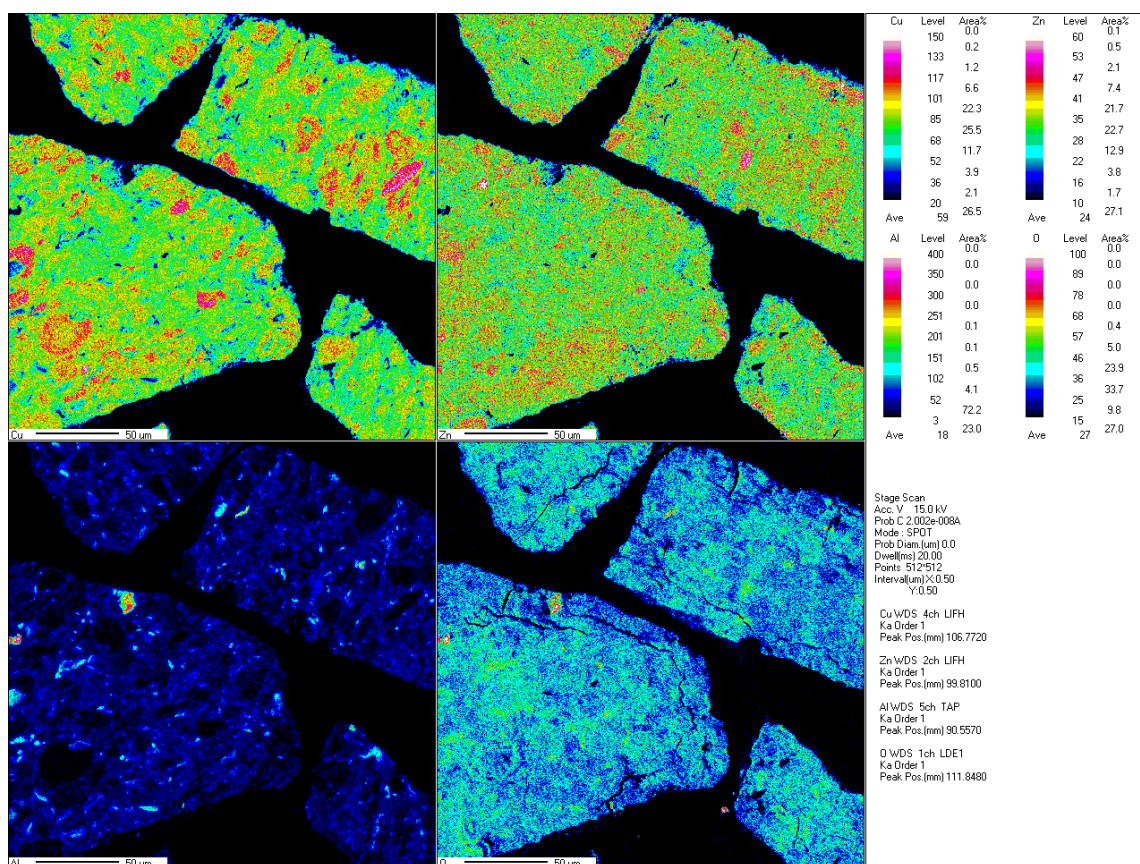


Fig. 4.1: Elementary distribution maps of the catalyst for Cu, Al, Zn, and O obtained by EPMA coupled with WDX.

calculated using the Brunauer-Emmett-Teller (BET) method and found to be $86.6 \text{ m}^2 \text{ g}^{-1}$ (N_2 physisorption, 3Flex, Micromeritics, USA).

The catalytic performance of the catalyst was tested in a standard tubular reactor (inner diameter: 8 mm, length: 30 mm) and is presented in Figure 4.2. The CO conversion increases with temperature and approaches equilibrium at temperatures above 300°C . Therefore, the reaction conditions for the SEWGS experiments were chosen such that kinetic constraints prevailed over thermodynamic limitations.

To identify a sorbent that can effectively adsorb CO_2 , the impact of calcination and impregnation procedures on commercial HTC (PURAL MG70, Sasol GmbH, Germany) was investigated. Figure 4.3A shows the influence of calcination temperature on the crystalline structure, as measured by X-Ray Diffraction (XRD). The untreated sample (MG70) has a layered structure, which is destroyed in all calcined samples (MG70-250, MG70-400, MG70-500). However, calcination at 250°C only resulted in an amorphous phase instead of the desired mixed oxide with basic sites for CO_2 adsorption. The full transition from layered double hydroxide to layered double oxide only occurred at 400°C and 500°C , as indicated by intense peaks representing MgO. The Thermogravimetric Analysis (TGA) results shown in Figure 4.3B illustrate the effect of calcination on thermal

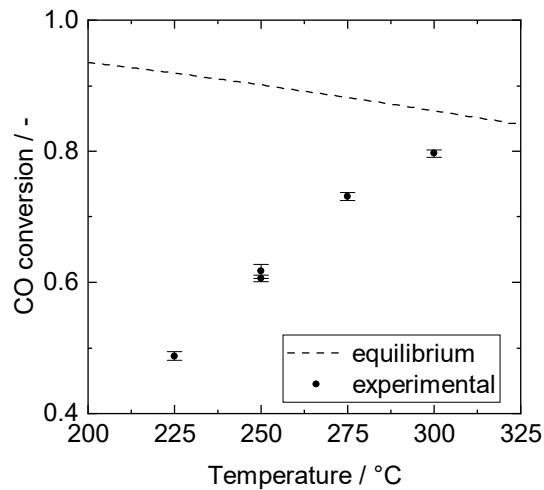


Fig. 4.2: CO conversion over temperature in catalyst performance experiments (1 g catalyst, 5 bar, 10% CO, steam-to-gas ratio 1, modified residence time $1.66 \times 10^{-5} \text{ g h mL}^{-1}$). Figure from [P1].

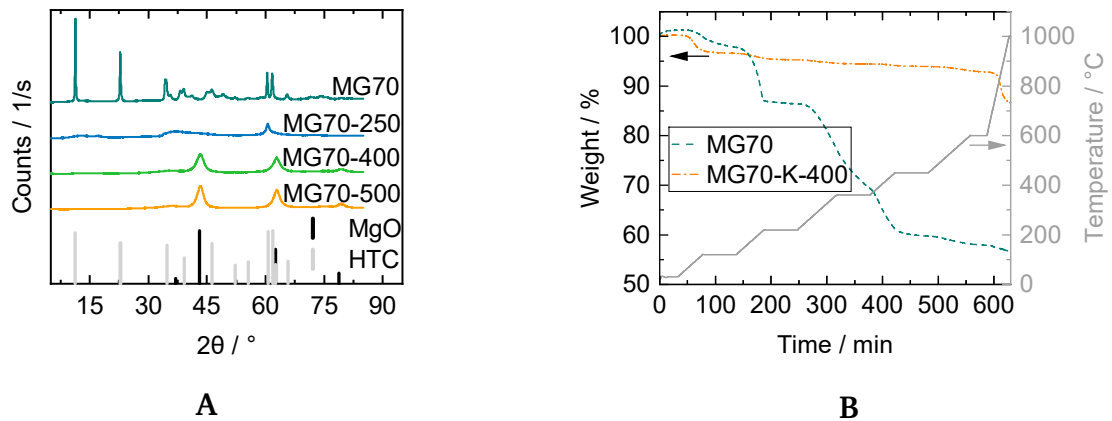


Fig. 4.3: **A)** XRD patterns for samples with varied calcination temperatures (250°C, 400°C, 500°C) compared with untreated sample (MG70). **B)** TGA results (sample weight and temperature over time) for untreated sample (MG70) and impregnated-calcined sample (MG70-K-400). Figure from [P1].

decomposition. The untreated sample (MG70) underwent three material changes up to 400°C, while the impregnated and calcined sample (MG70-K-400) only experienced minimal weight loss up to 100°C, which may be attributed to surface water adsorption during storage. Further material decomposition began at 500°C. Both characterization methods, XRD and TGA, indicate that calcination at 400°C resulted in the removal of unwanted compounds and led to the desired mixed oxide structure.

Figure 4.4 presents CO₂ chemisorption uptake measurements for calcined samples with (MG70-K-400, MG70-400-K-400) and without (MG70-400) potassium impregnation (potassium loading with incipient wetness impregnation: 20%). Two calcination-impregnation procedures are shown, namely calcination only after (MG70-K-400), or before and after (MG70-400-K-400) impregnation. The isotherms display a fast initial

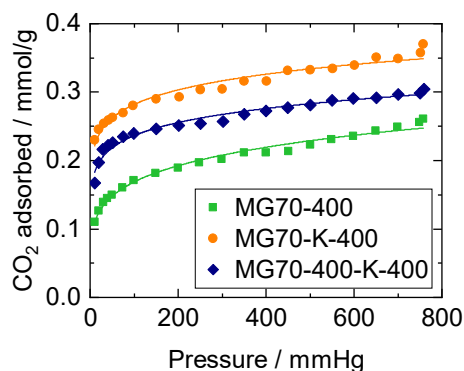


Fig. 4.4: CO₂ chemisorption isotherms at 250 °C for samples with varied calcination–impregnation procedures: calcined (MG70-400), impregnated–calcined (MG70-K-400), and calcined–impregnated–calcined (MG70-400-K-400). Straight lines: data fitted according to the Freundlich model. Figure from [P1].

rise in CO₂ uptake, followed by a less significant increase with increasing pressure, which can be described using the Freundlich model. As alkaline modification is known to enhance CO₂ sorption on HTC, the impregnated samples exhibit higher CO₂ uptake. The CO₂ equilibrium isotherms suggest that the calcination procedure before and after impregnation (MG70-400-K-400) was not advantageous compared to calcination only after impregnation (MG70-K-400). Incomplete reconstruction resulting from the memory effect during incipient wetness impregnation from mixed oxide back to layered double hydroxide during double calcination may account for the difference in adsorption capacity.

Based on the results of the characterization tests, the K-HDMO MG70-K-400 was found to be the most promising material for SEWGS applications. This sorbent exhibited the following textural properties: a BET surface area of 9 m² g⁻¹, an average pore width of 12.5 nm according to the Barrett-Joyner-Halenda (BJH) method, and a cumulative pore volume of 0.027 cm³ g⁻¹ from N₂ physisorption measurements on the adsorption branch. Moreover, EDX measurements at fixed probe positions revealed a Mg/Al ratio of (3.64 ± 0.54), which is close to the expected value of 3. The distribution of potassium was found to be inhomogeneous, with values ranging from 3% to 24%.

Figure 4.5 presents Scanning Electron Microscopy (SEM) images of crushed and sieved particles of the catalyst and sorbent. The particles have irregular and undefined shapes. Nevertheless, the catalyst and sorbent could be homogeneously mixed without experiencing any unmixing during reactor packing.

4.1.2 Sorption Parameters

In cyclic SEWGS breakthrough experiments, the reactor was packed with a homogeneous sorbent-catalyst mixture. Both, sorbent and catalyst, were crushed and sieved to obtain

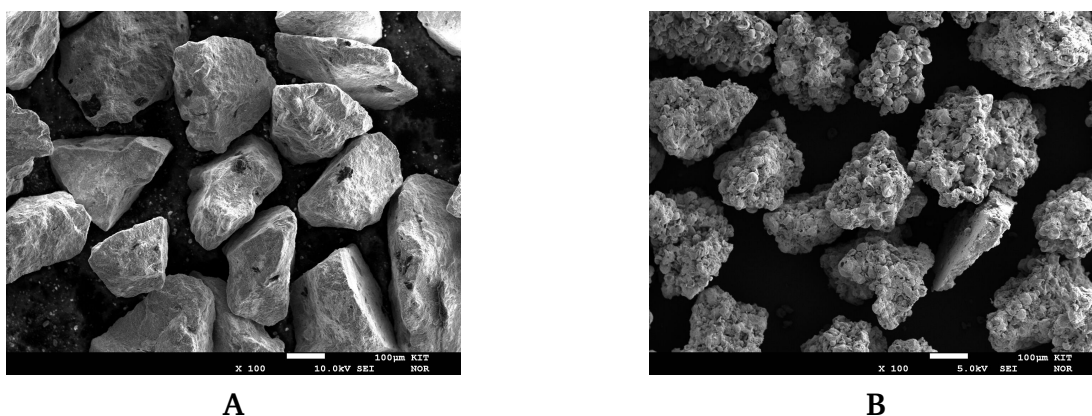


Fig. 4.5: SEM images (x100) of **A**) crushed and sieved Cu/ZnO-Al₂O₃ particles, **B**) impregnated-calcined K-HDMO sample (MG70-K-400). Figure **B** from [P1].

particles between 100 µm and 300 µm. An experimental cycle consisted of a reactive adsorption phase (feed: CO, H₂O, and N₂) and a desorption phase at lower pressure to regenerate the sorbent (feed: H₂O and N₂). At least five cycles were performed in each experiment. During the reactive adsorption phase, three stages could be identified: 1) pre-breakthrough stage with pure H₂ in the effluent, while the produced CO₂ was fully adsorbed; 2) breakthrough stage, where CO₂ breakthrough started; and 3) post-breakthrough stage, when CO₂ reached its steady-state concentration.

The amount of adsorbed CO₂ decreased significantly from the first to the second reactive adsorption phase in all of the cyclic breakthrough experiments, but it remained relatively stable in subsequent cycles. Incomplete regeneration during the comparatively short desorption phase was mainly responsible for the initial loss of available sorption capacity, as the adsorption kinetics are known to be up to ten times faster than the desorption kinetics. The “cycle average” adsorbed amount CO₂ of all follow-up cycles, also known as "cyclic working capacity", is a relevant indicator for the performance of a SEWGS system.

An extensive parameter study revealed the influence of pressure, steam-to-gas ratio, and CO and H₂O partial pressure during adsorption, as well as desorption feed composition and desorption time. Figure 4.6 presents exemplary the results for an increase of the CO fraction in the reactive adsorption feed. It shows that steady-state equilibrium conversion was attained for feed S/G ratios greater than 1 (2.5 % and 5 % CO). With an increase in CO fraction, the CO₂ breakthrough delay decreased, and 2.5 % CO exhibited significantly higher adsorption of CO₂ compared to other feeds. Several factors need to be considered to explain these observations: the sorbent saturation that is dependent on the rate of CO₂ production, the partial pressure of CO₂ as resulting driving force, the total amount of CO₂, and the average steam content throughout the bed length. At lower CO₂ partial

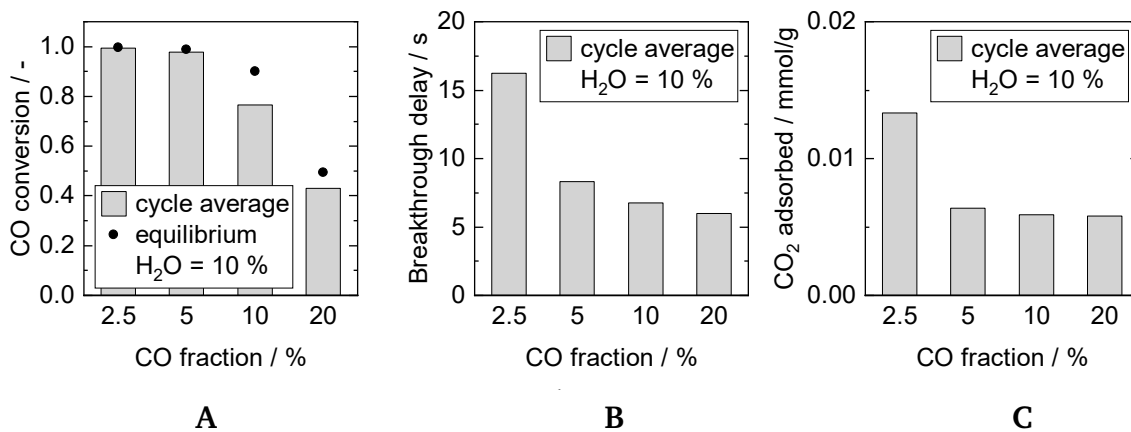


Fig. 4.6: Adsorption cycle average **A)** Steady-state CO conversion, **B)** breakthrough delay, and **C)** amount of adsorbed CO₂ for various CO fractions in the adsorption feed at 250 °C. Adsorption: 15 min, 8 bar, 2000 mL min⁻¹, 10 % H₂O. Desorption: 40 min, 1 bar, 1000 mL min⁻¹, 40 % H₂O. Figure from [P1].

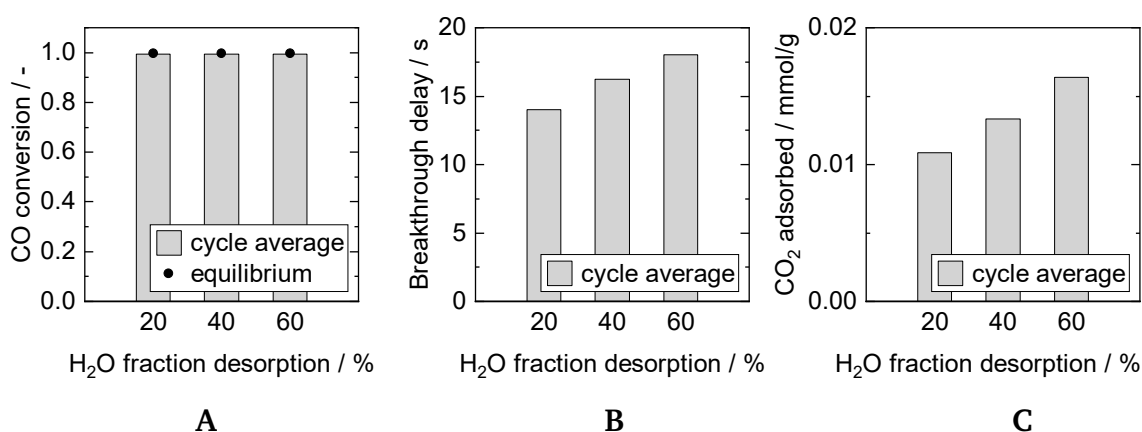


Fig. 4.7: Adsorption cycle average **A)** CO conversion, **B)** breakthrough delay, and **C)** amount of adsorbed CO₂ for various H₂O fractions in the desorption feed at 250 °C. Adsorption: 15 min, 8 bar, 2000 mL min⁻¹, 2.5 % CO, steam-to-gas ratio 4. Desorption: 40 min, 1 bar, 1000 mL min⁻¹. Figure from [P1].

pressures, the enhancement of the adsorption capacity caused by the presence of steam was observed to be predominant, resulting in a higher amount of adsorbed CO₂ for 2.5 % CO. A sufficient amount of steam, leading to a faster CO₂ production rate, was only present for S/G ratios of 1 or higher. Nevertheless, the sorbent's capacity was reached earlier with higher CO concentrations, caused by an overall increase of CO₂ fluxes of more than three-fold from 5 % CO to 20 % CO.

The findings depicted in Figure 4.7 illustrate how the H₂O fraction during sorbent regeneration impacts the adsorption properties in subsequent adsorption cycles. With an increase in the H₂O fraction, both the breakthrough time and the amount of CO₂ adsorbed increased. These results support the idea of different adsorption sites ([147]), which can either be regenerated with N₂ or H₂O.

4.1.3 Reactor Configurations

The SEWGS performance of five packed bed reactor configurations based on the multi-section column packing concept (Figure 4.8A) is displayed in Figure 4.8B. The most pronounced CO₂ uptake was measured for configuration C, where the bed was divided in two zones: the first zone (towards inlet) contained one quarter of the total sorbent mass homogeneously mixed with the total catalyst amount, whereas the second zone (3/4 of the reactor length, towards outlet) was packed with pure sorbent. Increasing the length of the catalyst-containing zone (with identical total amount of catalyst) resulted in a decrease in sorption capacity (configuration A, B, C). The presence of lengthy catalyst-free zones at the outlet increased the breakthrough delay, as the adsorption kinetics seemed significantly slower than the reaction kinetics. Configuration D demonstrated a higher CO conversion than configuration B, as it contained twice the amount of catalyst. Nonetheless, the adsorbed amount of CO₂ was similar in both configurations due to the same zone length. Configuration E did not exhibit a higher capacity than configuration D despite the inclusion of additional alternating zones. Here, the effect of thermodynamic equilibrium shift in the second catalyst zone during unsteady-state conditions was outweighed by the limitation from the sorption kinetics. Hence, the consideration of relatively fast reaction interacting with relatively slow adsorption kinetics is important for the reactor packing concept and the overall process design.

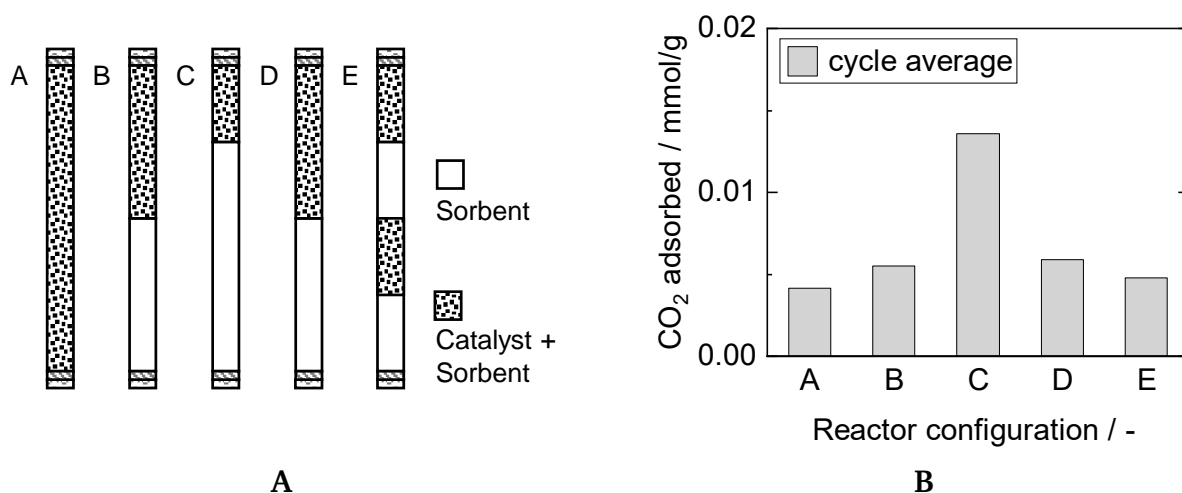


Fig. 4.8: **A)** SEWGS reactor configurations. A, B, and C have a total catalyst weight fraction of 0.05, whereas D and E have a total catalyst weight fraction of 0.11. **B)** Average amount of adsorbed CO₂ for various reactor configurations at 250 °C. Adsorption: 15 min, 8 bar, 2000 mL min⁻¹, 10 % CO, steam-to-gas ratio 1. Desorption: 40 min, 1 bar, 1000 mL min⁻¹, 40 % H₂O. Adapted figure from [P1].

4.2 Numerical Simulation Approaches²

This section compares the results of a SEWGS base case simulation using three different numerical approaches. The base case considered reactive adsorption in a rectangular-shaped reaction chamber filled with a homogeneous catalyst-sorbent mixture. All necessary kinetic parameters for the calculations were taken from the literature [56, 147]. First, it was shown that two conventional numerical methods, MoL and *pdepe* delivered reliable results. Then, the MoL approach was applied and extended to develop a novel Matlab[®] Simulink model, which is capable of performing dynamic simulations.

4.2.1 Conventional Methods: Method-of-Lines and Matlab[®]'s built-in Solver *pdepe*

The results of both methods, semi-discretization approach MoL and Matlab[®]'s built-in solver for PDEs (*pdepe*), converged with appropriate mesh settings. To enhance the accuracy of MoL simulations, it has been demonstrated that the adequacy of the grid discretization is essential. Figure 4.9A shows the sorbent loading with CO₂ across the reactor length for up to $N = 250$ cells at $t = 25$ s. Steep steps appear for low cell simulations, but the curves become smoother for $N > 100$, and the deviation from $N = 250$ is below 5% for $N = 100$. In *pdepe* simulations, which were highly sensitive to initial conditions, a sufficiently high number of mesh points in time and space was required to achieve numerical stability and prevent oscillations.

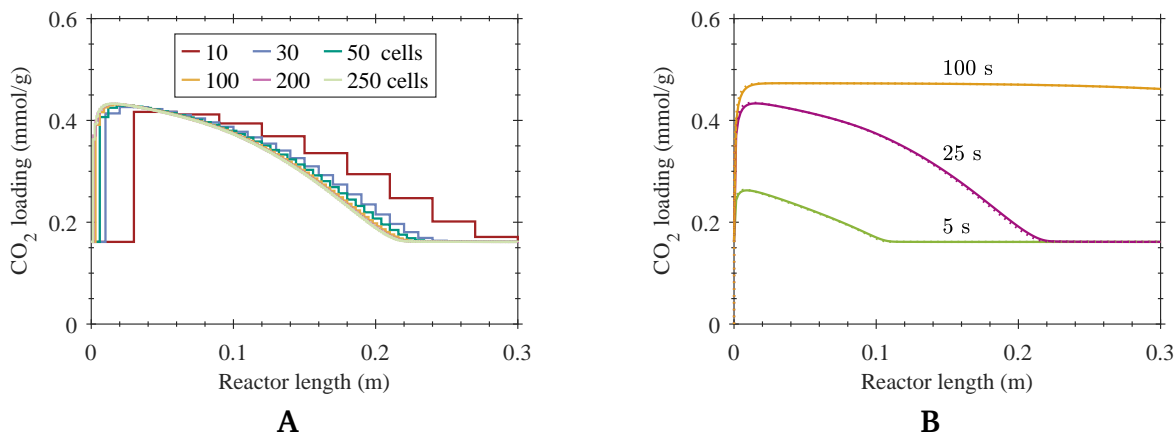


Fig. 4.9: CO₂ loading over the reactor length for reactive adsorption. **A)** MoL grid analysis with $N = 10$ to 250 cells at $t = 25$ s. **B)** Comparison of MoL ($N = 100$) and *pdepe* simulation results at various adsorption times. Solid lines: MoL, dotted lines: *pdepe*. Figure from [P2].

²This section contains content from [P2].

pdepe computations needed significantly lower computation time compared to MoL simulations, even with a higher number of mesh points (Table 4.1). This is due to the implemented runtime optimization of pdepe. The required MoL computation time increased almost exponentially with the number of cells, and a trade-off between accuracy and speed was inevitable.

Tab. 4.1: Computation time for MoL and pdepe simulations for reactive adsorption. Adapted table from [P2].

Number of cells (-)	MoL						pdepe
	10	30	50	100	200	250	3000
Computation time (min)	0.04	0.22	0.27	4.96	46.81	90.93	12.19

The base case results for both methods were - as expected - almost identical, as shown in Figure 4.9B in terms of CO₂ loading over the reactor length. The sorbent loading increases until reaching full saturation after around 100 s. Before CO₂ breaks through at the reactor outlet, complete conversion of CO in excess of H₂O in the feed is attained, and the produced CO₂ is entirely adsorbed.

The conservation properties of both solution algorithms were assessed in terms of the deviation from the molar balance (Figure 4.10). MoL as well as pdepe results showed insignificant deviations of less than 2%. The deviation in the case of the MoL emerges for a longer period of time at the reactor outlet compared to the deviation of the pdepe solution. Both deviations are more pronounced close to the reactor inlet at the beginning of the simulation. In both cases, the deviation is related to the adsorption process and approaches zero as soon as steady-state conditions are reached.

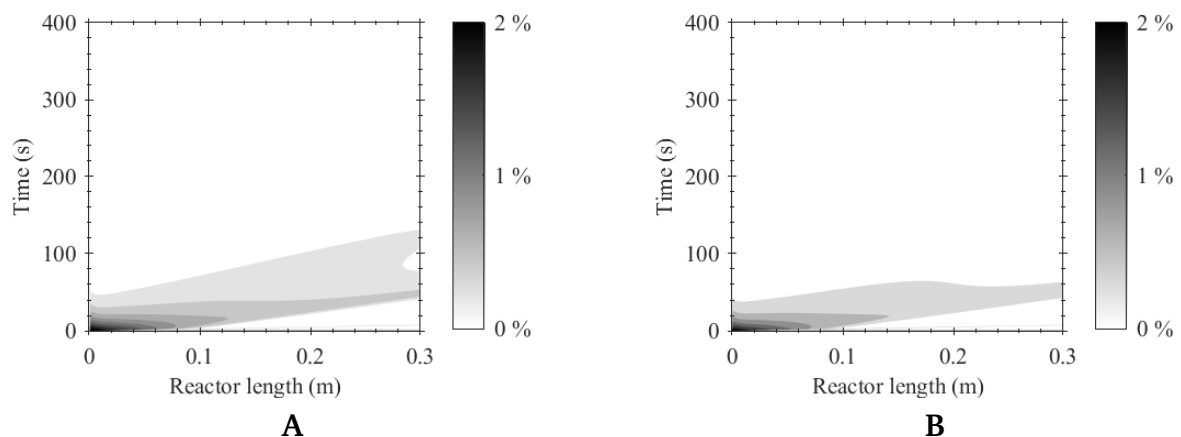


Fig. 4.10: Time and space-dependent deviation from molar balance for reactive adsorption. A) MoL ($N = 100$), and B) pdepe simulation results. Figure from [P2].

4.2.2 Novel graphical Implementation in Matlab[®] Simulink

After demonstrating that the semi-discretization method, MoL, produces reliable results when compared to the built-in Matlab[®] solver for PDEs (`pdepe`), a new graphical simulation approach based on the MoL concept was developed using Simulink. Simulink provides a graphical editor where the model can be created using hierarchical block diagrams. The editor includes libraries of pre-defined blocks consisting of elementary model components for continuous and discrete systems.

Unlike the other methods presented in Section 4.2.1, Simulink enables the implementation of a SEWGS reactor for a dynamic process on system-level with multiple reaction chambers. The cyclic process operating procedure can be executed by switching between different discrete modes of operation. Furthermore, automated adjustment of switching times during runtime according to specified conditions, such as exceeding a threshold of CO₂ concentration in the product stream, can be achieved with this approach. The implementation of such a complex system-level model is presented in detail in Chapter 4.3.

An overview of the main elements of the SEWGS model is displayed in Figure 4.11. Beginning with the blocks used to define the ODEs, which were derived from spatial discretization of the PDEs, the entire set of ODEs describes the adsorptive reaction phenomena within a single cell. This cell is then replicated in ten additional cells to create a group, and the desired number of these groups are then cascaded together to form a reaction chamber. The integrator block (marked in yellow in Figure 4.11) supplies the solver with an initial condition for computing the block's initial state and outputs the integral of its time-varying input signal at each time step. To enhance data access, a so-called *bus object* structure was created. This structure simplifies data handling, unlike the MoL and `pdepe` methods, which use a single, bulky matrix to store time- and space-dependent solutions.

Various solvers from the Matlab[®] solver library were tested on the Simulink model, aiming to achieve a solution within specified tolerance limits and a reasonable time frame. In Figure 4.12, the computation time is depicted as it relates to the number of cells implemented in the base case and the relative error tolerance. For $N = 100$, the solver `ode23t` achieved a sufficient level of precision (relative error tolerance of 10^{-3}), while reducing the computation time by almost 50% compared to the commonly used `ode15s`. Thus, this solver was applied in all simulations.

Figure 4.13 compares the results obtained from the MoL and the Simulink approach for the base case simulation. Both approaches yield satisfactory results and exhibit negligible differences, confirming that the graphical approach in Simulink is precise and reliable.

This finding suggests that the Simulink approach is suitable to be further extended to a more complex hybrid process model.

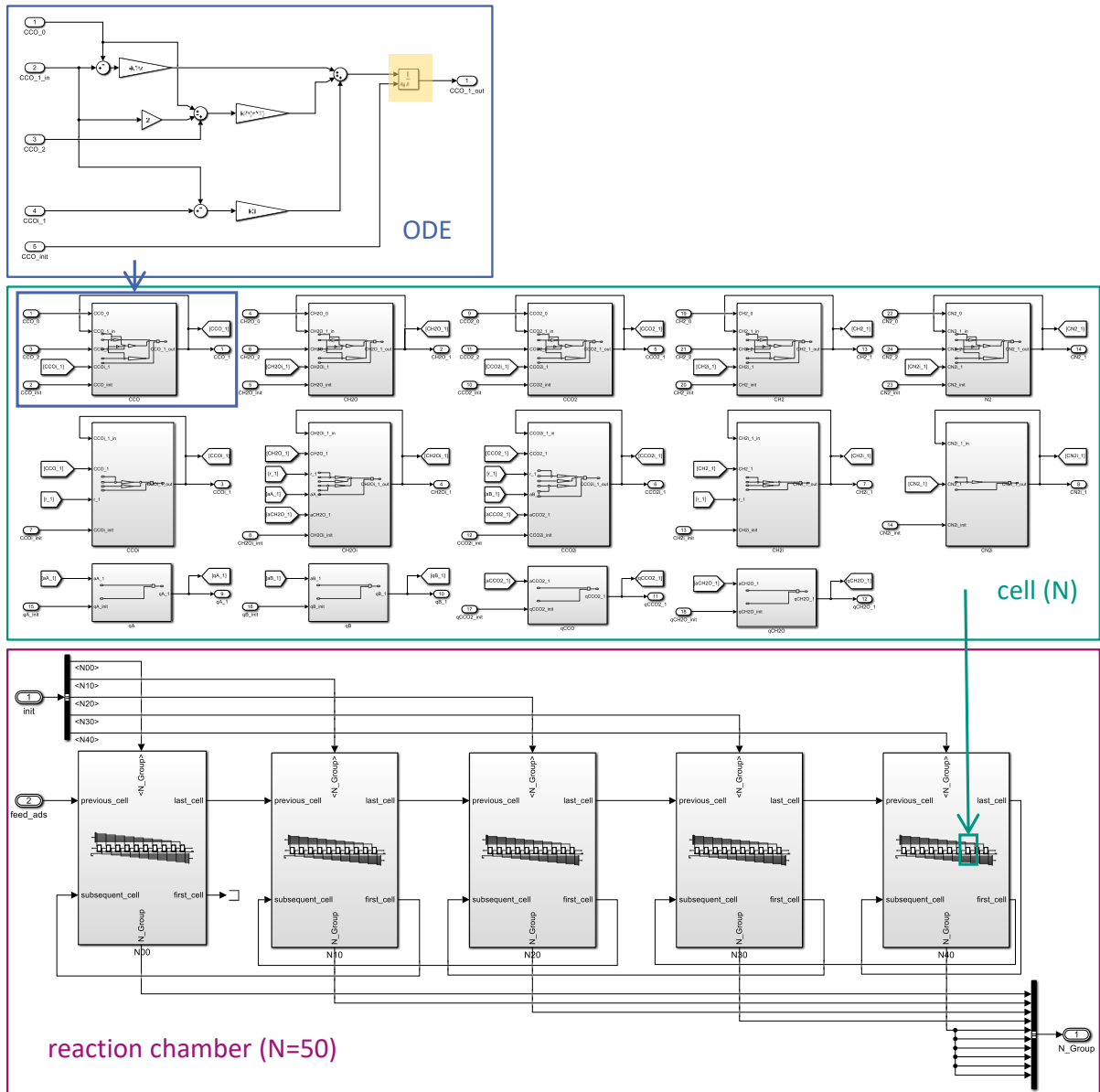


Fig. 4.11: Bottom-up Simulink implementation of the model equations discretized analogous to MoL. Exemplary ODE implementation of the CO concentration in the bulk phase. The integrator block is marked in yellow. 14 ODEs arrange the cell subsystem. N (here: $N = 50$) cells form the reaction chamber. Figure from [P2].

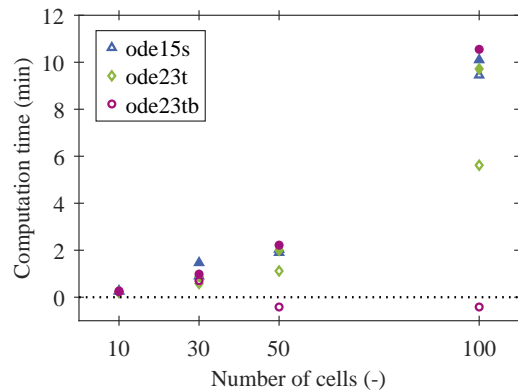


Fig. 4.12: Required computation time for Simulink simulations in one rectangular reaction chamber depending on the number of implemented cells, the chosen solver and the relative error tolerance. Filled symbols: relative error tolerance 10^{-6} ; open symbols: relative error tolerance 10^{-3} . The best results for $N = 100$ were obtained for solver ode23t with a relative error tolerance of 10^{-3} . Computation times below 0 indicate that a simulation did not converge and a smaller error tolerance was required.

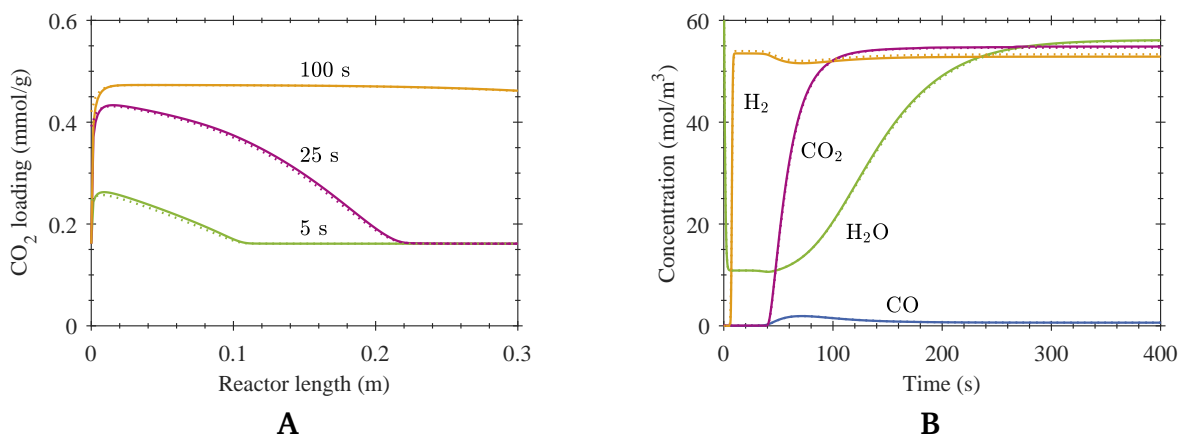


Fig. 4.13: Comparison of MoL and Simulink ($N = 100$) simulation results for reactive adsorption. **A)** CO_2 loading at various adsorption times over the reactor length, and **B)** bulk phase concentrations at the reactor outlet as a function of time. Solid lines: MoL; dotted lines: Simulink ($N = 100$). Figure from [P2].

4.3 Dynamic Reactor Modeling³

This section presents the simulation results of a dynamic SEWGS process on system level for the pilot plant reactor design. The model includes multiple reaction chambers and cyclic process operation, enabling time-resolved insights into every axial position of each reaction chamber. The simulation-driven process design resulted in an optimized operating procedure that enhances the process efficiency while maximizing the sorbent loading of the pilot plant reactor.

4.3.1 Pilot Plant Reactor Model

The pilot plant reactor shown in Figure 4.14A is composed of six identical parallel reaction chambers, which can be configured for continuous H_2 production in either a single stage or a serial configuration. The switch between modes is accomplished by using discrete valve positions, and an overview of the operating modes is depicted in Figure 4.14B.

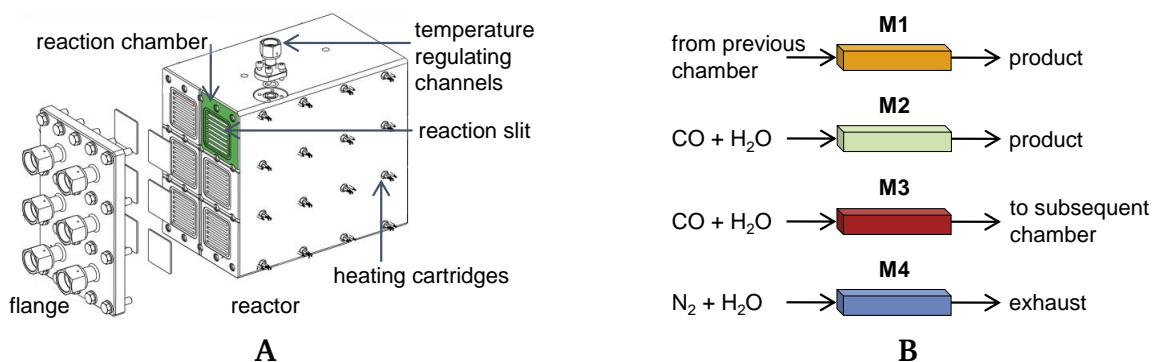


Fig. 4.14: **A)** Compact SEWGS pilot plant reactor with six individually fed reaction chambers. Each chamber consists of seven rectangular reaction slits. Adjacent microchannels for purge gas and heating cartridges enable advanced temperature control for isothermal operation in the slits. Uniform gas distribution in the slits is realized using sintered metal plates. **B)** Pilot plant reactor operating modes. Mode (M)2 stands for reactive adsorption with fresh feed, and M4 for regeneration with purge flow. M1 and M3 (both reactive adsorption) occur only in a serial configuration when the outlet of one reaction chamber is optionally connected to the inlet of the subsequent reaction chamber. Adapted figure from [P2] and [P3].

In the single stage configuration, one chamber operates in reactive adsorption mode (M2) with *fresh* feed ($CO + H_2O$) and produces CO_2 -free WGS product, while the others are in regeneration mode (M4) using N_2 and H_2O as regeneration feed. As soon as the sorbent in the reactive adsorption chamber becomes saturated and reaches a predefined CO_2 threshold in the outlet gas flow, the system switches to another chamber, which is then in M2.

³This section contains content from [P3].

In the serial configuration, chambers can be interconnected in series to maximize the sorbent loading and increase the time span of reactive adsorption. For instance, chamber 1 is in M2, while all the other chambers are in M4. Once the outlet of chamber 1 reaches a specific CO₂ threshold, it triggers a switch to M3. In M3, the gas flow leaving chamber 1 is directed to chamber 2, which is then in M1. While the sorbent loading in chamber 1 continues to increase, chamber 2 produces CO₂-free WGS product. When chamber 1 reaches another predefined threshold, such as 20% CO₂, it switches back to M4, and the cycle continues in chamber 2 with M2.

Figure 4.15 displays the graphical representation of the SEWGS pilot plant reactor, including its reaction chambers and valves, implemented in Simulink. To simulate the cyclic process operation, the valve positions are adjusted for either reactive adsorption or regeneration using a finite state machine implemented in Stateflow, an add-on for Simulink. This state machine operates by setting discrete valve positions to switch between modes of the chambers, similar to the process used in the actual plant. Specified events such as exceeding a threshold of CO₂ concentration in the product stream trigger

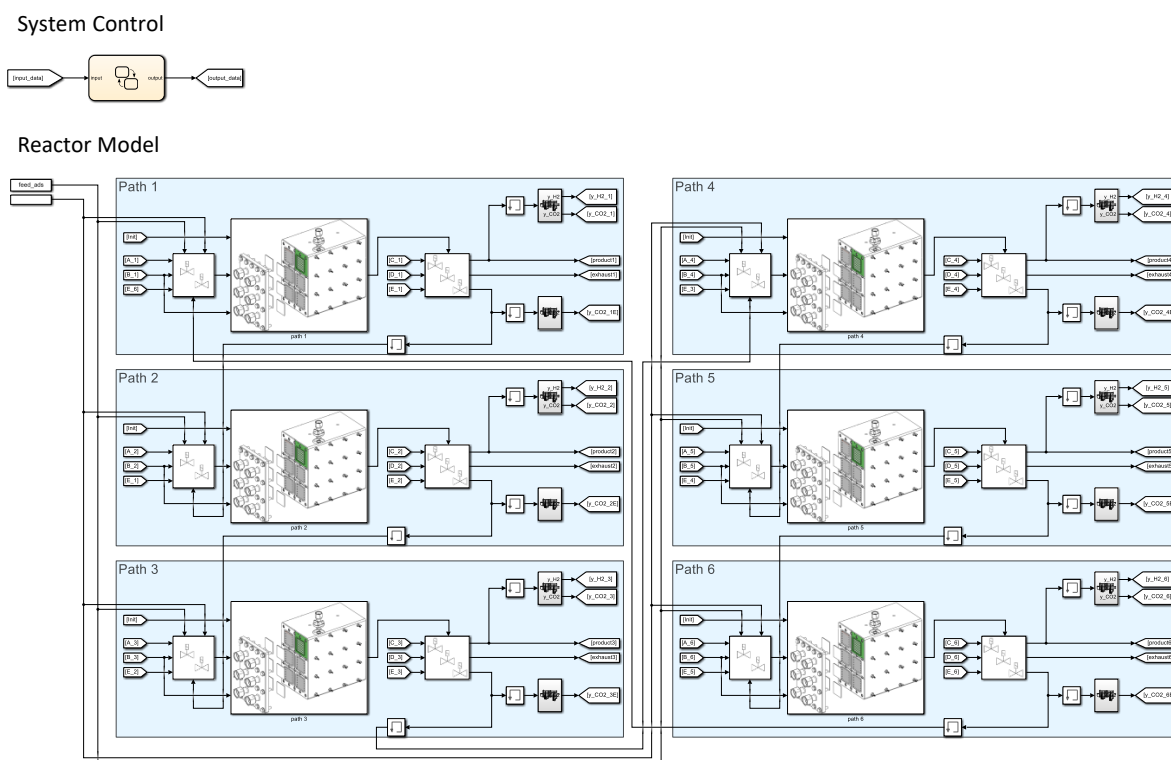


Fig. 4.15: Simulink model on system-level. The Stateflow chart (System Control in yellow) controls the system and adjusts the discrete states (valve positions) to enable automated operation. Six reaction chambers (Reactor Model in blue) can optionally be interconnected with valves. After an initialization step, the chambers operate alternately in reactive adsorption or regeneration mode to deliver a continuous product flow. Figure from [P2] and [P3].

the Stateflow machine to act. By employing this approach, the switching times can be optimized automatically during runtime.

As already stated in Section 3.2, the model takes into consideration the simultaneous occurrence of the WGS reaction on a Cu-based catalyst, CO₂ adsorption on a K-HDMO sorbent, and the subsequent desorption process. Detailed reactor parameters and operating conditions relevant for the pilot plant base case simulations are listed in Table 4.2.

Tab. 4.2: Reactor parameters and operating conditions used in the pilot plant base case simulation. Adapted table from [P3].

Reactor dimensions		
number of chambers		6
number of slits per chamber		7
rectangular slit dimensions		4 mm × 50 mm × 300 mm
General parameters		
bed void fraction	ε_b	0.4
particle void fraction	ε_p	0.5
bulk density	ρ	1096 kg m ⁻³
particle radius	d_p	200 μm
catalyst weight fraction ¹	w_{cat}	0.05
Adsorption parameters		
pressure	p	8 bar
temperature	T	250 °C
flow rate	F_{STP}	1000 mL min ⁻¹
CO volume fraction	$y_{CO,feed}$	0.3
H ₂ O volume fraction	$y_{H_2O,feed}$	0.6
N ₂ volume fraction	$y_{N_2,feed}$	0.1
Desorption parameters		
pressure	p	1 bar
temperature	T	250 °C
flow rate	F_{STP}	500 mL min ⁻¹
H ₂ O volume fraction	$y_{H_2O,feed}$	0.4
N ₂ volume fraction	$y_{N_2,feed}$	0.6

¹ Catalyst is homogeneously mixed with sorbent in the first quarter of the reactor length.

Various experiments were carried out to determine the kinetic parameters contained in the model equations in Chapter 3.2. The frequency factor as well as the activation energy in the empirical rate expression describing the WGS reaction were fitted according to experimental data at 250 °C, and breakthrough experiments were performed to adapt adsorption (pressure: 8 bar) and desorption (pressure: 1 bar) parameters. The experimental equilibrium isotherm for CO₂ sorption was implemented by using the Freundlich

model. All relevant parameters obtained by nonlinear regression from experimental data are given in Table 4.3.

Tab. 4.3: Kinetic and equilibrium parameters obtained by nonlinear regression from experimental data. Table adapted from [P3].

WGS reaction rate parameters	
k_{∞}	$2.01 \times 10^5 \text{ mol bar}^{-2} \text{ g}^{-1} \text{ h}^{-1}$
E_a	$51.845 \text{ kJ mol}^{-1}$
Isotherm parameters	
m_{Fr}	$0.177 \text{ mmol g}^{-1} \text{ bar}^{-m_{\text{Fr}}}$
n_{Fr}	4.545
Sorption kinetic parameters	
k_{ads}	0.1125 s^{-1}
k_{des}^1	$5.38 \times 10^{-4} \text{ s}^{-1}$
β_{des}	74000 J mol^{-1}

4.3.2 Base Case Simulation Results

The Simulink results for the pilot plant base case simulation are shown in Figure 4.16 for single stage configuration (A, C, E) and serial configuration (B, D, F). The switch was initiated in such a way that product purity in both configurations was maintained.

Figure 4.16A and B display typical operating schemes for all chambers during the first 1200 s. Both configurations facilitated continuous H_2 production with less than 5 % CO_2 in the product, as at least one reaction chamber was always in M1 or M2, respectively. The duration of M4 was identified as the limiting factor for sorbent regeneration. Figure 4.16C and D show the time spans of each operating mode for the first five cycles. After the first cycle, time spans decrease significantly but do not reach the initial level again due to limited regeneration time and incomplete sorbent regeneration. However, they stabilize and remain almost constant from the fourth cycle onwards. Figure 4.16E and F illustrate the relative sorbent loadings at the end of each operating mode, based on the maximum loadings. By interconnecting two subsequent chambers in serial configuration, it becomes possible to increase the sorbent usage by 7 % compared to single stage configuration while keeping the CO_2 volume fraction in the product flow below 5 %.

Not only the configuration, but also the accepted CO_2 content in the product influences the overall efficiency. Figure 4.17 displays the CO_2 loading at the end of each reactive adsorption mode in serial configuration across the length of the reactor. The switch from M2 to M3 was initiated when the CO_2 fraction in the product gas reached $y_{\text{CO}_2} > 0.05$, whereas the switch from M3 to M4 was triggered when $y_{\text{CO}_2} > 0.10$ (Figure 4.17A) or $y_{\text{CO}_2} > 0.15$ (Figure 4.17B). Increasing the M3-M4 threshold can improve sorbent loading,

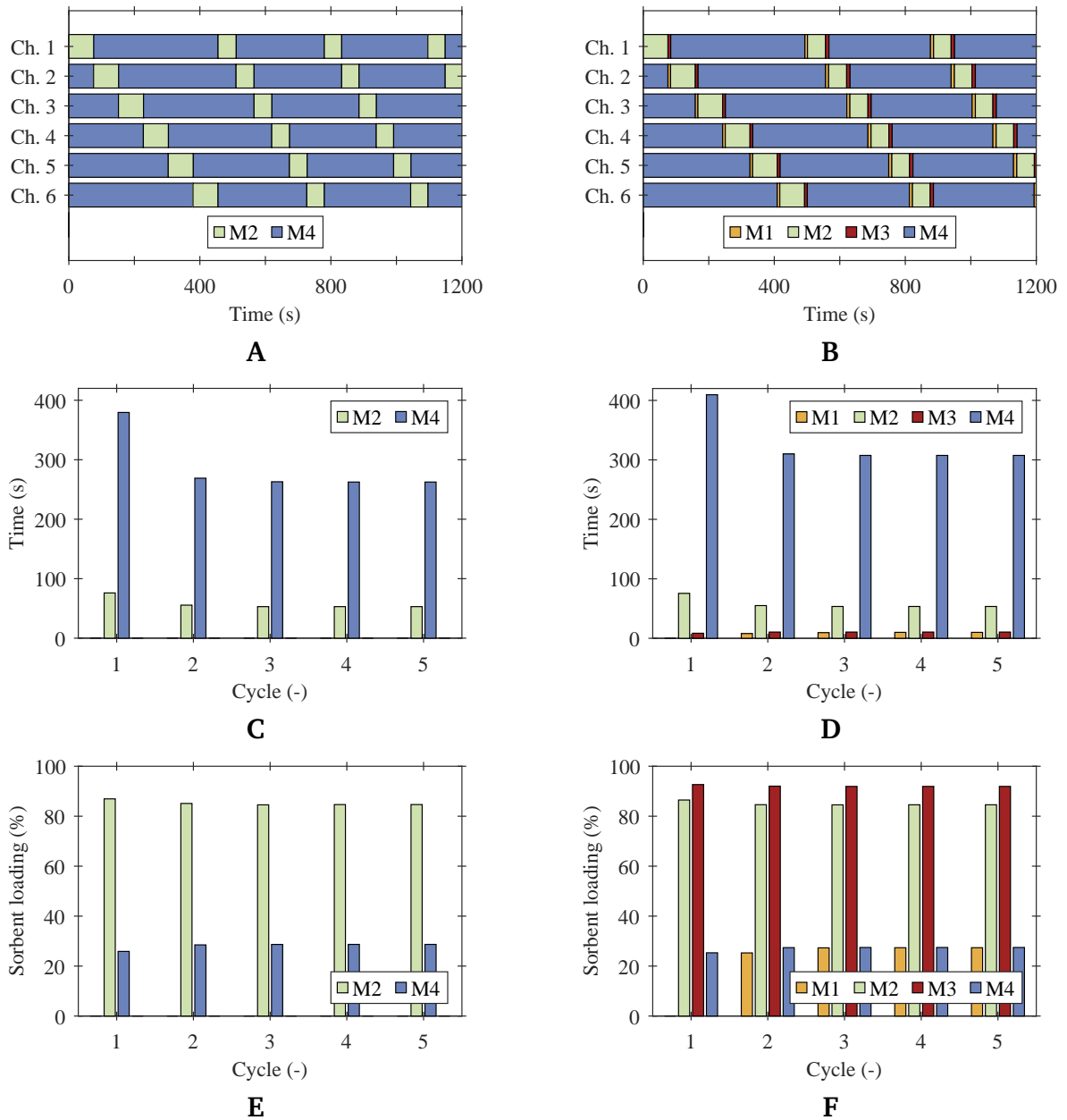


Fig. 4.16: Optimized cycle modes obtained by means of Simulink simulations for the pilot plant base case in single stage configuration (A,C,E) and serial configuration (B,D,F). The switch from M2 to M4 (single stage configuration) or M3 (serial configuration), respectively, is triggered as soon as $y_{CO_2} > 0.05$ at the outlet of the reaction chamber. The switch from M3 to M4 in serial configuration occurs when the CO_2 volume fraction to the subsequent chamber is $y_{CO_2} > 0.15$. A,B) Operating schedule for all six reaction chambers, C,D) time span of each operating mode for the first five cycles in chamber 1, and E,F) relative sorbent loading at the end of each operating mode for the first five cycles in chamber 1. Figure from [P3].

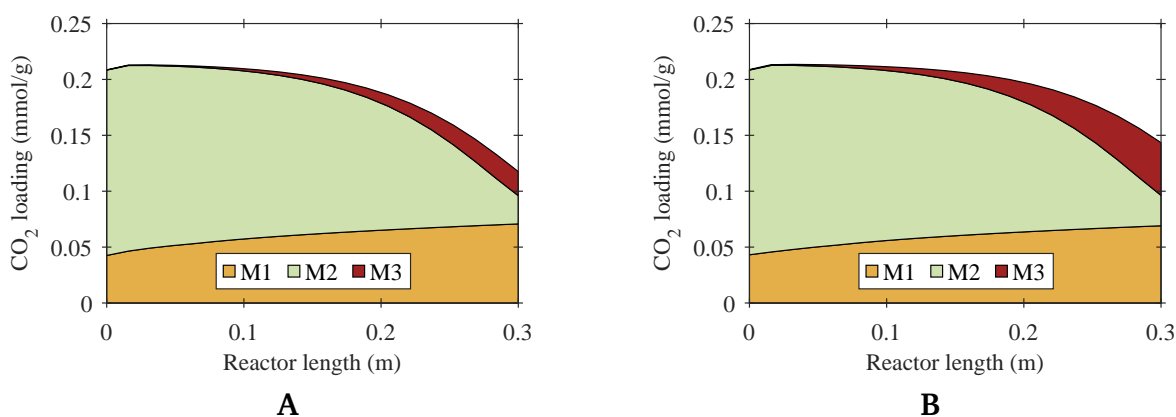


Fig. 4.17: CO₂ loading at the end of each reactive adsorption mode for cycle 5 in chamber 1 over the reactor length obtained by means of Simulink simulations for the pilot plant base case in serial configuration. The switch from M3 to M4 occurs when the CO₂ volume fraction to the subsequent chamber is **A)** $y_{\text{CO}_2} > 0.10$, and **B)** $y_{\text{CO}_2} > 0.15$. The switch from M2 to M3 is triggered as soon as $y_{\text{CO}_2} > 0.05$ at the outlet of the reaction chamber in both cases. Figure from [P3].

as demonstrated by the higher value at the end of M3 in Figure 4.17B compared to Figure 4.17A. This leads to longer cycle times and improved efficiencies.

Another critical operational parameter was identified to be the ratio of adsorption-to-desorption flow. As shown in Figure 4.18A for single stage configuration, both the duration of M2 and the sorbent loading at the end of M2 decrease with increasing flow ratio. The flow ratio had a significant impact on the sorbent loading throughout the entire reactor length, as illustrated in Figure 4.18B. To achieve acceptable switching times and process efficiencies, a balance must be found between maintaining reasonably high product flows and ensuring adequate sorbent loadings.

Hence, simulation-driven process design, as demonstrated by this case study, can greatly improve the utilization of the sorption capacity and consequently, enhance the performance of sorption-enhanced reaction processes.

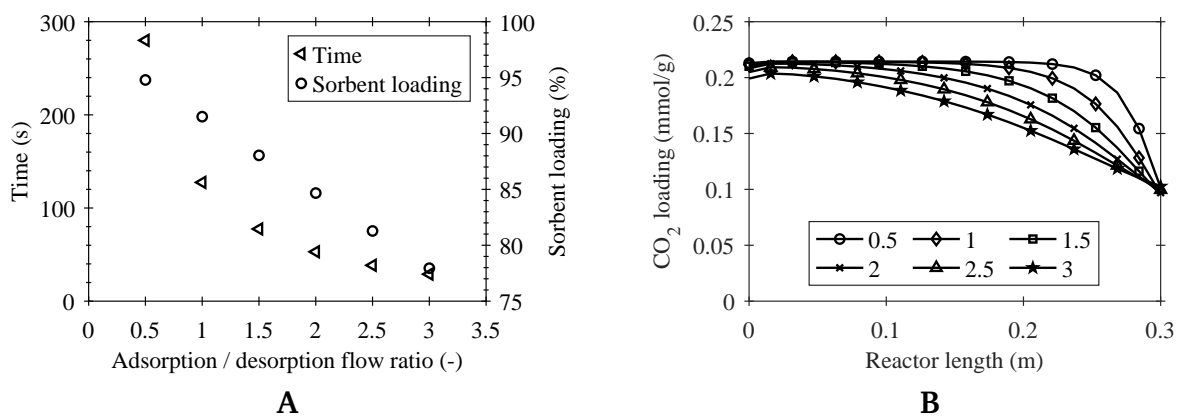


Fig. 4.18: Impact of changes in the adsorption-to-desorption flow ratio on the cyclic adsorption behaviour obtained by means of Simulink simulations for the pilot plant base case in single stage configuration. **A**) Time span of M2, and relative sorbent loading at the end of M2 as a function of the adsorption-to-desorption flow ratio (cycle 5 in chamber 1), and **B**) CO₂ loading at the end of M2 over the reactor length for various adsorption-to-desorption ratios (cycle 5 in chamber 1). The switch from M2 to M4 is triggered as soon as $y_{CO_2} > 0.05$ at the outlet of the reaction chamber in all cases. Figure from [P3].

4.4 Impact on subsequent Process Steps⁴

The potential impact of a possible slip of CO₂ that originates from incomplete separation in the SEWGS reactor on subsequent process steps, specifically FT and HC, is discussed in this section.

4.4.1 Experimental FT-HC Coupling

To investigate the effects of various syngas compositions, a series of experiments were conducted using a FT reactor coupled with a HC reactor. Each experiment began with a FT product reference measurement, followed by the redirection of the FT effluent into the HC reactor cascade for coupled operation. The experimental data was recorded and is presented in Figure 4.19, which depicts the exemplary curve of an experimental point in terms of the reaction temperatures in both reactors, as well as the conversion in the FT reactor. To attain steady-state operation, the process conditions were maintained constant in the FT reactor for around 24 h. FT reference samples were gathered in the traps for a minimum of 3 h towards the end of this period. After FT-HC coupling, steady-state HC samples were collected from the traps after approximately 24 h.

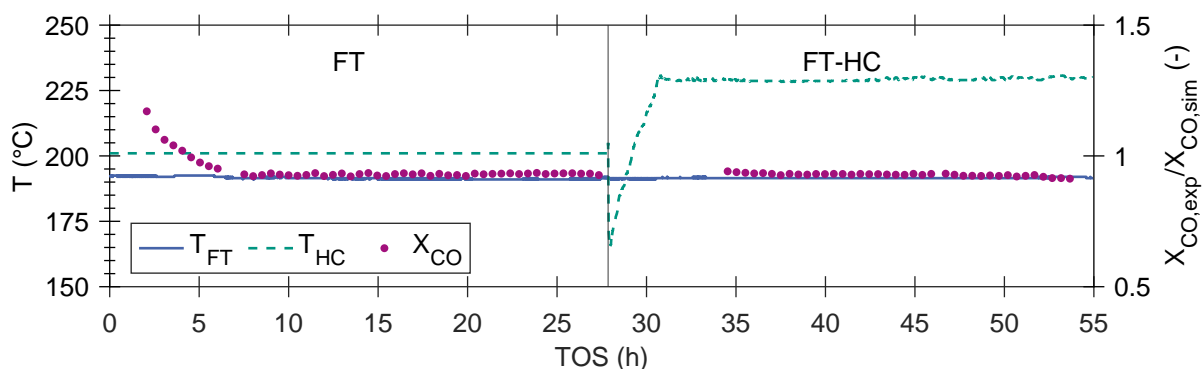


Fig. 4.19: Exemplary curve for FT-HC coupling experiments (shown here: Dil_CO2_1). Temperature, as well as CO conversion, remain constant in FT and HC steady-state operation during sampling. Figure from [P4].

The syngas compositions of interest, i.e., low CO₂ dilution (arising from incomplete CO₂ removal in the SEWGS reactor, Dil_CO2_2) and high CO₂ dilution (lack of CO₂ removal, Dil_CO2_1), as well as syngas with equivalent N₂ dilution (Dil_N2) and without any dilution (Ref_A) for comparative purposes, are presented in Table 4.4.

⁴This section contains content from [P4].

Tab. 4.4: FT feed (balanced in N₂), weight fractions of FT hydrocarbon product lumps, average chain length for FT and FT-HC measurements, and HC wax (C₂₂₊) conversion. System pressure: 20 bar, FT Weight Hourly Space Velocity (WHSV)¹: 4.5 h⁻¹, FT/HC catalyst mass ratio: 7.4, FT temperature: 195 °C to 200 °C (adjusted to maintain constant CO conversion), HC temperature: 230 °C. Adapted table from [P4].

	H ₂	CO	CO ₂	w _{C₁₀-C₁₄}	w _{C₁₅-C₂₂}	w _{C₂₂₊}	n _{C,FT}	n _{C,HC}	X _{C₂₂₊}
Dil_N2	38.8 %	19.4 %	0 %	0.17	0.22	0.39	20	11	86.0
Dil_CO2_1	38.8 %	19.4 %	38.8 %	0.17	0.21	0.40	20	9	94.8
Dil_CO2_2	38.8 %	19.4 %	5.0 %	0.18	0.21	0.39	20	11	81.7
Ref_A	64.7 %	32.3 %	0 %	0.22	0.22	0.28	17	11	77.0

¹ The desired value of 4.5 h⁻¹ was not reachable in Ref_A due to experimental restrictions. Here: 3.5 h⁻¹.

4.4.2 Hydrocarbon Products

Based on the results of the FT reference measurements, it can be inferred that neither N₂ nor CO₂ significantly influences the FT kinetics on the Co catalyst employed in this study. Instead, both gases act primarily as a diluent, as evidenced by the weight fractions of product "lumps" listed in Table 4.4. These hydrocarbon lumps are based on the number of carbon atoms and defined as follows: kerosene (C₁₀-C₁₄), gas oil (C₁₅-C₂₂), and waxes (C₂₂₊); not shown: gases (C₁-C₄), and naphtha (C₅-C₉). Due to technical limitations, achieving identical CO conversion in all experiments was not possible. In the reference measurement without dilution (Ref_A), the conversion was below half of the intended value. This could account for the distinct product distribution in Ref_A compared to the experiments with N₂- or CO₂-enriched syngas. A noticeable change in the product distribution towards shorter hydrocarbons was observed in all experiments when comparing the average chain length of FT-HC products to the corresponding FT reference measurement (Table 4.4). Although the wax conversion in the HC reactor cascade, is quite high (above 75 % in all experiments), it does not seem to correlate with the ratio of gas velocity and FT product (Table 4.4).

Figure 4.20 illustrates the FT and FT-HC product distribution for two experimental points (Figure 4.20A: Dil_N2, Figure 4.20B: Dil_CO2_1). In all experiments, the hydrocracking process only yielded hydrocarbon species up to C₁₄. The primary factor responsible for this effect might be the shape selectivity of the H-ZSM-5 catalyst, which could lead to pore mouth cracking.

The integral product selectivity for different hydrocarbon product lumps obtained from FT and FT-HC processes is presented in Figure 4.21. The data indicates that the wax fraction, along with some portions of the gas oil fraction, is selectively transformed into kerosene and naphtha in the HC.

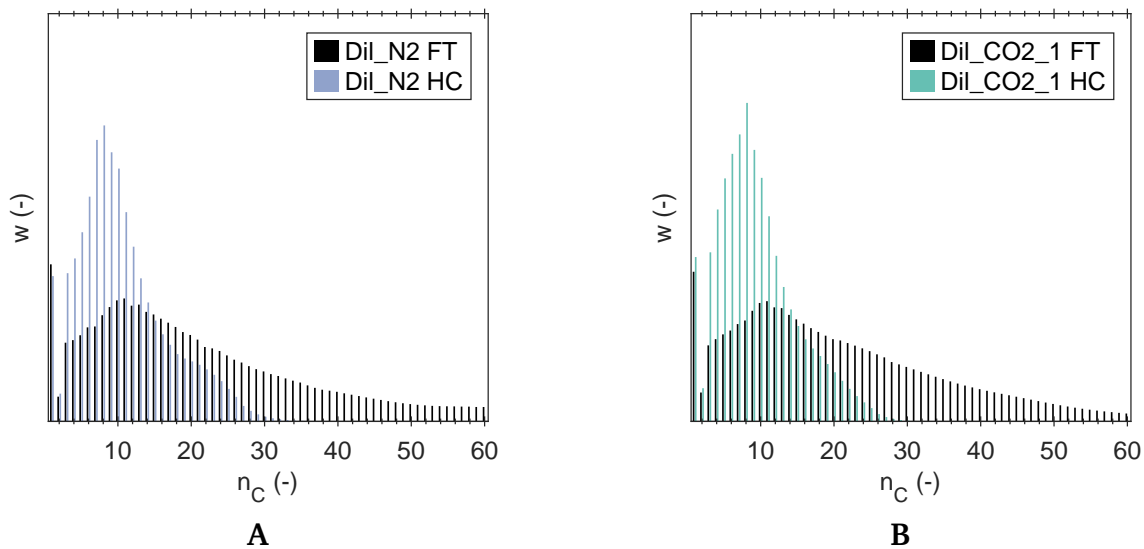


Fig. 4.20: Hydrocarbon weight fractions for FT and coupled FT-HC measurements. A) Dil_N2, and B) Dil_CO2_1. Figure B from [P4].

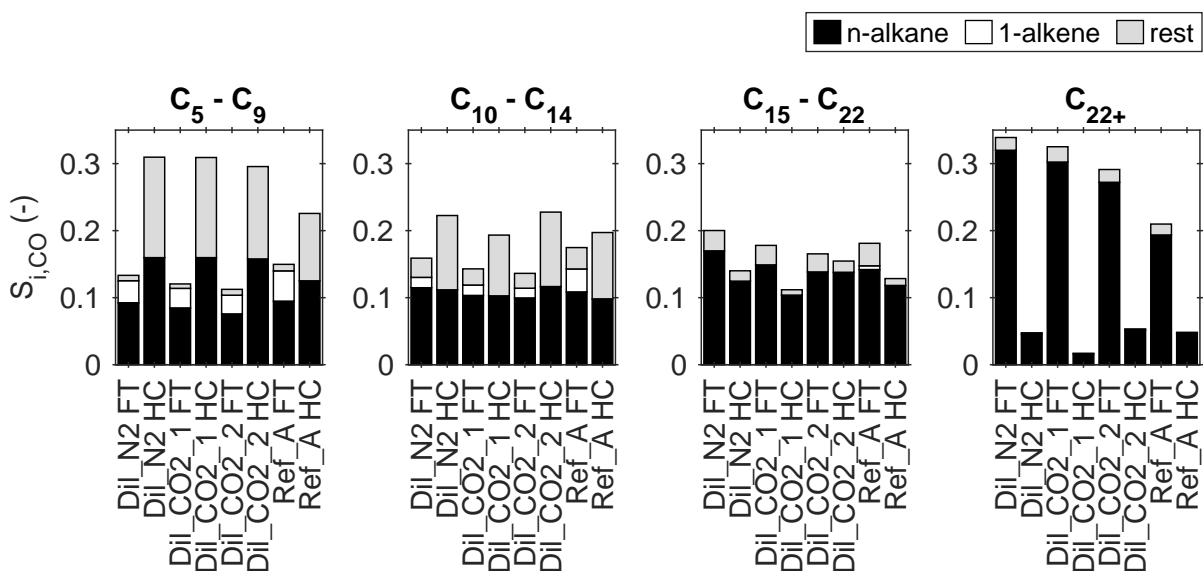


Fig. 4.21: Integral CO-related hydrocarbon selectivity of product lumps for FT and FT-HC measurements. In FT products, n-alkanes and 1-alkenes could be distinguished; in FT-HC products, only n-alkanes could be distinguished with the GC analysis on hand. Adapted figure from [P4].

Figure 4.22 provides a more in-depth analysis of the product composition concerning the content of n-alkanes. The n-alkane content in the naphtha and kerosene fraction is considerably lower in all FT-HC products compared to their FT counterparts. Nonetheless, a minor increase in the n-alkane fraction is observed in the gas oil and wax fractions. These findings suggest that the linear alkanes produced by the FT process underwent successful isomerization or dehydrogenation in the HC.

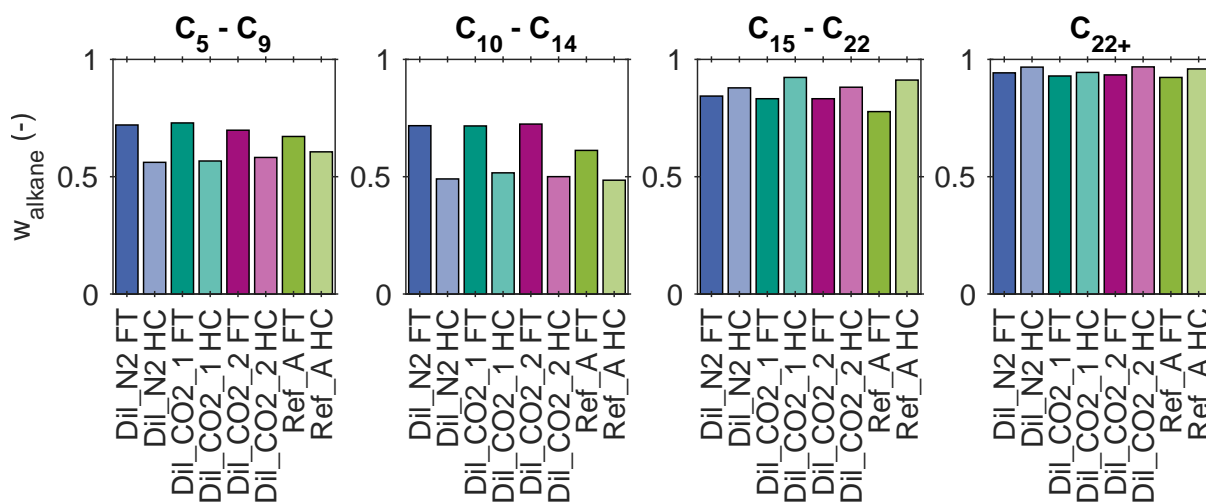


Fig. 4.22: Integral n-alkane fractions of product lumps for FT and FT-HC measurements. Adapted figure from [P4].

According to the experimental data, no significant differences were found between the pure syngas feed and the diluted feeds with N₂ and CO₂. Hence, the impact of dilution on the coupled FT-HC process's product distribution is insignificant, considering the limited parameter variations.

4.4.3 Carbonaceous Species in the Water Phase

Low-Temperature Fischer-Tropsch (LTFT) with Co catalysts is known to produce some oxygenates such as alcohols and carboxylic acids in addition to the majority of hydrocarbons. Short-chain primary alcohols selectively dissolve in the aqueous phase, while long-chain alcohols accumulate in the oil fraction. The weight fractions of C₁ to C₅ alcohols in the water phase, collected in the cold trap at 10 °C in FT reference measurements, are illustrated in Figure 4.23A. During coupled FT-HC operation, oxygenates from the FT product underwent further reactions on the bifunctional HC catalyst.

The conversion of alcohols in the HC stage is illustrated in Figure 4.23B, which indicates a more significant reduction in weight fraction for long-chain alcohols. Potential reactions, such as dehydroxylation on Brønsted acid sites and hydrogenation on Pt sites of the catalyst, may occur depending on the hydrogen partial pressure and the prevailing

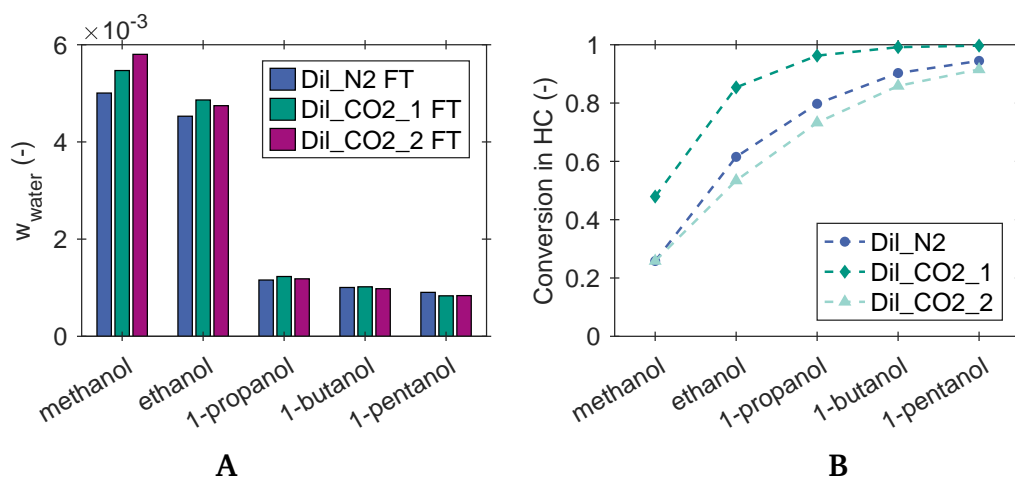


Fig. 4.23: C₁-C₅ alcohols in the water phase collected in the cold traps at 10 °C. **A)** Alcohol weight fractions in water phase for FT measurements, and **B)** conversion of alcohols in the HC for FT-HC measurements. Adapted figure from [P4].

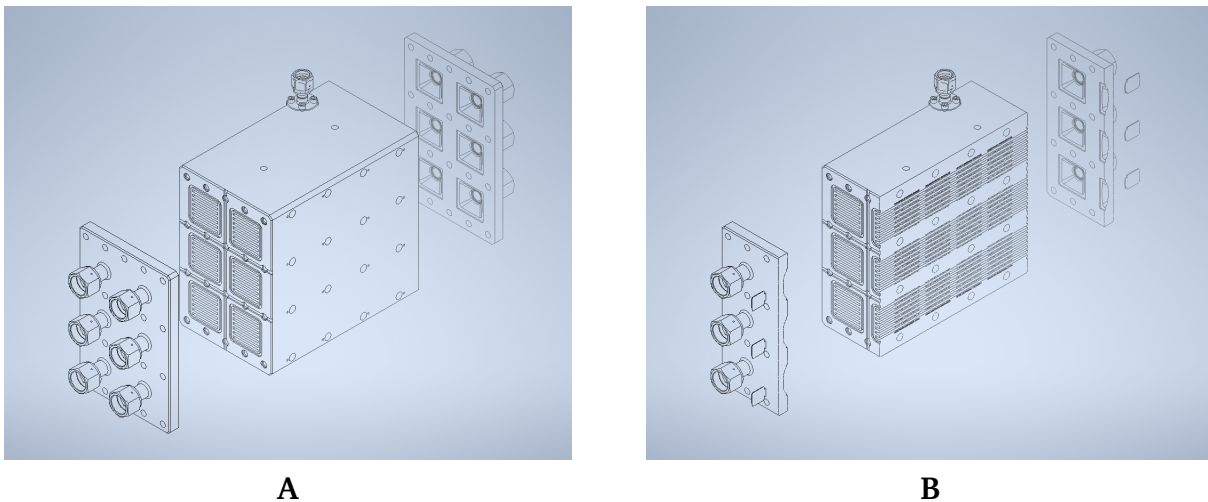
reaction conditions. These findings demonstrate that the subsequent coupling of HC with FT can minimize the loss of carbonaceous compounds to the water phase.

Scale-Up: SEWGS Module in the *Kerogreen* Pilot Plant

The scientific findings discussed in Chapter 4 were utilized in the design of a SEWGS module, which was integrated into the *Kerogreen* process chain (as presented in Section 1.3). The *Kerogreen* pilot plant was built at IMVT, KIT in Germany, and is composed of modules from various project partners. The plant is the first of its kind and aims to produce 0.1 kg h^{-1} kerosene crude. The planning and construction of the SEWGS module contributed a vital part to this work and is briefly presented in this chapter.

5.1 SEWGS Reactor: Design, Construction and Operating Strategies

Figure 5.1A shows an excerpt from the technical drawing of the diffusion-bonded SEWGS pilot plant reactor, which was manufactured in-house at IMVT. The reactor consists of six chambers, each of which has seven slits. Each slit measures 30 cm in length, 5 cm in width, and 0.4 cm in height. The slits were filled with a mixture of catalyst and sorbent particles with particle diameters ranging from 100 μm to 300 μm . Based on the findings presented in Section 4.1, the most promising mixture of Cu/ZnO- Al_2O_3 catalyst and potassium-loaded HTC sorbent calcined at 400 °C was used. The reactor was configured according to the best laboratory results [P1], with catalyst particles placed in zone 1 (one-quarter of the total sorbent mass homogeneously mixed with the total catalyst amount), and zone 2 (towards the reactor outlet) packed with the remaining sorbent. Due to the high quantities of sorbent material required, several powder processing steps, such as calcination under N_2 atmosphere at 400 °C, compaction, and sieving, were performed by an external company (hte GmbH, Germany). The reactor chambers were equipped with individual inlet ports, where sintered metal plates ensured uniform gas distribution (not shown in Figure 5.1). Further plates at the reactor outlet prevented the discharge of catalyst or sorbent particles. To maintain isothermal operating conditions, heating cartridges could be inserted into drilled holes in the reactor body. Additional microchannels between the reaction slits allowed temperature control through a preheated N_2 -steam mixture generated for the desorption process. Figure 5.1B shows a virtual cut in the flow direction of the technical drawing, which provides insight into the positioning of these adjacent cooling channels.



A

B

Fig. 5.1: Technical drawing of the SEWGS reactor with six individually accessible reaction chambers. **A)** Outside view with drilled holes for heating cartridges on the side, along with inlet and outlet flanges, and **B)** virtual cut in the flow direction to make the adjacent cooling channels visible. More information can be found in Figure 4.14A.

Figure 5.2 displays the SEWGS reactor in its filling rack, which facilitates easy rotation during filling, emptying, and leakage testing. To enable precise and user-friendly filling of the reactor slits, a custom-fitted movable funnel was designed and 3D-printed.

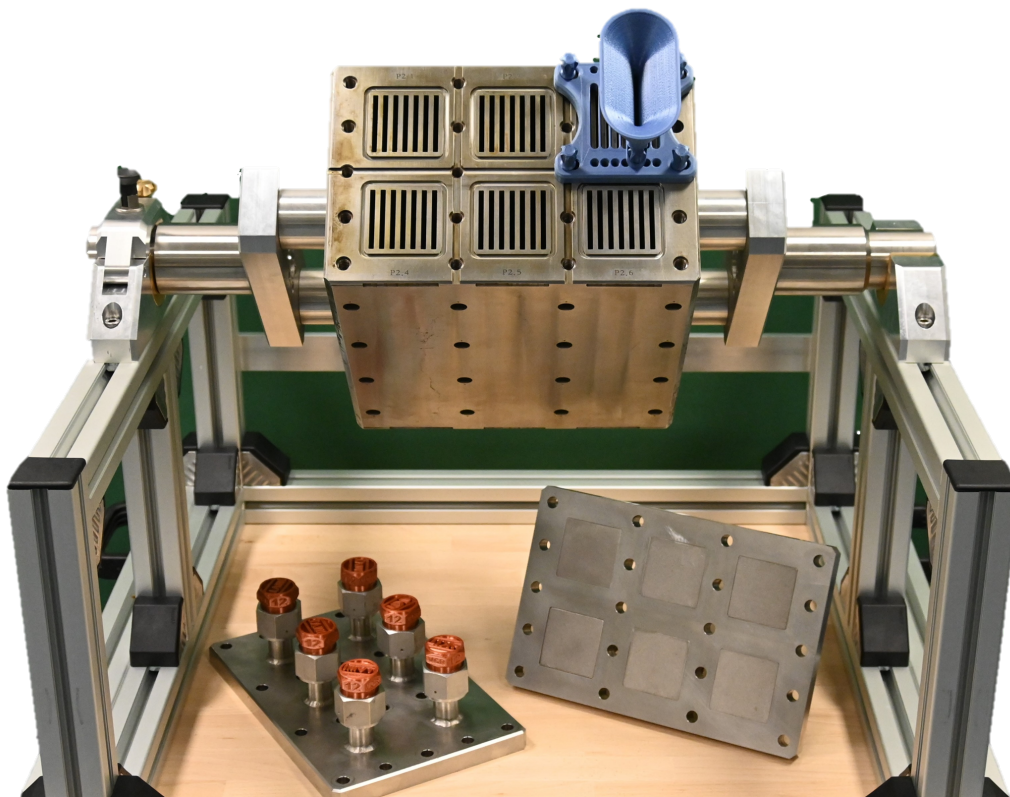


Fig. 5.2: Photograph of the SEWGS reactor mounted in its filling rack. The inlet and outlet flanges are positioned underneath. The blue 3D-printed funnel can be used for the precise filling of the reactor slits.

Valves were installed at both the inlet and outlet of the reaction chambers, as shown in Figure 5.3. By setting the valve positions, the prevailing modes in the reaction chambers can be dynamically controlled. Table 5.1 lists the corresponding valve positions for the reactive adsorption and regeneration modes, as defined in Figure 4.14B.

The reaction chambers can be operated in either a single stage or serial configuration. In each chamber, the reaction feed ($\text{CO} + \text{H}_2\text{O}$) can be supplied via valve A, or the regeneration feed ($\text{N}_2 + \text{H}_2\text{O}$) can be supplied via valve B. The effluent of each reaction chamber can be directed to the product line via valve C, or to the exhaust line via valve D. If the reactor is operated in serial configuration, the outlet of one reaction chamber can be redirected to the inlet of the subsequent reaction chamber via valve E. Typical cyclic operating strategies, in terms of the respective operating modes for single stage as well as serial configuration, are graphically depicted in Figure 5.4 and described in more detail in Section 4.3. In both configurations, chamber 1 always starts in M2 while the others start in M4. Then, cyclic operation begins once a pre-defined threshold is reached, such as the CO_2 content in the effluent.

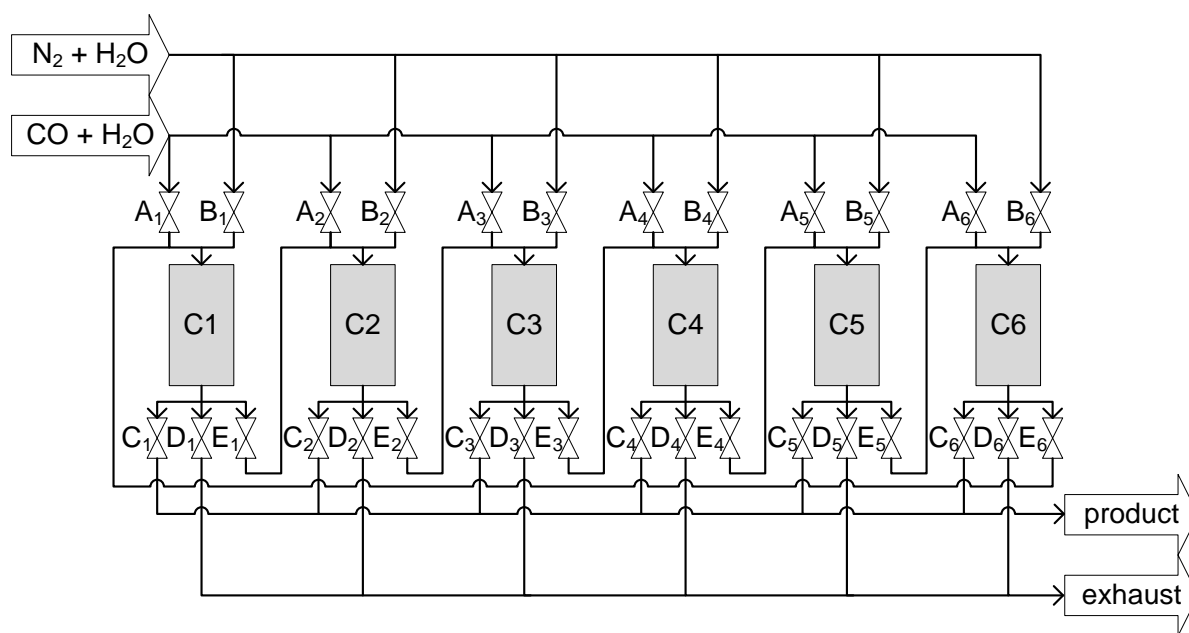


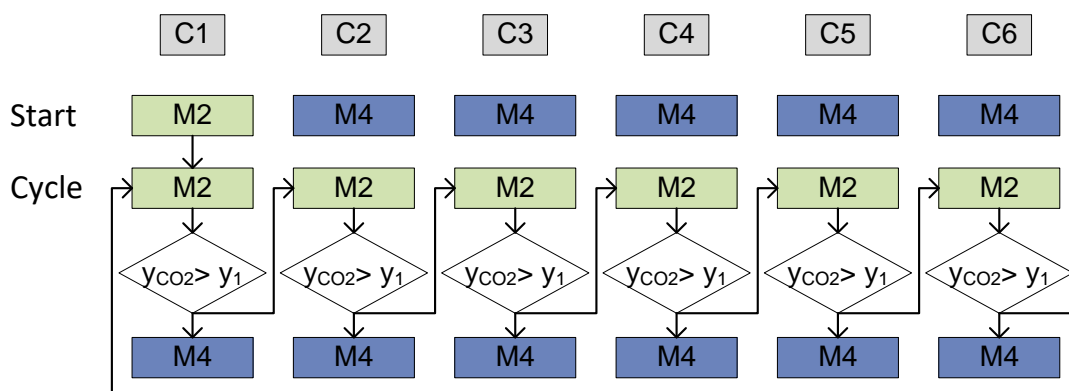
Fig. 5.3: Schematic drawing of the SEWGS reactor with six individually controlled reaction chambers and their corresponding valves at the inlets and outlets.

Tab. 5.1: Valve positions of a reaction chamber for all relevant modes. The modes are described in Figure 4.14B, and the valve positions are illustrated in Figure 5.3. The index i defines the respective chamber position (C1...C6 in Figure 5.3).

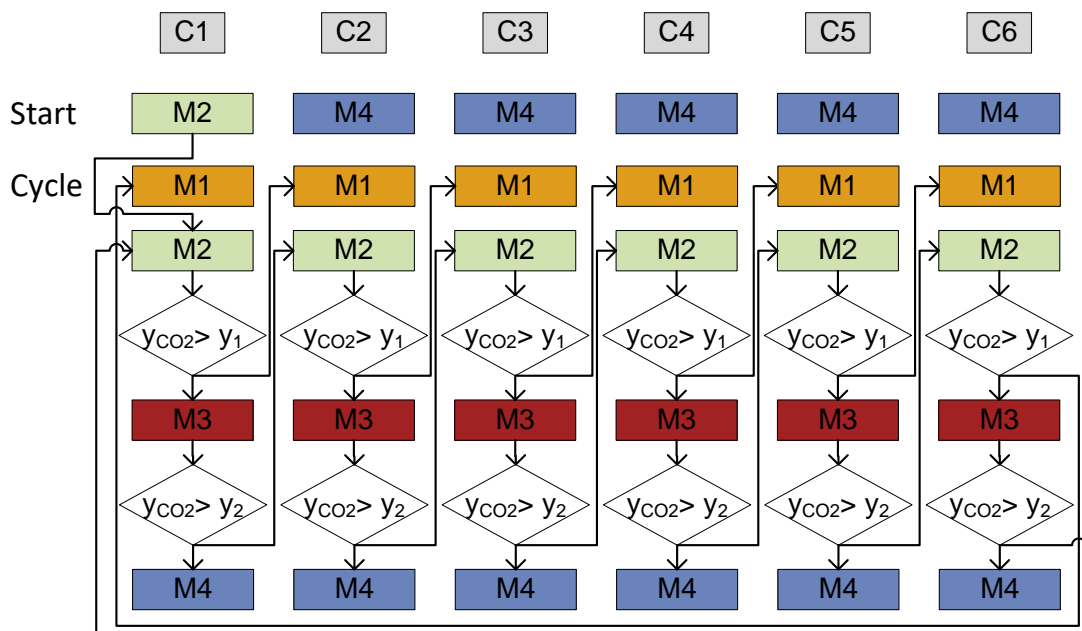
	A_i	B_i	C_i	D_i	E_i	E_{i-1}
M1	0	0	1	0	0	1
M2	1	0	1	0	0	0
M3	1	0	0	0	1	0
M4	0	1	0	1	0	0

i : 1...6, 1: valve open, 0: valve closed.

E_{i-1} for $i = 1$: E_6 .



A



B

Fig. 5.4: Cyclic operating strategies for A) single stage configuration, and B) serial configuration. The modes are described in Section 4.3, and the corresponding valve positions according to Figure 5.3 are listed in Table 5.1.

5.2 SEWGS Module: Planning, Construction and Implementation

The SEWGS module is embedded in the *Kerogreen* process chain. Hence, feed as well as product streams are connected to previous and subsequent modules, respectively. The SEWGS reactor serves as the central component of the SEWGS module. Figure 5.5 shows the Piping and Instrumentation Diagram (P&ID) with all relevant piping, valves, fittings, instruments, and connections of the module.

Computer Aided Design (CAD) drawings were used to plan the construction of the module to minimize the required space. The side view of the module is shown in Figure 5.6. The module measures approximately 1.20 m in length, 1.80 m in depth, and 1.75 m in height. A photograph of the completed SEWGS module can be found in Figure 5.7.

The SEWGS module was installed in a 30 ft container together with the other modules from the project partners for the full *Kerogreen* process pilot plant. This container is divided into three compartments: the safety control room, the synthesis compartment, and the plasmolysis compartment. An additional 10 ft container serves as a system control room for operators and is located next to the main container. The SEWGS module is situated within the synthesis compartment, which measures approximately 5 m in length, 2.2 m in depth, and 2.3 m in height. A photograph of the synthesis compartment is shown in Figure 5.8. The outlet of the SEWGS module is connected to the coupled FT-HC unit, where the produced syngas is utilized to synthesize hydrocarbons, mainly middle distillates. The middle distillates are further isomerized into naphtha, kerosene, and diesel. This mixture is then distilled to yield synthetic paraffinic kerosene. The inlet of the SEWGS module is connected to the CO purification unit. This PSA module supplies pure CO from a CO-CO₂ mixture, which was preliminary provided by a plasmolysis system. The plasmolysis unit produces approximately 0.7 kg h⁻¹ of CO via plasma-driven CO₂ splitting with integrated oxygen separation (not shown in Figure 5.8).

In terms of general infrastructure, the container provides electricity, several vents for gas disposal, a syngas compressor between SEWGS and FT, and access to various gases for inertization, purging, reduction, start-up, and CO₂ feed. Additionally, ventilation systems and electrical room heaters ensure stable operating conditions. Cooling machines are installed on the backside and the rooftop of the container, supplying cooling cycles for various heat exchangers in the system. The container is equipped with various safety measures, including H₂, CO and O₂ sensors (Safety Integrity Level (SIL) 1), fire detectors, and safety vents connected to safety valves in the system.

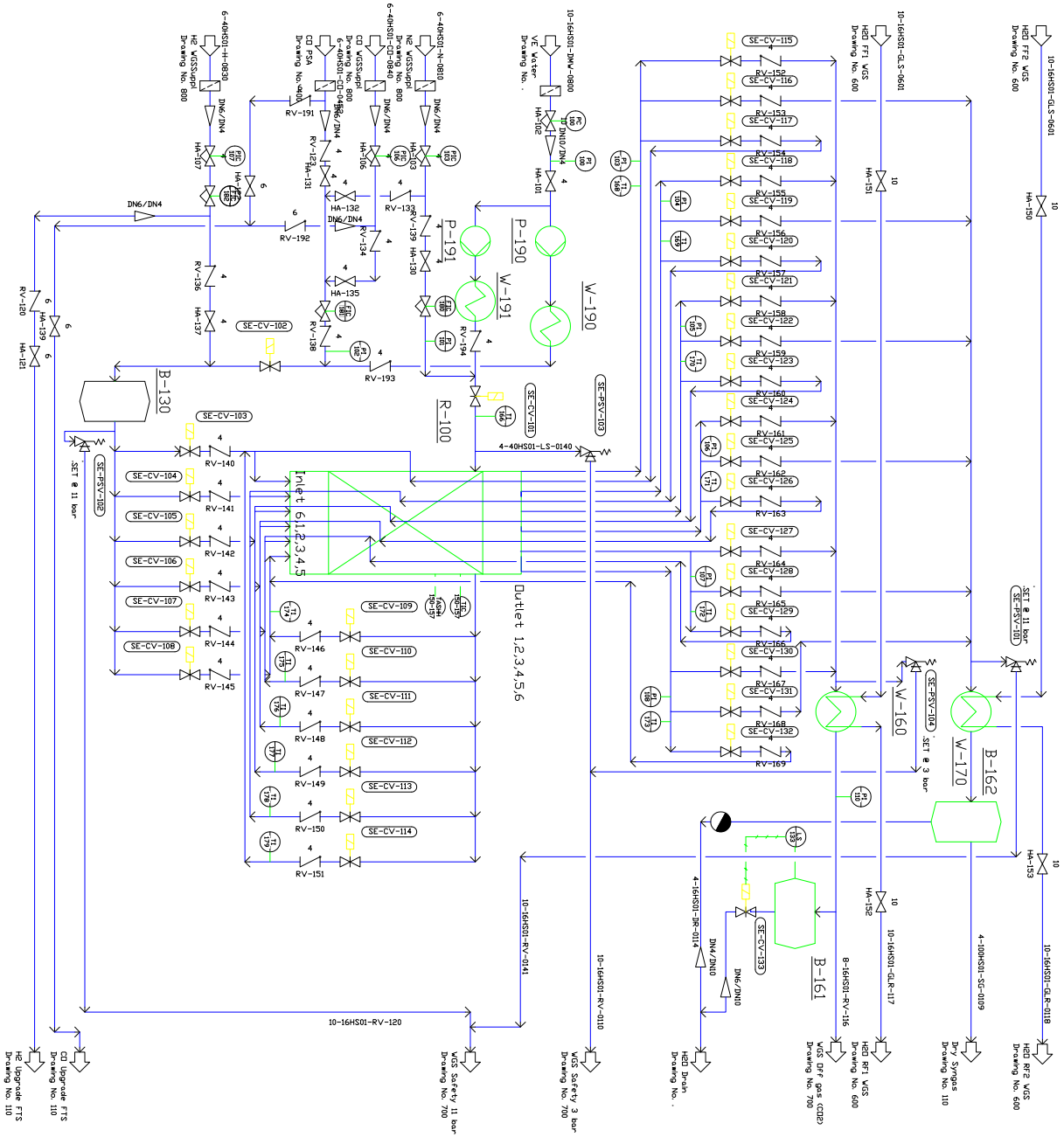


Fig. 5.5: P&ID of the SEWGS module.

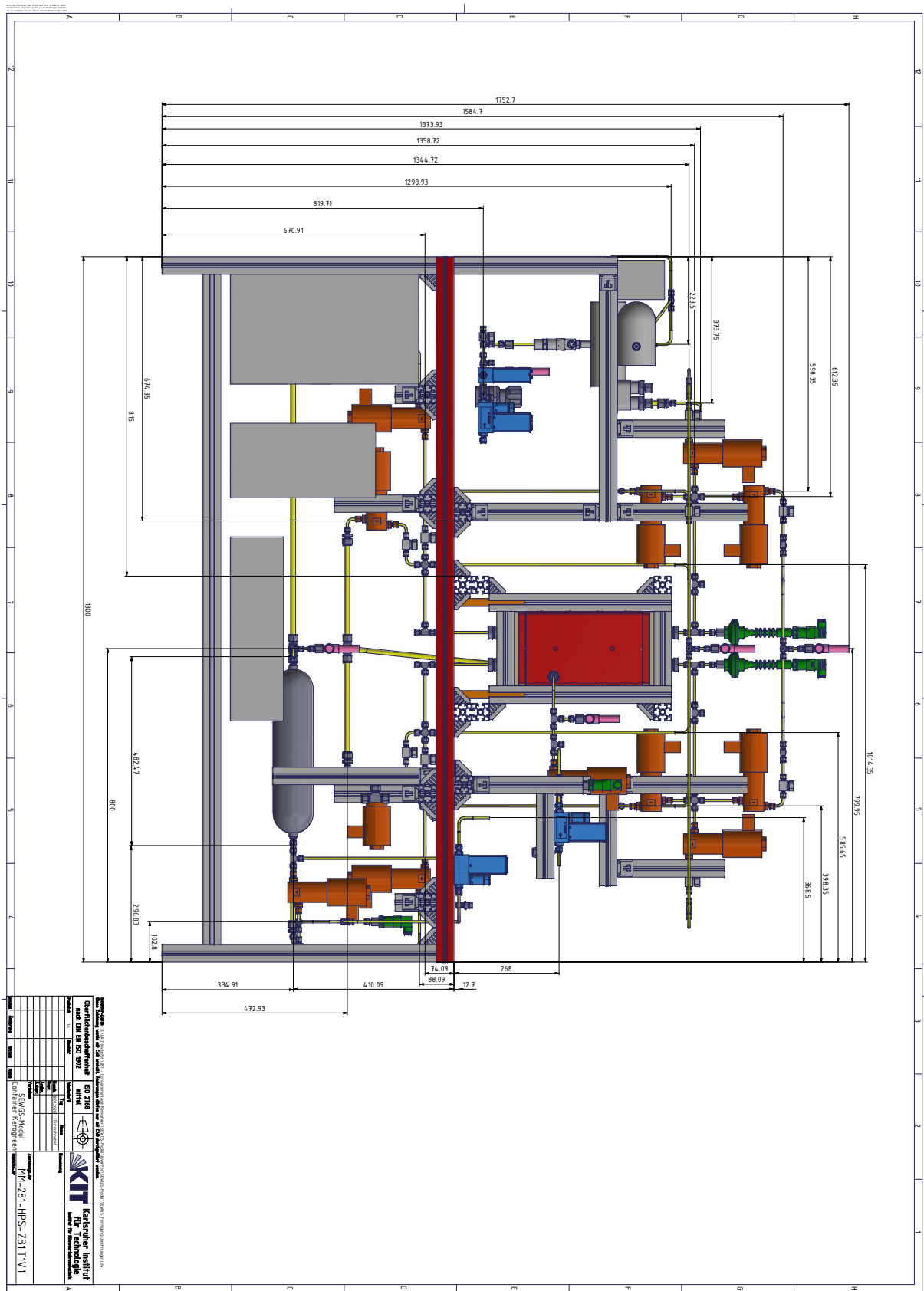


Fig. 5.6: CAD drawing (side view) of the SEWGS module.



Fig. 5.7: Photograph of the SEWGS module (front view), located at IMVT, KIT, Germany. ©Bramsiepe/KIT



Fig. 5.8: Photograph of the *Kerogreen* container with FT-HC, SEWGS, and CO purification modules (provided by the project partners INERATEC GmbH, KIT and HyGear B.V., respectively), located at IMVT, KIT, Germany. ©Bramsiepe/KIT

The aviation sector is a major contributor to greenhouse gas emissions. Fossil fuels must be replaced with sustainable alternatives for contributing to the ambitious climate targets stated in the Paris Agreement on Climate Change [2, 3]. Synthetic e-fuels, typically produced in PtL processes, are among the discussed options to serve as SAF.

A novel PtL process was currently developed in the EU project *Kerogreen* [22]. Here, captured CO₂ is dissociated into CO and O₂ using microwave plasma technology. Solid oxide membranes are utilized to electrochemically separate the O₂, while the residual mixture of CO and CO₂ is purified into pure CO by passing through a PSA unit. Subsequently, the CO reacts with water in the WGS reaction to produce syngas. Syngas is chemically converted into a range of hydrocarbons in a FT reactor. The output of the FT reactor consists of a wide range of hydrocarbons, which can be utilized as a synthetic jet fuel after cracking down heavy hydrocarbons into the desired kerosene fraction. By using air-captured CO₂ as feedstock, a closed carbon cycle can be achieved and *Kerogreen* e-fuels are considered to be carbon neutral. Furthermore, synthetically produced e-fuels offer the advantage of clean combustion without the generation of soot particles.

In this thesis, an innovative syngas production route from pure CO was developed. The potential influence of a CO₂ slip from this step on the subsequent FT crude cracking to kerosene was evaluated. Additionally, a technical solution was provided for conducting this process step in a single unit operation in a container-sized pilot plant.

The syngas production technology did not employ electrolysis. Instead, pure CO was converted to CO₂ and H₂ via the WGS reaction in a packed-bed SEWGS reactor. Here, the produced CO₂ was removed in-situ through selective adsorption on a solid sorbent to shift the thermodynamic equilibrium towards the product side. Thus, the desired syngas ratio (H₂:CO = 2) could be adjusted by using a CO bypass flow. The subsequent e-fuels synthesis was performed in a micro-structured FT reactor coupled with a HC reactor cascade.

The objective of this thesis was accomplished by investigating a variety of aspects, as outlined in Section 1.4. The main results and conclusions can be summarized as follows and are graphically presented in Figure 6.1:

- **SEWGS: Lab-Scale Experiments** (Section 4.1)

Characterization tests and CO₂ breakthrough experiments revealed suitable materials, namely an active WGS catalyst and a stable CO₂ sorbent, as well as relevant sorption parameters and a beneficial reactor configuration. The chosen Cu/ZnO-Al₂O₃ catalyst showed the best activity and stability among the three copper-based

commercial catalysts tested. The most promising sorbent was found to be a hydrotalcite-derived material that was obtained after impregnation of hydrotalcite with potassium and calcination at 400 °C. Lab-scale experiments revealed, that the sorption properties were significantly impacted by the water content during both the reactive adsorption and desorption phase. Also, the reactor filling with sorbent and catalyst particles was found to be crucial: the most effective reactor configuration was a two-zone filling with a quarter of the total sorbent mass homogeneously mixed with the total catalyst amount in the first zone and the remaining sorbent packed in the second zone. The experimental results demonstrated that choosing appropriate process conditions is highly important for efficient SEWGS operation, i.e. all influencing factors, such as water content, temperature, and pressure, must be considered carefully.

- **SEWGS: Modeling and Simulation** (Section 4.2 and Section 4.3)

Simulation-driven process design was applied to optimize the intended cyclic operation procedure of the SEWGS reactor. Therefore, a complex Matlab® Simulink model on system scale was developed and employed to quantify the influence of design configurations and key operating parameters. The dynamic Simulink simulations resulted in practical guidelines for the efficient operation of the SEWGS pilot plant reactor. A case study revealed that the interconnection of reaction chambers in the so-called serial configuration resulted in a 7% increase in sorbent loading compared to the simple single stage operation without interconnections.

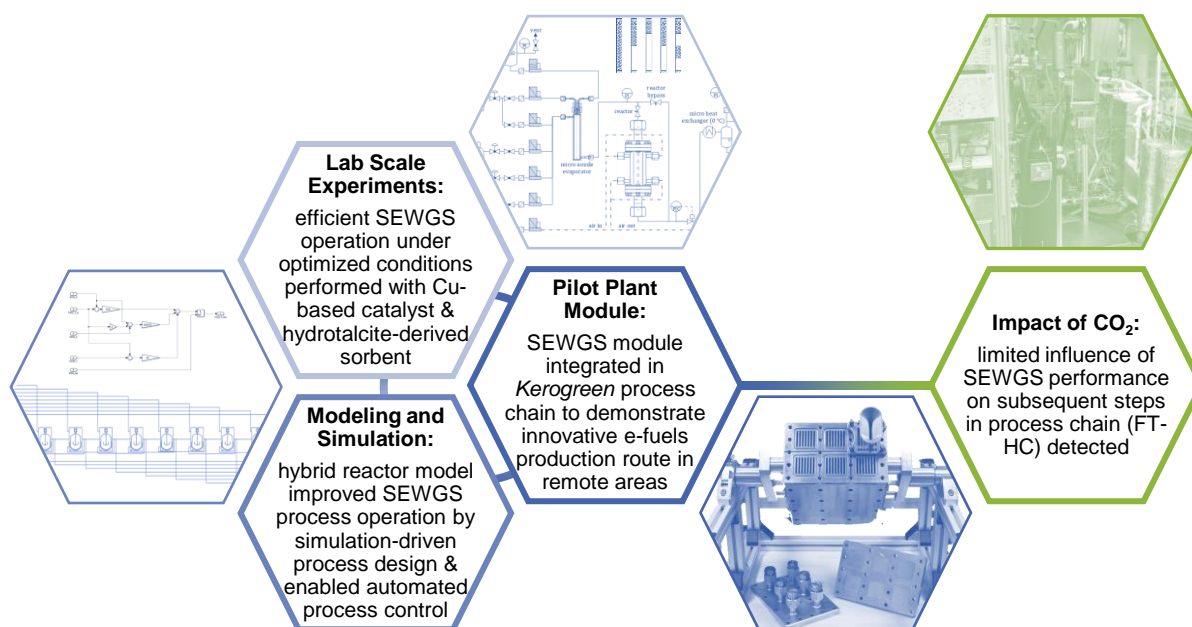


Fig. 6.1: Overview of the main investigation results of this thesis. Detailed information regarding *SEWGS: Lab-Scale Experiments* can be found in Section 4.1, *SEWGS: Modeling and Simulation* in Section 4.2 and Section 4.3, *SEWGS: Pilot Plant Module* in Section 4.3 and Chapter 5, and *FT-HC: Impact of CO₂* in Section 4.4.

The developed operation procedures could directly be implemented for automated plant control.

- **SEWGS: Pilot Plant Module** (Section 4.3 and Chapter 5)

An automatically controlled SEWGS module was designed and successfully implemented in a first-of-its-kind demonstration plant in a 30 ft container. This *Kerogreen* plant aims to produce 0.1 kg h^{-1} synthetic kerosene. Thanks to its modular, scalable, and compact design, the automated technology is well suited for decentralized operation. As such, it can be utilized in remote areas, including those near offshore wind turbine parks.

- **FT-HC: Impact of CO₂** (Section 4.4)

The impact of possible CO₂ slip from the SEWGS step on consecutive steps in the *Kerogreen* process chain was elucidated by means of an experimental study. FT syncrude upgrade through direct HC was proven to be a relatively robust process, which is not remarkably influenced by possible variations of the CO₂ content in the feed. Nevertheless, it was shown that direct coupling of FT with HC can reduce the loss of carbonaceous species to the water phase through conversion processes on the bifunctional HC catalyst. Provided that the diluting effect of CO₂ in case of a SEWGS stage malfunction is considered in the reactor design, the investigated syngas production route is ideally suited for producing synthetic kerosene in the given process framework.

After resuming the key findings of this work, several suggestions for future research emerge. One of the most pressing topics is the development of advanced CO₂ sorbent materials that can operate at high temperatures and pressures. The next step would be to optimize these materials for use in SEWGS systems to achieve an even higher CO₂ adsorption capacity than the materials that are presently available. Additionally, SEWGS process operation could be intensified through adapted simulation studies using the presented Simulink model. Expanding the experimental data set could facilitate the further development of the mathematical models and improve the precision of the kinetic coefficients. The novel graphical modeling approach could also be applied to other time- and space-dependent problems to enhance automated process control. Regarding the SEWGS module in the *Kerogreen* pilot plant, final test runs are to be performed. The results will provide important data regarding the long-term stability of the syngas production step and the overall proof-of-concept of the *Kerogreen* process chain. A comprehensive characterization of the hydrocarbon product produced in the pilot plant should be carried out to determine its suitability as a substitute for fossil kerosene, including its drop-in quality and aging properties. Moreover, a life cycle assessment and life cycle costing analysis of SAF produced via this novel route yields valuable information about the scalability of this technology in relation to world-scale requirements.

Apart from the life cycle assessment, which has been performed in the consortium of the project, the life cycle costing analysis of the *Kerogreen* process based on experimental pilot plant data is of utmost importance. Preliminary research has revealed that the major limitations of other PtL production technologies, some of which are nearly ready for market implementation, are their accessibility and expenses associated with renewable energy and CO₂ [148]. Consequently, e-fuels have a higher price point compared to conventional fossil fuels [15–18]. Based on a fundamental PtL cost model, the 2020 production cost of e-kerosene was estimated to be ten times higher than fossil kerosene in the EU. This price gap is expected to decrease significantly up to two and a half times by 2050 [148]. Strategic political decisions are required to enhance the visibility and importance of synthetic liquid fuels. Such measures may include financial incentives through high carbon prices, or obligations on fuel suppliers and aircraft operators for providing and using SAF-blended fuel [149]. As recently announced by the European Commission [150], an agreement was reached on the law regarding the mandate for blending SAF. According to a proposal of the ReFuelEU Aviation Initiative, jet fuel suppliers will be required to blend SAF with jet fuel loaded at airports within the EU in increasing amounts from 2025 [151]. Synthetic e-fuels produced from captured CO₂ are subject to a 0.7 % quota starting in 2030, increasing to 28 % in 2050. To conclude: it was shown that the production of synthetic kerosene via a technology totally different from established electrolysis-based routes is technically feasible. This technology could, if also competitive from an economic point of view, contribute a vital part towards sustainable aviation.

Symbols and Abbreviations

Latin Symbols

Symbol	Description	Unit
a	adsorption/ desorption rate	$\text{mol kg}^{-1} \text{s}^{-1}$
\bar{c}	particle void phase concentration	mol m^{-3}
c	bulk phase concentration	mol m^{-3}
D	dispersion coefficient	$\text{m}^2 \text{s}^{-1}$
d	diameter	m
e	power-law exponent	–
E_a	activation energy	J mol^{-1}
F	flow rate	mL min^{-1}
k	rate coefficient	s^{-1}
K_{eq}	WGS equilibrium constant	–
k_{∞}	frequency factor	$\text{mol bar}^{-2} \text{g}^{-1} \text{h}^{-1}$
m	Freundlich constant	$\text{mmol g}^{-1} \text{bar}^{-n_{\text{Fr}}}$
N	number of cells	–
n	Freundlich adsorption intensity	–
n_{C}	hydrocarbon chain length	–
p	(partial) pressure	bar
q	sorbent loading	mol kg^{-1}
R	gas constant	$\text{J mol}^{-1} \text{K}^{-1}$
r	reaction rate	$\text{mol g}^{-1} \text{h}^{-1}$
S	selectivity	–
T	temperature	K
t	time	s
u	gas velocity	m s^{-1}
w	weight fraction	–
X	conversion	–
y	volume fraction	–
z	axial coordinate	m

Greek Symbols

Symbol	Description	Unit
α	chain growth probability	–
β	activation energy change	J mol^{-1}
δ	power law equilibrium approach	–
ε	void fraction	–
ν	stoichiometric reaction coefficient	–
ρ	bulk density	kg m^{-3}

Indices

Index	Description
ads	adsorption
ax	axial
b	bed
cat	catalyst
des	desorption
eq	equilibrium
exp	experimental
Fr	Freundlich model
LDF	Linear Driving Force model
max	maximum
p	particle
sim	simulation
STP	Standard Temperature and Pressure
WGS	Water-Gas Shift reaction

Abbreviations

Abbreviation	Description
AEL	Alkaline Electrolyzer
ASF	Anderson-Schulz-Flory
ASTM	American Society for Testing and Materials
BET	Brunauer-Emmett-Teller
BJH	Barrett-Joyner-Halenda
CAD	Computer Aided Design
DAC	Direct Air Capture
DME	Dimethyl Ether
DTO	Dimethyl Ether-to-Olefins
EDX	Energy-Dispersive X-Ray Spectroscopy
EL	Electrolysis
EPMA	Electron Probe Micro Analysis
FEU	Forty Foot Equivalent Unit
FID	Flame Ionization Detector
FT	Fischer-Tropsch
GC	Gas Chromatograph
HC	Hydrocracking
HDMO	Hydrotalcite-Derived Mixed Oxide
HTC	Hydrotalcite
HT	High-Temperature
IMVT	Institute for Micro Process Engineering
K-HDMO	Potassium-impregnated Hydrotalcite-Derived Mixed Oxide
K-HTC	Potassium-impregnated Hydrotalcite
KIT	Karlsruhe Institute of Technology
LDH	Layered Double Hydroxide
LDO	Layered Double Oxide
LTFT	Low-Temperature Fischer-Tropsch
LT	Low-Temperature
MOF	Metal Organic Framework
MTO	Methanol-to-Olefins
Matlab [®]	Programming and numeric computing platform (The MathWorks Inc., USA)
MoL	Method-of-Lines
M	Mode
ODE	Ordinary Differential Equation
PBMR	Packed Bed Microchannel Reactor

Abbreviation	Description
PDE	Partial Differential Equation
PEM-EL	Polymer Electrolyte Membrane Electrolyzer
PGA	Process Gas Analyzer
PSA	Pressure Swing Adsorption
P&ID	Piping and Instrumentation Diagram
PtG	Power-to-Gas
PtL	Power-to-Liquid
P	Publication
SAF	Sustainable Aviation Fuel
SEM	Scanning Electron Microscopy
SEWGS	Sorption-Enhanced Water-Gas Shift
SIL	Safety Integrity Level
SOEC	Solid-Oxide Electrolysis Cell
Simulink	Matlab-based graphical programming environment for modeling, simulating, and analyzing dynamical systems
TCD	Thermal Conductivity Detector
TGA	Thermogravimetric Analysis
TOS	Time-On-Stream
TRL	Technology Readiness Level
WDX	Wavelength-Dispersive X-Ray Spectroscopy
WGS	Water-Gas Shift
WHSV	Weight Hourly Space Velocity
XRD	X-Ray Diffraction
ode15s	solver for stiff ODEs in Matlab
ode23t	solver for moderately stiff ODEs in Matlab
pdepe	solver for systems of parabolic and elliptic PDEs in Matlab
ox	oxidized site
rWGS	reverse Water-Gas Shift
red	reduced site
syncrude	synthetic crude
syngas	synthesis gas (CO + H ₂)

Bibliography

- [1] M. Crippa, D. Guizzardi, M. Muntean, E. Schaaf, F. Monforti-Ferrario, M. Banja, J. Olivier, E. Vignati, E. Solazzo, G. Grassi, and S. Rossi. „GHG emissions of all world: 2021 report“. Luxembourg: Publications Office of the European Union, 2021.
- [2] United Nations. „Paris Agreement“. 2015. URL: https://unfccc.int/sites/default/files/english_paris_agreement.pdf last visited: July 15, 2022.
- [3] Intergovernmental Panel on Climate Change. „Global Warming of 1.5°C. An IPCC Special Report on the impacts of global warming of 1.5°C above pre-industrial levels and related global greenhouse gas emission pathways, in the context of strengthening the global response to the threat of climate change, sustainable development, and efforts to eradicate poverty“. Cambridge University Press, Cambridge, UK and New York, NY, USA, 2018. DOI: 10.1017/9781009157940.
- [4] D. S. Lee, D. W. Fahey, A. Skowron, M. R. Allen, U. Burkhardt, Q. Chen, S. J. Doherty, S. Freeman, P. M. Forster, J. Fuglestvedt, A. Gettelman, R. R. de León, L. L. Lim, M. T. Lund, R. J. Millar, B. Owen, J. E. Penner, G. Pitari, M. J. Prather, R. Sausen, and L. J. Wilcox. “The contribution of global aviation to anthropogenic climate forcing for 2000 to 2018”. *Atmospheric environment* 244 (2021), p. 117834. DOI: 10.1016/j.atmosenv.2020.117834.
- [5] G. Fleming and I. de Lépinay. „Environmental trends in aviation to 2050“. 2019. URL: https://icao.int/environmental-protection/Documents/EnvironmentalReports/2019/ENVReport2019_pg17-23.pdf last visited: July 15, 2022.
- [6] United Nations Environment Programme. „Emissions Gap Report 2021: The Heat Is On – A world of climate promises not yet delivered“. Nairobi, 2021. URL: <https://www.unep.org/emissions-gap-report-2021> last visited: July 15, 2022.
- [7] International Air Transport Association. „Recovery delayed as international travel remains locked down“. 28.07.2020. URL: <https://www.iata.org/en/pressroom/pr/2020-07-28-02/> last visited: July 15, 2022.
- [8] United Nations Environment Programme. „Emissions Gap Report 2020“. Nairobi, 2020. URL: <https://www.unep.org/emissions-gap-report-2020> last visited: July 15, 2022.
- [9] J. S. Langford and D. K. Hall. “Electrified Aircraft Propulsion”. *The Bridge* 50.20 (2020).
- [10] S. Jürgens, P. Oßwald, M. Selinsek, P. Piermartini, J. Schwab, P. Pfeifer, U. Bauder, S. Ruoff, B. Rauch, and M. Köhler. “Assessment of combustion properties of non-hydroprocessed Fischer–Tropsch fuels for aviation”. *Fuel Processing Technology* 193 (2019), pp. 232–243. DOI: 10.1016/j.fuproc.2019.05.015.
- [11] International Energy Agency. „Renewables 2019. Analysis and Forecasts to 2024.“ Paris, 2019. URL: <https://www.iea.org/reports/renewables-2019> last visited: July 15, 2022.

- [12] International Energy Agency. „Renewables 2018. Analysis and Forecasts to 2023.“ Paris, 2018. URL: <https://www.iea.org/reports/renewables-2018> last visited: July 15, 2022.
- [13] Atmosfair. „Eröffnung E-Kerosin Anlage“. 3.10.2021. URL: <https://www.atmosfair.de/de/ab-10-45-uhr-livestream-eroeffnung-e-kerosin-anlage/> last visited: Apr. 23, 2023.
- [14] J. Fuhrman, H. McJeon, P. Patel, S. C. Doney, W. M. Shobe, and A. F. Clarens. “Food–energy–water implications of negative emissions technologies in a +1.5 °C future”. *Nature Climate Change* 10.10 (2020), pp. 920–927. DOI: 10.1038/s41558-020-0876-z.
- [15] Agora Verkehrswende, Agora Energiewende and Frontier Economics. „The Future Cost of Electricity-Based Synthetic Fuels“. 2018.
- [16] P. Schmidt, V. Batteiger, A. Roth, W. Weindorf, and T. Raksha. “Power-to-Liquids as Renewable Fuel Option for Aviation: A Review”. *Chemie Ingenieur Technik* 90.1-2 (2018), pp. 127–140. DOI: 10.1002/cite.201700129.
- [17] S. A. Isaacs, M. D. Staples, F. Allroggen, D. S. Mallapragada, C. P. Falter, and S. R. H. Barrett. “Environmental and Economic Performance of Hybrid Power-to-Liquid and Biomass-to-Liquid Fuel Production in the United States”. *Environmental science & technology* 55.12 (2021), pp. 8247–8257. DOI: 10.1021/acs.est.0c07674.
- [18] V. Becattini, P. Gabrielli, and M. Mazzotti. “Role of Carbon Capture, Storage, and Utilization to Enable a Net-Zero-CO₂-Emissions Aviation Sector”. *Industrial & Engineering Chemistry Research* 60.18 (2021), pp. 6848–6862. DOI: 10.1021/acs.iecr.0c05392.
- [19] European Commission. „A European Strategy for Low-Emission Mobility“. Brussels, 28.07.2016. URL: [https://ec.europa.eu/transparency/documents-register/detail?ref=COM\(2016\)501&lang=en](https://ec.europa.eu/transparency/documents-register/detail?ref=COM(2016)501&lang=en) last visited: July 15, 2022.
- [20] H. Kirsch, L. Brübach, M. Loewert, M. Riedinger, A. Gräfenhahn, T. Böltken, M. Klumpp, P. Pfeifer, and R. Dittmeyer. “CO₂-neutrale Fischer-Tropsch-Kraftstoffe aus dezentralen modularen Anlagen: Status und Perspektiven”. *Chemie Ingenieur Technik* 92.1-2 (2020), pp. 91–99. DOI: 10.1002/cite.201900120.
- [21] W. L. Becker, R. J. Braun, M. Penev, and M. Melaina. “Production of Fischer-Tropsch liquid fuels from high temperature solid oxide co-electrolysis units”. *Energy* 47.1 (2012), pp. 99–115. DOI: 10.1016/j.energy.2012.08.047.
- [22] Kerogreen. „Kerogreen – towards sustainable and green aviation fuel production“. 2022. URL: <https://www.kerogreen.eu/> last visited: July 15, 2022.
- [23] A. Tremel. „Electricity-based fuels“. SpringerBriefs in applied sciences and technology. Cham, Switzerland: Springer, 2018.
- [24] T. Fröhlich, S. Blömer, D. Münter, and L.-A. Brischke. „CO₂-Quellen für die PtX-Herstellung in Deutschland – Technologien, Umweltwirkung, Verfügbarkeit“. Heidelberg, 2019.
- [25] Climeworks. „Orca: the first large-scale plant“. 2021. URL: <https://climeworks.com/roadmap/orca> last visited: May 12, 2023.

- [26] Climeworks. „Mammoth: our newest facility“. 2022. URL: <https://climeworks.com/roadmap/mammoth> last visited: May 12, 2023.
- [27] C. Panzone, R. Philippe, A. Chappaz, P. Fongarland, and A. Bengaouer. “Power-to-Liquid catalytic CO₂ valorization into fuels and chemicals: focus on the Fischer-Tropsch route”. *Journal of CO₂ Utilization* 38 (2020), pp. 314–347. DOI: 10.1016/j.jcou.2020.02.009.
- [28] Forschungsstelle für Energiewirtschaft e.V. „Elektrolyse – die Schlüsseltechnologie für PtX“. 23.04.2019. URL: <https://www.ffe.de/veroeffentlichungen/elektrolyse-die-schlueseltechnologie-fuer-power-to-x/> last visited: May 12, 2023.
- [29] D. M. A. Dueñas, M. Riedel, M. Riegraf, R. Costa, and K. A. Friedrich. “High Temperature Co-electrolysis for Power-to-X”. *Chemie Ingenieur Technik* 92.1-2 (2020), pp. 45–52. DOI: 10.1002/cite.201900119.
- [30] Sunfire. „Sunfire SYNLINK SOEC“. URL: <https://www.sunfire.de/en/syngas> last visited: Mar. 12, 2023.
- [31] „Progress within Kopernikus P2X research project: High-temperature electrolyzer successfully commissioned“. Dresden, 7.02.2023. URL: <https://www.sunfire.de/en/news/detail/progress-within-kopernikus-p2x-research-project-high-temperature-electrolyzer-successfully-commissioned> last visited: Mar. 12, 2023.
- [32] V. Dieterich, A. Buttler, A. Hanel, H. Spliethoff, and S. Fendt. “Power-to-liquid via synthesis of methanol, DME or Fischer-Tropsch-fuels: a review”. *Energy & Environmental Science* 13.10 (2020), pp. 3207–3252. DOI: 10.1039/d0ee01187h.
- [33] C. Fuchs, U. Arnold, and J. Sauer. “(Co-)Oligomerization of Olefins to Hydrocarbon Fuels: Influence of Feed Composition and Pressure”. *Chemie Ingenieur Technik* 95.5 (2023), pp. 651–657. DOI: 10.1002/cite.202200209.
- [34] BMU, BMVI, BMWi, BMZ, and BDL. „PtL-Roadmap. Nachhaltige strombasierte Kraftstoffe für den Luftverkehr in Deutschland“. Berlin, 2021.
- [35] D. T. Burns, G. Piccardi, and L. Sabbatini. “Some people and places important in the history of analytical chemistry in Italy”. *Microchimica Acta* 160.1-2 (2008), pp. 57–87. DOI: 10.1007/s00604-007-0769-0.
- [36] L. Mond and C. Langer. “Process of obtaining hydrogen gas: US Patent”. Pat. 417068. 10.12.1889.
- [37] S. A. Topham. “The History of the Catalytic Synthesis of Ammonia”. In: *Catalysis*. Ed. by J. R. Anderson and M. Boudart. Berlin, Heidelberg: Springer Berlin Heidelberg, 1985, pp. 1–50. DOI: 10.1007/978-3-642-93281-6_1.
- [38] P. Smirniotis. „Water Gas Shift Reaction: Research Developments and Applications“. Burlington: Elsevier Science, 2015.
- [39] Atmosfair. „atmosfair FairFuel“. 2021. URL: https://fairfuel.atmosfair.de/wp-content/uploads/2021/10/Kurzbeschreibung_atmosfair_PtL-Kerosin_092021.pdf last visited: May 12, 2023.

- [40] DLR. „Technologie-Plattform für Power-to-Liquid Kraftstoffe“. 14.03.2023. URL: www.now-gmbh.de/wp-content/uploads/2023/03/FKEK23_Technologie-Plattform-fuer-Power-to-Liquid-Kraftstoffe_Aigner.pdf last visited: May 12, 2023.
- [41] „Technologie-Plattform PtL: DLR forscht für industrielle Produktion strombasierter Kraftstoffe“. 15.03.2023. URL: <https://www.dlr.de/de/aktuelles/nachrichten/2023/01/technologie-plattform-ptl-dlr-forscht-fuer-industrielle-produktion> last visited: May 12, 2023.
- [42] KIT. „Anlage zur Synthese von E-Fuel (Power-to-Liquid)“. URL: https://www.elab2.kit.edu/img/Fact%20Sheets/Fact-Sheet-P2L_DE.pdf last visited: May 12, 2023.
- [43] KIT. „Die Labore und Anlagen des EnergyLab2.0“. URL: <https://www.elab2.kit.edu/ueberblick.php> last visited: May 12, 2023.
- [44] „PtL-Anlage am KIT produziert Kraftstoffe aus Luft und Strom“. 29.07.2021. URL: <https://www.springerprofessional.de/betriebsstoffe/erneuerbare-energien/ptl-anlage-am-kit-produziert-kraftstoffe-aus-luft-und-strom/17081894> last visited: May 12, 2023.
- [45] infraserv höchst. „Bau der weltweit größten Power-to-Liquid-Pionieranlage im Industriepark Höchst“. 2023. URL: <https://www.infraserv.com/de/unternehmen/nachhaltigkeit/power-to-liquid-pionieranlage/> last visited: May 12, 2023.
- [46] „Spatenstich für e-fuel Produktionsanlage in Frankfurt“. 19.04.2023. URL: <https://www.ineratec.de/de/news/spatenstich-fuer-e-fuel-produktionsanlage-frankfurt> last visited: May 12, 2023.
- [47] INERATEC. „Inbetriebnahmestart in Hamburg“. 2.03.2022. URL: <https://www.ineratec.de/de/inbetriebnahmestart-in-hamburg> last visited: Aug. 22, 2023.
- [48] J. M. Moe. “Design of water-gas shift reactors”. *Chem.Eng.Prog.* 58.3 (1962).
- [49] D. S. Newsome. “The Water-Gas Shift Reaction”. *Catalysis Reviews* 21.2 (1980), pp. 275–318. DOI: 10.1080/03602458008067535.
- [50] D. Mendes, A. Mendes, L. M. Madeira, A. Iulianelli, J. M. Sousa, and A. Basile. “The water-gas shift reaction: from conventional catalytic systems to Pd-based membrane reactors – a review”. *Asia-Pacific Journal of Chemical Engineering* 5.1 (2010), pp. 111–137. DOI: 10.1002/apj.364.
- [51] B. Smith R J, M. Loganathan, and M. S. Shantha. “A Review of the Water Gas Shift Reaction Kinetics”. *International Journal of Chemical Reactor Engineering* 8.1 (2010). DOI: 10.2202/1542-6580.2238.
- [52] A. A. Gokhale, J. A. Dumesic, and M. Mavrikakis. “On the mechanism of low-temperature water gas shift reaction on copper”. *Journal of the American Chemical Society* 130.4 (2008), pp. 1402–1414. DOI: 10.1021/ja0768237.
- [53] C.-H. Lin, C.-L. Chen, and J.-H. Wang. “Mechanistic Studies of Water-Gas-Shift Reaction on Transition Metals”. *The Journal of Physical Chemistry C* 115.38 (2011), pp. 18582–18588. DOI: 10.1021/jp2034467.

- [54] C. Ratnasamy and J. P. Wagner. "Water Gas Shift Catalysis". *Catalysis Reviews* 51.3 (2009), pp. 325–440. DOI: 10.1080/01614940903048661.
- [55] T. Vanherwijnen. "Kinetics and mechanism of the CO shift on Cu/ZnO". *Journal of Catalysis* 63.1 (1980), pp. 83–93. DOI: 10.1016/0021-9517(80)90061-5.
- [56] Y. Choi and H. G. Stenger. "Water gas shift reaction kinetics and reactor modeling for fuel cell grade hydrogen". *Journal of Power Sources* 124.2 (2003), pp. 432–439. DOI: 10.1016/S0378-7753(03)00614-1.
- [57] R. L. Keiski, O. Desponds, Y.-F. Chang, and G. A. Somorjai. "Kinetics of the water–gas shift reaction over several alkane activation and water–gas shift catalysts". *Applied Catalysis A: General* 101.2 (1993), pp. 317–338. DOI: 10.1016/0926-860X(93)80277-W.
- [58] N. Koryabkina. "Determination of kinetic parameters for the water–gas shift reaction on copper catalysts under realistic conditions for fuel cell applications". *Journal of Catalysis* (2003). DOI: 10.1016/S0021-9517(03)00050-2.
- [59] C. V. Ovesen, B. S. Clausen, B. S. Hammershøi, G. Steffensen, T. Askgaard, I. Chorkendorff, J. K. Nørskov, P. B. Rasmussen, P. Stoltze, and P. Taylor. "A Microkinetic Analysis of the Water–Gas Shift Reaction under Industrial Conditions". *Journal of Catalysis* 158.1 (1996), pp. 170–180. DOI: 10.1006/jcat.1996.0016.
- [60] T. Salmi and R. Hakkarainen. "Kinetic Study of the Low–Temperature Water–Gas Shift Reaction over a Cu–ZnO Catalyst". *Applied Catalysis* 49.2 (1989), pp. 285–306. DOI: 10.1016/S0166-9834(00)83024-9.
- [61] H. Kušar, S. Hočevár, and J. Levec. "Kinetics of the water–gas shift reaction over nanostructured copper–ceria catalysts". *Applied Catalysis B: Environmental* 63.3-4 (2006), pp. 194–200. DOI: 10.1016/j.apcatb.2005.09.019.
- [62] D. Iruretagoyena Ferrer. „Supported Layered Double Hydroxides as CO₂ Adsorbents for Sorption–enhanced H₂ Production“. Cham: Springer International Publishing, 2016. DOI: 10.1007/978-3-319-41276-4.
- [63] Z. Yong, Mata, and A. E. Rodrigues. "Adsorption of Carbon Dioxide onto Hydrotalcite-like Compounds (HTlcs) at High Temperatures". *Industrial & Engineering Chemistry Research* 40.1 (2001), pp. 204–209. DOI: 10.1021/ie000238w.
- [64] B. Dou, C. Wang, Y. Song, H. Chen, B. Jiang, M. Yang, and Y. Xu. "Solid sorbents for in–situ CO₂ removal during sorption-enhanced steam reforming process: A review". *Renewable and Sustainable Energy Reviews* 53 (2016), pp. 536–546. DOI: 10.1016/j.rser.2015.08.068.
- [65] X. Zhu, S. Li, Y. Shi, and N. Cai. "Recent advances in elevated–temperature pressure swing adsorption for carbon capture and hydrogen production". *Progress in Energy and Combustion Science* 75 (2019), p. 100784. DOI: 10.1016/j.pecs.2019.100784.
- [66] L. M. Mulloth and J. E. Finn. „Carbon Dioxide Adsorption on a 5A Zeolite Designed for CO₂ Removal in Spacecraft Cabins“. Moffett Field, California, 1998.

- [67] R. V. Siriwardane, M.-S. Shen, E. P. Fisher, and J. A. Poston. “Adsorption of CO₂ on Molecular Sieves and Activated Carbon”. *Energy & Fuels* 15.2 (2001), pp. 279–284. DOI: 10.1021/ef000241s.
- [68] C. Chen, D.-W. Park, and W.-S. Ahn. “CO₂ capture using zeolite 13X prepared from bentonite”. *Applied Surface Science* 292 (2014), pp. 63–67. DOI: 10.1016/j.apsusc.2013.11.064.
- [69] G. Yin, Z. Liu, Q. Liu, and W. Wu. “The role of different properties of activated carbon in CO₂ adsorption”. *Chemical Engineering Journal* 230 (2013), pp. 133–140. DOI: 10.1016/j.cej.2013.06.085.
- [70] B. Guo, L. Chang, and K. Xie. “Adsorption of Carbon Dioxide on Activated Carbon”. *Journal of Natural Gas Chemistry* 15.3 (2006), pp. 223–229. DOI: 10.1016/S1003-9953(06)60030-3.
- [71] C. Chen and W.-S. Ahn. “CO₂ capture using mesoporous alumina prepared by a sol–gel process”. *Chemical Engineering Journal* 166.2 (2011), pp. 646–651. DOI: 10.1016/j.cej.2010.11.038.
- [72] A. R. Millward and O. M. Yaghi. “Metal–organic frameworks with exceptionally high capacity for storage of carbon dioxide at room temperature”. *Journal of the American Chemical Society* 127.51 (2005), pp. 17998–17999. DOI: 10.1021/ja0570032.
- [73] S. Ye, X. Jiang, L.-W. Ruan, B. Liu, Y.-M. Wang, J.-F. Zhu, and L.-G. Qiu. “Post–combustion CO₂ capture with the HKUST-1 and MIL-101(Cr) metal–organic frameworks: Adsorption, separation and regeneration investigations”. *Microporous and Mesoporous Materials* 179 (2013), pp. 191–197. DOI: 10.1016/j.micromeso.2013.06.007.
- [74] M. Ding, R. W. Flaig, H.-L. Jiang, and O. M. Yaghi. “Carbon capture and conversion using metal–organic frameworks and MOF–based materials”. *Chemical Society reviews* 48.10 (2019), pp. 2783–2828. DOI: 10.1039/c8cs00829a.
- [75] C. A. Trickett, A. Helal, B. A. Al-Maythaly, Z. H. Yamani, K. E. Cordova, and O. M. Yaghi. “The chemistry of metal–organic frameworks for CO₂ capture, regeneration and conversion”. *Nature Reviews Materials* 2.8 (2017). DOI: 10.1038/natrevmats.2017.45.
- [76] M. Bhagiyalakshmi, J. Y. Lee, and H. T. Jang. “Synthesis of mesoporous magnesium oxide: Its application to CO₂ chemisorption”. *International Journal of Greenhouse Gas Control* 4.1 (2010), pp. 51–56. DOI: 10.1016/j.ijggc.2009.08.001.
- [77] T. Harada and T. A. Hatton. “Colloidal Nanoclusters of MgO Coated with Alkali Metal Nitrates/Nitrites for Rapid, High Capacity CO₂ Capture at Moderate Temperature”. *Chemistry of Materials* 27.23 (2015), pp. 8153–8161. DOI: 10.1021/acs.chemmater.5b03904.
- [78] N. D. Hutson and B. C. Attwood. “High temperature adsorption of CO₂ on various hydrotalcite–like compounds”. *Adsorption* 14.6 (2008), pp. 781–789. DOI: 10.1007/s10450-007-9085-6.

- [79] K. B. Lee, A. Verdooren, H. S. Caram, and S. Sircar. “Chemisorption of carbon dioxide on potassium–carbonate–promoted hydrotalcite”. *Journal of colloid and interface science* 308.1 (2007), pp. 30–39. DOI: 10.1016/j.jcis.2006.11.011.
- [80] Z. Yong and A. E. Rodrigues. “Hydrotalcite–like compounds as adsorbents for carbon dioxide”. *Energy Conversion and Management* 43.14 (2002), pp. 1865–1876. DOI: 10.1016/S0196-8904(01)00125-X.
- [81] V. Rives. “Characterisation of layered double hydroxides and their decomposition products”. *Materials Chemistry and Physics* 75.1-3 (2002), pp. 19–25. DOI: 10.1016/S0254-0584(02)00024-X.
- [82] E. Ochoa-Fernández, M. Rønning, X. Yu, T. Grande, and Chen. “Compositional Effects of Nanocrystalline Lithium Zirconate on Its CO₂ Capture Properties”. *Industrial & Engineering Chemistry Research* 47.2 (2008), pp. 434–442. DOI: 10.1021/ie0705150.
- [83] A. Iwan, H. Stephenson, W. C. Ketchie, and A. A. Lapkin. “High temperature sequestration of CO₂ using lithium zirconates”. *Chemical Engineering Journal* 146.2 (2009), pp. 249–258. DOI: 10.1016/j.cej.2008.06.006.
- [84] A. Solieman, J. W. Dijkstra, W. G. Haije, P. D. Cobden, and R. W. van den Brink. “Calcium oxide for CO₂ capture: Operational window and efficiency penalty in sorption–enhanced steam methane reforming”. *International Journal of Greenhouse Gas Control* 3.4 (2009), pp. 393–400. DOI: 10.1016/j.ijggc.2009.02.002.
- [85] C. C. Dean, J. Blamey, N. H. Florin, M. J. Al-Jeboori, and P. S. Fennell. “The calcium looping cycle for CO₂ capture from power generation, cement manufacture and hydrogen production”. *Chemical Engineering Research and Design* 89.6 (2011), pp. 836–855. DOI: 10.1016/j.cherd.2010.10.013.
- [86] R. Filitz, A. M. Kierzkowska, M. Broda, and C. R. Müller. “Highly efficient CO₂ sorbents: development of synthetic, calcium–rich dolomites”. *Environmental science & technology* 46.1 (2012), pp. 559–565. DOI: 10.1021/es2034697.
- [87] S. Wang, H. Shen, S. Fan, Y. Zhao, X. Ma, and J. Gong. “Enhanced CO₂ adsorption capacity and stability using CaO-based adsorbents treated by hydration”. *AIChE Journal* 59.10 (2013), pp. 3586–3593. DOI: 10.1002/aic.14126.
- [88] R. V. Siriwardane, C. Robinson, M. Shen, and T. Simonyi. “Novel Regenerable Sodium–Based Sorbents for CO₂ Capture at Warm Gas Temperatures”. *Energy & Fuels* 21.4 (2007), pp. 2088–2097. DOI: 10.1021/ef070008v.
- [89] M. A. Soria, S. Tosti, A. Mendes, and L. M. Madeira. “Enhancing the low temperature water–gas shift reaction through a hybrid sorption–enhanced membrane reactor for high–purity hydrogen production”. *Fuel* 159 (2015), pp. 854–863. DOI: 10.1016/j.fuel.2015.07.035.
- [90] J. Wang, Y. Zhang, N. Altaf, D. O’Hare, and Q. Wang. “Layered Double Hydroxides–derived Intermediate–temperature CO₂ Adsorbents”. In: *Pre-combustion Carbon Dioxide Capture Materials*. Ed. by Q. Wang. The Royal Society of Chemistry, 2018, pp. 1–60. DOI: 10.1039/9781788013390-00001.

- [91] F. Cavani, F. Trifirò, and A. Vaccari. “Hydrotalcite–type anionic clays: Preparation, properties and applications”. *Catalysis Today* 11.2 (1991), pp. 173–301. DOI: 10.1016/0920-5861(91)80068-K.
- [92] M. Bublinski. „CO₂–Abtrennung aus Synthesegasen mit Hydrotalciten unter Hochtemperatur–Hochdruckbedingungen“. 2017. DOI: 10.18419/opus-9209.
- [93] M. León, E. Díaz, S. Bennici, A. Vega, S. Ordóñez, and A. Auroux. “Adsorption of CO₂ on Hydrotalcite-Derived Mixed Oxides: Sorption Mechanisms and Consequences for Adsorption Irreversibility”. *Industrial & Engineering Chemistry Research* 49.8 (2010), pp. 3663–3671. DOI: 10.1021/ie902072a.
- [94] E. R. van Selow, P. D. Cobden, A. D. Wright, R. W. van den Brink, and D. Jansen. “Improved sorbent for the sorption–enhanced water–gas shift process”. *Energy Procedia* 4 (2011), pp. 1090–1095. DOI: 10.1016/j.egypro.2011.01.159.
- [95] T. Yamamoto, T. Kodama, N. Hasegawa, M. Tsuji, and Y. Tamaura. “Synthesis of hydrotalcite with high layer charge for CO₂ adsorbent”. *Energy Conversion and Management* 36.6-9 (1995), pp. 637–640. DOI: 10.1016/0196-8904(95)00086-S.
- [96] S. Walspurger, L. Boels, P. D. Cobden, G. D. Elzinga, W. G. Haije, and R. W. van den Brink. “The crucial role of the K⁺–aluminium oxide interaction in K⁺–promoted alumina– and hydrotalcite–based materials for CO₂ sorption at high temperatures”. *ChemSusChem* 1.7 (2008), pp. 643–650. DOI: 10.1002/cssc.200800085.
- [97] M. Salomé Macedo, M. A. Soria, and L. M. Madeira. “High temperature CO₂ sorption using mixed oxides with different Mg/Al molar ratios and synthesis pH”. *Chemical Engineering Journal* 420 (2021), p. 129731. DOI: 10.1016/j.cej.2021.129731.
- [98] H. Du, C. T. Williams, A. D. Ebner, and J. A. Ritter. “In Situ FTIR Spectroscopic Analysis of Carbonate Transformations during Adsorption and Desorption of CO₂ in K-Promoted HTlc”. *Chemistry of Materials* 22.11 (2010), pp. 3519–3526. DOI: 10.1021/cm100703e.
- [99] J. M. Lee, Y. J. Min, K. B. Lee, S. G. Jeon, J. G. Na, and H. J. Ryu. “Enhancement of CO₂ sorption uptake on hydrotalcite by impregnation with K₂CO₃”. *Langmuir : the ACS journal of surfaces and colloids* 26.24 (2010), pp. 18788–18797. DOI: 10.1021/1a102974s.
- [100] E. L. Oliveira, C. A. Grande, and A. E. Rodrigues. “CO₂ sorption on hydrotalcite and alkali–modified (K and Cs) hydrotalcites at high temperatures”. *Separation and Purification Technology* 62.1 (2008), pp. 137–147. DOI: 10.1016/j.seppur.2008.01.011.
- [101] M. H. Halabi, M. de Croon, J. van der Schaaf, P. D. Cobden, and J. C. Schouten. “High capacity potassium-promoted hydrotalcite for CO₂ capture in H₂ production”. *International Journal of Hydrogen Energy* 37.5 (2012), pp. 4516–4525. DOI: 10.1016/j.ijhydene.2011.12.003.
- [102] X. Zhu, Y. Shi, and N. Cai. “High–pressure carbon dioxide adsorption kinetics of potassium–modified hydrotalcite at elevated temperature”. *Fuel* 207 (2017), pp. 579–590. DOI: 10.1016/j.fuel.2017.06.137.

- [103] A. C. Faria, R. Trujillano, V. Rives, C. V. Miguel, A. E. Rodrigues, and L. M. Madeira. “Alkali metal (Na, Cs and K) promoted hydrotalcites for high temperature CO₂ capture from flue gas in cyclic adsorption processes”. *Chemical Engineering Journal* 427 (2022), p. 131502. DOI: 10.1016/j.cej.2021.131502.
- [104] N. N. A. H. Meis, J. H. Bitter, and K. P. de Jong. “On the Influence and Role of Alkali Metals on Supported and Unsupported Activated Hydrotalcites for CO₂ Sorption”. *Industrial & Engineering Chemistry Research* 49.17 (2010), pp. 8086–8093. DOI: 10.1021/ie902016f.
- [105] D. P. Debecker, E. M. Gaigneaux, and G. Busca. “Exploring, tuning, and exploiting the basicity of hydrotalcites for applications in heterogeneous catalysis”. *Chemistry (Weinheim an der Bergstrasse, Germany)* 15.16 (2009), pp. 3920–3935. DOI: 10.1002/chem.200900060.
- [106] Y. Ding and E. Alpay. “Equilibria and kinetics of CO₂ adsorption on hydrotalcite adsorbent”. *Chemical Engineering Science* 55.17 (2000), pp. 3461–3474. DOI: 10.1016/S0009-2509(99)00596-5.
- [107] H. T. J. Reijers, S. E. A. Valster-Schiermeier, P. D. Cobden, and R. W. van den Brink. “Hydrotalcite as CO₂ Sorbent for Sorption-Enhanced Steam Reforming of Methane”. *Industrial & Engineering Chemistry Research* 45.8 (2006), pp. 2522–2530. DOI: 10.1021/ie050563p.
- [108] Y.-J. Wu, P. Li, J.-G. Yu, A. F. Cunha, and A. E. Rodrigues. “K-Promoted Hydrotalcites for CO₂ Capture in Sorption Enhanced Reactions”. *Chemical Engineering & Technology* 36.4 (2013), pp. 567–574. DOI: 10.1002/ceat.201200694.
- [109] M. Ram Reddy, Z. Xu, G. Lu, and J. Diniz -Da Costa. “Influence of Water on High-Temperature CO₂ Capture Using Layered Double Hydroxide Derivatives”. *Industrial & Engineering Chemistry Research* 47.8 (2008), pp. 2630–2635. DOI: 10.1021/ie0716060.
- [110] W. Gluud, K. Keller, R. Schönfelder, and W. Klemm. “Production of Hydrogen”. *US Patent US1816523* (1931).
- [111] D. P. Harrison. “Sorption-Enhanced Hydrogen Production: A Review”. *Industrial & Engineering Chemistry Research* 47.17 (2008), pp. 6486–6501. DOI: 10.1021/ie800298z.
- [112] G. Manzolini, A. Giuffrida, P. D. Cobden, H. van Dijk, F. Ruggeri, and F. Consonni. “Techno-economic assessment of SEWGS technology when applied to integrated steel-plant for CO₂ emission mitigation”. *International Journal of Greenhouse Gas Control* 94 (2020), p. 102935. DOI: 10.1016/j.ijggc.2019.102935.
- [113] A. E. Rodrigues, L. M. Madeira, Y.-J. Wu, and R. Faria. „Sorption enhanced reaction processes“. Vol. volume 1. Sustainable chemistry series. New Jersey: World Scientific, 2018.
- [114] M. Gazzani, E. Macchi, and G. Manzolini. “CO₂ capture in integrated gasification combined cycle with SEWGS – Part A: Thermodynamic performances”. *Fuel* 105 (2013), pp. 206–219. DOI: 10.1016/j.fuel.2012.07.048.

- [115] H. M. Jang, K. B. Lee, H. S. Caram, and S. Sircar. “High-purity hydrogen production through sorption enhanced water gas shift reaction using K_2CO_3 -promoted hydrotalcite”. *Chemical Engineering Science* 73 (2012), pp. 431–438. DOI: 10.1016/j.ces.2012.02.015.
- [116] E. R. van Selow, P. D. Cobden, P. A. Verbraeken, J. R. Hufton, and R. W. van den Brink. “Carbon Capture by Sorption-Enhanced Water-Gas Shift Reaction Process using Hydrotalcite-Based Material”. *Industrial & Engineering Chemistry Research* 48.9 (2009), pp. 4184–4193. DOI: 10.1021/ie801713a.
- [117] C. H. Lee and K. B. Lee. “Application of one-body hybrid solid pellets to sorption-enhanced water gas shift reaction for high-purity hydrogen production”. *International Journal of Hydrogen Energy* 39.31 (2014), pp. 18128–18134. DOI: 10.1016/j.ijhydene.2014.04.160.
- [118] M. A. Soria, C. Rocha, S. Tosti, A. Mendes, and L. M. Madeira. “ CO_x free hydrogen production through water-gas shift reaction in different hybrid multifunctional reactors”. *Chemical Engineering Journal* 356 (2019), pp. 727–736. DOI: 10.1016/j.cej.2018.09.044.
- [119] Y. Ding and E. Alpay. “Adsorption-enhanced steam-methane reforming”. *Chemical Engineering Science* 55.18 (2000), pp. 3929–3940. DOI: 10.1016/S0009-2509(99)00597-7.
- [120] H. T. J. Reijers, J. Boon, G. D. Elzinga, P. D. Cobden, W. G. Haije, and R. W. den van Brink. “Modeling Study of the Sorption-Enhanced Reaction Process for CO_2 Capture. II. Application to Steam-Methane Reforming”. *Industrial & Engineering Chemistry Research* 48.15 (2009), pp. 6975–6982. DOI: 10.1021/ie8013204.
- [121] I. Aloisi, A. Di Giuliano, A. Di Carlo, P. U. Foscolo, C. Courson, and K. Gallucci. “Sorption enhanced catalytic Steam Methane Reforming: Experimental data and simulations describing the behaviour of bi-functional particles”. *Chemical Engineering Journal* 314 (2017), pp. 570–582. DOI: 10.1016/j.cej.2016.12.014.
- [122] A. Di Giuliano, K. Gallucci, F. Giancaterino, C. Courson, and P. U. Foscolo. “Multicycle sorption enhanced steam methane reforming with different sorbent regeneration conditions: Experimental and modelling study”. *Chemical Engineering Journal* 377 (2019), p. 119874. DOI: 10.1016/j.cej.2018.09.035.
- [123] N. H. Florin and A. T. Harris. “Enhanced hydrogen production from biomass with in situ carbon dioxide capture using calcium oxide sorbents”. *Chemical Engineering Science* 63.2 (2008), pp. 287–316. DOI: 10.1016/j.ces.2007.09.011.
- [124] B. Dou, G. L. Rickett, V. Dupont, P. T. Williams, H. Chen, Y. Ding, and M. Ghadiri. “Steam reforming of crude glycerol with in situ CO_2 sorption”. *Bioresource technology* 101.7 (2010), pp. 2436–2442. DOI: 10.1016/j.biortech.2009.10.092.
- [125] L. He, H. Berntsen, and Chen. “Approaching sustainable H_2 production: sorption enhanced steam reforming of ethanol”. *The journal of physical chemistry. A* 114.11 (2010), pp. 3834–3844. DOI: 10.1021/jp906146y.

- [126] S. Guffanti, C. G. Visconti, J. van Kampen, J. Boon, and G. Groppi. “Reactor modelling and design for sorption enhanced dimethyl ether synthesis”. *Chemical Engineering Journal* 404 (2021), p. 126573. DOI: 10.1016/j.cej.2020.126573.
- [127] S. Guffanti, C. G. Visconti, and G. Groppi. “Model Analysis of the Role of Kinetics, Adsorption Capacity, and Heat and Mass Transfer Effects in Sorption Enhanced Dimethyl Ether Synthesis”. *Industrial & Engineering Chemistry Research* 60.18 (2021), pp. 6767–6783. DOI: 10.1021/acs.iecr.1c00521.
- [128] J. van Kampen, J. Boon, J. Vente, and M. van Sint Annaland. “Sorption enhanced dimethyl ether synthesis for high efficiency carbon conversion: Modelling and cycle design”. *Journal of CO₂ Utilization* 37 (2020), pp. 295–308. DOI: 10.1016/j.jcou.2019.12.021.
- [129] J. Boon, P. D. Cobden, H. van Dijk, and M. van Sint Annaland. “High-temperature pressure swing adsorption cycle design for sorption-enhanced water-gas shift”. *Chemical Engineering Science* 122 (2015), pp. 219–231. DOI: 10.1016/j.ces.2014.09.034.
- [130] P. V. Kherdekar, S. Roy, and D. Bhatia. “Dynamic Modeling and Optimization of a Fixed-Bed Reactor for the Partial Water-Gas Shift Reaction”. *Industrial & Engineering Chemistry Research* 60.25 (2021), pp. 9022–9036. DOI: 10.1021/acs.iecr.0c06042.
- [131] L. A. Živković, A. Pohar, B. Likozar, and N. M. Nikačević. “Reactor conceptual design by optimization for hydrogen production through intensified sorption- and membrane-enhanced water-gas shift reaction”. *Chemical Engineering Science* 211 (2020), p. 115174. DOI: 10.1016/j.ces.2019.115174.
- [132] B. Najmi, O. Bolland, and K. E. Colombo. “A systematic approach to the modeling and simulation of a Sorption Enhanced Water Gas Shift (SEWGS) process for CO₂ capture”. *Separation and Purification Technology* 157 (2016), pp. 80–92. DOI: 10.1016/j.seppur.2015.11.013.
- [133] V.-C. Sandu, A.-M. Cormos, I.-D. Dumbrava, A. Imre-Lucaci, C.-C. Cormos, R. de Boer, J. Boon, and S. Sluijter. “Assessment of CO₂ capture efficiency in packed bed versus 3D-printed monolith reactors for SEWGS using CFD modeling”. *International Journal of Greenhouse Gas Control* 111 (2021), p. 103447. DOI: 10.1016/j.ijggc.2021.103447.
- [134] D. Jansen, E. van Selow, P. Cobden, G. Manzolini, E. Macchi, M. Gazzani, R. Blom, P. P. Henriksen, R. Beavis, and A. Wright. “SEWGS Technology is Now Ready for Scale-up!” *Energy Procedia* 37 (2013), pp. 2265–2273. DOI: 10.1016/j.egypro.2013.06.107.
- [135] H. A. J. van Dijk, P. D. Cobden, L. Lukashuk, L. de van Water, M. Lundqvist, G. Manzolini, C.-C. Cormos, C. van Dijk, L. Mancuso, J. Johns, and D. Bellqvist. “STEPWISE Project: Sorption-Enhanced Water-Gas Shift Technology to Reduce Carbon Footprint in the Iron and Steel Industry”. *Johnson Matthey Technology Review* 62.4 (2018), pp. 395–402. DOI: 10.1595/205651318X15268923666410.
- [136] F. Sebastiani, J. James, H. van Dijk, J. A. Pieterse, J. Boon, and P. D. Cobden. “Modelling of CO₂ and H₂O Interaction During Adsorption Cycles on Hydrotalcite for SEWGS Applications”. *SSRN Electronic Journal* (2021). DOI: 10.2139/ssrn.3811608.

- [137] A. Steynberg, ed. „Fischer–Tropsch technology“. 1. ed. Vol. 152. Studies in surface science and catalysis. Amsterdam u.a.: Elsevier, 2004. URL: <http://www.loc.gov/catdir/enhancements/fy0634/2006274114-d.html>.
- [138] D. Chakrabarti, V. Prasad, and A. de Klerk. “Mechanism of the Fischer–Tropsch Process”. In: *Fischer–Tropsch Synthesis, Catalysts, and Catalysis*. Ed. by B. H. Davis and M. L. Occelli. Chemical industries. Bosa Roca: CRC Press, 2016, pp. 183–222.
- [139] A. de Klerk. „Fischer–Tropsch refining“. Weinheim: Wiley-VCH, 2011.
- [140] F. G. Botes, L. P. Dancuart, H. G. Nel, A. P. Steynberg, A. P. Vogel, B. B. Breman, and J. Font Freide. “Middle distillate fuel production from synthesis gas via the Fischer–Tropsch process”. In: *Advances in Clean Hydrocarbon Fuel Processing*. Elsevier, 2011, pp. 329–362. DOI: 10.1533/9780857093783.4.329.
- [141] H. Kirsch. „Dezentrale Synthese strombasierter flüssiger Kraftstoffe über die Fischer–Tropsch Route“. 2021. DOI: 10.5445/IR/1000129949.
- [142] T. Hanaoka, T. Miyazawa, K. Shimura, and S. Hirata. “Jet fuel synthesis from Fischer–Tropsch product under mild hydrocracking conditions using Pt-loaded catalysts”. *Chemical Engineering Journal* 263 (2015), pp. 178–185. DOI: 10.1016/j.cej.2014.11.042.
- [143] J. Weitkamp. “Catalytic Hydrocracking—Mechanisms and Versatility of the Process”. *ChemCatChem* 4.3 (2012), pp. 292–306. DOI: 10.1002/cctc.201100315.
- [144] R. Brosius, P. J. Kooyman, and J. C. Q. Fletcher. “Selective Formation of Linear Alkanes from n–Hexadecane Primary Hydrocracking in Shape–Selective MFI Zeolites by Competitive Adsorption of Water”. *ACS Catalysis* 6.11 (2016), pp. 7710–7715. DOI: 10.1021/acscatal.6b02223.
- [145] MATLAB. „Version R2020b“. 2020. URL: <https://www.mathworks.com/help/matlab/> last visited: May 1, 2023.
- [146] SIMULINK. „Simulation and Model-Based Design“. 2020. URL: <https://www.mathworks.com/products/simulink.html> last visited: May 1, 2023.
- [147] K. Coenen, F. Gallucci, E. Hensen, and M. van Sint Annaland. “Kinetic model for adsorption and desorption of H₂O and CO₂ on hydrotalcite-based adsorbents”. *Chemical Engineering Journal* 355 (2019), pp. 520–531. DOI: 10.1016/j.cej.2018.08.175.
- [148] Y. Zhou, S. Searle, and N. Pavlenko. „Current and future cost of e-kerosene in the United States and Europe. WORKING PAPER 2022-14“. 2022.
- [149] European Commission. „European Green Deal: Commission proposes transformation of EU economy and society to meet climate ambitions“. Brussels, 14.07.2021. URL: https://ec.europa.eu/commission/presscorner/detail/en/IP_21_3541 last visited: May 1, 2023.
- [150] European Commission. „European Green Deal: new law agreed to cut aviation emissions by promoting sustainable aviation fuels“. Brussels, 26.04.2023. URL: https://ec.europa.eu/commission/presscorner/detail/en/ip_23_2389 last visited: May 1, 2023.

- [151] European Commission. „Proposal for a regulation of the European Parliament and of the Council on ensuring a level playing field for sustainable air transport“. Brussels, 14.07.2021. URL: <https://eur-lex.europa.eu/legal-content/EN/TXT/?uri=CELEX:52021PC0561> last visited: May 1, 2023.

Peer-reviewed Publications from the Author

- [P1] T. J. Stadler, P. Barbig, J. Kiehl, R. Schulz, T. Klövekorn, and P. Pfeifer. “Sorption-Enhanced Water-Gas Shift Reaction for Synthesis Gas Production from Pure CO: Investigation of Sorption Parameters and Reactor Configurations”. *Energies* 14.2 (2021), p. 355. DOI: 10.3390/en14020355.
- [P2] T. J. Stadler, J.-H. Knoop, S. Decker, and P. Pfeifer. “Numerical Simulation Approach for a Dynamically Operated Sorption-Enhanced Water-Gas Shift Reactor”. *Processes* 10.6 (2022), p. 1160. DOI: 10.3390/pr10061160.
- [P3] T. J. Stadler, L. J. Bender, and P. Pfeifer. “Dynamic simulation of a compact sorption-enhanced water-gas shift reactor”. *Frontiers in Chemical Engineering* 4 (2022). DOI: 10.3389/fceng.2022.1000064.
- [P4] T. J. Stadler, B. Bertin-Mente, R. Dittmeyer, L. T. Brübach, T. Böltken, and P. Pfeifer. “Influence of CO₂-Rich Syngas on the Selectivity to C₁₀-C₁₄ in a Coupled Fischer-Tropsch/Hydrocracking Process”. *Chemie Ingenieur Technik* 94.3 (2022), pp. 289–298. DOI: 10.1002/cite.202100172.

Publications

PI Choice of Materials, Sorption Parameters and Reactor Configurations

Sorption-Enhanced Water-Gas Shift Reaction for Synthesis Gas Production from Pure CO: Investigation of Sorption Parameters and Reactor Configurations

Published in Energies 2021, 14, 355

Publishing Date 11 January 2021

DOI <https://doi.org/10.3390/en14020355>

Article

Sorption-Enhanced Water-Gas Shift Reaction for Synthesis Gas Production from Pure CO: Investigation of Sorption Parameters and Reactor Configurations

Tabea J. Stadler *, Philipp Barbig, Julian Kiehl, Rafael Schulz, Thomas Klövekorn and Peter Pfeifer

Institute for Micro Process Engineering (IMVT), Karlsruhe Institute of Technology, 76344 Eggenstein-Leopoldshafen, Germany; philipp.barbig@student.kit.edu (P.B.); julian.kiehl@student.kit.edu (J.K.); rafael.schulz@student.kit.edu (R.S.); thomas.kloevekorn@student.kit.edu (T.K.); peter.pfeifer@kit.edu (P.P.)
* Correspondence: tabea.stadler@kit.edu; Tel.: +49-721-608-24117

Abstract: A sorption-enhanced water-gas shift (SEWGS) system providing CO₂-free synthesis gas (CO + H₂) for jet fuel production from pure CO was studied. The water-gas shift (WGS) reaction was catalyzed by a commercial Cu/ZnO/Al₂O₃ catalyst and carried out with in-situ CO₂ removal on a 20 wt% potassium-promoted hydrotalcite-derived sorbent. Catalyst activity was investigated in a fixed bed tubular reactor. Different sorbent materials and treatments were characterized by CO₂ chemisorption among other analysis methods to choose a suitable sorbent. Cyclic breakthrough tests in an isothermal packed bed microchannel reactor (PBMR) were performed at significantly lower modified residence times than those reported in literature. A parameter study gave an insight into the effect of pressure, adsorption feed composition, desorption conditions, as well as reactor configuration on breakthrough delay and adsorbed amount of CO₂. Special attention was paid to the steam content. The significance of water during adsorption as well as desorption confirmed the existence of different adsorption sites. Various reactor packing concepts showed that the interaction of relatively fast reaction and relatively slow adsorption kinetics plays a key role in the SEWGS process design at low residence time conditions.

Keywords: sorption-enhanced water-gas shift reaction; synthesis gas production; Power-to-Liquid; jet fuel production; CO₂ sorption; potassium-promoted hydrotalcite; divided section packing



Citation: Stadler, T.J.; Barbig, P.; Kiehl, J.; Schulz, R.; Klövekorn, T.; Pfeifer, P. Sorption-Enhanced Water-Gas Shift Reaction for Synthesis Gas Production from Pure CO: Investigation of Sorption Parameters and Reactor Configurations. *Energies* **2021**, *14*, 355. <https://doi.org/10.3390/en14020355>

Received: 29 November 2020

Accepted: 28 December 2020

Published: 11 January 2021

Publisher's Note: MDPI stays neutral with regard to jurisdictional claims in published maps and institutional affiliations.



Copyright: © 2021 by the authors. Licensee MDPI, Basel, Switzerland. This article is an open access article distributed under the terms and conditions of the Creative Commons Attribution (CC BY) license (<https://creativecommons.org/licenses/by/4.0/>).

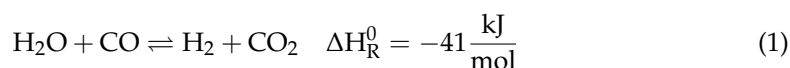
1. Introduction

The mitigation of anthropogenic climate change is a key challenge of today's society. CO₂ emissions contribute significantly to the atmospheric greenhouse effect and need to be reduced drastically to constrain global average temperature rise well below 2 °C [1]. The transport sector causes one quarter of Europe's greenhouse gas emissions and relies significantly on fossil fuels [2]. Sustainable alternatives, such as mobility based on electrochemical storage or hydrogen from renewable sources, can be employed to defossilize the transport sector. However, not all means of transport, such as aviation, marine or long-haul truck transport can rely on those technologies due to volumetric and gravimetric restrictions. For such applications, CO₂ neutral synthetic fuels produced via Power-to-Liquid (PtL) processes are promising [2].

The Kerogreen project aims to investigate an advanced PtL conversion route from water and captured CO₂ to carbon neutral jet fuel powered by renewable energy sources [3]. In this project, the crucial step of CO₂ activation is tackled by means of CO₂ plasma splitting into CO and O₂ [4,5]. To circumvent product recombination, O₂ is separated by a solid oxide electrolyte cell. The remaining reaction mixture is fed into a pressure swing adsorption unit to remove unreacted CO₂. The purified CO is then partly converted with steam to produce hydrogen via the water-gas shift reaction (WGS). After the removal of formed

CO₂, the synthesis gas (CO + H₂) reacts in the subsequent Fischer-Tropsch (FT) reactor to hydrocarbons with a wide chain length distribution. The kerosene yield is increased in a hydrocracking unit, where hydrocarbons greater C₁₄ are cracked down to the kerosene range [6,7].

In the WGS (Equation (1)) step, two main targets are pursued: First, providing synthesis gas with a H₂/CO ratio of approximately 2 for the subsequent FT synthesis and, secondly, removing the byproduct CO₂ in order to recycle it to the plasma unit. Both requirements can be realized in a single unit operation: a sorption-enhanced water-gas shift (SEWGS) system. Here, the heterogeneously catalyzed WGS reaction is carried out simultaneously with in-situ CO₂ adsorption on a highly selective sorbent. This promising CO₂ capture technology is proposed in the literature for high purity hydrogen production from synthesis gas of reformers [8,9]. Thermodynamic limitations are overcome by an equilibrium shift towards the product side resulting in near full CO conversion and, consequently, near fuel cell grade H₂. However, in the Kerogreen process, near pure CO is fed to the process and CO₂ removal, rather than full CO conversion, is envisaged.



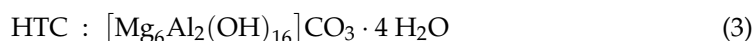
From a thermodynamic point of view, the moderately exothermic WGS reaction favors low temperatures, whereas higher temperatures are desired for kinetic reasons at initial reaction conditions. Equilibrium conversion is not dependent on pressure and can be calculated based on the equilibrium constant reported by Moe (Equation (2), [10]).

$$K_{\text{eq}} = \exp\left(\left(\frac{4577.8}{T}\right) - 4.33\right) \quad (2)$$

Cu/ZnO/Al₂O₃ catalysts are commonly used for low temperature WGS (200 °C–300 °C) [11,12]. Pressure dependent side reactions, such as methanol synthesis, are not expected in a mild pressure range of up to 15 bar from thermodynamic calculations. Although the WGS reaction mechanism is not yet clearly revealed, an appropriate empirical rate expression proposed by Choi et al. (Equation (S1)) could be applied [13].

Various materials are suggested as CO₂ sorbents, namely calcium oxide [14], magnesium oxide [15], lithium zirconate [16], lithium silicate [17], activated carbon [18], molecular sieves [19], zeolites [20] and metal organic frameworks [21]. The use of these materials in this SEWGS study is discarded due to, for example, low thermal stability, low CO₂ sorption capacity at WGS conditions, poor performance in the presence of water, high temperatures required for regeneration or low cyclic working capacity.

Apart from these sorbents, layered double hydroxides, so-called hydrotalcite materials (HTCs), are identified as suitable CO₂ sorbents under WGS conditions [22,23]. Their chemical composition can be described with Equation (3) [24]. HTCs change their structure during thermal treatment and reveal basic sites, which are required for CO₂ adsorption in their mixed oxide form (hydrotalcite-derived compounds, HTdcs) [25]. Positively charged brucite-like layers are compensated with counter-anions (CO₃²⁻) and water in the interlayer region. HTdcs exhibit good cyclic, mechanical, and thermal stability, as well as relatively fast adsorption and desorption kinetics. They can be regenerated with low energy input [8,26]. Thanks to their low costs, nearly infinite selectivity for CO₂ and acceptable adsorption capacity (typically lower than 1 mmol/g), HTdcs are preferred candidates for SEWGS [27]. Impregnation with alkali metal ions, usually potassium, enhances their sorption capacity [28,29].



In this work, the experimental results for a laboratory scale SEWGS reaction concept using a Cu/ZnO/Al₂O₃ catalyst and a potassium-impregnated HTC as sorbent are presented. Initially, the catalyst and sorbent characteristics are determined. Then, the

combination of catalyst and sorbent in five reactor configurations with different packing concepts is tested in automated cyclic breakthrough experiments. A slit-like packed bed microchannel reactor (PBMR) first applied in methanation studies is used in the detailed SEWGS parameter study [30]. In this reactor, plug flow performance and good heat transfer characteristics are expected. Thus, temperature gradients observed at certain conditions in a tubular reactor for catalyst performance studies are absent. The influence of various adsorption parameters, namely pressure and feed composition, as well as the effect of desorption time and feed on the subsequent adsorption phase is shown. The importance of the steam content in the adsorption and the desorption phase is investigated in detail. Such detailed analysis is missing in the literature to design a full-scale system in the framework of the Kerogreen project. The parameter study is conducted at significantly lower modified residence times than those previously reported in the literature [31–33].

2. Materials and Methods

2.1. Materials

2.1.1. Catalyst and Sorbent Preparation

Commercial Cu/ZnO/Al₂O₃ pellets were used as the WGS catalyst. The pellets were crushed and sieved in order to obtain particles in the range of 100 µm to 300 µm. Catalyst reduction was carried out in-situ for the catalyst performance investigations and the SEWGS breakthrough measurements. The catalyst was reduced while heating up to 240 °C in 3% H₂ flow (balanced in N₂), then the flow was switched to pure H₂ and the temperature further increased to 250 °C.

A commercially available HTC from Sasol GmbH (PURAL MG70, herein called MG70) with Al₂O₃:MgO = 30:70 was treated with different calcination and impregnation procedures to obtain hydrotalcite-derived mixed oxides as CO₂ sorbents. MG70 powder was calcined ex-situ in N₂ atmosphere for 10 h at 250 °C, 400 °C and 500 °C, respectively. Incipient wetness impregnation with potassium carbonate (K₂CO₃, ≥ 99%, Sigma-Aldrich) was applied to achieve a potassium loading of 20 wt% on MG70. This value was reported in the literature for reaching a maximum CO₂ adsorption capacity [34–36]. Impregnated samples were either calcined before, after, or before and after impregnation. All HTdc samples listed in Table 1 were characterized by various methods (see Section 2.1.3). Sample MG70-K-400 revealed the most promising results, thus particles in the range of 100 µm to 300 µm of this material were used in the SEWGS breakthrough measurements.

Table 1. Hydrotalcite-derived compounds (HTdcs) samples with optional calcination before and/or after impregnation.

Sample	Calcination/°C	K-Impregnation/wt%	Calcination/°C
MG70	-	-	-
MG70-250	250	-	-
MG70-400	400	-	-
MG70-500	500	-	-
MG70-K-400	-	20	400
MG70-400-K	400	20	-
MG70-400-K-400	400	20	400

2.1.2. Catalyst Performance Measurements

Catalyst activity tests were performed in a tubular stainless-steel reactor (TR, 8 mm inner diameter, 30 mm length). Nearly isothermal conditions (gradients ±2 K) could be achieved by a programmable tubular furnace and were controlled by an axially moveable K-type thermocouple in the sufficiently diluted catalyst bed. The catalyst loading was 1 g, the reaction pressure is 5 bar, and the steam-to-gas (S/G) ratio in the feed gas was kept constant at 1 (Equation (4)). The reaction tests were performed at temperatures between 225 °C and 300 °C. The modified residence times at reaction conditions were set between 1.3×10^{-5} g·h/mL and 2.2×10^{-5} g·h/mL (Equation (5)). Feed and product gas

composition were analyzed in a gas chromatograph (GC, Agilent 7890) equipped with two columns (HP-Plot/Q and Molsieve 5Å) and two detectors (TCD and FID). Argon was used as carrier gas and N₂ as internal standard. Carbon balances for all results reported in this work were within 3% of closure. Blank activity was evaluated before the experiments with inert filling. No byproduct formation was observed. The steady-state conversion was determined according to Equation (6).

$$S/G = \frac{\dot{n}_{\text{H}_2\text{O},0}}{\dot{n}_{\text{CO},0}} \quad (4)$$

$$\tau_{\text{mod}} = \frac{m_{\text{cat}}}{\dot{V}_0} \quad (5)$$

$$X_{\text{CO}} = \frac{\dot{n}_{\text{CO},0} - \dot{n}_{\text{CO}}}{\dot{n}_{\text{CO},0}} \quad (6)$$

2.1.3. Sorbent Characterization and Sorption Capacity Measurements

The crystalline structures of all HTdcs were studied by powder X-ray diffraction (XRD) in a D8 Advance (Bruker AXS) diffractometer with Cu K α 1,2 radiation (0.154060 nm and 0.154440 nm, respectively) operating in a 2 θ range of 5–85° with a step width of 0.019° 2 θ . The total counting time per step was 288 s. The raw data was evaluated with the software DIFFRAC.EVA Version 5.1 (zero shift correction and mineral phases identification).

The thermal decomposition of two samples (MG70 and MG70-K-400) was investigated by thermogravimetric analysis (TGA) in a STA 449 F3 Jupiter (Netzsch). The samples were heated with a heating rate of max. 10 K/min up to 1000 °C under N₂ atmosphere.

Textural properties of three samples (MG70-400, MG70-K-400 and MG70-400-K-400) were determined by N₂ physisorption at –196 °C in a 3Flex Surface Characterization instrument (Micromeritics). Adsorption and desorption isotherms were recorded after degassing the samples in vacuum (<1 mmHg) at 400 °C for 3 h. Surface area was calculated according to the BET method. Average pore width and total pore volume, corresponding to the cumulative pore volumes between 17 and 3000 Å, were determined from the adsorption branch using the BJH method.

Electron probe micro analysis (EPMA) was performed for various samples on a JXA 8530F (Jeol) coupled with energy dispersive spectroscopy (EDS) to investigate the sample composition at fixed probe positions and to compare the sample surface (SE and BSE images). Pressed powder (0.2 g, 30 kN for 30 s) tablets with a plane surface were used for EDS analysis.

CO₂ chemisorption uptake measurements were also performed in the above mentioned 3Flex Surface Characterization instrument (Micromeritics). Samples were pretreated in situ at the respective calcination temperature in N₂ flow for 3 h and outgassed in vacuum (<5 × 10^{–3} mmHg) at analysis temperature (250 °C) for 2 h. During the measurement, the samples (~0.5 g) were flushed stepwise with CO₂ until equilibrium was reached. Pressure increments were 10 mmHg from 0 to 50 mmHg, 25 to 100 mmHg and 50 to 760 mmHg.

2.2. SEWGS Breakthrough Experiments

As the highest and most reproducible sorption capacity was obtained for MG70-K-400 (see Section 3.2), all SEWGS tests were conducted with this sorbent. CO₂ breakthrough experiments were carried out in a two-slit packed PBMR in the experimental setup shown in Figure 1 [30]. Both reaction slits (2 × 5 × 10 mm³) were filled with catalyst and sorbent particles. Five programmable heating cartridges controlled by K-type thermocouples were placed along the bed ensure isothermal reaction conditions together with a microchannel air-cooling system. An additional thermocouple was placed inside the fixed bed. Constant and precise water dosage was enabled by a liquid flow controller (LFC, Brooks) and pulsation-free evaporation by an inhouse-manufactured micro nozzle. N₂ and CO were

fed with mass flow controllers (MFC, Brooks). The pressure in the system was adjusted by an automated regulating valve (Flowserve).

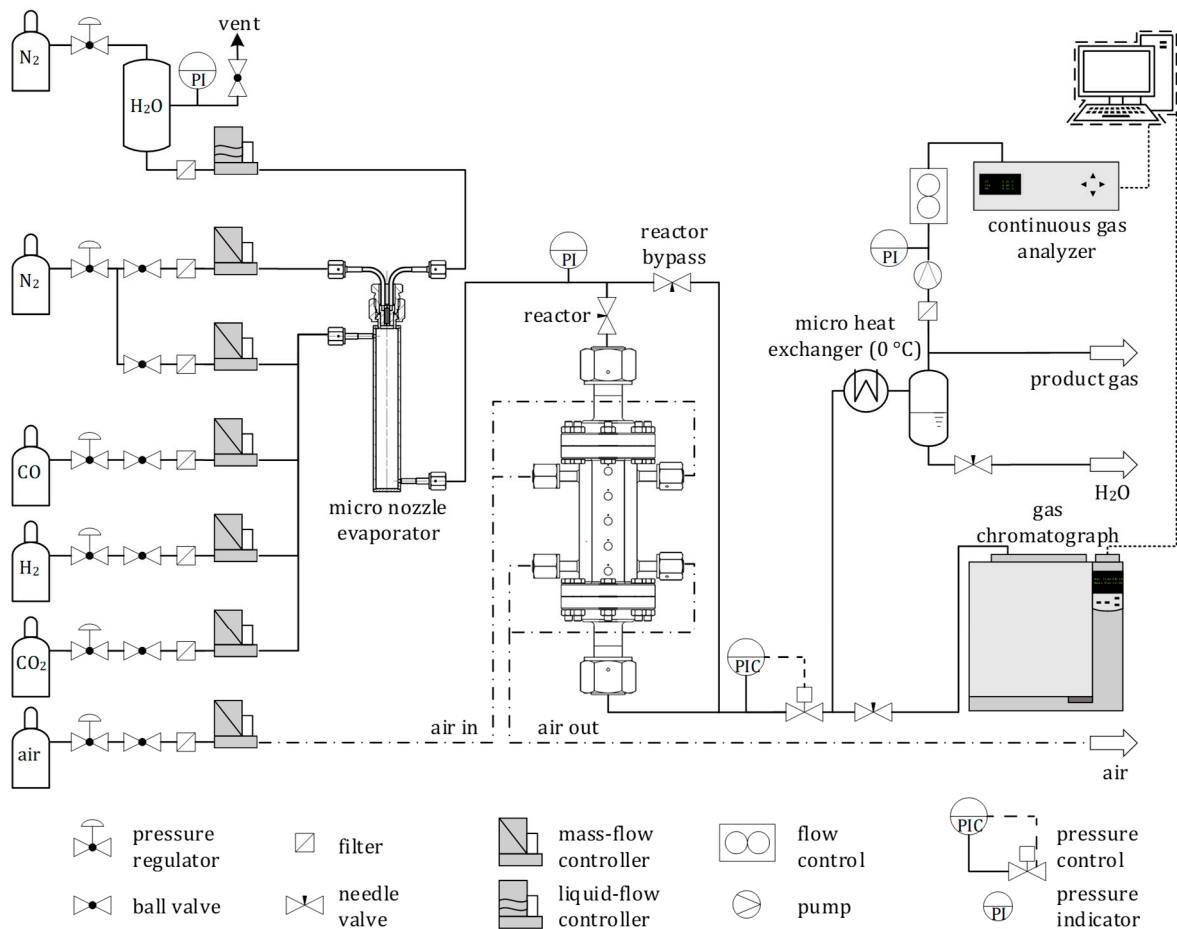


Figure 1. Schematic drawing of experimental sorption-enhanced water-gas shift (SEWGS) setup.

The composition of the wet product gas was analyzed by a GC (see Section 2.1.2) to detect possible byproduct formation. The volume fractions of CO, CO₂ and H₂ in the dry effluent were continuously monitored in a process gas analyzer (PGA, X-STREAM Enhanced, Emerson).

CO and CO₂ fractions were recorded by nondispersive infrared detectors (NDIR), and H₂ by a TCD. Prior to the PGA, H₂O was condensed in a micro heat exchanger with cooling liquid kept at about 0 °C.

Preliminary tests without catalyst (sorbent only) ensured that the sorbent was not catalytically active for the WGS reaction at 250 °C, as neither products nor byproducts of any kind were found in the effluent. The measurement systems, GC and PGA, operated within 1% of accuracy between each other. Therefore, comparability was confirmed and only PGA breakthrough curves were discussed in this work to monitor the time-resolved evolution of the gases in the SEWGS breakthrough experiments.

In all breakthrough experiments, at least five adsorption and reaction (herein only called adsorption) and desorption cycles were conducted. Prior to the first adsorption, a 90 min desorption step was carried out (40% H₂O in N₂, 1000 mL/min, 1 bar). After the last desorption step of an experiment, the bed was purged with N₂ for 12 h overnight (1000 mL/min, 1 bar). This procedure was proven to deliver good regeneration of the sorbent in preliminary trials with pure HTdc in the fixed bed. In the adsorption experiments, adsorption temperature, total adsorption flow rate, and adsorption time as well as all desorption parameters were kept constant, whereas adsorption feed composition (balanced

in N₂) and adsorption pressure were varied. In the desorption experiments, desorption temperature, desorption pressure as well as all adsorption parameters were kept constant. The varied desorption parameters were time and H₂O volume fraction (balanced in N₂). An overview of all parameters is given in Table 2.

Table 2. Adsorption and desorption parameters used in the SEWGS breakthrough experiments.

Temperature	<i>T</i>	250
Adsorption time	<i>t</i> _{ads} /min	15
Adsorption pressure	<i>p</i> _{ads} /bar	3, 4, 8 *
Total adsorption volume flow (STP)	<i>V</i> _{ads} /mL/min	2000
Adsorption volume fraction CO	<i>y</i> _{CO,ads} /%	2.5 *, 5, 10, 20
Adsorption volume fraction H ₂ O	<i>y</i> _{H₂O,ads} /%	10 *, 20, 40
Desorption time	<i>t</i> _{des} /min	15, 20, 30, 40 **
Desorption pressure	<i>p</i> _{des} /bar	1
Total desorption volume flow (STP)	<i>V</i> _{des} /mL/min	1000
Desorption volume fraction H ₂ O	<i>y</i> _{H₂O,des} /%	20, 40 **, 60

* adsorption parameters in desorption experiments, ** desorption parameters in adsorption experiments.

Five fixed bed configurations were investigated in this work (Figure 2). Mode A consisted of a homogeneous mixture of catalyst and sorbent with a total catalyst weight fraction of 0.05 in both slits of the PBMR (Equation (7)). In mode B, the fixed bed in both channels was divided into two almost equally long zones: half of the sorbent mass was mixed with the same total catalyst amount as in mode A in the first zone (corresponding zone weight fraction is 0.10), and the other half of the sorbent mass was loaded into the second zone. In mode C, the bed was also divided into two zones. The first zone contained one quarter of the total sorbent mass and the same total catalyst amount as used in mode A and B, yielding a zone weight fraction of 0.17. The second zone was loaded with the remaining sorbent. Experimental catalyst and sorbent mass are listed in Table 3. Variations in sorbent mass and the non-precise doubling of the weight fraction arose from changes in the bulk density of different sorbent batches and the stepwise manual filling process. In mode D and E, the total amount of catalyst was doubled to achieve a total catalyst weight fraction of 0.11. Zone distribution in mode D equaled mode B, where the second zone (half of the length) was filled with pure sorbent. Mode E consisted of four equally distributed zones which were alternately filled with mixed sorbent and catalyst and pure sorbent.

$$w_{\text{cat}} = \frac{m_{\text{cat}}}{m_{\text{cat}} + m_{\text{sorb}}} \quad (7)$$

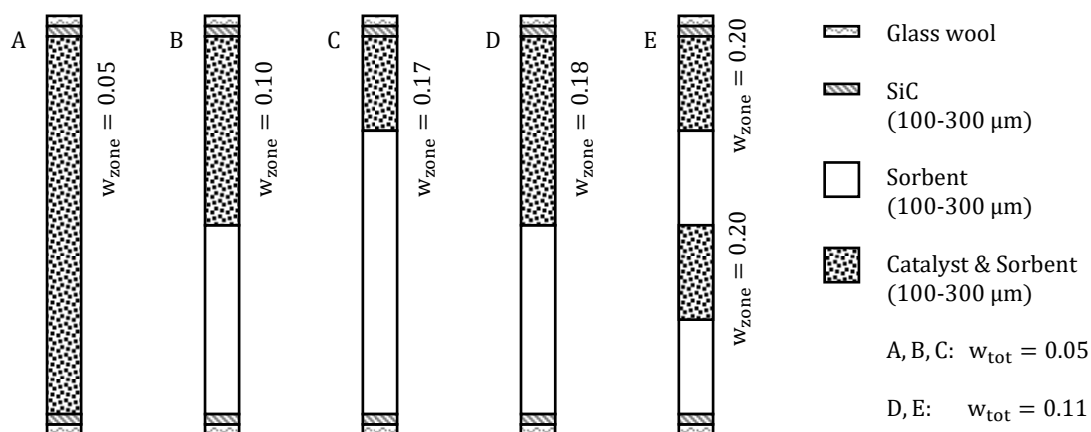


Figure 2. Investigated SEWGS reactor configurations.

Table 3. Experimental catalyst and sorbent mass for different reactor configurations.

		Mode A	Mode B	Mode C	Mode D	Mode E
Catalyst mass	m_{cat}/g	0.58	0.58	0.58	1.22	1.22
Sorbent mass	m_{sorb}/g	11.0	9.7	11.0	9.7	9.7

The CO conversion was calculated from PGA data according to Equation (8), whereas the dry volume flow and the dry N_2 volume fraction was obtained by Equations (9) and (10), respectively. CO_2 breakthrough delay compared to H_2 was evaluated with Equation (11). As H_2 was not adsorbed, the H_2 content in the effluent showed the residence time behavior in the setup from feed dosage until the PGA measurement. Due to measurement reasons, the H_2 signal in the PGA was retarded and needed to be shifted in absolute time before determining the CO_2 breakthrough delay. The amount of adsorbed CO_2 until 0.2% CO_2 was detected in the dry effluent was determined using Equation (12). Note that this value (herein called CO_2 adsorbed) does not represent the full adsorption capacity of the sorbent. It rather refers to a sorption time limit for allowed CO_2 breakthrough which is influenced by the sorption kinetics and was used as reference for internal comparison of the experiments. The value of 0.2% CO_2 as reference point for both breakthrough delay and adsorbed amount of CO_2 was chosen based on a first assumption of the tolerable amount of CO_2 in the feed for the FT reactor in the Kerogreen process.

$$X_{\text{CO}} = \frac{\dot{V}_0 \cdot y_{\text{CO},0} - \dot{V}_{\text{dry}} \cdot y_{\text{CO,dry}}}{\dot{V}_0 \cdot y_{\text{CO},0}} \quad (8)$$

$$\dot{V}_{\text{dry}} = \dot{V}_0 \cdot \frac{y_{\text{N}_2,0}}{y_{\text{N}_2,\text{dry}}} \quad (9)$$

$$y_{\text{N}_2,\text{dry}} = 1 - y_{\text{CO}_2,\text{dry}} - y_{\text{CO,dry}} - y_{\text{H}_2,\text{dry}} \quad (10)$$

$$\Delta t = t(y_{\text{CO}_2,\text{dry}} = 0.2\%) - t(y_{\text{H}_2,\text{dry}} = 0.2\%) \quad (11)$$

$$n_{\text{ads}} = \frac{p}{R \cdot T} \cdot \frac{1}{m_{\text{sorb}}} \cdot \left(\int_0^{y_{\text{CO}_2,\text{dry}}=0.2\%} \dot{V}_{\text{dry}} \cdot y_{\text{H}_2,\text{dry}} \cdot dt - \int_0^{y_{\text{CO}_2,\text{dry}}=0.2\%} \dot{V}_{\text{dry}} \cdot y_{\text{CO}_2,\text{dry}} \cdot dt \right) \quad (12)$$

3. Results and Discussion

3.1. Catalyst Performance

Catalyst activity tests in the TR revealed that no byproducts, e.g., methane, were formed. The reaction was rather limited kinetically than thermodynamically within the studied parameter range, as CO conversion increased with temperature and approached equilibrium only at 300 °C (Figure 3a). Assuming complete CO_2 removal, the reaction rate could be shifted from 0.21 mol/(g·h) to 0.43 mol/(g·h) at 60% CO conversion (and a temperature of 250 °C) according to the rate expression from Choi et al. (Equation (S1)) [13]. The temperature of 250 °C was chosen for the SEWGS experiments as Cu catalysts tend to sinter at temperatures above 300 °C. Figure 3b shows that CO conversion slightly increased with modified residence time but was still far away from thermodynamic equilibrium. This suggests that kinetic constraints prevailed under the given reaction conditions. Therefore, SEWGS experiments were carried out at modified residence times of about 2×10^{-5} g·h/mL.

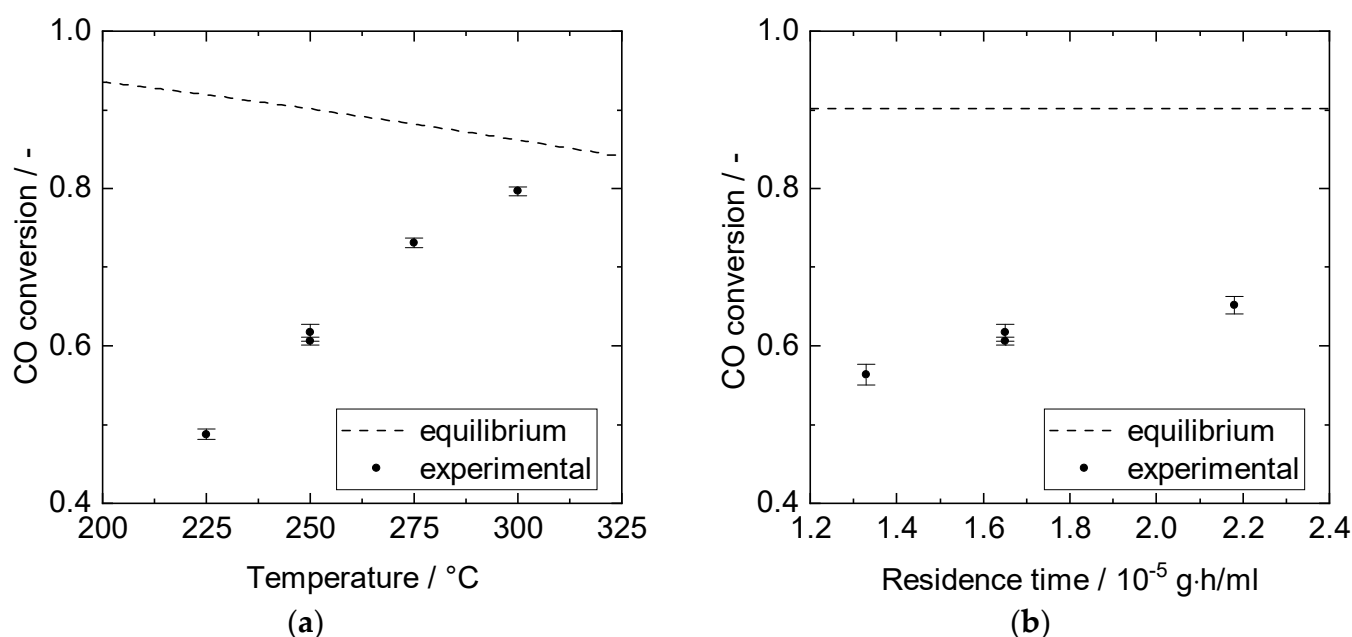


Figure 3. Cu/ZnO/Al₂O₃ catalyst performance in experiments (1 g catalyst TR, 5 bar, 10% CO, S/G = 1). (a) CO conversion over temperature for modified residence time of 1.66×10^{-5} g·h/mL. (b) CO conversion over modified residence time at 250 °C.

3.2. Structural Properties and CO₂ Capture Performance of Sorbent

XRD patterns of all samples are depicted in Figure 4. Untreated MG70 showed the typical diffractogram of HTC compared to HTC reference from powder diffraction file (PDF) 35-0965. Sharp and intense peaks at $\sim 11^\circ$, 23° , 35° , and 60° corresponding to the (003), (006), (012) and (110) planes indicated a well-formed crystalline layered structure with a rhombohedral symmetry. The patterns of the calcined samples revealed that the layered structure was destroyed after heat treatment (Figure 4a). For MG70-250, mainly weak and broad peaks corresponding to the amorphous phase were observed. MG70-400 and MG70-500 showed broad but more intensive and distinguishable reflections at $\sim 43^\circ$ and 62° , which represent the diffraction by the (200) and (220) planes of periclase (see MgO, PDF 65-0476). Aluminum compounds were assumed to be well-dispersed or formed an amorphous phase [37]. These results indicated that full transition from layered double hydroxide to layered double oxide was obtained through the applied calcination treatment at 400 °C and 500 °C, whereas calcination at SEWGS reaction temperature (250 °C) was not sufficient. According to literature, calcination at 400 °C leads to the best CO₂ uptake properties [38,39]. In diffractograms of various impregnation—calcination procedures, typical K₂CO₃ reflections were identified in all impregnated samples (PDF 49-1093) (Figure 4b). Therefore, the applied impregnation treatment seemed to be applicable. The different impregnation—calcination procedures did not seem to influence the crystalline structure observed in the XRD patterns.

TGA was performed to study the thermal decomposition up to 1000 °C of untreated MG70 and of impregnated—calcined MG70-K-400. For MG70, a total mass loss of 43% was found. Three material changes could be observed (Figure 5a): removal of surface and interlayer water (80–120 °C), hydroxyl groups as water vapor ($\sim 200^\circ$), and further hydroxyl groups and carbonate anions ($\sim 400^\circ$). These expected findings are discussed in detail elsewhere [24,40,41]. The impregnated and calcined sample MG70-K-400 exhibited a marginal weight loss up to $\sim 100^\circ$ C, which was mainly attributed to surface water adsorbed during storage. Reddy et al. suggested to perform in situ calcination to avoid this effect [38]. For SEWGS, in situ calcination at 400 °C prior operation and catalyst in situ reduction could be feasible, but it can be definitely excluded as a sorbent regeneration procedure.

Such regeneration is not feasible due to the instability of the admixed Cu/ZnO/Al₂O₃ catalyst. As this catalyst is prone to oxidation, it would require re-reduction after that kind of sorbent regeneration. In this work, initial sorbent calcination was performed ex situ to avoid cross contamination between catalyst and sorbent. Water adsorption was minimized by keeping storage time after calcination as short as possible prior to the SEWGS experiments. Nonetheless, TGA as well as XRD results showed that the applied calcination treatment at 400 °C ensured the removal of all unwanted compounds and led to the desired mixed oxide structure.

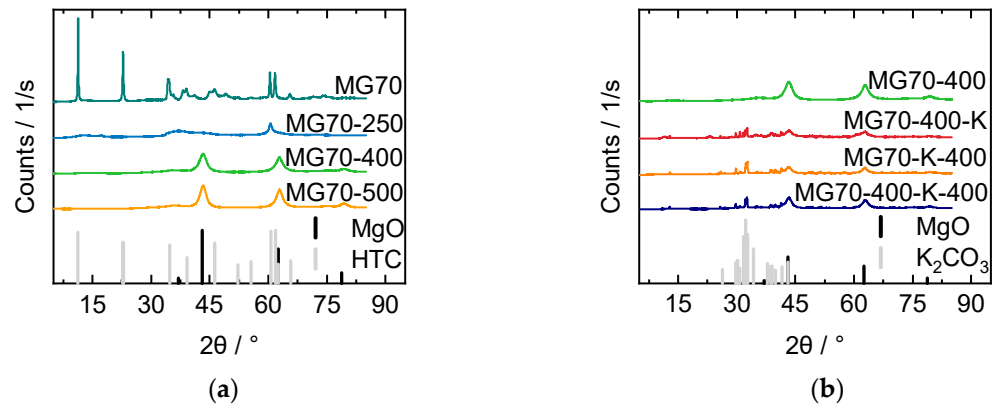


Figure 4. X Ray diffraction (XRD) patterns for (a) samples with varied calcination temperatures (250, 400 and, 500 °C) compared with untreated sample (MG70) and (b) varied calcination—impregnation procedure: calcined—impregnated sample (MG70-400-K), impregnated—calcined sample (MG70-K-400), and calcined—impregnated—calcined sample (MG70-400-K-400) compared with nonimpregnated (but calcined) sample (MG70-400).

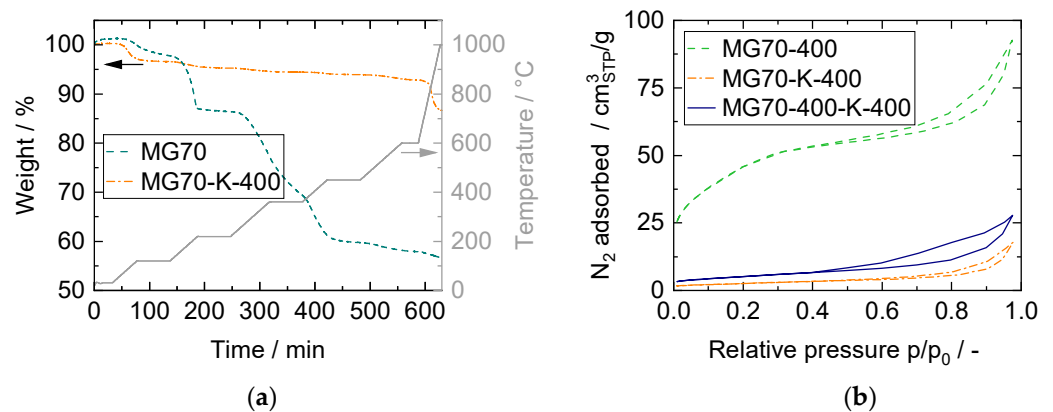


Figure 5. (a) Thermogravimetric analysis (TGA) results. Sample weight and temperature over time for untreated sample (MG70) and impregnated—calcined sample (MG70-K-400). (b) N₂ physisorption isotherms at −196 °C for calcined sample (MG70-400), impregnated—calcined sample (MG70-K-400), and calcined—impregnated—calcined sample (MG70-400-K-400).

The morphological characteristics of the samples calcined at 400 °C (as last step) were investigated by N₂ physisorption at −196 °C. The adsorption and desorption isotherms (Figure 5b) corresponded to mesoporous solids with pore diameters between 2 nm and 50 nm (type IV, IUPAC [42]). Hysteresis loops did not exhibit any limiting adsorption at high relative pressure, which is typical for type H3 hysteresis loops [42]. Such curve shape gives rise to the assumption of open large pores corresponding to aggregates of platelike particles that form slit-shaped pores [25,27]. The impregnated samples exhibited a more pronounced difference between adsorption and desorption branch, possibly due to enlarged pore networks caused by pore blocking during impregnation. Textural

properties were within the range of values reported in literature and are summarized in Table S1 [25,41,43,44]. The specific surface area decreased significantly, as expected, due to potassium impregnation. All pore diameters were above 2 nm; hence, gas molecule diffusion did not limit CO₂ adsorption.

EPMA results showed that the shapes of untreated and impregnated samples were not regular or defined, as can be seen in SE images (Figure S1). Neither needle-like nor flat structures were detected. In images employing back-scattered electrons (BSE, Figure S2), brighter zones were visible that indicated the presence of heavier components. Although incipient wetness impregnation is known to result in good material distribution, a clear preference of potassium to deposit on certain phases of the support was visible. This preference of inhomogeneous distribution was further validated by EDS analysis performed at various probe positions (Table S2, Figure S3) and was also observed by others [45–47]. EDS measurements further revealed Mg/Al ratios close to the expected value of 3.

CO₂ chemisorption isotherms obtained for dry conditions at SEWGS temperature (250 °C) are depicted in Figure 6. All curves exhibit the typically fast initial rise followed by a less pronounced increase of CO₂ uptake as function of the CO₂ pressure, as reported in the literature [48]. This behavior can be fairly described by means of the Freundlich model [22,49]. The optimized Freundlich parameters (Equation (S2)) used for data fitting in Figure 6 are listed in Table S3 and are comparable to other works [43,50,51]. As CO₂ equilibrium sorption measurements in this work were only performed up to 1 bar and for dry conditions, the given values are valuable information for the comparison of the different samples, but they do not represent SEWGS conditions.

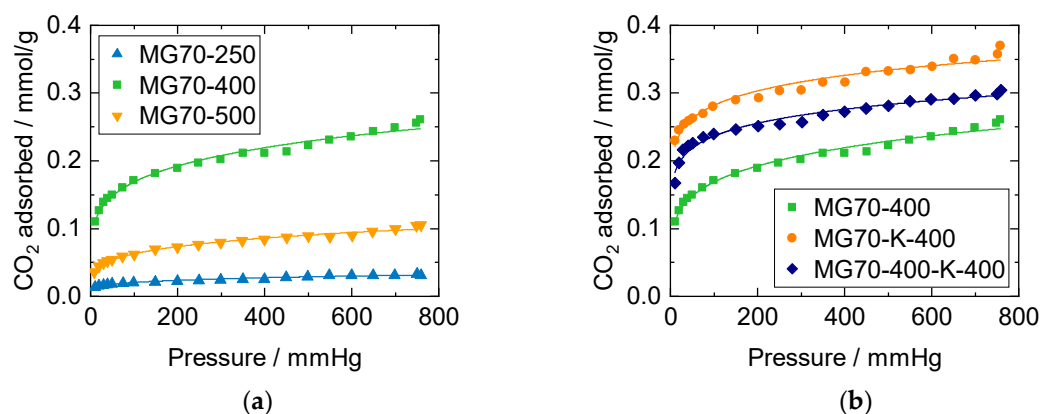


Figure 6. CO₂ chemisorption isotherms at 250 °C for (a) samples with varied calcination temperatures (250, 400 and 500 °C), and (b) varied calcination—impregnation procedures: calcined (MG70-400), impregnated—calcined (MG70-K-400), and calcined—impregnated—calcined (MG70-400-K-400). Straight lines: data fitted according to the Freundlich model (Table S3).

The highest sorption capacity in Figure 6a was reached for the sample calcined at 400 °C, compared to those calcined at 250 °C and 500 °C, respectively. This behavior can be explained by the above-mentioned findings: XRD patterns revealed that calcination at 250 °C did not lead to the desired mixed oxide with basic sites for CO₂ adsorption. Additionally, according to TGA measurements, further material decomposition started at 500 °C.

In Figure 6b, isotherms of samples with and without potassium impregnation are shown. It is well-known that CO₂ sorption on HTdcs can be improved by alkaline modification, and especially with potassium promising results were obtained [28,50,52,53]. Meis et al. attributed this enhancement to an increase in low-coordinated oxygen sites through alkali metal incorporation, and Rocha et al. assumed K to act as a chemical promoter [43,54]. Interestingly, CO₂ equilibrium isotherms in Figure 6b suggest that the procedure, in which the sample was calcined before, and once again after impregnation

(MG70-400-K-400, was not beneficial compared to the procedure in which the sample was calcined only after impregnation (MG70-K-400). The difference in adsorption capacity was more pronounced for higher pressures and might be due to an incomplete reconstruction (based on the so-called memory effect during incipient wetness impregnation) from the mixed oxide (after the first calcination) back to the layered double hydroxide in the case of twofold calcination. This decrease in adsorption sites was not correlated with surface area and pore volume. Therefore, sorption properties were more related to the chemical structure of the surface than the accessible surface area or pore volume, as indicated elsewhere [25,47,55]. As MG70-K-400 exhibited the best CO₂ adsorption characteristics, this material was selected for the following SEWGS experiments.

3.3. SEWGS Performance

The following section summarizes the results of an extensive SEWGS parameter study in the PBMR. First, the stability and the influence of various process conditions are demonstrated for selected examples of different reactor configurations. Finally, all investigated reactor modes are compared under otherwise identical process conditions.

In Figure 7a, a typical SEWGS breakthrough curve is shown. Three process stages can be distinguished as: (1) pre-breakthrough, where pure H₂ is obtained and CO₂ is adsorbed completely, (2) breakthrough stage, where CO₂ breakthrough begins, and (3) post-breakthrough, where CO₂ has reached steady-state concentration (equal to H₂ due to equimolar WGS reaction). A graphical illustration of data evaluation according to Equations (11) and (12) is depicted in Figure 7b.

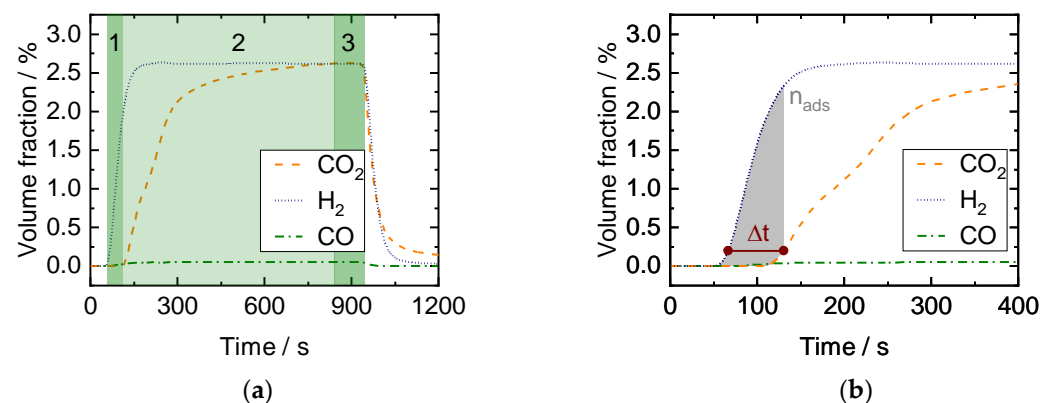


Figure 7. Measurement in the packed bed microchannel reactor (PBMR): (a) Exemplary CO, CO₂, and H₂ breakthrough curves for an adsorption step starting at t = 0 s measured in the PGA with (1) pre-breakthrough, (2) breakthrough, and (3) post-breakthrough stage. (b) Determination of CO₂ breakthrough time (Equation (11)) and adsorbed amount of CO₂ (Equation (12)).

3.3.1. Cyclic Stability

In the twelve-cycle run in Figure 8a, the steady-state conversion remains constant, whereas the adsorbed amount of CO₂ drops by 58% after the first cycle (Figure 8b). The steady-state conversion was measured after reaching the post-breakthrough phase and confirmed that no catalyst deactivation took place, neither due to the conditions nor by adding the sorbent.

All performed cyclic adsorption and desorption experiments exhibited a remarkable decrease of CO₂ adsorption capacity from the first to the second adsorption phase but stayed almost stable in subsequent cycles. The initial loss of available sorption capacity was mainly attributed to incomplete regeneration during the comparatively short desorption phase, as the adsorption kinetics were known to be ten times faster than desorption [27,56]. Furthermore, irreversible bulk polydentate carbonate formation took place, leading to a decrease of adsorption sites [29]. Nevertheless, even the initial amount adsorbed was already lower than the expected full adsorption capacity due to the limited adsorption

kinetics. The resulting cyclic working capacity, herein denoted as “cycle average” of all follow-up cycles, is more relevant to industrial applications than the initial capacity. Therefore, this value is provided in further figures of this work.

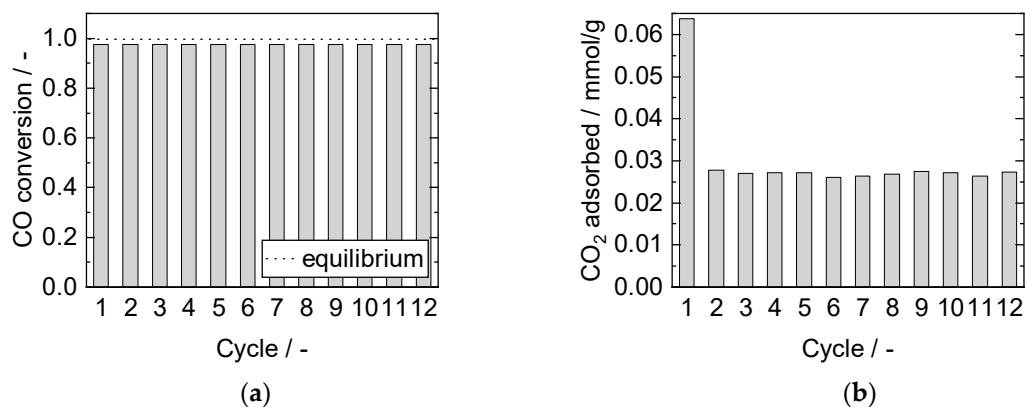


Figure 8. (a) CO conversion and (b) adsorbed amount of CO₂ for 12 adsorption cycles. Adsorption: 15 min, 8 bar, 2000 mL/min, 2.5% CO, S/G = 4. Desorption: 40 min, 1 bar, 1000 mL/min, 40% H₂O. PBMR, Mode C, 250 °C.

3.3.2. Reproducibility

Reproducibility of the measured sorption capacities was proven to be difficult, as the conditions a sorbent has seen, its history, have a remarkable influence on the adsorption characteristics [51,57]. For that reason, only experiments with similar history (e.g., no changes in desorption water content between the experiments) are compared with one another in this work. More information concerning this issue is given in (Figures S4 and S5).

3.3.3. Variation of Adsorption Parameters

Influence of Total Pressure

Results obtained in SEWGS experiments at different pressures are presented in Figure S6. Steady-state conversion approached equilibrium with increasing pressure due to faster adsorption kinetics (Equation (S1)). Breakthrough time, as well as adsorbed amount of CO₂, increased with pressure as the sorption equilibrium shifted to higher loadings and the reaction rate increased. This observation is in line with other works on CO₂ uptake on HTdcs at higher pressures [8,58,59]. Pressures above 8 bar were not assessed as no significant enhancement was expected, according to Zhu et al. [27].

Influence of CO Partial Pressure at Constant H₂O Partial Pressure

The impact resulting from an increase of the CO fraction (2.5% to 20%, constant H₂O fraction of 10%) in the feed is presented in Figure 9. Equilibrium conversion in steady-state was achieved for S/G ratios greater than 1 in the feed (2.5% and 5% CO), see Figure 9a. The CO₂ breakthrough time decreased with increasing CO fraction, and the amount of adsorbed CO₂ was significantly higher for 2.5% CO than for the other feeds (Figure 9b,c). Here, several influences overlap: sorbent saturation depends on CO₂ production rate during reaction (which is probably lowest for 2.5% CO), the resulting driving force (partial pressure of CO₂), the overall amount of CO₂ produced (highest at 10% and 20% CO) and the mean steam content over the bed length. It has been widely shown that the presence of steam during CO₂ adsorption enhances the adsorption capacity of HTdcs [44,60].

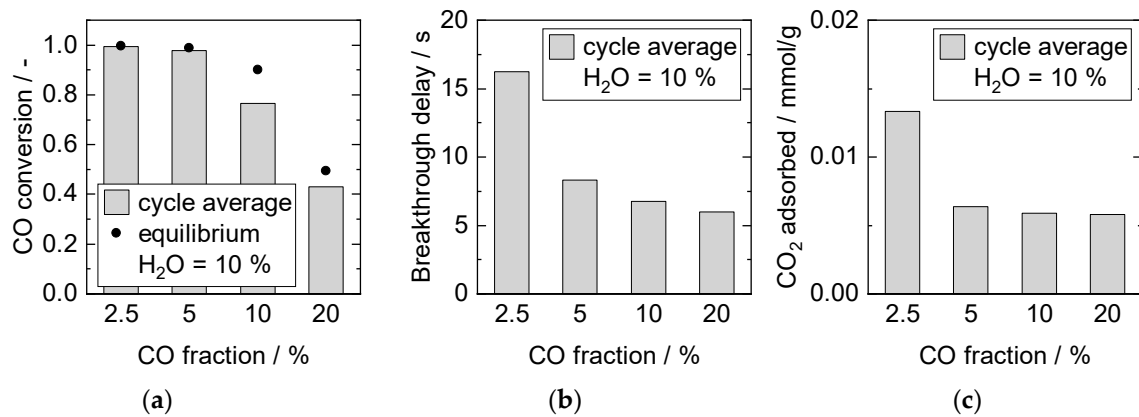


Figure 9. Adsorption cycle average (a) CO conversion, (b) breakthrough delay, and (c) adsorbed amount of CO₂. Adsorption: 15 min, 8 bar, 2000 mL/min, 10% H₂O. Desorption: 40 min, 1 bar, 1000 mL/min, 40% H₂O. PBMR, Mode D, 250 °C.

This steam effect appeared to dominate for lower CO₂ partial pressures, as the adsorbed amount was higher for 2.5% CO. Furthermore, steam also influenced the SEWGS reaction, as enough steam leading to a faster CO₂ production rate was only present for S/G ratios above or equal 1. However, at overall higher CO₂ fluxes caused by higher CO concentrations (more than factor 3 from 5% CO to 20% CO), the capacity of the sorbent was earlier at breakthrough.

Influence of H₂O Partial Pressure at Constant CO Partial Pressure

The influence of steam on the adsorption capacity was further investigated by keeping the CO fraction constant at 10%, whilst increasing the H₂O fraction above the required S/G ratio of 1. The results of these experiments are shown in Figure 10. Equilibrium conversion in steady-state increased with S/G ratio and was nearly reached for S/G ratios greater than 1. Longer breakthrough times and higher amounts of adsorbed CO₂ were detected in the presence of excess steam during the adsorption process at 20% H₂O. With 40% steam, the breakthrough time did not diminish compared to 20%. However, the amount of CO₂ adsorbed decreased by this further steam addition.

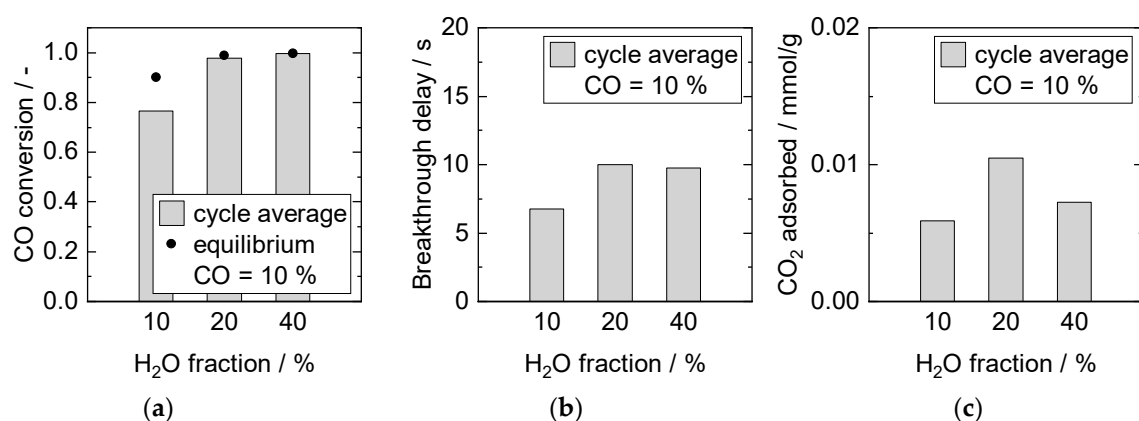


Figure 10. Adsorption cycle average (a) CO conversion, (b) breakthrough delay, and (c) adsorbed amount of CO₂. Adsorption: 15 min, 8 bar, 2000 mL/min, 10% CO. Desorption: 40 min, 1 bar, 1000 mL/min, 40% H₂O. PBMR, Mode D, 250 °C.

Such observations were in line with investigations on pure sorbent conducted by Soria et al. [8]. They reported a positive effect on sorption capacity up to 15% H₂O, but no further improvement with increasing H₂O volume fraction up to 25% (with 15% CO₂ in the feed). A potential reason might be found in competing adsorption on adsorption sites

that can be occupied by either H₂O or CO₂, depending on the respective partial pressure of these compounds. For specific sites, steam was required to remove CO₂, see Section 3.3.4.

Influence of CO and H₂O Partial Pressure at Constant S/G Ratio

Figure 11 displays the results for experiments with constant S/G ratio of 4 and simultaneously increasing CO and H₂O fraction. In all cases, equilibrium conversion was reached at steady-state conditions. With increasing reactants concentration, breakthrough time decreased. The amount of CO₂ adsorbed rose (2.5% to 5% CO), and then dropped significantly (5% to 10% CO). Multiple related impact factors overlapped again in these experiments. The following three parameters increased with increasing feed gas concentration: (1) total amount of produced CO₂, (2) CO₂ production rate, thus higher driving force for CO₂ adsorption, and (3) mean amount of steam present in the gas phase. The amount of produced CO₂ depended primarily on the CO concentration and conversion. It affected the breakthrough delay inversely. Even though a higher CO₂ partial pressure leading to a sorption equilibrium shift was obtained for 10% CO, the reaction rate increase was followed by slower adsorption kinetics, resulting in less CO₂ adsorbed. Therefore, kinetic constraints arising from relatively slow adsorption kinetics might become prevalent for high CO₂ production rates. As discussed above, the positive influence of steam seemed to be limited up to 40% H₂O in these experiments, which was reached at 10% CO for S/G = 4 and added to the effect of the kinetics gap.

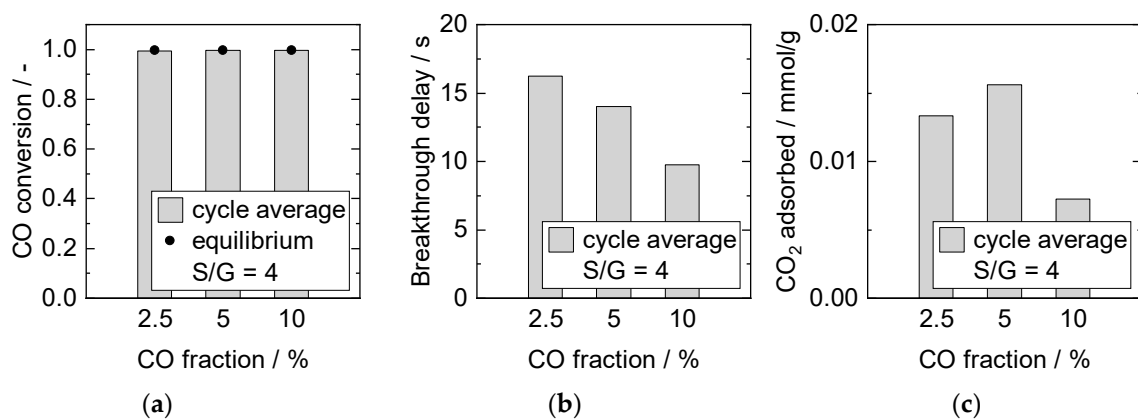


Figure 11. Adsorption cycle average (a) CO conversion, (b) breakthrough delay, and (c) adsorbed amount of CO₂. Adsorption: 15 min, 8 bar, 2000 mL/min, S/G = 4. Desorption: 40 min, 1 bar, 1000 mL/min, 40% H₂O. PBMR, Mode D, 250 °C.

3.3.4. Variation of Desorption Parameters

Influence of H₂O Partial Pressure during Desorption

In previous studies, Soria et al. reported significant process improvement with 15% H₂O (balanced in N₂) in the desorption flow compared to pure N₂ [61]. The results depicted in Figure 12 demonstrate further the influence of the H₂O fraction during sorbent regeneration on the adsorption properties in the subsequent adsorption cycles. Breakthrough time as well as amount of CO₂ adsorbed increased with increasing H₂O fraction. These experimental results can be explained with the HTdc sorption model developed by Coenen et al. [51,57,62,63]. They distinguished three different adsorption sites: (A) H₂O adsorption only, (B) CO₂ adsorption only (mainly on basic sites caused by MgO), and (C) competitive adsorption of H₂O and CO₂ (mainly due to K-promotion). Sites A and B were regenerated with N₂, whereas steam was needed to desorb CO₂ from site C (and vice versa). Hence, sorbent activation (of site C) and regeneration could be enhanced with steam.

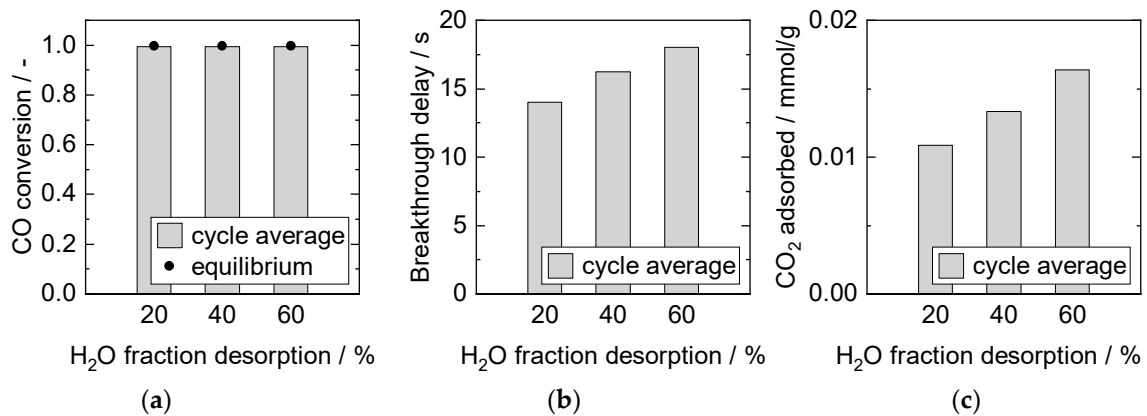


Figure 12. Adsorption cycle average (a) CO conversion, (b) breakthrough delay, and (c) adsorbed amount of CO₂. Adsorption: 15 min, 8 bar, 2000 mL/min, 2.5% CO, S/G = 4. Desorption: 40 min, 1 bar, 1000 mL/min. PBMR, Mode D, 250 °C.

Influence of Desorption Time

An increase in desorption time in SEWGS experiments resulted in longer breakthrough delays and higher amounts of CO₂ adsorbed in the subsequent adsorption cycles (Figure 13). This outcome indicates that desorption equilibrium was not reached. It is in line with literature data for sorption on HTdc, as desorption kinetics are reported to be slow [22, 27,56]. The literature also suggests that a temperature increase during desorption further enhances the sorbent regeneration and enables shorter desorption times [57,64]. Changing the temperature during desorption was not straightforward in the SEWGS system, first because the applied Cu/ZnO/Al₂O₃ catalyst tended to lose activity due to sintering at temperatures above 300 °C, and second because of energy losses in a temperature swing process.

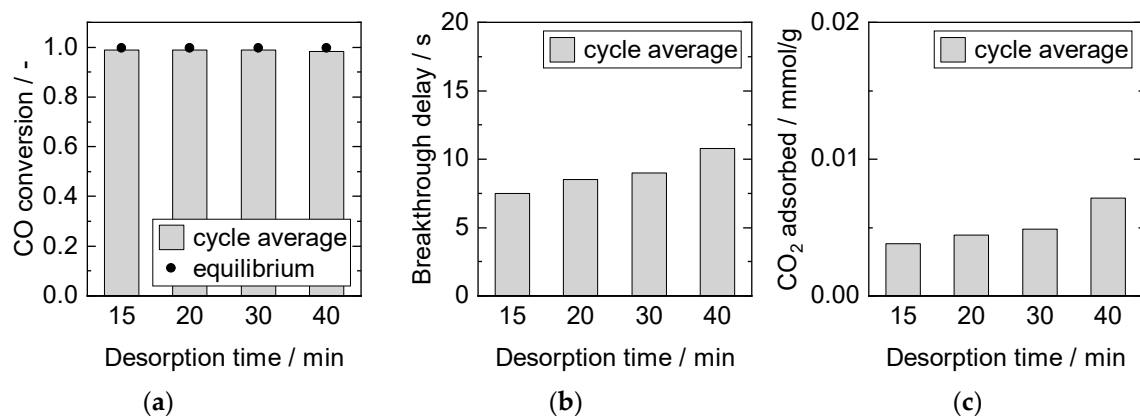


Figure 13. Adsorption cycle average (a) CO conversion, (b) breakthrough delay, and (c) adsorbed amount of CO₂. Adsorption: 15 min, 8 bar, 2000 mL/min, 2.5% CO, S/G = 4. Desorption: 1 bar, 1000 mL/min, 40% H₂O. PBMR, Mode E, 250 °C.

3.3.5. Variation of Reactor Configuration

Different reactor configurations based on the multi-section column packing concept introduced by Jang et al. were tested in the PBMR. Jang et al. concluded in a numerical study that the SEWGS process could be enhanced by loading a catalyst and sorbent mixture with higher catalyst weight ratio in the first section of a column reactor than in the second section [65].

Here, in this work, both slits of the PBMR were equally divided in multiple sections (2 and 4) and packed identically (see Figure 2). In contrast to previous studies [31–33],

significantly lower modified residence times (\sim factor 10) were studied. Hence, kinetic influences were allowed and the results are quantified with respect to the desired process conditions. Figure 14 shows the achieved steady-state CO conversion and the adsorbed amount of CO₂ for all configurations investigated.

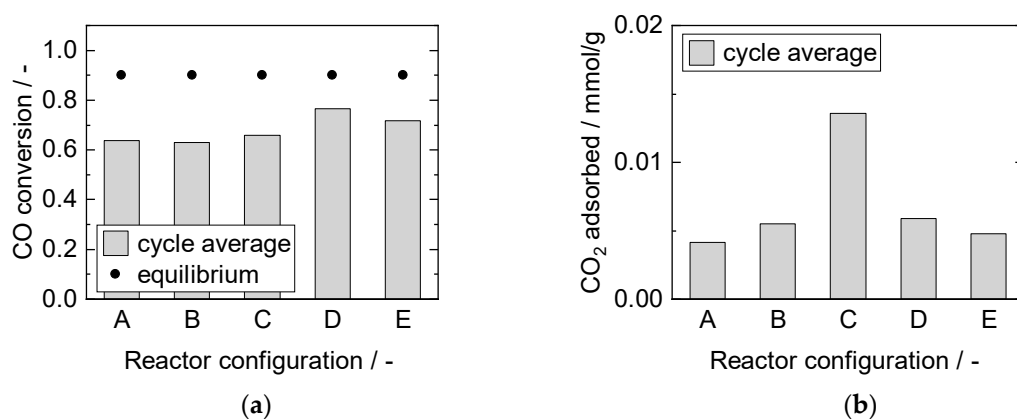


Figure 14. Adsorption cycle average (a) CO conversion, and (b) adsorbed amount of CO₂. Adsorption: 15 min, 8 bar, 2000 mL/min, 10% CO, S/G = 1. Desorption: 40 min, 1 bar, 1000 mL/min, 40% H₂O. PBMR, 250 °C.

For modes A, B and C, comparable steady-state CO conversions well below thermodynamic equilibrium were reached. A decrease in the catalyst containing zone length led to an increase in sorption capacity. Long catalyst-free zones at the outlet increased the breakthrough time, as the adsorption kinetics appeared to be considerably slower than the reaction kinetics. This conclusion is in line with the results from the operational parameter variation (see Section 3.3.2). Mode D exhibited higher CO conversion compared to mode B, owing to the doubled amount of catalyst. The adsorbed amount of CO₂, however, was within the same range for both modes, attributable to the identical zone length. The total CO₂ flux led to equally lower breakthrough times in consequence (not shown). Alternating zones in mode E did not improve the capacity in comparison with mode D. In this case, the limitation from the sorption kinetics outweighed the potential effect of thermodynamic reaction equilibrium shift in the second catalyst zone in unsteady-state conditions; the amount of CO₂ adsorbed dropped slightly. Also, slightly lower steady-state conversion was reached in mode E, possibly caused by better heat distribution. It appears that for the investigated packing concepts under the observed process conditions, the zone length of pure sorbent at the outlet was decisive. The main influencing factor on sorption characteristics with regard to reactor configurations was the difference in adsorption and reaction rate.

Experimental results for a S/G ratio of 2 are depicted in Figure S7. In this case, steady-state CO conversion reaches equilibrium for mode D and E and similar trends regarding CO₂ adsorption were observed.

4. Conclusions

A SEWGS system providing CO₂-free synthesis gas for the production of carbon neutral jet fuel in a PtL process starting from CO₂ splitting into CO and O₂ in a plasma source was investigated. The SEWGS fixed bed reactor contained a mixture of catalyst and sorbent particles to carry out WGS reaction and CO₂ adsorption simultaneously. This experimental study provided catalyst and sorbent characteristics, insight into the influence of various SEWGS operation conditions, and results on the CO₂ uptake of five different reactor configurations.

Activity tests with a commercial Cu/ZnO/Al₂O₃ catalyst, a reaction temperature of 250 °C and modified residence times around 2×10^{-5} g·h/mL were set. The HTdc sample calcined only once after 20 wt% potassium impregnation (MG70-K-400) from HTC starting

material possessed the best sorption capacity and was chosen for the SEWGS parameter study.

In automated cyclic adsorption and desorption breakthrough experiments in the isothermal PBMR, the influence of adsorption pressure, adsorption feed composition, desorption conditions and reactor configuration on breakthrough delay and adsorbed amount of CO₂ was studied. A constant cyclic working capacity was reached after an initial drop between the first and the second adsorption cycle. This effect was mainly attributed to bulk carbonate formation and incomplete sorbent regeneration due to much slower desorption kinetics.

In accordance to the proposed adsorption isotherm models [58], an increase in pressure led to higher amounts of adsorbed CO₂. The amount of water available during the adsorption phase was found to be crucial. Up to around 20% steam content in the feed, the sorption properties were enhanced. At 40% steam, a contradictory effect was observed, which was related to H₂O and CO₂ competing for adsorption sites. A total increase in CO₂ flux reduced the breakthrough time at certain conditions but the right choice of some excess steam could counteract this effect or at least increase the amount of CO₂ adsorbed. Variations in desorption conditions revealed that the desorption process exhibited low sorption kinetics and could also be improved with steam. High feed loading with steam in the desorption process and long desorption times helped to increase the amount of CO₂ adsorbed during the following adsorption phase. The significance of water during adsorption, as well as desorption, confirmed the existence of different adsorption sites.

Several catalyst and sorbent packing concepts with varying catalyst weight fraction and zone distribution suggested that the length of the catalyst-free zone at the outlet was a main influencing factor on the cyclic sorption capacity. As the SEWGS tests were performed at significantly lower modified residence times than those previously reported [31–33], it was shown for the first time that the interaction of relatively fast reaction and relatively slow adsorption kinetics seem to play a key role in the SEWGS process design.

In general, the results suggest that the investigated SEWGS concept is a promising option to provide synthesis gas for carbon neutral jet fuel production in the Kerogreen process. Improving the sorption capacity of HTdcs would result in longer breakthrough times, so this is recommended for further study.

Supplementary Materials: The following are available online at <https://www.mdpi.com/1996-1073/14/2/355/s1>. Figure S1. SE image of (a) untreated sample (MG70) ($\times 100$), (b) impregnated—calcined sample (MG70-K-400) ($\times 100$), (c) untreated sample (MG70) ($\times 1000$), and (d) impregnated—calcined sample (MG70-K-400) ($\times 1000$). Figure S2. BSE image ($\times 500$) of pressed powder (a) calcined—impregnated sample (MG70-400-K), (b) impregnated—calcined sample (MG70-K-400), and (c) calcined—impregnated—calcined sample (MG70-400-K-400). Figure S3. Probe positions marked for EDS analysis of pressed powder (a) untreated sample (MG70), (b) calcined sample (MG70-400), (c) impregnated—calcined sample (MG70-K-400), (d) calcined—impregnated sample (MG70-400-K), and (e) calcined—impregnated—calcined sample (MG70-400-K-400). Results are listed in Table S2. Figure S4. Adsorption cycle average (a) CO conversion, (b) breakthrough delay, and (c) adsorbed amount of CO₂ for reproduced experiments after different sorbent histories. Adsorption: 15 min, 8 bar, 2000 mL/min, 2.5% CO, S/G = 4. Desorption: 40 min, 1 bar, 1000 mL/min, 40% H₂O. PBMR, Mode B, 250 °C. Figure S5. Adsorption cycle average (a) CO conversion, (b) breakthrough delay, and (c) adsorbed amount of CO₂ for reproduced experiments after comparable sorbent histories. Adsorption: 15 min, 8 bar, 2000 mL/min, 2.5% CO, S/G = 4. Desorption: 40 min, 1 bar, 1000 mL/min, 40% H₂O. PBMR, Mode C, 250 °C. Figure S6. Adsorption cycle average (a) CO conversion, (b) breakthrough delay, and (c) adsorbed amount of CO₂. Adsorption: 15 min, 2000 mL/min, 2.5% CO, S/G = 4. Desorption: 40 min, 1 bar, 1000 mL/min, 40% H₂O. PBMR, Mode C, 250 °C. Figure S7. Adsorption cycle average (a) CO conversion, and (b) adsorbed amount of CO₂. Adsorption: 15 min, 8 bar, 2000 mL/min, 10% CO, S/G = 2. Desorption: 40 min, 1 bar, 1000 mL/min, 40% H₂O. PBMR, 250 °C. Table S1. BET surface area, BJH average pore width and cumulative pore volume. Table S2. EDS results: Mg/Al ratio (average) and potassium content (probe positions in Figure S3). Table S3. Freundlich equation (Equation (S2)) parameters kF and n , and fitting parameter $R2$.

Author Contributions: Conceptualization, T.J.S. and P.P.; methodology, T.J.S.; software, T.J.S.; validation, T.J.S. and P.P.; formal analysis, P.B., J.K., R.S., T.K., and T.J.S.; investigation, P.B., J.K., R.S., T.K., and T.J.S.; resources, T.J.S. and P.P.; data curation, T.J.S.; writing—original draft preparation, T.J.S.; writing—review and editing, J.K., and P.P.; visualization, T.J.S.; supervision, P.P.; project administration, P.P.; funding acquisition, P.P. All authors have read and agreed to the published version of the manuscript.

Funding: The work presented in this paper is part of the European project Kerogreen, which has received funding from the European Union’s Horizon 2020 research and innovation programme under grant agreement no. 763909.

Institutional Review Board Statement: Not applicable.

Informed Consent Statement: Not applicable.

Data Availability Statement: Not applicable.

Acknowledgments: The authors gratefully acknowledge the donation of sorbent material from Sasol GmbH. The authors acknowledge support by the KIT-Publication Fund of the Karlsruhe Institute of Technology. The authors would like to thank Uta Gerhards and Florian Messerschmidt (KIT, IMVT) for EPMA, Christina Odemer (KIT, IAM) for TGA, and Peter G. Weidler (KIT, IFG) for XRD analysis. The authors kindly acknowledge the experimental support of Adrian da Silva Moreira and Jan Speck. Many thanks go to our colleagues Cornelia Schorle (technical support) and Paul Kant (electrical support).

Conflicts of Interest: The authors declare no conflict of interest.

List of Abbreviations

BET	Brunauer-Emmett-Teller
BJH	Barrett-Joyner-Halenda
BSE	Back-scattered electrons
EDS	Energy dispersive spectroscopy
EPMA	Electron probe micro analysis
Eq.	Equation
FID	Flame ionization detector
FT	Fischer-Tropsch
GC	Gas chromatograph
HTC	Hydrotalcite
HTdc	Hydrotalcite-derived compounds
LFC	Liquid flow controller
MFC	Mass flow controller
NDIR	Nondispersive infrared detector
PBMR	Packed bed microchannel reactor
PDF	Powder diffraction file
PGA	Process gas analyzer
PtL	Power-to-Liquid
S/G	Steam-to-gas ratio
SE	Secondary electrons
SEWGS	Sorption-enhanced water-gas shift
TCD	Thermal conductivity detector
TGA	Thermogravimetric analysis
TR	Tubular reactor
WGS	Water-gas shift
XRD	X-ray diffraction

List of Symbols

ΔH_R^0	Reaction enthalpy	kJ/mol
K_{eq}	Equilibrium constant	-
k_F	Freundlich constant	mmol/g·bar ^{1/n}
m	Mass	g
n_{ads}	Specific amount of CO ₂ adsorbed	mmol/g
\dot{n}	Molar flow	mol/s
n	Adsorption intensity	-
p	Pressure	bar
R	Ideal gas constant	J/mol·K
r	Reaction rate	mol/g·h
τ_{mod}	Modified residence time	g·h/mL
T	Temperature	K
t	Time	s
\dot{V}	Volume flow	mL/min
w	Weight fraction	-
X_{CO}	CO conversion	-
y	Volume fraction	-

List of Indices

0	Feed
ads	Adsorption/adsorbed
cat	Catalyst
des	Desorption
dry	After condensation
sorb	Sorbent

References

- United Nations. Paris Agreement. Available online: <https://unfccc.int/process-and-meetings> (accessed on 17 November 2020).
- European Commission. A European Strategy for Low-Emission Mobility. Available online: <https://eur-lex.europa.eu/legal-content/en/TXT/?uri=CELEX:52016DC0501> (accessed on 17 November 2020).
- Goede, A.P.H. CO₂ neutral fuels. *EPJ Web Conf.* **2018**, *189*, 10. [CrossRef]
- Viegas, P.; Vialetto, L.; Wolf, A.J.; Peeters, F.J.J.; Groen, P.W.C.; Righart, T.W.H.; Bongers, W.A.; van de Sanden, M.C.M.; Diomede, P. Insight into contraction dynamics of microwave plasmas for CO₂ conversion from plasma chemistry modelling. *Plasma Sources Sci. Technol.* **2020**, *29*, 105014. [CrossRef]
- Soldatov, S.; Link, G.; Silberer, L.; Schmedt, C.M.; Carbone, E.; D'Isa, F.; Jelonnek, J.; Dittmeyer, R.; Navarrete, A. Time-Resolved Optical Emission Spectroscopy Reveals Nonequilibrium Conditions for CO₂ Splitting in Atmospheric Plasma Sustained with Ultrafast Microwave Pulsation. *ACS Energy Lett.* **2020**, *11*, 124–130. [CrossRef]
- Kirsch, H.; Brübach, L.; Loewert, M.; Riedinger, M.; Gräfenhahn, A.; Böltken, T.; Klumpp, M.; Pfeifer, P.; Dittmeyer, R. CO₂-neutrale Fischer-Tropsch-Kraftstoffe aus dezentralen modularen Anlagen: Status und Perspektiven. *Chem. Ing. Tech.* **2020**, *92*, 91–99. [CrossRef]
- Ramirez, A.; Sarathy, S.M.; Gascon, J. CO₂ Derived E-Fuels: Research Trends, Misconceptions, and Future Directions. *Trends Chem.* **2020**, *2*, 785–795. [CrossRef]
- Soria, M.A.; Tosti, S.; Mendes, A.; Madeira, L.M. Enhancing the low temperature water–gas shift reaction through a hybrid sorption-enhanced membrane reactor for high-purity hydrogen production. *Fuel* **2015**, *159*, 854–863. [CrossRef]
- Jang, H.M.; Lee, K.B.; Caram, H.S.; Sircar, S. High-purity hydrogen production through sorption enhanced water gas shift reaction using K₂CO₃-promoted hydrotalcite. *Chem. Eng. Sci.* **2012**, *73*, 431–438. [CrossRef]
- Moe, J.M. Design of water-gas shift reactors. *Chem. Eng. Prog.* **1962**, *58*, 3.
- Mendes, D.; Mendes, A.; Madeira, L.M.; Iulianelli, A.; Sousa, J.M.; Basile, A. The water-gas shift reaction: From conventional catalytic systems to Pd-based membrane reactors—A review. *Asia Pac. J. Chem. Eng.* **2010**, *5*, 111–137. [CrossRef]
- Smith, R.J.B.; Loganathan, M.; Shantha, M.S. A Review of the Water Gas Shift Reaction Kinetics. *Int. J. Chem. React. Eng.* **2010**, *8*, 8. [CrossRef]
- Choi, Y.; Stenger, H.G. Water gas shift reaction kinetics and reactor modeling for fuel cell grade hydrogen. *J. Power Sources* **2003**, *124*, 432–439. [CrossRef]

14. Wang, S.; Shen, H.; Fan, S.; Zhao, Y.; Ma, X.; Gong, J. Enhanced CO₂ adsorption capacity and stability using CaO-based adsorbents treated by hydration. *AIChE J.* **2013**, *59*, 3586–3593. [[CrossRef](#)]
15. Bhagiyalakshmi, M.; Lee, J.Y.; Jang, H.T. Synthesis of mesoporous magnesium oxide: Its application to CO₂ chemisorption. *Int. J. Greenh. Gas Control* **2010**, *4*, 51–56. [[CrossRef](#)]
16. Iwan, A.; Stephenson, H.; Ketchie, W.C.; Lapkin, A.A. High temperature sequestration of CO₂ using lithium zirconates. *Chem. Eng. J.* **2009**, *146*, 249–258. [[CrossRef](#)]
17. Hu, Y.; Liu, W.; Yang, Y.; Qu, M.; Li, H. CO₂ capture by Li₄SiO₄ sorbents and their applications: Current developments and new trends. *Chem. Eng. J.* **2019**, *359*, 604–625. [[CrossRef](#)]
18. Yin, G.; Liu, Z.; Liu, Q.; Wu, W. The role of different properties of activated carbon in CO₂ adsorption. *Chem. Eng. J.* **2013**, *230*, 133–140. [[CrossRef](#)]
19. Siriwardane, R.V.; Shen, M.-S.; Fisher, E.P.; Poston, J.A. Adsorption of CO₂ on Molecular Sieves and Activated Carbon. *Energy Fuels* **2001**, *15*, 279–284. [[CrossRef](#)]
20. Mulloth, L.M.; Finn, J.E. *Carbon Dioxide Adsorption on a 5A Zeolite Designed for CO₂ Removal in Spacecraft Cabins*; NASA/TM-1998-208752; NASA: Washington, DC, USA, 1998.
21. Millward, A.R.; Yaghi, O.M. Metal-organic frameworks with exceptionally high capacity for storage of carbon dioxide at room temperature. *J. Am. Chem. Soc.* **2005**, *127*, 17998–17999. [[CrossRef](#)]
22. Reijers, H.T.J.; Boon, J.; Elzinga, G.D.; Cobden, P.D.; Haije, W.G.; van den Brink, R.W. Modeling Study of the Sorption-Enhanced Reaction Process for CO₂ Capture. I. Model Development and Validation. *Ind. Eng. Chem. Res.* **2009**, *48*, 6966–6974. [[CrossRef](#)]
23. Van Selow, E.R.; Cobden, P.D.; Wright, A.D.; van den Brink, R.W.; Jansen, D. Improved sorbent for the sorption-enhanced water-gas shift process. *Energy Procedia* **2011**, *4*, 1090–1095. [[CrossRef](#)]
24. Rives, V. Characterisation of layered double hydroxides and their decomposition products. *Mater. Chem. Phys.* **2002**, *75*, 19–25. [[CrossRef](#)]
25. León, M.; Díaz, E.; Bennici, S.; Vega, A.; Ordóñez, S.; Auroux, A. Adsorption of CO₂ on Hydrotalcite-Derived Mixed Oxides: Sorption Mechanisms and Consequences for Adsorption Irreversibility. *Ind. Eng. Chem. Res.* **2010**, *49*, 3663–3671. [[CrossRef](#)]
26. Yong, Z.; Mata, A.V.; Rodrigues, A.E. Adsorption of Carbon Dioxide onto Hydrotalcite-like Compounds (HTLcs) at High Temperatures. *Ind. Eng. Chem. Res.* **2001**, *40*, 204–209. [[CrossRef](#)]
27. Zhu, X.; Shi, Y.; Cai, N. High-pressure carbon dioxide adsorption kinetics of potassium-modified hydrotalcite at elevated temperature. *Fuel* **2017**, *207*, 579–590. [[CrossRef](#)]
28. Lee, J.M.; Min, Y.J.; Lee, K.B.; Jeon, S.G.; Na, J.G.; Ryu, H.J. Enhancement of CO₂ sorption uptake on hydrotalcite by impregnation with K₂CO₃. *Langmuir* **2010**, *26*, 18788–18797. [[CrossRef](#)] [[PubMed](#)]
29. Du, H.; Williams, C.T.; Ebner, A.D.; Ritter, J.A. In Situ FTIR Spectroscopic Analysis of Carbonate Transformations during Adsorption and Desorption of CO₂ in K-Promoted HTlc. *Chem. Mater.* **2010**, *22*, 3519–3526. [[CrossRef](#)]
30. Belimov, M.; Metzger, D.; Pfeifer, P. On the temperature control in a microstructured packed bed reactor for methanation of CO/CO₂ mixtures. *AIChE J.* **2017**, *63*, 120–129. [[CrossRef](#)]
31. Lee, C.H.; Lee, K.B. Application of one-body hybrid solid pellets to sorption-enhanced water gas shift reaction for high-purity hydrogen production. *Int. J. Hydrog. Energy* **2014**, *39*, 18128–18134. [[CrossRef](#)]
32. Lee, C.H.; Lee, K.B. Sorption-enhanced water gas shift reaction for high-purity hydrogen production: Application of a Na-Mg double salt-based sorbent and the divided section packing concept. *Appl. Energy* **2017**, *205*, 316–322. [[CrossRef](#)]
33. Hu, Y.; Cui, H.; Cheng, Z.; Zhou, Z. Sorption-enhanced water gas shift reaction by in situ CO₂ capture on an alkali metal salt-promoted MgO-CaCO₃ sorbent. *Chem. Eng. J.* **2019**, *377*, 119823. [[CrossRef](#)]
34. Othman, M.R.; Helwani, Z.; Martunus; Fernando, W.J.N. Synthetic hydrotalcites from different routes and their application as catalysts and gas adsorbents: A review. *Appl. Organometal. Chem.* **2009**, *23*, 335–346. [[CrossRef](#)]
35. Reijers, H.T.J.; Valster-Schiermeier, S.E.A.; Cobden, P.D.; van den Brink, R.W. Hydrotalcite as CO₂ Sorbent for Sorption-Enhanced Steam Reforming of Methane. *Ind. Eng. Chem. Res.* **2006**, *45*, 2522–2530. [[CrossRef](#)]
36. Yang, J.-I.; Kim, J.-N. Hydrotalcites for adsorption of CO₂ at high temperature. *Korean J. Chem. Eng.* **2006**, *23*, 77–80. [[CrossRef](#)]
37. Carriazo, D.; del Arco, M.; Martín, C.; Rives, V. A comparative study between chloride and calcined carbonate hydrotalcites as adsorbents for Cr(VI). *Appl. Clay Sci.* **2007**, *37*, 231–239. [[CrossRef](#)]
38. Ram Reddy, M.K.; Xu, Z.P.; Lu, G.Q.; da Costa, J.C.D. Layered Double Hydroxides for CO₂ Capture: Structure Evolution and Regeneration. *Ind. Eng. Chem. Res.* **2006**, *45*, 7504–7509. [[CrossRef](#)]
39. Pérez-Ramírez, J.; Abelló, S.; van der Pers, N.M. Memory effect of activated Mg-Al hydrotalcite: In situ XRD studies during decomposition and gas-phase reconstruction. *Chemistry* **2007**, *13*, 870–878. [[CrossRef](#)]
40. Yang, W.; Kim, Y.; Liu, P.K.; Sahimi, M.; Tsotsis, T.T. A study by in situ techniques of the thermal evolution of the structure of a Mg-Al-CO₃ layered double hydroxide. *Chem. Eng. Sci.* **2002**, *57*, 2945–2953. [[CrossRef](#)]
41. Iruretagoyena Ferrer, D. *Supported Layered Double Hydroxides as CO₂ Adsorbents for Sorption-Enhanced H₂ Production*; Springer International Publishing: Cham, Switzerland, 2016; ISBN 9783319412764.
42. Thommes, M.; Kaneko, K.; Neimark, A.V.; Olivier, J.P.; Rodriguez-Reinoso, F.; Rouquerol, J.; Sing, K.S. Physisorption of gases, with special reference to the evaluation of surface area and pore size distribution (IUPAC Technical Report). *Pure Appl. Chem.* **2015**, *87*, 1051–1069. [[CrossRef](#)]

43. Rocha, C.; Soria, M.A.; Madeira, L.M. Doping of hydrotalcite-based sorbents with different interlayer anions for CO₂ capture. *Sep. Purif. Technol.* **2020**, *235*, 116140. [[CrossRef](#)]
44. Halabi, M.H.; de Croon, M.; van der Schaaf, J.; Cobden, P.D.; Schouten, J.C. High capacity potassium-promoted hydrotalcite for CO₂ capture in H₂ production. *Int. J. Hydrogen Energy* **2012**, *37*, 4516–4525. [[CrossRef](#)]
45. Hanif, A.; Dasgupta, S.; Divekar, S.; Arya, A.; Garg, M.O.; Nanoti, A. A study on high temperature CO₂ capture by improved hydrotalcite sorbents. *Chem. Eng. J.* **2014**, *236*, 91–99. [[CrossRef](#)]
46. Oliveira, E.L.; Grande, C.A.; Rodrigues, A.E. CO₂ sorption on hydrotalcite and alkali-modified (K and Cs) hydrotalcites at high temperatures. *Sep. Purif. Technol.* **2008**, *62*, 137–147. [[CrossRef](#)]
47. Miguel, C.V.; Trujillano, R.; Rives, V.; Vicente, M.A.; Ferreira, A.; Rodrigues, A.E.; Mendes, A.; Madeira, L.M. High temperature CO₂ sorption with gallium-substituted and promoted hydrotalcites. *Sep. Purif. Technol.* **2014**, *127*, 202–211. [[CrossRef](#)]
48. Ebner, A.D.; Reynolds, S.P.; Ritter, J.A. Understanding the Adsorption and Desorption Behavior of CO₂ on a K-Promoted Hydrotalcite-like Compound (HTlc) through Nonequilibrium Dynamic Isotherms. *Ind. Eng. Chem. Res.* **2006**, *45*, 6387–6392. [[CrossRef](#)]
49. Soares, J.; Casarin, G.L.; José, H.J.; Moreira, R.D.F.P.M.; Rodrigues, A.E. Experimental and Theoretical Analysis for the CO₂ Adsorption on Hydrotalcite. *Adsorption* **2005**, *11*, 237–241. [[CrossRef](#)]
50. Silva, J.M.; Trujillano, R.; Rives, V.; Soria, M.A.; Madeira, L.M. High temperature CO₂ sorption over modified hydrotalcites. *Chem. Eng. J.* **2017**, *325*, 25–34. [[CrossRef](#)]
51. Coenen, K.; Gallucci, F.; Hensen, E.; van Sint Annaland, M. Kinetic model for adsorption and desorption of H₂O and CO₂ on hydrotalcite-based adsorbents. *Chem. Eng. J.* **2019**, *355*, 520–531. [[CrossRef](#)]
52. Walspurger, S.; Boels, L.; Cobden, P.D.; Elzinga, G.D.; Haije, W.G.; van den Brink, R.W. The crucial role of the K⁺-aluminium oxide interaction in K⁺-promoted alumina- and hydrotalcite-based materials for CO₂ sorption at high temperatures. *ChemSusChem* **2008**, *1*, 643–650. [[CrossRef](#)]
53. Walspurger, S.; Cobden, P.D.; Safonova, O.V.; Wu, Y.; Anthony, E.J. High CO₂ storage capacity in alkali-promoted hydrotalcite-based material: In situ detection of reversible formation of magnesium carbonate. *Chemistry* **2010**, *16*, 12694–12700. [[CrossRef](#)]
54. Meis, N.N.A.H.; Bitter, J.H.; de Jong, K.P. On the Influence and Role of Alkali Metals on Supported and Unsupported Activated Hydrotalcites for CO₂ Sorption. *Ind. Eng. Chem. Res.* **2010**, *49*, 8086–8093. [[CrossRef](#)]
55. Hutson, N.D.; Attwood, B.C. High temperature adsorption of CO₂ on various hydrotalcite-like compounds. *Adsorption* **2008**, *14*, 781–789. [[CrossRef](#)]
56. Ebner, A.D.; Reynolds, S.P.; Ritter, J.A. Nonequilibrium Kinetic Model That Describes the Reversible Adsorption and Desorption Behavior of CO₂ in a K-Promoted Hydrotalcite-like Compound. *Ind. Eng. Chem. Res.* **2007**, *46*, 1737–1744. [[CrossRef](#)]
57. Coenen, K.; Gallucci, F.; Cobden, P.; van Dijk, E.; Hensen, E.; van Sint Annaland, M. Chemisorption working capacity and kinetics of CO₂ and H₂O of hydrotalcite-based adsorbents for sorption-enhanced water-gas-shift applications. *Chem. Eng. J.* **2016**, *293*, 9–23. [[CrossRef](#)]
58. Boon, J.; Cobden, P.D.; van Dijk, H.; Hoogland, C.; van Selow, E.R.; van Sint Annaland, M. Isotherm model for high-temperature, high-pressure adsorption of and on K-promoted hydrotalcite. *Chem. Eng. J.* **2014**, *248*, 406–414. [[CrossRef](#)]
59. Lee, K.B.; Verdooren, A.; Caram, H.S.; Sircar, S. Chemisorption of carbon dioxide on potassium-carbonate-promoted hydrotalcite. *J. Colloid Interface Sci.* **2007**, *308*, 30–39. [[CrossRef](#)]
60. Ram Reddy, M.K.; Xu, Z.P.; Diniz da Costa, J.C. Influence of Water on High-Temperature CO₂ Capture Using Layered Double Hydroxide Derivatives. *Ind. Eng. Chem. Res.* **2008**, *47*, 2630–2635. [[CrossRef](#)]
61. Soria, M.A.; Rocha, C.; Tosti, S.; Mendes, A.; Madeira, L.M. CO_x free hydrogen production through water-gas shift reaction in different hybrid multifunctional reactors. *Chem. Eng. J.* **2019**, *356*, 727–736. [[CrossRef](#)]
62. Coenen, K.; Gallucci, F.; Pio, G.; Cobden, P.; van Dijk, E.; Hensen, E.; van Sint Annaland, M. On the influence of steam on the CO₂ chemisorption capacity of a hydrotalcite-based adsorbent for SEWGS applications. *Chem. Eng. J.* **2017**, *314*, 554–569. [[CrossRef](#)]
63. Coenen, K.; Gallucci, F.; Hensen, E.; van Sint Annaland, M. CO₂ and H₂O chemisorption mechanism on different potassium-promoted sorbents for SEWGS processes. *J. CO₂ Util.* **2018**, *25*, 180–193. [[CrossRef](#)]
64. Wu, Y.-J.; Li, P.; Yu, J.-G.; Cunha, A.F.; Rodrigues, A.E. K-Promoted Hydrotalcites for CO₂ Capture in Sorption Enhanced Reactions. *Chem. Eng. Technol.* **2013**, *36*, 567–574. [[CrossRef](#)]
65. Jang, H.M.; Kang, W.R.; Lee, K.B. Sorption-enhanced water gas shift reaction using multi-section column for high-purity hydrogen production. *Int. J. Hydrog. Energy* **2013**, *38*, 6065–6071. [[CrossRef](#)]

Supplementary Materials

Supplement to 3.1. Catalyst performance

WGS rate equation acc. to Choi et al. with reaction rate r_{CO} in mol/(g·h), temperature T in K, pressure p in atm, and equilibrium constant K_{eq} calculated from Eq. (2).

$$r_{CO} = 2.96 \cdot 10^5 \cdot \exp\left(-\frac{47400}{R \cdot T}\right) \cdot \left(p_{H_2O} \cdot p_{CO} - \frac{p_{CO_2} \cdot p_{H_2}}{K_{eq}}\right) \quad (S1)$$

Supplement to 3.2. Structural properties and CO₂ capture performance of sorbent

Table S1. BET surface area, BJH average pore width and cumulative pore volume.

Sample	surface area / m ² /g	pore width / nm	pore volume / cm ³ /g
MG70-400	170	3.95	0.123
MG70-K-400	9	12.50	0.027
MG70-400-K-400	18	9.50	0.042

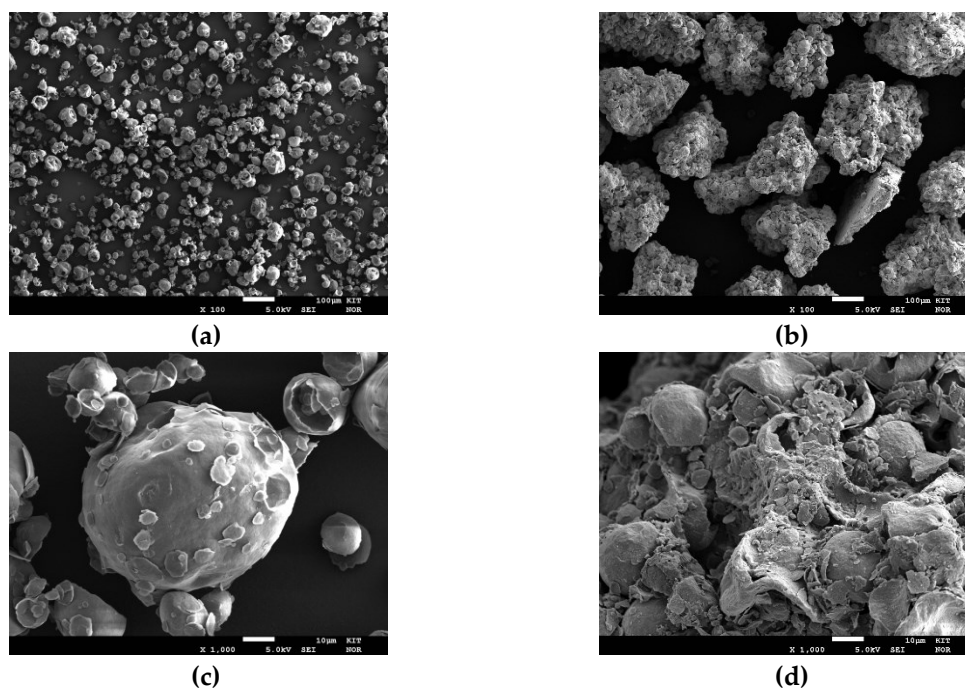


Figure S1. SE image of (a) untreated sample (MG70) (x100), (b) impregnated – calcined sample (MG70-K-400) (x100), (c) untreated sample (MG70) (x1000), and (d) impregnated – calcined sample (MG70-K-400) (x1000).

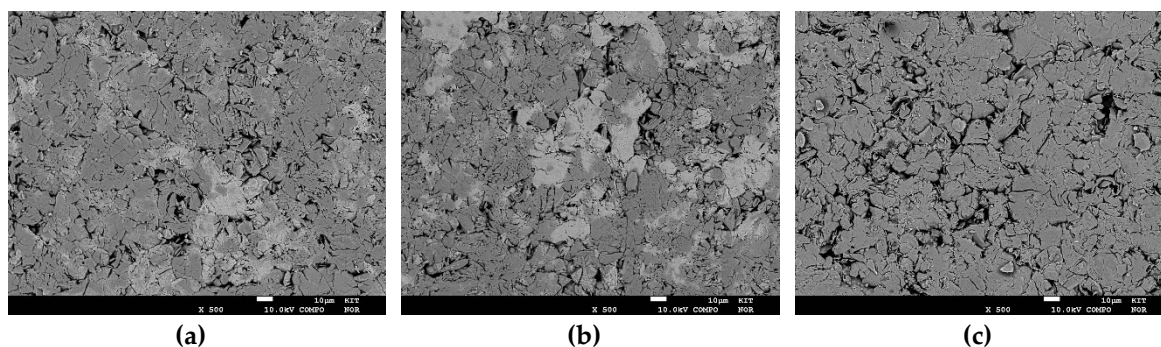


Figure S2. BSE image (x500) of pressed powder (a) calcined – impregnated sample (MG70-400-K), (b) impregnated – calcined sample (MG70-K-400), and (c) calcined – impregnated – calcined sample (MG70-400-K-400).

Table S2. EDS results: Mg/Al ratio (average) and potassium content (probe positions in Figure S3).

Sample	Mg/Al / -	K 1 / wt%	K 2 / wt%	K 3 / wt%	K 4 / wt%
MG70	3.05 ± 0.05	-	-	-	-
MG70-400	3.10 ± 0.01	-	-	-	-
MG70-K-400	3.64 ± 0.54	6.55	2.95	23.97	23.14
MG70-400-K	3.21 ± 0.08	37.81	35.02	6.10	9.71
MG70-400-K-400	3.12 ± 0.02	6.89	3.19	6.55	

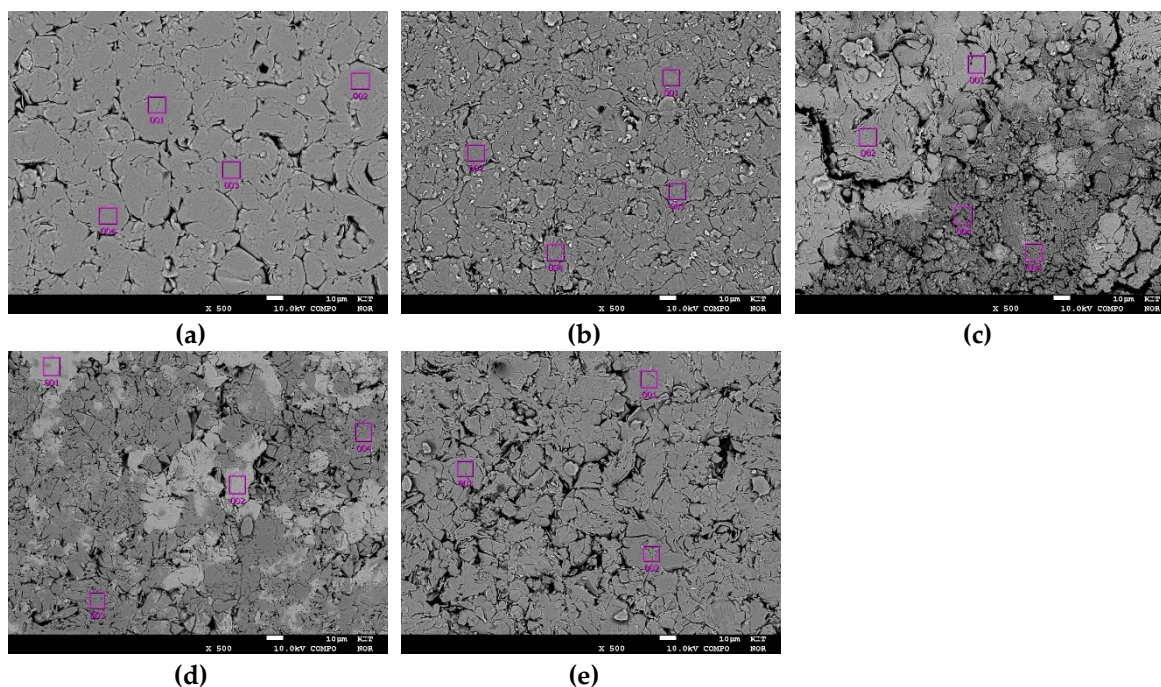


Figure S3. Probe positions marked for EDS analysis of pressed powder (a) untreated sample (MG70), (b) calcined sample (MG70-400), (c) impregnated – calcined sample (MG70-K-400), (d) calcined – impregnated sample (MG70-400-K), and (e) calcined – impregnated – calcined sample (MG70-400-K-400). Results are listed in Table S2.

Table S3. Freundlich equation (Eq. (S2)) parameters k_F and n , and fitting parameter R^2 .

Sample	k_F / mmol/(g·bar ^{1/n})	n / -	R^2 / -
MG70-250	0.008	4.687	0.966
MG70-400	0.071	5.280	0.984
MG70-500	0.022	4.399	0.985
MG70-K-400	0.174	9.512	0.970
MG70-400-K-400	0.141	8.924	0.967

Freundlich model equation for CO₂ adsorption isotherm with n_{ads} being the specific amount of moles CO₂ adsorbed in mmol/g, Freundlich constant k_F in mmol/(g·bar^{1/n}), partial pressure of CO₂ p_{CO_2} in bar, and adsorption intensity n .

$$n_{ads} = k_F \cdot p_{CO_2}^{1/n} \quad (S2)$$

Supplement to 3.3 SEWGS performance

Supplement to 3.3.2 Long term stability

The sorbent in Figure S4 has seen a higher water content (in other experiments at different conditions) between the reproduced experiments (II and III), what resumed in an increase in both, breakthrough time and sorption capacity. This might be due to adsorption site activation caused by steam, see section 3.3.3 and 3.3.4. However, the sorbent in the example depicted in Figure S5 had a comparable time on stream but was not exposed to different conditions between the repetitions, and no noteworthy difference in breakthrough delay or in adsorbed CO₂ could be detected.

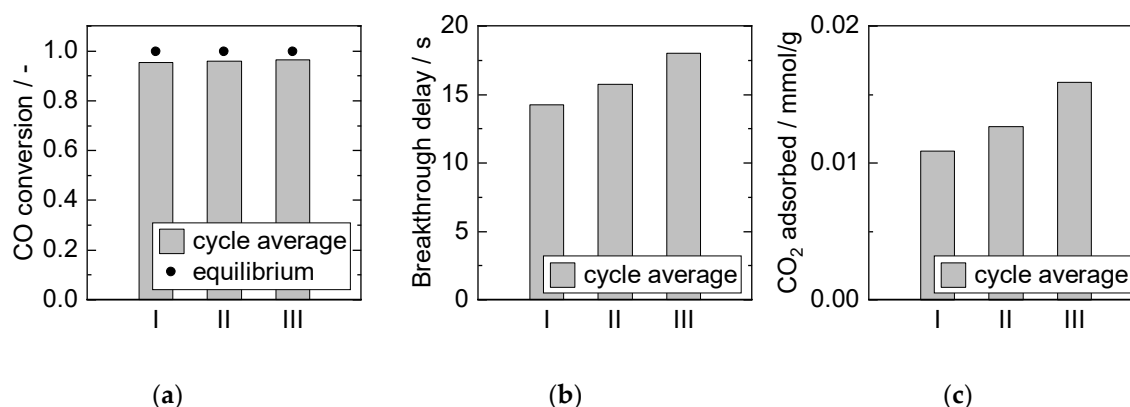


Figure S4. Adsorption cycle average (a) CO conversion, (b) breakthrough delay, and (c) adsorbed amount of CO₂ for reproduced experiments after different sorbent “histories”. Adsorption: 15 min, 8 bar, 2000 ml/min, 2.5 % CO, S/G = 4. Desorption: 40 min, 1 bar, 1000 ml/min, 40 % H₂O. PBMR, Mode B, 250 °C.

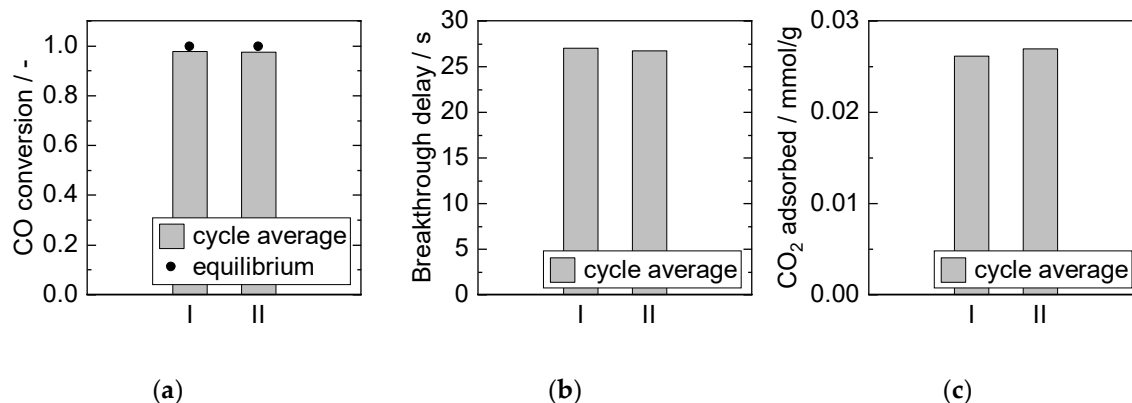


Figure S5. Adsorption cycle average (a) CO conversion, (b) breakthrough delay, and (c) adsorbed amount of CO₂ for reproduced experiments after comparable sorbent “histories”. Adsorption: 15 min, 8 bar, 2000 ml/min, 2.5 % CO, S/G = 4. Desorption: 40 min, 1 bar, 1000 ml/min, 40 % H₂O. PBMR, Mode C, 250 °C.

Supplement to 3.3.3 Variation of adsorption parameters

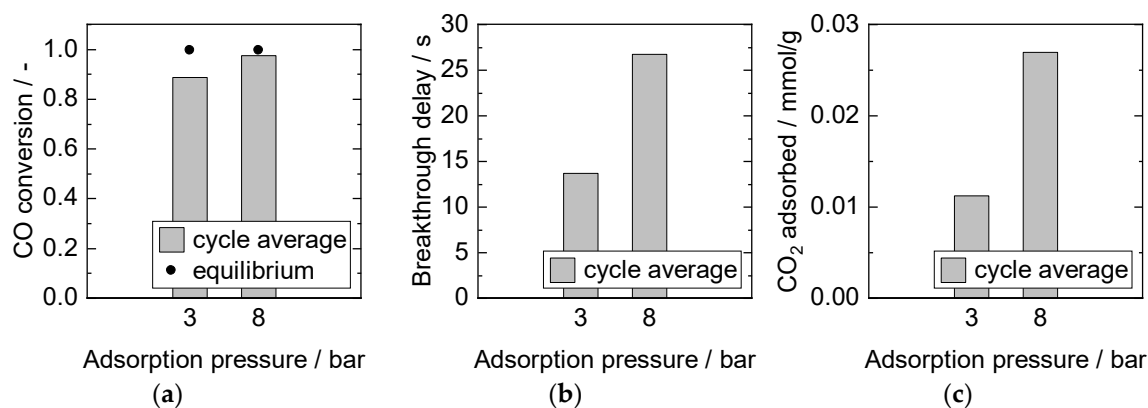


Figure S6. Adsorption cycle average (a) CO conversion, (b) breakthrough delay, and (c) adsorbed amount of CO₂. Adsorption: 15 min, 2000 ml/min, 2.5 % CO, S/G = 4. Desorption: 40 min, 1 bar, 1000 ml/min, 40 % H₂O. PBMR, Mode C, 250 °C.

Supplement to 3.3.5 Variation of reactor configuration

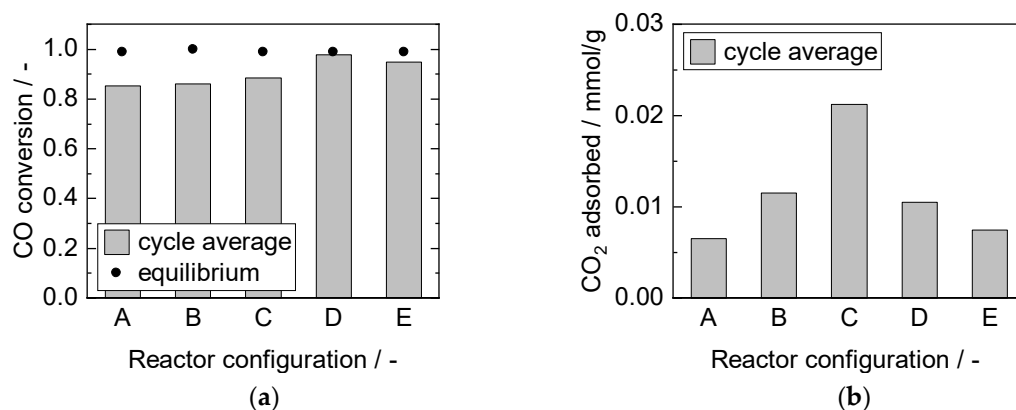


Figure S7. Adsorption cycle average (a) CO conversion, and (b) adsorbed amount of CO₂. Adsorption: 15 min, 8 bar, 2000 ml/min, 10 % CO, S/G = 2. Desorption: 40 min, 1 bar, 1000 ml/min, 40 % H₂O. PBMR, 250 °C.

P II Numerical Simulation Approaches

Numerical Simulation Approach for a Dynamically Operated Sorption-Enhanced Water-Gas Shift Reactor



Published in Processes 2022, 10, 1160

Publishing Date 9 June 2022

DOI <https://doi.org/10.3390/pr100611605>

Article

Numerical Simulation Approach for a Dynamically Operated Sorption-Enhanced Water-Gas Shift Reactor

Tabea J. Stadler ¹, Jan-Hendrik Knoop ¹, Simon Decker ² and Peter Pfeifer ^{1,*}

¹ Institute for Micro Process Engineering (IMVT), Karlsruhe Institute of Technology (KIT), Hermann-von-Helmholtz-Platz 1, 76344 Eggenstein-Leopoldshafen, Germany

² Elektrotechnisches Institut (ETI), Karlsruhe Institute of Technology (KIT), Kaiserstr. 12, 76131 Karlsruhe, Germany

* Correspondence: peter.pfeifer@kit.edu

Abstract: A dynamically operated sorption-enhanced water–gas shift reactor is modelled to leverage its performance by means of model-based process design. This reactor shall provide CO₂-free synthesis gas for e-fuel production from pure CO. The nonlinear model equations describing simultaneous adsorption and reaction are solved with three numerical approaches in MATLAB: a built-in solver for partial differential equations, a semi-discretization method in combination with an ordinary differential equation solver, and an advanced graphic implementation of the latter method in Simulink. The novel implementation in Simulink offers various advantages for dynamic simulations and is expanded to a process model with six reaction chambers. The continuous conditions in the reaction chambers and the discrete states of the valves, which enable switching between reactive adsorption and regeneration, lead to a hybrid system. Controlling the discrete states in a finite-state machine in Stateflow enables automated switching between reactive adsorption and regeneration depending on predefined conditions, such as a time span or a concentration threshold in the product gas. The established chemical reactor simulation approach features unique possibilities in terms of simulation-driven development of operating procedures for intensified reactor operation. In a base case simulation, the sorbent usage for serial operation with adjusted switching times is increased by almost 15%.

Keywords: sorption-enhanced water–gas shift (SEWGS); reactor modeling; nonlinear hybrid dynamic system simulation; method-of-lines (MoL); pdepe solver; MATLAB Simulink Stateflow



Citation: Stadler, T.J.; Knoop, J.-H.; Decker, S.; Pfeifer, P. Numerical Simulation Approach for a Dynamically Operated Sorption-Enhanced Water-Gas Shift Reactor. *Processes* **2022**, *10*, 1160. <https://doi.org/10.3390/pr10061160>

Academic Editors: Liming Dai and Jialin Tian

Received: 19 May 2022

Accepted: 7 June 2022

Published: 9 June 2022

Publisher's Note: MDPI stays neutral with regard to jurisdictional claims in published maps and institutional affiliations.



Copyright: © 2022 by the authors. Licensee MDPI, Basel, Switzerland. This article is an open access article distributed under the terms and conditions of the Creative Commons Attribution (CC BY) license (<https://creativecommons.org/licenses/by/4.0/>).

1. Introduction

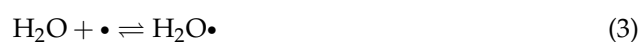
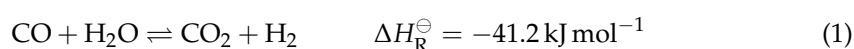
In November 2021, the participants of the Conference of the Parties COP26 in Glasgow agreed on a stronger commitment to the aims set in the Paris Agreement back in 2015: reducing the limitation of global warming to 1.5 °C [1,2]. To reach this ambitious goal, anthropogenic greenhouse gas emissions must be drastically reduced. Potential for reduction is especially possible in the transport sector, where fossil fuels must be replaced by sustainable alternatives. A promising substitute in the case of aviation is synthetic jet fuel produced in so-called Power-to-Liquid processes [3].

Such a process is developed in the Kerogreen project. In this project, a container-sized pilot plant is being built, in which captured CO₂, H₂O, and renewable energy are converted to the target product kerosene [4]. One unit operation within the process chain comprises a compact sorption-enhanced water–gas shift (SEWGS) reactor. Here, purified CO from a plasma reactor is partly converted with steam to produce hydrogen. Two main targets are pursued in this process step:

1. Providing synthesis gas (syngas) with a H₂/CO ratio of approximately two for the subsequent Fischer–Tropsch synthesis.
2. Removing the by-product CO₂ and refeeding it to the plasma reactor.

In sorption-enhanced reactors, or, in other words, *adsorptive reactors*, a chemical reaction and an adsorptive separation of one product component are carried out simultaneously [5]. Simultaneous reaction and adsorption usually take place in fixed bed reactors filled with solid catalyst and sorbent material.

In our case of the SEWGS reactor, the exothermic water–gas shift reaction (WGS, Equation (1)) on a Cu-based catalyst is combined with in-situ adsorption of CO₂ on a potassium-impregnated hydrotalcite sorbent (K-HTC). Many experimental studies have proven the feasibility of this technology [6–8]; a comprehensive overview is given in [9]. According to Le Chatelier’s principle, the selective removal of the product component CO₂ (Equation (2)) shifts the reaction equilibrium towards the product side. Hence, higher yields of the desired product component H₂ can be obtained, and the undesired product component CO₂ can be recycled. Depending on prevailing operating conditions, H₂O is also adsorbed on K-HTC (Equation (3)).



Due to its limited adsorption capacity, the sorbent gets saturated with adsorbate during the reactive adsorption phase and needs to be regenerated for further use. Regeneration can either be realized by temperature swing (temperature swing adsorption, TSA), pressure swing (pressure swing adsorption, PSA), or a combination thereof (PTSA) and is often stimulated by a concentration change (purge flow). The adsorption capacity of the sorbent is lowered by changing the prevailing process conditions: increasing the temperature or decreasing the pressure releases the adsorbate from the sorbent. To ensure continuous flow and concentration of product gas, several (at least two) parallel reactors must be operated in periodically switching modes: at least one in reactive adsorption mode and one (or more) in regeneration (desorption) mode [10]. Usually, the required regeneration time is longer than the time span of reactive adsorption. Hence, sorption-enhanced reactor systems consist of multiple (about six to nine) equivalent reactors [11], which are operated in periodically switching modes. Depending on the process concept, these modes may include for a PSA:

- pressurization (feed: reactants);
- reactive adsorption (feed: reactants);
- depressurization (no feed, often purged);
- regeneration (feed: purge gas).

A periodic reactive adsorption and regeneration cycle consists of a consecutive sequence of all relevant steps and is repeated continuously. To enhance performance and efficiency, ideal operating conditions for periodic cycles must be ensured.

Modeling and simulation techniques are precious tools to develop optimized process strategies. They aim to perform simulative parameter studies based on sorption-enhanced reactor models to gather deeper understanding of the interior states of the reactor system. Several approaches for reactive adsorption models were developed over the last years, and detailed studies on the intrinsic adsorption and reaction behavior are available for specific applications.

Sorption-enhanced processes are time- and space-dependent and can be described by a system of coupled partial differential equations (PDE). Although single PDEs might be solved analytically, numerical solvers are needed to compute coupled PDEs. Besides the complex and time-consuming development of a customised solving algorithm for a special problem, more general commercial numeric tools, such as built-in solvers in MATLAB (The MathWorks Inc., USA), COMSOL Multiphysics (COMSOL Inc., Sweden), or gPROMS (Siemens PSE, UK) are available for solving PDE systems. Furthermore, semi-discretization methods (Method-of-Lines, MoL) can be used to transform a PDE into a system of ordinary differential equations (ODE) [12], which can then be solved by well-established ODE

solving algorithms. Table 1 gives a short overview of selected studies employing those methods for (reactive) adsorption processes.

Table 1. Overview of selected studies employing different numerical methods for solving (reactive) adsorption models.

Reaction	Adsorption	Numerical Solution	Reference
-	CO ₂ on K-HTC	MATLAB: MoL (N = 500) / ode15s solver	[13]
SMR	CO ₂ on K-HTC	MATLAB: MoL / ode15s solver	[14]
WGS	CO ₂ on K-HTC	gPROMS: CFDM (N = 600) / DASOLV solver	[15]
WGS	CO ₂	COMSOL Multiphysics: FEM	[16]
SMR	CO ₂ on CaO-mayenite	MATLAB: pdepe solver	[17]
DMES	H ₂ O on LTA zeolite	MATLAB: MoL (N = 30) / ode15s solver	[18]
DMES	H ₂ O on LTA zeolite 3A	gPROMS: BFDM (N = 60) / DASOLV solver	[19,20]
WGS	CO ₂ on K-HTC	MATLAB: MoL (N = 250) / ode15s solver	[21]
SMR	CO ₂ on CaO	MATLAB: pdepe solver	[22]
-	CO ₂ on K-HTC	gPROMS	[23]

Whereas most studies focus on the model description of simultaneous adsorption and reaction in one reactor, the dynamic modeling of multiple interconnected reactors has received less attention. Only few studies have investigated full-cycle behavior [15,16,18,23,24].

Najmi et al., for example, developed a multi-train SEWGS model that consists of eight parallel reactors [15]. They implemented a set of PDEs describing reactive adsorption, regeneration, and various PSA process cycle steps in gPROMS (axial discretization in 600 elements by centered finite difference method (CFDM), time integration by DASOLV solver) and created an operating schedule that switches the set of equations between reactive adsorption and desorption after defined cycle times.

Recently, van Kampen et al. presented an elaborated model study on the sorption-enhanced dimethyl-ether synthesis, in which they demonstrated a full-cycle design for a three column PTSA system [18]. The numerical solution was realized by means of spatial discretization according to MoL with 30 finite differences (FD) and time integration with MATLAB ode15s solver for pre-defined time spans of reactive adsorption/regeneration steps.

In this contribution, we apply a novel numerical solution approach that has not been described previously for dynamic sorption-enhanced reactor modeling. It is based on the graphical implementation of the ODE system obtained via MoL in the MATLAB Simulink programming environment. Simulink enables the implementation and analysis of the SEWGS reactor as a dynamic system. The cyclic process operation procedure is implemented with the Simulink add-on Stateflow. Stateflow is a tool to create state-machines and flow-charts in Simulink. With Simulink and Stateflow, the hybrid system consisting of parallel and periodically operated fixed beds and the discrete switches between different modes can be fully described.

With this model, switching times for reactive adsorption and regeneration no longer need to be predefined. Instead, they can be adjusted automatically during run time according to a defined threshold, e.g., the CO₂ content in the reaction chamber outlet.

2. SEWGS Model

2.1. Model Development

A one-dimensional, time- and space resolved dynamic reactor model was developed to investigate numerical approaches and process configurations. The packed bed reactor dimensions and operating conditions were chosen in accordance with the pilot plant reactor in the Kerogreen project. This reactor consists of six individually fed reaction chambers embedded in one diffusion-bonded apparatus (Figure 1).

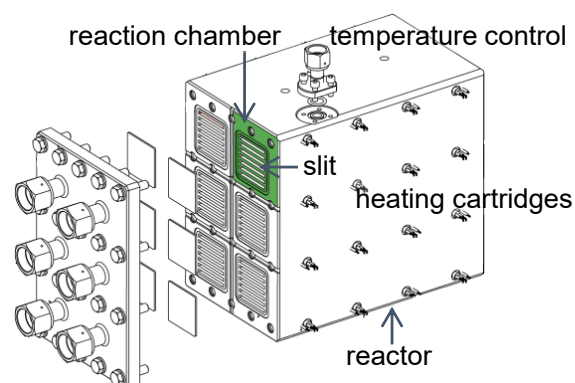


Figure 1. Pilot plant SEWGS reactor with six individually fed reaction chambers. Every chamber consists of seven slits. Isothermal conditions are ensured with adjacent channels between the slits for tempering with purge gas.

In cyclic operation, the chambers can be operated in parallel or in series: the outlet of one reaction chamber can be coupled with the inlet of the next reaction chamber for a serial configuration. Each reaction chamber consists of seven rectangular slits ($h = 4$ mm, $w = 50$ mm, $l = 300$ mm). The slits are filled with a homogeneous mixture of K-HTC and Cu/ZnO-Al₂O₃ catalyst particles. Due to the rather low adsorption capacity of K-HTC, the SEWGS reactor in the Kerogreen pilot plant employs a PSA concept with fast switching times for continuous H₂ production. Contrary to concepts with large, thick vessels as reactor compartments, where severe back-mixing can occur, the slits are assumed to behave like ideal plug flow reactors.

The SEWGS reactor merges several elements of process intensification [25,26]. In terms of processing methods, it can be classified as a multi-functional reactor for dynamically operated reactive separation processes. In terms of equipment, the SEWGS reactor exhibits excellent heat transfer properties due to adjacent tempering micro-channels between the slits that basically form a micro heat-exchanger and enable isothermal operation conditions in the reaction chambers. Sending purge gas (N₂ with steam) through the tempering channels prior to entering the chambers in desorption mode leads to a negligible temperature difference between adsorption and desorption slits. The model is based on the following assumptions and considerations:

- Homogeneous distribution of uniformly sized catalyst and sorbent particles according to their weight fraction assumed as one phase
- Uniform gas distribution in the reaction chambers
- Isothermal conditions in the slits
- Negligible pressure drop in the slits
- Constant superficial velocity (which is only the case for sufficient dilution, [27])
- No gradients rectangular to flow direction
- Axial dispersion considered with axial dispersion coefficient
- External mass transfer limitations neglected (Maers criterion)
- Internal mass transfer limitations considered (Weisz–Prater criterion) and implemented with linear driving force (LDF) model (Glueckauf criterion)
- WGS reaction [28] and simultaneous adsorption of CO₂ and H₂O on three different sorption sites (A: H₂O only, B: CO₂ only, C: H₂O and CO₂ comparatively) [29]
- Equilibrium-based desorption of H₂O and CO₂.

2.2. Model Equations

The mole balances for species $i = \text{CO}, \text{H}_2\text{O}, \text{CO}_2, \text{H}_2, \text{N}_2$ in the bulk gas phase are given in Equation (4). A heterogeneous LDF approximation was used for intraparticle mass transfer limitations to account for the porous character of the particles.

$$\varepsilon_b \frac{\partial c_i}{\partial t} = -u \frac{\partial c_i}{\partial z} + \varepsilon_b D_{ax,i} \frac{\partial^2 c_i}{\partial z^2} + (1 - \varepsilon_b) k_{LDF,i} (\bar{c}_i - c_i) \quad (4)$$

The required initial conditions are implemented according to the prevailing conditions in the reaction chambers before the switch (e.g., end of desorption mode before reactive adsorption) and the boundary conditions according to Equation (5) at the inlet (Dirichlet) and Equation (6) at the outlet (Neumann) of the reaction chambers. The initial conditions for the first reactive adsorption step result from a 2 h regeneration step to represent a fresh sorbent.

$$\text{at } z = 0 \quad c_i = c_{i,feed} \quad t > 0 \quad (5)$$

$$\text{at } z = 1 \quad \frac{\partial c_i}{\partial z} = 0 \quad t > 0 \quad (6)$$

The mole balances for species $i = \text{CO}, \text{H}_2\text{O}, \text{CO}_2, \text{H}_2, \text{N}_2$ in the particle void phase, where reaction and adsorption or desorption are assumed to take place on the solid surface, are given in Equation (7) for an axial dependent averaged particle concentration. The stoichiometric reaction coefficient ν_i is -1 for the reactants (CO and H_2O), 1 for the products (CO_2, H_2), and 0 for inert N_2 . The adsorption rates of H_2O and CO_2 are given in Equation (8) and Equation (9), respectively. Initial conditions are defined analogous to the bulk phase.

$$\varepsilon_p \frac{\partial \bar{c}_i}{\partial t} = \varepsilon_p k_{LDF,i} (c_i - \bar{c}_i) + w_{cat} \rho \nu_i r_{WGS} - (1 - w_{cat}) \rho a_{ads,i} \quad (7)$$

$$a_{ads,H_2O} = \frac{\partial q_{A,H_2O}}{\partial t} + \frac{\partial q_{C,H_2O}}{\partial t} \quad (8)$$

$$a_{ads,CO_2} = \frac{\partial q_{B,CO_2}}{\partial t} + \frac{\partial q_{C,CO_2}}{\partial t} \quad (9)$$

The adsorption kinetics of adsorbate species H_2O and CO_2 on adsorption site A (H_2O only), B (CO_2 only), and C (H_2O and CO_2) of K-HTC sorbent are taken from Coenen et al. and are specified in Equation (10) (identical approach for q_{A,H_2O}) and Equation (11) (identical approach for q_{C,H_2O}), respectively [29]. The initial conditions are chosen according to the prevailing conditions in the reaction chambers before the switch.

$$\frac{\partial q_{B,CO_2}}{\partial t} = k_{B,ads} \cdot (q_{B,CO_2}^{eq} - q_{B,CO_2}) \quad \text{with} \quad q_{B,CO_2}^{eq} = k_B \cdot p_{CO_2}^{n_B} \quad (10)$$

$$\begin{aligned} \frac{\partial q_{C,CO_2}}{\partial t} &= k_{C,ads} \cdot p_{CO_2}^m \cdot (q_{C,max} - q_{C,H_2O} - q_{C,CO_2}) \\ &+ k_{C,rep1} \cdot q_{C,H_2O} \cdot p_{CO_2}^m - k_{C,rep2} \cdot q_{C,CO_2} \cdot p_{H_2O}^m - k_{C,des,CO_2} \cdot q_{C,CO_2} \end{aligned} \quad (11)$$

The desorption of site A and B was modelled with an equilibrium-dependent desorption coefficient (Equation (12), identical approach for q_{A,H_2O}). For site C, comparative replacement of CO_2 by H_2O takes place (Equation (11)). The heterogeneity of the surface is considered by a modified Elovich approach, shown for site B in Equation (13) (identical approach for site A and C) [29].

$$\frac{\partial q_{B,CO_2}}{\partial t} = k_{B,des} \cdot (q_{B,CO_2}^{eq} - q_{B,CO_2}) \quad (12)$$

$$k_{B,des} = k_{B,des}^1 \cdot \exp \left(- \frac{\left(-\beta_{B,des} \cdot \frac{q_{B,CO_2}}{q_{B,max}} \right)}{R \cdot T} \right) \quad (13)$$

The WGS reaction rate expression over a $\text{Cu}/\text{ZnO}-\text{Al}_2\text{O}_3$ catalyst is taken from Choi et al. and presented in Equation (14) [28]. The reaction equilibrium constant results from Equation (15) [30].

$$r_{\text{WGS}} = k_{\infty} \cdot \exp\left(-\frac{E_a}{R \cdot T}\right) \cdot \left(p_{\text{H}_2\text{O}} \cdot p_{\text{CO}} - \frac{p_{\text{H}_2} \cdot p_{\text{CO}_2}}{K_{\text{eq}}}\right) \quad (14)$$

$$K_{\text{eq}} = \exp\left(\frac{4577.8}{T} - 4.33\right) \quad (15)$$

The axial dispersion coefficient was determined with Equation (16) [19] with gas mixture diffusion coefficients from [31].

$$D_{\text{ax},i} = D_{\text{mix},i} \cdot \sqrt{\varepsilon_b} + u \cdot r_p \quad (16)$$

The linear driving force approximation coefficients were calculated according to Equation (17) [32] with effective diffusion coefficients from [31].

$$k_{\text{LDF},i} = \frac{15 \cdot D_{\text{eff},i}}{r_p^2} \quad (17)$$

2.3. Model Parameters

For the comparison of numerical solution approaches, a base case was investigated. The operating conditions and parameters for this base case are listed in Table 2. An overview of the kinetic coefficients is given in Appendix A, Table A1.

Table 2. Parameters and operating conditions used in the base case simulation.

General Parameters	
ε_b	0.4
ε_p	0.5
ρ	1096 kg m ⁻³
r_p	100 μm
w_{cat}	0.05
Adsorption Parameters	
p	8 bar
T	250 °C
F_{STP}	2000 mL/min
$y_{\text{CO,feed}}$	0.3
$y_{\text{H}_2\text{O,feed}}$	0.6
$y_{\text{N}_2\text{,feed}}$	0.1
Desorption Parameters	
p	1 bar
T	250 °C
F_{STP}	1000 mL/min
$y_{\text{H}_2\text{O,feed}}$	0.4
$y_{\text{N}_2\text{,feed}}$	0.6

3. Numerical Simulation Approaches

Three practical numerical simulation approaches for solving the SEWGS model are presented in the following sections. The simulations were performed on one core of the multi core processor Intel(R) Core(TM) i7-6700HQ CPU @ 2.60 GHz, with 8 GB of installed RAM memory using MATLAB version R2020b, 64-bit.

3.1. Built-In Solver

The system of coupled PDEs was solved with MATLAB's built-in solver pdepe for parabolic and elliptic PDEs in one dimension. This solver solves initial-boundary value problems in the form of Equation (18) with two independent variables: one spatial variable and time. The coefficients of Equation (18) have to be provided in the function handle pdefun, whereas initial and boundary conditions are specified in icfun and bcfun. The

boundary conditions must be coded according to Equation (19) [33]. At least one PDE must be parabolic. Therefore, the axial dispersion term in Equation (4) is required for the applicability of `pdepe` and the proper definition of boundary conditions.

$$c^* \left(z, t, v, \frac{\partial v}{\partial z} \right) \frac{\partial v}{\partial t} = z^{-m^*} \frac{\partial}{\partial z} \left(z^{m^*} f^* \left(z, t, v, \frac{\partial v}{\partial z} \right) \right) + s^* \left(z, t, v, \frac{\partial v}{\partial z} \right) \quad (18)$$

$$p^*(z, t, v) + q^*(z, t) f^* \left(z, t, v, \frac{\partial v}{\partial z} \right) = 0 \quad (19)$$

The `pdepe` solver transforms the system of PDEs into a system of ODEs by means of spatial discretization with a piecewise Petrov–Galerkin method on a set of user-defined nodes (`xmesh`) [34]. The resulting ODE system is integrated in time with the built-in solver `ode15s` for stiff differential algebraic equations (DAEs). DAEs arise from elliptic equations in the PDE system. The variable time step integration of `ode15s` delivers the numerical solution at specified points of time, defined in `tspan`. With this procedure, both time step and computing formula are adapted dynamically to obtain high accuracy in short computational time [35]. The `pdepe` solver provides a user-friendly implementation and is capable of solving nonlinear and coupled equations reliably for suitably defined meshes [36].

3.2. Method-of-Lines (MoL)

Another approach for solving coupled PDE systems is the MoL, a semi-discretization method [12]. Spatial derivatives in the PDEs are substituted by algebraic approximations to obtain a set of ODEs that can be solved with well-established solving algorithms. Here, spatial discretization is realized on a uniform grid in an axial direction (z -direction) with FD. For the first-order convective terms, a backward FD is used (Equation (20)), and for the second-order dispersion terms, implicit central differences are defined (Equation (21)). The resulting error O is neglected. The MoL resembles a CSTR cascade: with decreasing length of Δz , the number of cells N in the cascade increases and the error diminishes.

$$\frac{\partial v}{\partial z} \approx \frac{v_n - v_{n-1}}{\Delta z} + O(\Delta z) \quad \text{with} \quad n = 1, \dots, N \quad (20)$$

$$\frac{\partial^2 v}{\partial z^2} \approx \frac{v_{n+1} - 2v_n + v_{n-1}}{\Delta z^2} + O(\Delta z^2) \quad \text{with} \quad n = 1, \dots, N - 1 \quad (21)$$

The boundary conditions are implemented as differential equations on the first node ($n = 0$, Dirichlet), and on the last node ($n = N$, Neumann), analogous to Equation (5) and Equation (6) (*method of false boundaries*).

The obtained ODE system of $N + 1$ equations is numerically solved in time with MATLAB's `ode15s` for best comparability with the `pdepe` results. This variable-step, variable-order solver is based on numerical differentiation formulas and is recommended for stiff problems and DAEs. A convergence analysis with up to 250 cells is performed to examine the adequacy of the spatial discretization.

3.3. Simulink

Simulink is a graphical programming environment used for modeling, simulation, and analysis of dynamical systems that is based on MATLAB [37].

3.3.1. Model Implementation and Data Structure

In the third approach presented in this paper, the model equations are implemented in Simulink based on the idea of the MoL. In Simulink, the model is constructed in hierarchical block diagrams in the graphical editor, where libraries of predefined blocks of elementary model components for continuous-time and discrete-time systems are available [37]. Those blocks are connected with signal lines to visually build the model.

The SEWGS model equations are discretized in space to obtain ODEs for N cells, as described in Section 3.2. The ODEs are implemented in a block diagram as shown in

Figure 2 for the bulk concentration of CO [38]. Fourteen ODEs are needed to describe one cell (Figure 2). All ODEs of one cell have to be evaluated as a time-dependent single unit. Therefore, they are classified as one *atomic subsystem*. For simplified programming, the cell subsystem is stored in a separate file to be used multiple times as a *referenced subsystem* in the main model file, the so-called *parent model*. Ten subsequent cells are arranged in a *group* subsystem to enable easy scale-up and data storage. A reaction chamber comprises the desired number of groups in a cascade, as shown in Figure 2 for $N = 50$.

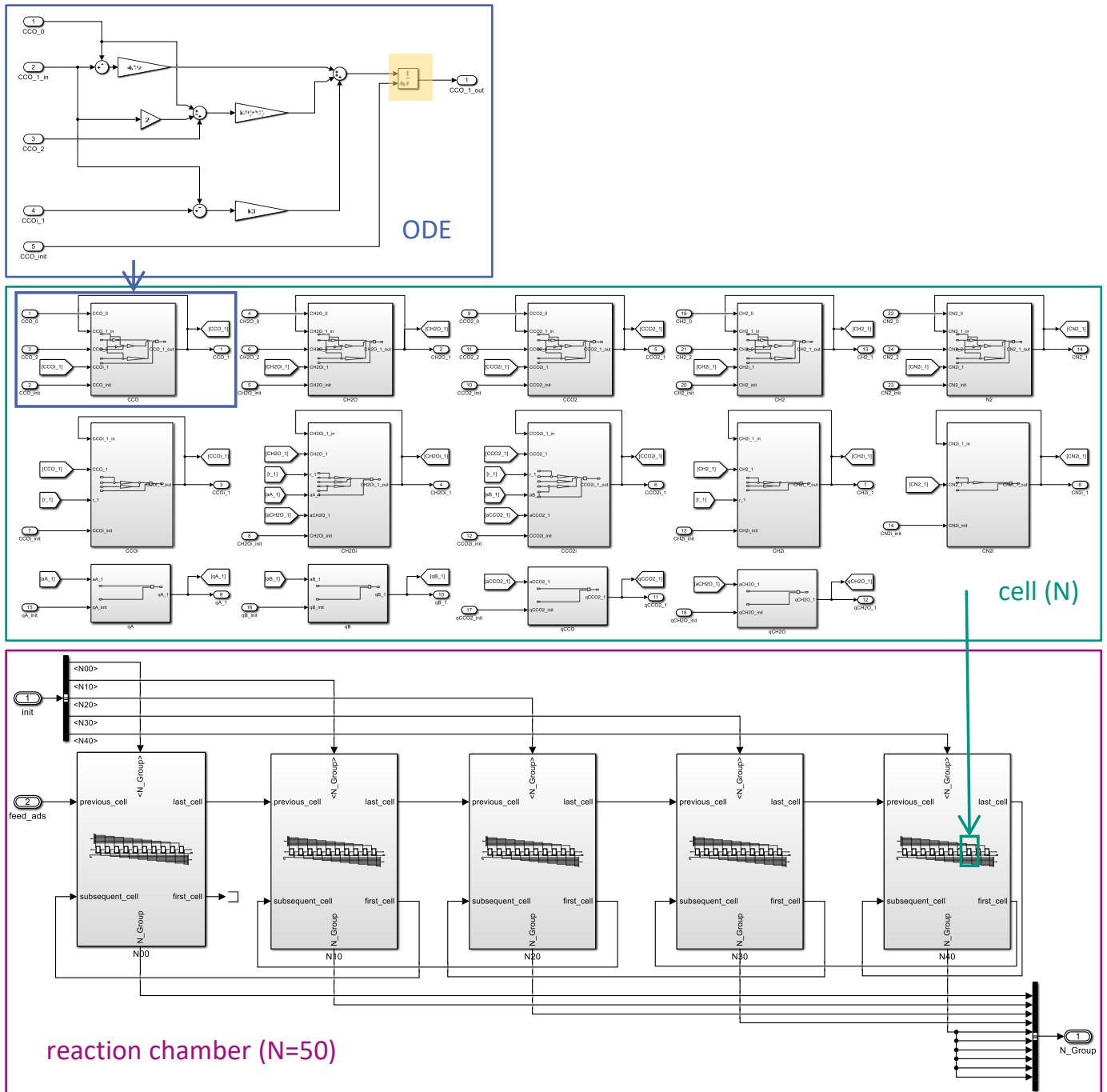


Figure 2. Bottom-up Simulink implementation of the model equations for one reaction chamber discretized analogous to MoL. Exemplary ODE implementation of the CO concentration in the bulk phase. The integrator block is marked in yellow. Fourteen ODEs arrange the cell subsystem; N (here: $N = 50$) cells form the reaction chamber.

The integrator block (marked in yellow in Figure 2) provides the selected solver (Section 3.3.2) with an initial condition that is used to compute the block's initial state at the start of the simulation and outputs the value of the integral of its time-dependent input signal at every time step.

A comprehensive *bus object* structure had to be developed for user-friendly and reliable data access. Simulink bus objects are equivalent to a structure definition in C. All relevant data belonging to one cell are stored together in one *cell bus object*. Ten cells are grouped in a superordinated *group bus object*. The desired number of groups form the whole reaction chamber and are contained in a *chamber bus object*. Each data point in every cell can easily be accessed via dot notation: e.g., the CO₂ concentration leaving the 25th cell is addressed as N20.N05.CC02. This structure simplifies data handling enormously, compared to the methods presented in Sections 3.1 and 3.2, where the overall time- and space dependent solution is contained in one voluminous matrix.

3.3.2. Solver Selection

The solver choice depends on the dynamics of the system, the solution stability, the solver robustness, and especially the computation speed when solving complex systems [39]. The different solvers suggested by the MATLAB solver library for ODEs were tested for the SEWGS model, with the aim to solve the model successfully within specified tolerance limits and in a reasonable duration. Figure 3 shows the required computation time for appropriate solvers depending on the implemented number of cells for the base case: reactive adsorption in one reaction chamber. Computation times below 0 indicate that a simulation did not converge, and a smaller error tolerance was required. With solver ode23t, the computation time was reduced by almost half compared to the commonly used solver ode15s with sufficient precision (relative error tolerance of 10^{-3}). This solver is used to speed-up all Simulink simulations presented in this paper.

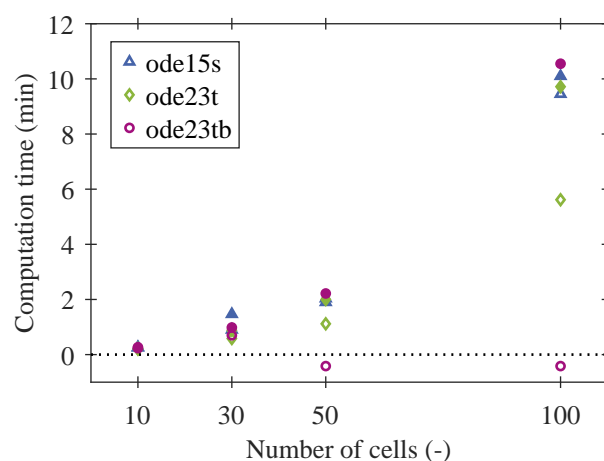


Figure 3. Required computation time depending on the number of implemented cells, chosen solver, and relative error tolerance. Filled symbols: relative error tolerance 10^{-6} ; open symbols: relative error tolerance 10^{-3} . The best results for $N = 100$ are obtained for solver ode23t with a relative error tolerance of 10^{-3} . Computation times below 0 indicate that a simulation did not converge.

3.3.3. Cyclic Process Design

A complex model, consisting of six parallel reaction chambers, is developed for continuous H₂ production. The automated switching logic from reactive adsorption to regeneration mode is realized with a finite-state-machine implemented in the Simulink tool Stateflow. Stateflow enables mode logic, fault management, and task scheduling in discrete or hybrid systems. A Stateflow machine contains Stateflow charts with objects such as states, events, transitions, etc. [40].

For the implemented periodic process, the valve positions (corresponding to the real plant) for either reactive adsorption or regeneration are triggered after an initialization step in all chambers by the Stateflow machine. One reaction chamber starts in reactive adsorption mode, while the other chambers are in regeneration mode. As soon as a specified event triggers the Stateflow machine, such as reaching a threshold concentration in the outlet flow or a predefined time span, the valve positions are changed in a way that the next reaction chamber starts its reactive adsorption period. A graphical overview of the SEWGS Simulink model is given in Figure 4.

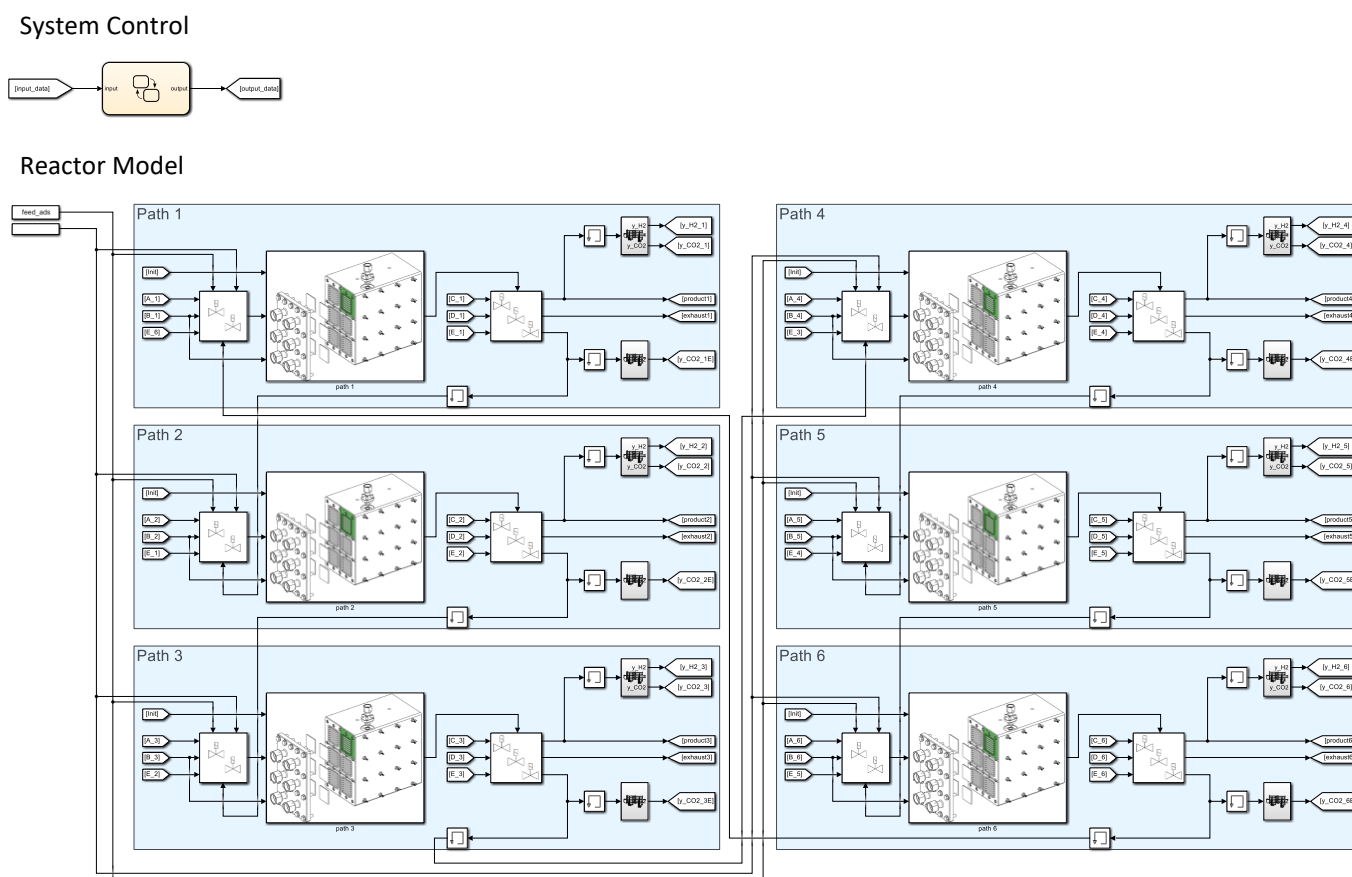


Figure 4. Simulink model consisting of six reaction chambers (blue), which are operated in either reaction or regeneration mode after an initialization step. Subsequent reaction chambers can optionally be connected. The cyclic process operation is controlled with a Stateflow machine (yellow).

In this paper, the dynamic adaptation of switching times depending on the CO₂ content in the reaction chamber outlet is investigated for a partly serial reaction chamber configuration.

4. Results and Discussion

In the following sections, the simulation results for reactive adsorption in one reaction chamber are compared for three numerical approaches. Furthermore, the cyclic process design for the SEWGS reactor consisting of six reaction chambers is presented.

4.1. Reactive Adsorption

The accuracy of the MoL simulations depends primarily on the adequacy of the grid discretization. In Figure 5a, the sorbent loading with CO₂ over the reactor length is shown for 10 to 250 cells at $t = 25$ s. The curves exhibit step steps for simulations with few cells, and the smoothness increases significantly for $N > 100$. The grid (in)dependence is

depicted in Figure 5b. For $N > 100$, the deviation from $N = 250$ is less than 5%, except for the initial conditions in the differently sized first cell.

The required computation time increased almost exponentially with the number of cells (see Appendix A, Table A2). Therefore, a trade-off between accuracy and computation time must be made, and $N = 100$ was chosen for the following MoL simulations.

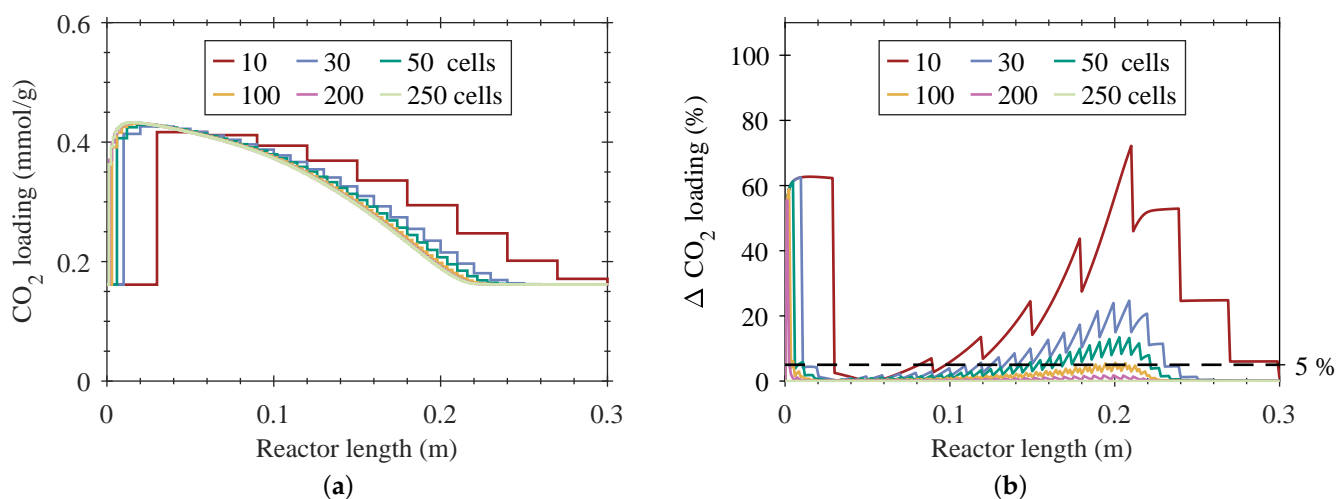


Figure 5. MoL grid analysis with $N = 10$ to 250 cells for reactive adsorption in one reaction chamber. (a) CO_2 loading, and (b) deviation of CO_2 loading from $N = 250$ as a function of the reactor length at $t = 25$ s.

The pdepe simulations have proven to be extremely sensitive to initial conditions. A sufficiently high number of mesh points in time and space needs to be chosen to ensure numerical stability and to avoid oscillations. The computation time for pdepe was significantly lower compared to MoL simulations with a comparable number of mesh points due to pdepe's run-time optimization (see Appendix A, Table A2). For both methods, MoL and pdepe, convergence could be reached with appropriate mesh settings.

In the base case, the CO_2 loading of the sorbent over the reactor length increases with time until it reaches full saturation after approximately 100 s (Figure 6a). At the same time, the CO_2 concentration at the reactor outlet approaches its steady-state value (Figure 6b). The defined breakthrough (CO_2 volume fraction in the product > 0.05) of CO_2 at the reactor outlet can be noticed after approximately 40 s. Prior to that point, CO is fully converted in excess of H_2O in the feed, and the produced CO_2 is adsorbed completely.

In order to access the conservation properties of the numerical solution algorithms, the deviation from the molar balance depending on time and space was calculated (see Appendix A, Figure A1). Both methods, pdepe and MoL, exhibit only minor deviations from a closed molar balance ($< 2\%$). The deviation is more pronounced for pdepe close to the reactor inlet at $t < 50$ s. For MoL, the deviation emerges for a longer period of time at the reactor outlet. In both cases, it approaches zero as soon as steady-state conditions are reached. The deviations were attributed to the adsorption process and could—especially for undiluted feeds—possibly be improved by taking into account prevailing velocity changes, as suggested by DiGiuliano et al. [27].

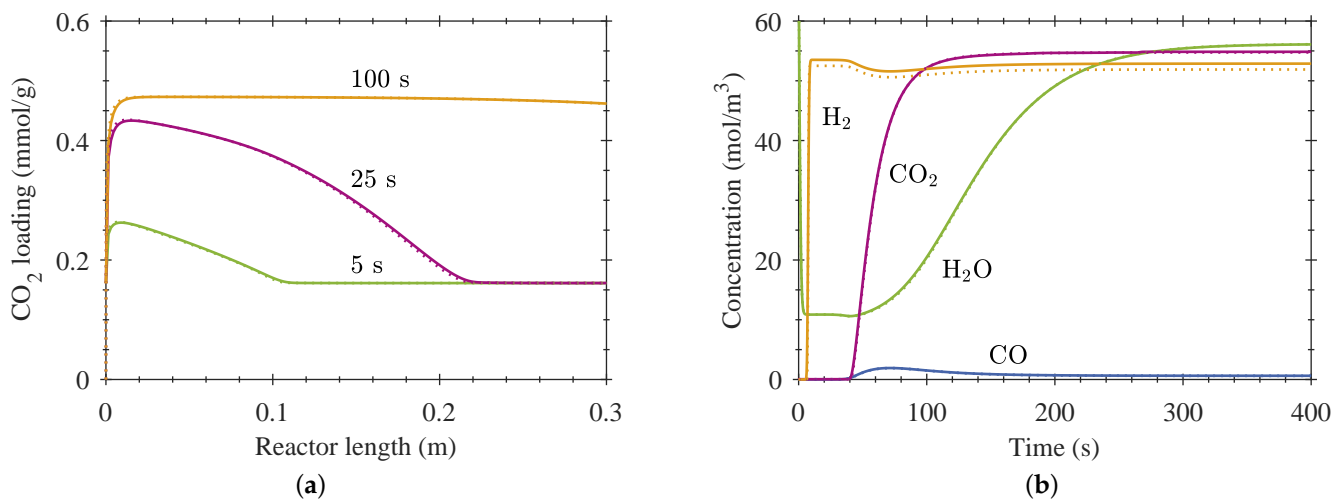


Figure 6. Comparison of pdepe and MoL ($N = 100$) simulation results for reactive adsorption in one reaction chamber. (a) CO₂ loading at various adsorption times as a function of the reactor length, and (b) bulk phase concentrations at reactor outlet as a function of time. Solid lines: MoL; dotted lines: pdepe.

After having shown that both approaches, pdepe as well as simple uniform semi-discretization with MoL, lead to satisfying results for the SEWGS simulation, the MoL results were compared with the corresponding Simulink results for $N = 100$. As expected, hardly any deviation between the curves of the two methods can be distinguished (Figure 7). Therefore, it was concluded that the graphical approach in Simulink performs with sufficient precision and reliability and can be expanded to a more complex hybrid process model.

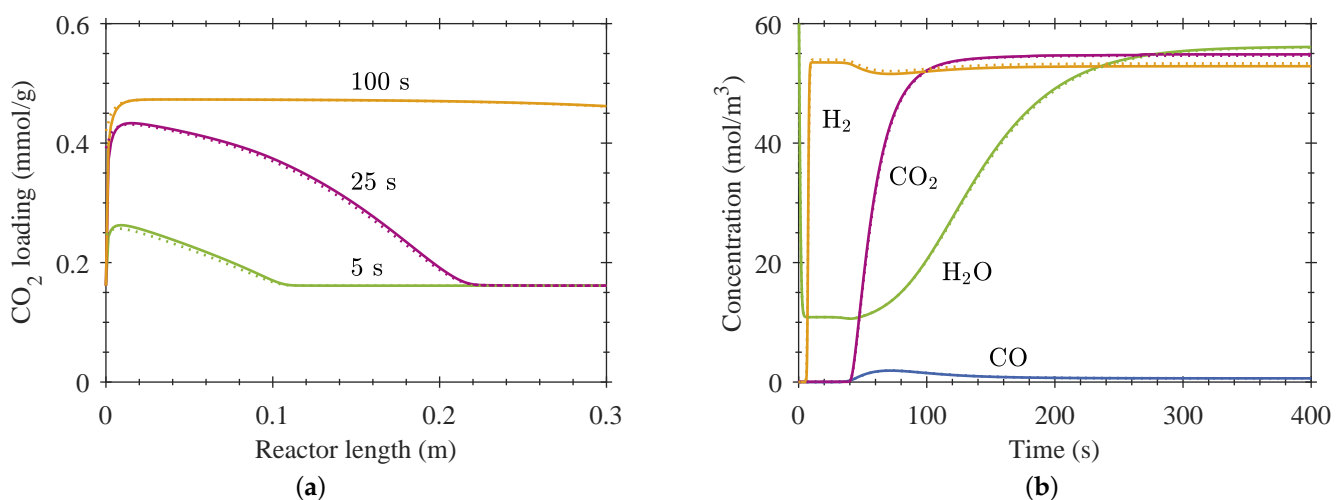


Figure 7. Comparison of MoL and Simulink ($N = 100$) simulation results for reactive adsorption in one reaction chamber. (a) CO₂ loading at various adsorption times as a function of the reactor length, and (b) bulk phase concentrations at reactor outlet as a function of time. Solid lines: MoL; dotted lines: Simulink ($N = 100$).

4.2. Process Design

The hybrid Simulink Stateflow model consisting of six reaction chambers, switching opportunities (valves), and process control (Stateflow machine) (Figure 4) is used to simulate cyclic SEWGS process operation. An interconnected reaction chamber configuration was investigated for optimized sorbent usage (Figure 8): chamber 1 starts in reactive adsorption mode (M2) with *fresh* feed (CO + H₂O) and produces CO₂-free WGS product, whereas all other chambers are in regeneration mode (M4). The regeneration feed consists

of N_2 and H_2O to increase CO_2 desorption from both sorption sites (B and C). As soon as the sorbent in chamber 1 is no longer capable of adsorbing all produced CO_2 and the gas flow leaving chamber 1 reaches a CO_2 volume fraction of 5%, a switch to M3 is triggered. In M3, the gas flow leaving chamber 1 is fed into chamber 2, which is then in M1. While the sorbent loading in chamber 1 is still increasing, CO_2 -free WGS product is produced in chamber 2. Chamber 1 switches from M3 to M4 when a threshold of 20% CO_2 volume fraction is reached. The cycle then continues in chamber 2 with M2.

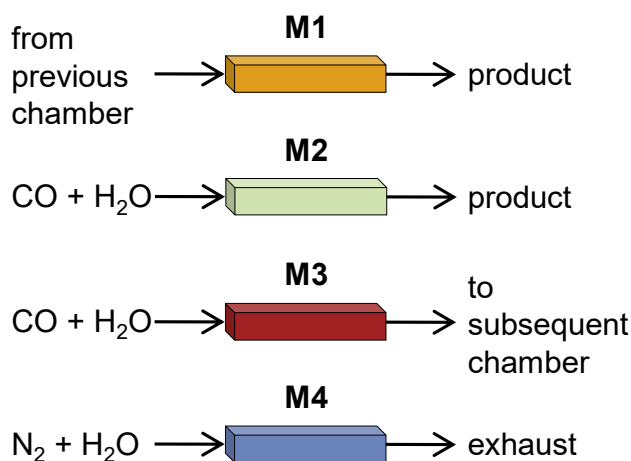


Figure 8. Process operation modes. M1: feed from previous chamber, outlet product; M2: reaction feed, outlet product; M3: reaction feed, outlet to subsequent chamber; M4: regeneration feed, outlet exhaust.

A typical operation scheme is depicted in Figure 9a for the first 900 s for all chambers. According to the operational concept, the interconnected chambers in M1 and M3 are dependent on each other. The resulting time span for M4 is the limiting factor for the sorbent regeneration. As always one chamber is either in M1 or M2, a constant product gas flow is ensured, and a nearly CO_2 -free product flow leaves the reactor. Figure 9b shows the H_2 volume fraction in the product flow of the total reactor (six chambers) and of chamber 1. The H_2 volume fraction approaches a constant value of about 0.62 after the first cycle; the rest of the product gas flow consists of inert N_2 and unreacted H_2O .

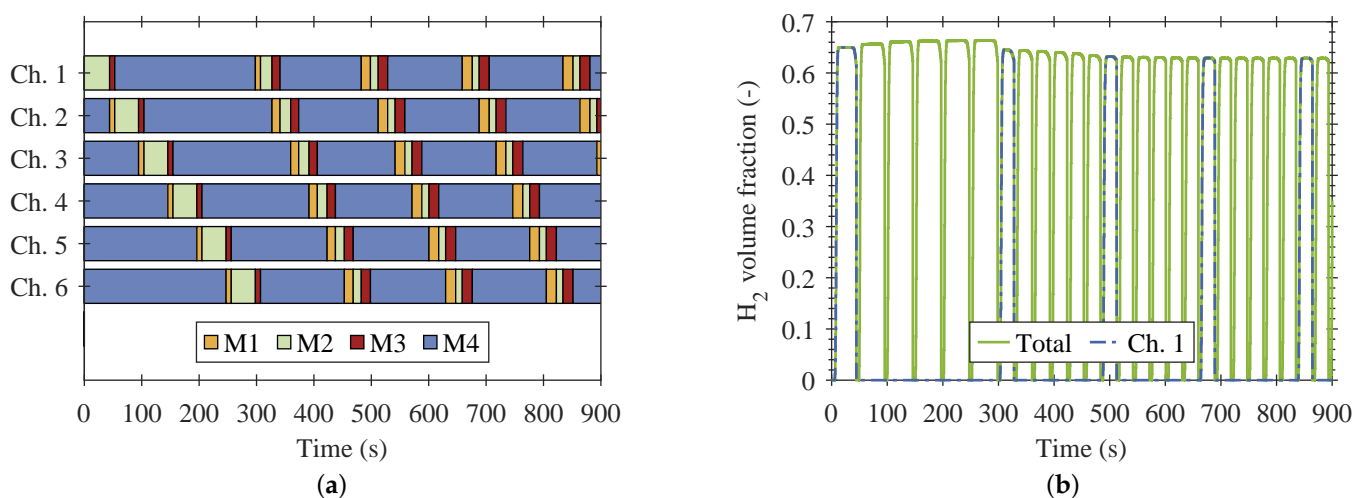


Figure 9. (a) Operation scheme for six reaction chambers, and (b) H_2 volume fraction in the product for all chambers combined ("total") and for chamber 1 for the first 900 s. Switching condition M2 to M3: CO_2 volume fraction in product > 0.05 ; M3 to M4: CO_2 volume fraction to subsequent chamber > 0.2 .

The time span in which a chamber stays in each mode and the resulting sorbent loading at the end of each mode as a function of the cycle number is shown for chamber 1 in Figure 10. The relative sorbent loading refers to the maximum loading after 400 s reactive adsorption. A significant reduction of the cycle time span by almost 50% is visible after the first cycle. Due to the limited regeneration time, the initial time span of reactive adsorption can no longer be reached in subsequent cycles, as the sorbent cannot be fully regenerated. After the third cycle, the time spans for the different modes as well as the relative sorbent loadings approach constant values. Hence, the overall system is operating in steady-state. The interconnection of two subsequent chambers in M3 and M1 allows for an increased sorbent usage from 72.6% (at the end of M2) to 87.1% (at the end of M3) for the prevailing process conditions, while maintaining the CO₂ volume fraction in the product flow below 5%.

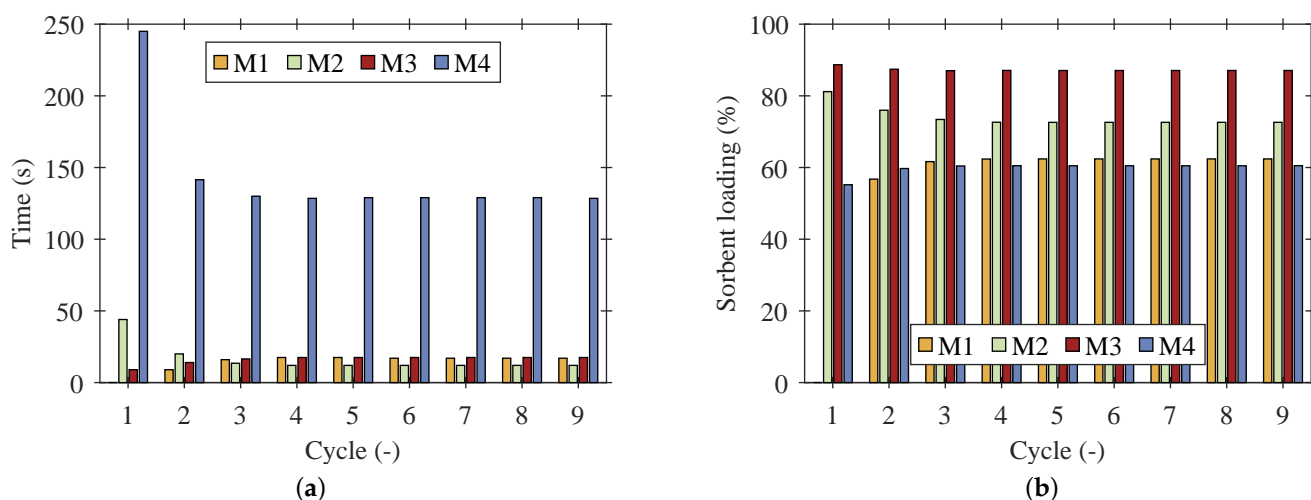


Figure 10. Cyclic operation in six reaction chambers; results shown for nine cycles in chamber 1. (a) Time span of the modes depending on the cycle number, and (b) relative sorbent loading at the end of the modes.

These results show the feasibility of the novel Matlab Simulink Stateflow implementation of the SEWGS model for process optimization. Using a Simulink implementation for a chemical reactor and utilizing Stateflow simplifies the following: simulation-driven development of operating procedures, performance evaluation of larger and more complex systems, and safe failure management. These advantages enable rapid prototyping with MATLAB code generation into programming language for automation systems (PLC) [41] and could thus simplify real plant operation.

5. Conclusions

A dynamically operated compact SEWGS reactor was modelled to optimize its operation procedure. The reactor consists of six identical reaction chambers, which are operated in cycles of reactive adsorption and desorption. The model contains coupled PDEs and is based on kinetic expressions for adsorption, reaction, and desorption.

A novel simulation approach for time- and space-dependent cyclic reactor operation was presented. This approach enables automated adjustment of switching times during runtime according to specified conditions, such as exceeding a threshold of CO₂ concentration in the product stream. For that reason, switching times do not need to be pre-defined and can be optimized dynamically.

First, the applicability of the novel method was verified by comparison with existing and well-established methods for reactive adsorption in one reaction chamber. Therefore, a base case simulation was implemented and solved with MATLAB's pdepe solver. These results were compared with those obtained via MoL (spatial discretization with FD and

ODE system solution with MATLAB's ode15s solver) to determine the required number of spatial discretization cells and to justify the discretization scheme.

Then, the MoL equations were implemented graphically in MATLAB Simulink. Only minor deviations between the results of all methods verify the discretization and suggest the reliability of the MoL implementation in Simulink.

Finally, the basic model was expanded to a complex model distinguishing between initialization, reactive adsorption, and regeneration modes. A comprehensive data structure for reliable data handling was established. A Stateflow machine was designed to simulate automated cyclic switching between six reaction chambers for continuous synthesis gas production. Overall process modeling included a configuration of subsequent interconnected reactor chambers for optimized sorbent usage, while the CO₂ volume fraction in the product flow could still be kept below 5%. Due to automated switching between interconnected reaction chambers, an increase of sorbent usage from 72.6% to 87.1% could be elaborated in the presented case.

This case study has shown that carefully chosen operating parameters and process configurations together with simulation-driven process design can significantly enhance the exploitation of the full sorption capacity and therefore increase the efficiency of sorption-enhanced reaction processes. The novel simulation approach can serve as a practical example for dynamic reactor modeling.

Author Contributions: Conceptualization, T.J.S., methodology, T.J.S.; software, T.J.S., J.-H.K., and S.D.; validation, T.J.S., formal analysis, T.J.S., investigation, T.J.S., resources, T.J.S., data curation, T.J.S., writing—original draft preparation, T.J.S., writing—review and editing, T.J.S. and P.P.; visualization, T.J.S., supervision, P.P.; project administration, P.P.; funding acquisition, P.P. All authors have read and agreed to the published version of the manuscript.

Funding: The work presented in this paper is part of the European project Kerogreen, which has received funding from the European Union's Horizon 2020 research and innovation programme under grant agreement no. 763909.

Conflicts of Interest: The authors declare no conflict of interest.

Abbreviations

The following abbreviations are used in this manuscript:

BFDM	Backward finite difference method of first order
CFDM	Centered finite difference method of second order
Ch.	Chamber
CSTR	Continuously stirred tank reactor
DAE	Differential algebraic equation
DASOLV	Implicit backward differentiation formula solver in gPROMS
DMES	Dimethyl ether synthesis
FD	Finite Difference
FEM	Finite elements method
K-HTC	K ₂ CO ₃ -promoted hydrotalcite
LDF	Linear driving force model
M1-M4	Mode 1-4
MoL	Method-of-lines
ODE	Ordinary differential equation
ode15s	Solver for stiff ODEs in MATLAB
PDE	partial differential equation
pdepe	Solver for systems of parabolic and elliptic PDEs in MATLAB
PLC	Programmable logic controller
PSA	Pressure swing adsorption
PTSA	Pressure temperature swing adsorption
SEWGS	Sorption-enhanced water–gas shift
SMR	Steam-methane reforming
TSA	Temperature swing adsorption
WGS	Water–gas shift

The following symbols are used in this manuscript:

$\beta_{j,\text{des},(i)}$	activation energy change	(J mol ⁻¹)
ε_b	bed void fraction	(-)
ε_p	particle void fraction	(-)
ν_i	stoichiometric reaction coefficient	(-)
ρ	bulk density	(kg m ⁻³)
$a_{\text{ads},i}$	adsorption rate	(mol kg ⁻¹ s ⁻¹)
c^*	pdepe diagonal matrix	(-)
c_i	bulk phase concentration	(mol m ⁻³)
\bar{c}_i	particle void phase concentration	(mol m ⁻³)
$D_{\text{ax},i}$	axial dispersion coefficient	(m ² s ⁻¹)
$D_{\text{eff},i}$	effective diffusion coefficient	(m ² s ⁻¹)
$D_{\text{mix},i}$	gas mixture diffusion coefficient	(m ² s ⁻¹)
E_a	activation energy	(J mol ⁻¹)
eq	equilibrium	(-)
f^*	pdepe flux term coefficient	(-)
F_{STP}	volumetric flow rate at STP	(ml min ⁻¹)
h	slit height	(mm)
ΔH_R^\ominus	standard reaction enthalpy	(kJ mol ⁻¹)
i	species CO, H ₂ O, CO ₂ , H ₂ , N ₂	(-)
j	sorption site A, B, C	(-)
$k_{C,\text{rep}1}$	exchange rate coefficient 1	(bar ⁻¹ s ⁻¹)
$k_{C,\text{rep}2}$	exchange rate coefficient 2	(bar ⁻¹ s ⁻¹)
K_{eq}	equilibrium constant	(-)
k_j	Freundlich adsorption coefficient	(mol kg ⁻¹ bar ⁻¹)
$k_{j,\text{ads}}$	adsorption coefficient	(s ⁻¹)
$k_{j,\text{des},(i)}$	desorption coefficient	(s ⁻¹)
$k_{j,\text{des},(i)}^1$	desorption coefficient	(s ⁻¹)
$k_{\text{LDF},i}$	linear driving force coefficient	(s ⁻¹)
k_∞	frequency factor	(mol bar ⁻² g ⁻¹ h ⁻¹)
l	slit length	(mm)
m	tiny value exponent	(-)
m^*	pdepe symmetry constant	(-)
n	index variable	(-)
N	number of cells	(-)
n_j	Freundlich adsorption intensity	(-)
O	approximation error	(-)
p^*	pdepe boundary coefficient	(-)
$p_{(i)}$	(partial) pressure	(bar)
q^*	pdepe boundary coefficient	(-)
$q_{j,i}$	sorbent loading of species i on site j	(mol kg ⁻¹)
r_p	particle radius	(m)
r_{WGS}	WGS reaction rate	(mol kg ⁻¹ s ⁻¹)
R	gas constant	(J mol ⁻¹ K ⁻¹)
s^*	pdepe source term coefficient	(-)
t	time	(s)
T	temperature	(K)
u	gas velocity	(m s ⁻¹)
v	dependent variable	(-)
w	slit width	(mm)
w_{cat}	catalyst weight fraction	(-)
y_i	volume fraction	(-)
z	axial coordinate	(m)

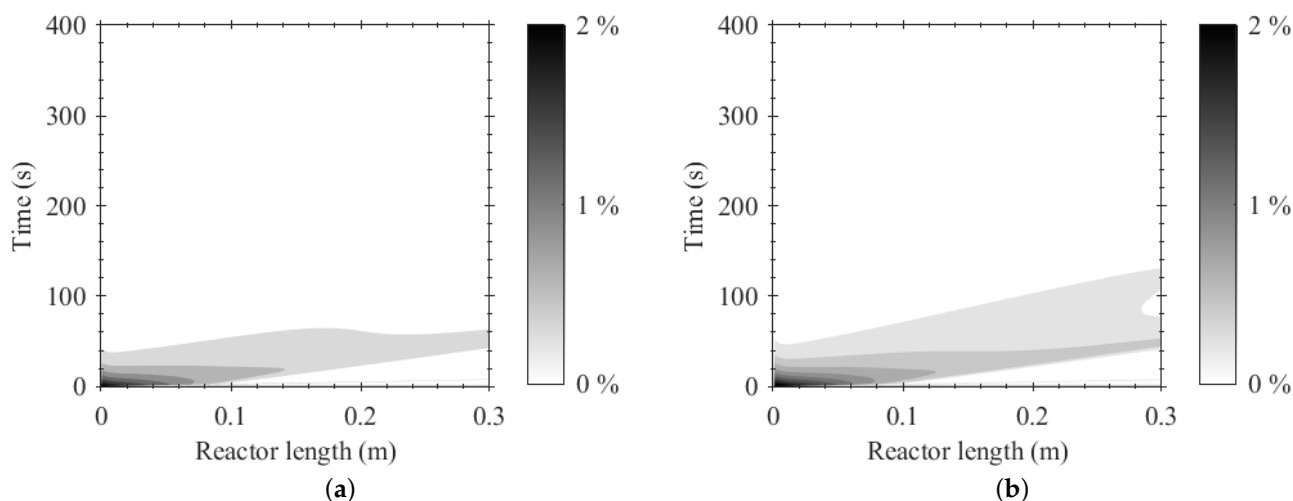
Appendix A

Table A1. Kinetic coefficients. Adapted from [28,29].

Adsorption / Desorption	
$k_{A,ads}$	$4.18 \times 10^{-2} \text{ s}^{-1}$
k_A	$1.69 \text{ mol kg}^{-1} \text{ bar}^{-1}$
n_A	0.235
$k_{A,des}^1$	$7.84 \times 10^{-9} \text{ s}^{-1}$
$\beta_{A,des}$	$1.72 \times 10^5 \text{ J mol}^{-1}$
$k_{B,ads}$	$9.29 \times 10^{-2} \text{ s}^{-1}$
k_B	$0.31 \text{ mol kg}^{-1} \text{ bar}^{-1}$
n_B	0.239
$k_{B,des}^1$	$4.41 \times 10^{-5} \text{ s}^{-1}$
$\beta_{B,des}$	$6.27 \times 10^4 \text{ J mol}^{-1}$
$k_{C,ads}$	$0.1 \text{ bar}^{-1} \text{ s}^{-1}$
$k_{C,rep1}$	$5.0 \times 10^{-3} \text{ bar}^{-1} \text{ s}^{-1}$
$k_{C,rep2}$	$1.4 \times 10^{-2} \text{ bar}^{-1} \text{ s}^{-1}$
k_{C,des,H_2O}^1	$5.23 \times 10^{-11} \text{ s}^{-1}$
k_{C,des,CO_2}^1	$2.06 \times 10^{-10} \text{ s}^{-1}$
β_{C,des,H_2O}	$5.41 \times 10^4 \text{ J mol}^{-1}$
β_{C,des,CO_2}	$5.00 \times 10^4 \text{ J mol}^{-1}$
m	1×10^{-16}
WGS Reaction	
k_∞	$2.96 \times 10^5 \text{ mol bar}^{-2} \text{ g}^{-1} \text{ h}^{-1}$
E_a	$47.400 \text{ J mol}^{-1}$

Table A2. Computation time for pdepe and MoL simulations for reactive adsorption in one reaction chamber.

Number of Cells (-)	MoL						pdepe
	10	30	50	100	200	250	3000
Computation Time (min)	0.04	0.22	0.27	4.96	46.81	90.93	12.19

Figure A1. Time and space-dependent deviation from molar balance for reactive adsorption in one reaction chamber: (a) pdepe, and (b) MoL ($N = 100$) simulation results.

References

1. UN. COP26 Outcomes. In Proceedings of the UN Climate Change Conference at the SEC, Glasgow, UK, 31 October–13 November 2021.
2. United Nations/Framework Convention on Climate Change. Adoption of the Paris Agreement. In Proceedings of the 21st Conference of the Parties, Paris, France, 30 November–11 December 2015.
3. European Commission. *A European Strategy for Low-Emission Mobility*; EEA: Copenhagen, Denmark, 2020.
4. Goede, A.P.H. CO₂ neutral fuels. *EPJ Web Conf.* **2018**, *189*, 00010. <https://doi.org/10.1051/epjconf/201818900010>
5. Rodrigues, A.E.; Madeira, L.M.; Wu, Y.J.; Faria, R. Sorption enhanced reaction processes. In *Sustainable Chemistry Series*; World Scientific: New Jersey, NJ, USA, 2018; Volume 1.
6. Lee, C.H.; Lee, K.B. Application of one-body hybrid solid pellets to sorption-enhanced water gas shift reaction for high-purity hydrogen production. *Int. J. Hydrogen Energy* **2014**, *39*, 18128–18134. <https://doi.org/10.1016/j.ijhydene.2014.04.160>
7. Soria, M.A.; Rocha, C.; Tosti, S.; Mendes, A.; Madeira, L.M. CO_x free hydrogen production through water-gas shift reaction in different hybrid multifunctional reactors. *Chem. Eng. J.* **2019**, *356*, 727–736. <https://doi.org/10.1016/j.cej.2018.09.044>
8. Stadler, T.J.; Barbig, P.; Kiehl, J.; Schulz, R.; Klövekorn, T.; Pfeifer, P. Sorption-Enhanced Water-Gas Shift Reaction for Synthesis Gas Production from Pure CO: Investigation of Sorption Parameters and Reactor Configurations. *Energies* **2021**, *14*, 355. <https://doi.org/10.3390/en14020355>
9. Zhu, X.; Li, S.; Shi, Y.; Cai, N. Recent advances in elevated-temperature pressure swing adsorption for carbon capture and hydrogen production. *Prog. Energy Combust. Sci.* **2019**, *75*, 100784. <https://doi.org/10.1016/j.pecs.2019.100784>
10. Harrison, D.P. Sorption-Enhanced Hydrogen Production: A Review. *Ind. Eng. Chem. Res.* **2008**, *47*, 6486–6501. <https://doi.org/10.1021/ie800298z>
11. Gazzani, M.; Macchi, E.; Manzolini, G. CO₂ capture in integrated gasification combined cycle with SEWGS—Part A: Thermodynamic performances. *Fuel* **2013**, *105*, 206–219. <https://doi.org/10.1016/j.fuel.2012.07.048>
12. Schiesser, W.E. *A Compendium of Partial Differential Equation Models: Method of Lines Analysis with MATLAB*; Cambridge University Press: Cambridge, UK, 2009.
13. Lee, K.B.; Verdooren, A.; Caram, H.S.; Sircar, S. Chemisorption of carbon dioxide on potassium-carbonate-promoted hydrotalcite. *J. Colloid Interface Sci.* **2007**, *308*, 30–39. <https://doi.org/10.1016/j.jcis.2006.11.011>
14. Reijers, H.T.J.; Boon, J.; Elzinga, G.D.; Cobden, P.D.; Haije, W.G.; van den Brink, R.W. Modeling Study of the Sorption-Enhanced Reaction Process for CO₂ Capture. I. Model Development and Validation. *Ind. Eng. Chem. Res.* **2009**, *48*, 6966–6974. <https://doi.org/10.1021/ie801319q>
15. Najmi, B.; Bolland, O.; Colombo, K.E. A systematic approach to the modeling and simulation of a Sorption Enhanced Water Gas Shift (SEWGS) process for CO₂ capture. *Sep. Purif. Technol.* **2016**, *157*, 80–92. <https://doi.org/10.1016/j.seppur.2015.11.013>
16. Karagöz, S.; Tsotsis, T.T.; Manousiouthakis, V.I. Multi-scale modeling and simulation of a novel membrane reactor (MR)/adsorptive reactor (AR) process. *Chem. Eng. Process. Process. Intensif.* **2019**, *137*, 148–158. <https://doi.org/10.1016/j.cep.2019.01.012>
17. Di Giuliano, A.; Gallucci, K.; Giancaterino, F.; Courson, C.; Foscolo, P.U. Multicycle sorption enhanced steam methane reforming with different sorbent regeneration conditions: Experimental and modelling study. *Chem. Eng. J.* **2019**, *377*, 119874. <https://doi.org/10.1016/j.cej.2018.09.035>
18. van Kampen, J.; Boon, J.; Vente, J.; van Sint Annaland, M. Sorption enhanced dimethyl ether synthesis for high efficiency carbon conversion: Modelling and cycle design. *J. CO₂ Util.* **2020**, *37*, 295–308. <https://doi.org/10.1016/j.jcou.2019.12.021>
19. Guffanti, S.; Visconti, C.G.; van Kampen, J.; Boon, J.; Groppi, G. Reactor modelling and design for sorption enhanced dimethyl ether synthesis. *Chem. Eng. J.* **2021**, *404*, 126573. <https://doi.org/10.1016/j.cej.2020.126573>
20. Guffanti, S.; Visconti, C.G.; Groppi, G. Model Analysis of the Role of Kinetics, Adsorption Capacity, and Heat and Mass Transfer Effects in Sorption Enhanced Dimethyl Ether Synthesis. *Ind. Eng. Chem. Res.* **2021**, *60*, 6767–6783. <https://doi.org/10.1021/acs.iecr.1c00521>
21. Jang, H.M.; Lee, K.B.; Caram, H.S.; Sircar, S. High-purity hydrogen production through sorption enhanced water gas shift reaction using K₂CO₃-promoted hydrotalcite. *Chem. Eng. Sci.* **2012**, *73*, 431–438. <https://doi.org/10.1016/j.ces.2012.02.015>
22. Aloisi, I.; Di Giuliano, A.; Di Carlo, A.; Foscolo, P.U.; Courson, C.; Gallucci, K. Sorption enhanced catalytic Steam Methane Reforming: Experimental data and simulations describing the behaviour of bi-functional particles. *Chem. Eng. J.* **2017**, *314*, 570–582. <https://doi.org/10.1016/j.cej.2016.12.014>
23. Zheng, Y.; Shi, Y.; Li, S.; Yang, Y.; Cai, N. Elevated temperature hydrogen/carbon dioxide separation process simulation by integrating elementary reaction model of hydrotalcite adsorbent. *Int. J. Hydrogen Energy* **2014**, *39*, 3771–3779. <https://doi.org/10.1016/j.ijhydene.2013.12.167>
24. Boon, J.; Cobden, P.D.; van Dijk, H.; van Sint Annaland, M. High-temperature pressure swing adsorption cycle design for sorption-enhanced water—Gas shift. *Chem. Eng. Sci.* **2015**, *122*, 219–231. <https://doi.org/10.1016/j.ces.2014.09.034>
25. Stankiewicz, A.I.; Moulijn, J.A. Process intensification: Transforming chemical engineering. *Chem. Eng. Prog.* **2000**, *96*, 22–34.
26. Keil, F.J. Process intensification. *Rev. Chem. Eng.* **2018**, *34*, 135–200. <https://doi.org/10.1515/revce-2017-0085>
27. Di Giuliano, A.; Pellegrino, E. Numerical integration strategies of PFR dynamic models with axial dispersion and variable superficial velocity: the case of CO₂ capture by a solid sorbent. *Heliyon* **2019**, *5*, e02040. <https://doi.org/10.1016/j.heliyon.2019.e02040>
28. Choi, Y.; Stenger, H.G. Water gas shift reaction kinetics and reactor modeling for fuel cell grade hydrogen. *J. Power Sources* **2003**, *124*, 432–439. [https://doi.org/10.1016/S0378-7753\(03\)00614-1](https://doi.org/10.1016/S0378-7753(03)00614-1)

29. Coenen, K.; Gallucci, F.; Hensen, E.; van Sint Annaland, M. Kinetic model for adsorption and desorption of H₂O and CO₂ on hydrotalcite-based adsorbents. *Chem. Eng. J.* **2019**, *355*, 520–531. <https://doi.org/10.1016/j.cej.2018.08.175>.
30. Moe, J.M. Design of water-gas shift reactors. *Chem. Eng. Prog.* **1962**, *58*, 8.
31. Poling, B.E.; Prausnitz, J.M.; O'Connell, J.P. *The Properties of Gases and Liquids*, 5th ed.; McGraw-Hill: New York, NY, USA, 2001.
32. Yang, R.T. *Gas Separation by Adsorption Processes*; Butterworths series in chemical engineering; Butterworths: Boston, MA, USA, 1987.
33. MathWorks. Solve 1-D parabolic and elliptic PDEs—MATLAB pdepe. Available online: <https://de.mathworks.com/help/matlab/ref/pdepe.html> (accessed on 19 January 2022).
34. Skeel, R.D.; Berzins, M. A Method for the Spatial Discretization of Parabolic Equations in One Space Variable. *SIAM J. Sci. Stat. Comput.* **1990**, *11*, 1–32. <https://doi.org/10.1137/0911001>.
35. Shampine, L.F.; Reichelt, M.W. The Matlab ODE suite. *SIAM J. Sci. Comput.* **1997**, *18*, 1–22.
36. Ukrainczyk, N.; Koenders, E.A.B. Numerical Model for Chloride Ingress in Cement Based Materials: Method of Lines Implementation for Solving Coupled Multi-species Diffusion with Binding. *Comput. Mater. Civ. Eng.* **2016**, *1*, 109–119.
37. MathWorks. Simulink Product Description—MATLAB & Simulink. Available online: <https://de.mathworks.com/help/simulink/gs/product-description.html> (accessed on 19 January 2022).
38. Puente León, F.; Jäkel, H. *Signale und Systeme*, 7th ed.; De Gruyter Studium, De Gruyter Oldenbourg: Berlin, Germany; Boston, MA, USA, 2019.
39. MathWorks. Choose a Solver—MATLAB & Simulink. Available online: <https://de.mathworks.com/help/simulink/ug/choose-a-solver.html> (accessed on 19 January 2022).
40. MathWorks. Overview of Stateflow Objects—MATLAB & Simulink. Available online: <https://de.mathworks.com/help/stateflow/ug/overview-of-stateflow-objects.html> (accessed on 19 January 2022).
41. Bayrak, G.; Abrishamchian, F.; Vogel-Heuser, B. Effiziente Steuerungsprogrammierung durch automatische Modelltransformation von Matlab/Simulink/Stateflow nach IEC 61131-3. *Autom. Prax.* **2008**, *50*, 49–55.

P III Dynamic Reactor Modeling

Dynamic simulation of a compact sorption-enhanced water-gas shift reactor

Published in Frontiers in Chemical Engineering 2022, 4:1000064
Publishing Date 25 October 2022
DOI <https://doi.org/10.3389/fceng.2022.1000064>



OPEN ACCESS

EDITED BY

Jurriaan Boon,
Netherlands Organisation for Applied
Scientific Research, Netherlands

REVIEWED BY

Zhiming Zhou,
East China University of Science and
Technology, China
Ki Bong Lee,
Korea University, South Korea
Vladimir Dikic,
Netherlands Organisation for Applied
Scientific Research, Netherlands

*CORRESPONDENCE

Peter Pfeifer,
peter.pfeifer@kit.edu

SPECIALTY SECTION

This article was submitted to Chemical
Reaction Engineering,
a section of the journal
Frontiers in Chemical Engineering

RECEIVED 21 July 2022

ACCEPTED 10 October 2022

PUBLISHED 25 October 2022

CITATION

Stadler TJ, Bender LJ and Pfeifer P
(2022), Dynamic simulation of a
compact sorption-enhanced water-gas
shift reactor.
Front. Chem. Eng. 4:1000064.
doi: 10.3389/fceng.2022.1000064

COPYRIGHT

© 2022 Stadler, Bender and Pfeifer. This
is an open-access article distributed
under the terms of the [Creative
Commons Attribution License \(CC BY\)](#).
The use, distribution or reproduction in
other forums is permitted, provided the
original author(s) and the copyright
owner(s) are credited and that the
original publication in this journal is
cited, in accordance with accepted
academic practice. No use, distribution
or reproduction is permitted which does
not comply with these terms.

Dynamic simulation of a compact sorption-enhanced water-gas shift reactor

Tabea J. Stadler, Laila J. Bender and Peter Pfeifer*

Institute for Micro Process Engineering (IMVT), Karlsruhe Institute of Technology (KIT), Karlsruhe, Germany

This work presents the dynamic simulation of a novel sorption-enhanced water-gas shift reactor used for synthesis gas production from pure CO in an e-fuels synthesis process. Due to the intended decentralized plant installation associated with fluctuating feed, process intensification and a compact reactor system is required. An optimized operating procedure was obtained by simulation-driven process design to maximize the sorbent loading and operate the process as efficient as possible. The process simulation is based on a simplified heterogeneous packed bed reactor model. The model accounts for simultaneous water-gas shift (WGS) reaction on a Cu-based catalyst and CO₂ adsorption on a K-impregnated hydrotalcite-derived mixed oxide as well as subsequent desorption. An empirical rate expression was chosen to describe the water-gas shift reaction according to experimental data at 250°C. Breakthrough experiments were performed and used to adapt kinetic adsorption (pressure: 8 bar) and desorption (pressure: 1 bar) parameters. The experimental CO₂ sorption equilibrium isotherm was fitted with the Freundlich model. The reactor model was extended to a complex hybrid system scale model for the pilot plant reactor consisting of six individually accessible reaction chambers. Cyclic operation with automatized switching time adjustment was accomplished by a finite state machine. A case study exploited the benefits of a serial process configuration of reaction chambers. It could be shown that the sorbent loading can be remarkably increased through optimized operating strategies depending on the process conditions. Hence, the development of the hybrid model marks a crucial step towards the planned pilot plant operation and control.

KEYWORDS

sorption-enhanced water-gas shift reaction, dynamic simulation, MATLAB Simulink Stateflow, experimental model validation, simulation-driven process optimization, micro-structured reactor design, high-temperature CO₂ adsorption

1 Introduction

Global CO₂ emissions unexpectedly dropped by 5.4% in 2020 due to the COVID pandemic, but pre-COVID levels have been reached again rapidly (UNEP, 2021). International aviation is among the top emitters. It released about 1 Gt CO₂ to the atmosphere in 2018 (Lee et al., 2021) and the global aviation industry expects

emissions to increase to about 1.2–1.9 Gt CO₂ in 2050 (Fleming and de L epinay, 2019). Although these predictions were made before the pandemic, they do not lose their long-term significance, because the pandemic-related impacts are expected to be only relevant until around 2024 (IATA, 2020).

To still achieve the Paris climate goals and limit global warming to well below 1.5°C, net zero CO₂ emissions have to be reached by around 2050 (IPCC, 2018). Hence, also the aviation sector has to undergo a transition away from fossil fuels until 2050. The decarbonization of aviation is especially demanding due to extremely long technology and fleet turnover times. Therefore, it is highly likely that planes still have to be powered with hydrocarbons in the upcoming decades. Sustainable aviation fuels (SAF) as fossil fuel substitutes remain the only reasonable near- to mid-term solution.

SAF can be classified into biofuels produced from biomass, and e-fuels obtained from renewable energy, CO₂ and water. Biofuel production technologies are already available in industrial scale, but biofuel availability is limited by natural and ethical constraints. The global SAF demand in 2050 cannot be met completely by biofuels under sustainable aspects, such as protecting ecosystems and ensuring availability of land and water without competition. E-fuels production, however, is primarily limited by the cost and availability of renewable energy.

Established e-fuels process routes include H₂ production *via* water electrolysis in combination with CO generation *via* reverse water-gas shift reaction from air-captured CO₂ (Kirsch et al., 2020). Synthesis gas (CO and H₂) is then chemically converted to e-fuels *via* Fischer-Tropsch reaction and further downstream processing steps (Stadler et al., 2022a).

The Kerogreen project currently investigates a novel e-fuels process route with an advanced synthesis gas production concept (Goede, 2018; Kerogreen, 2022). Compact, decentralized plants close to renewable energy production sites are envisaged. Here, CO₂ is split into CO and O₂ in a plasmolysis unit. Pure CO partly reacts with steam to H₂ *via* water-gas shift (WGS) reaction. The by-product CO₂ is removed *in-situ* and recycled to the plasmolysis unit. The energy for the plasmolysis unit is provided by renewable sources.

For the WGS process step with simultaneous CO₂ separation, the sorption-enhanced water-gas shift (SEWGS) reaction concept was chosen. SEWGS applications were first described by Gluud et al. (1931) and have been broadly discussed for H₂ production, purification, and pre-combustion capture technologies in the past decade (Jansen et al., 2013; Petrescu et al., 2019; Sebastiani et al., 2022). The concept is based on a homogeneous mixture of solid catalyst and sorbent material in a packed bed reactor. The catalyst

enables the exothermic WGS reaction (Eq. 1) while the sorbent is capable to adsorb the produced CO₂ under the prevailing process conditions, e.g., at elevated temperature (200°C–450°C). Hence, the thermodynamic boundary conditions are shifted towards favorable H₂ generation according to LeChatelier's principle.



The most intensively discussed materials for CO₂ adsorption include calcium oxide (Wang et al., 2013), magnesium oxide (Bhagiyalakshmi et al., 2010), lithium zirconate (Iwan et al., 2009), lithium silicate (Hu et al., 2019), activated carbon (Yin et al., 2013), molecular sieves (Siriwardane et al., 2001), zeolites (Mulloth and Finn, 1998), metal organic frameworks (Millward and Yaghi, 2005), and layered double hydroxides (Rives, 2002). Hydrotalcites (HTC) belong to the latter group and change their structure during thermal treatment to a hydrotalcite-derived mixed oxide (HDMO) form, so that suitable basic properties for CO₂ adsorption under WGS conditions are revealed (Le on et al., 2010; van Selow et al., 2011; Salom e Macedo et al., 2021). HDMOs are frequently employed in SEWGS processes due to their stable thermal and mechanical properties, good performance in the presence of steam, high adsorption selectivity towards CO₂, relatively fast sorption kinetics, low energy requirement for regeneration, and cyclic performance (Yong et al., 2001; Soria et al., 2015). Additionally, their cheap price makes them interesting for large scale applications. The relatively low adsorption capacity of HDMOs (typically below 1 mmol g⁻¹) can be improved by means of impregnation with alkali metal ions, namely potassium, to obtain potassium-impregnated hydrotalcite-derived mixed oxides (K-HDMO) (Oliveira et al., 2008; Du et al., 2010; Lee et al., 2010; Halabi et al., 2012; Zhu et al., 2017; Faria et al., 2022). K-HDMO was chosen as CO₂ adsorption material in this work.

Various catalysts (Fe-, Ni-, Cu-based) are applied in SEWGS systems (Lee et al., 2008; Beaver et al., 2009; Li et al., 2012; Cunha et al., 2015; Moreira et al., 2016; Cunha et al., 2017). The choice of catalyst depends mainly on the intended process operating conditions as well as on the employed sorbent. Occasionally, it has been reported that specific sorbent materials can exhibit sufficient catalytic activity, so that a separate catalyst may even be omitted (van Selow et al., 2013). Promising candidates in combination with K-HDMOs are Cu-based low-temperature WGS catalysts with operating temperatures from 200°C to 300°C (Soria et al., 2019). Such a catalyst was chosen in this work.

A major challenge in sorption-enhanced processes is caused by the relatively fast sorbent saturation. To enable continuous production, the sorbent has to be regenerated at

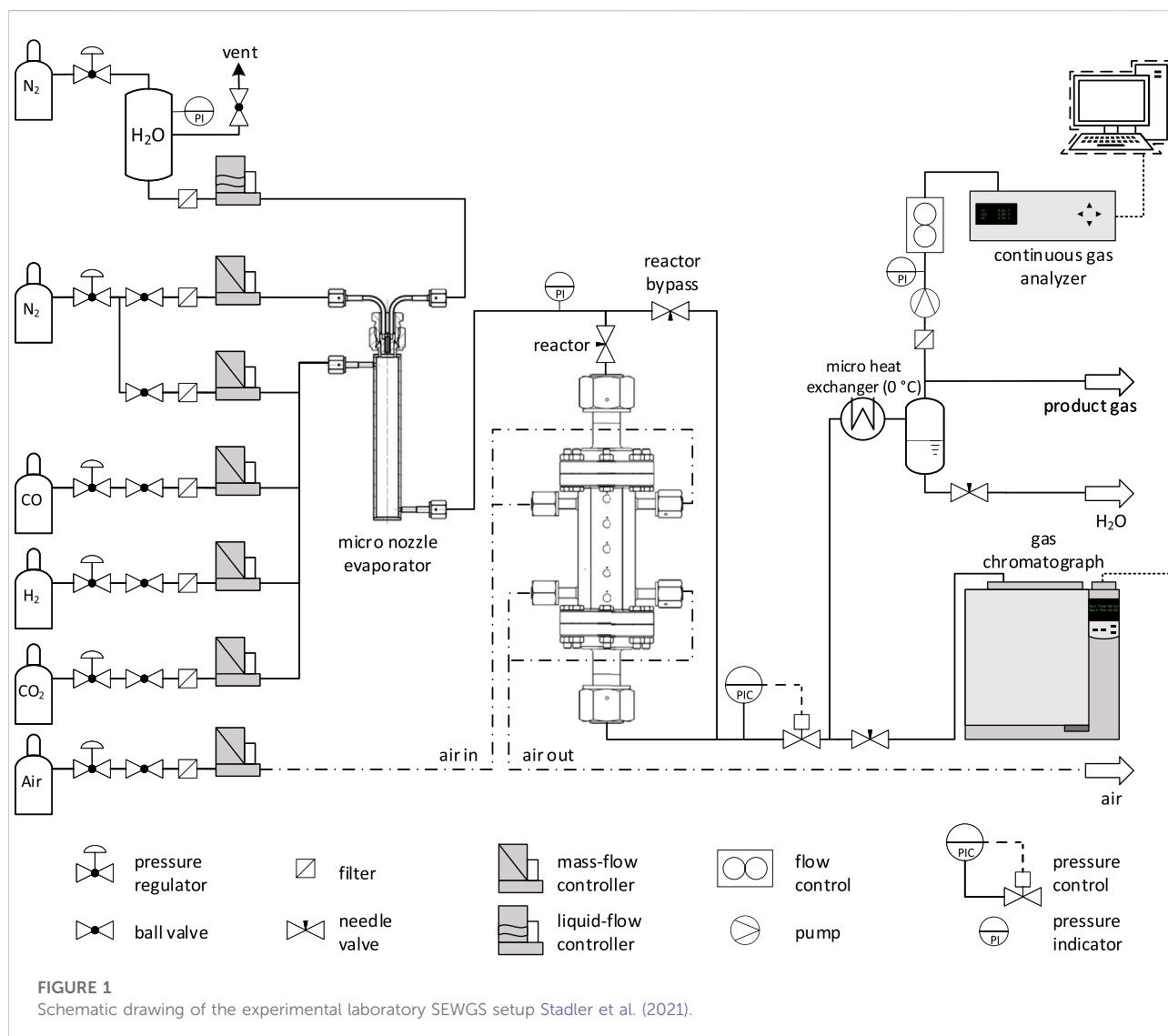
least at full saturation and cyclic operation of not less than two reactors is inevitable. A cycle may include reactive adsorption, depressurization, regeneration, and pressurization. Always (at least) one reactor is in reactive adsorption mode, while the other(s) is (are) in regeneration mode. The regeneration can either be triggered by temperature or by pressure changes. Typically, pressure swing adsorption (PSA) concepts are chosen for SEWGS systems alongside with purge gas for additional partial pressure reduction (Zhu et al., 2019). Due to the rather complex nature of a PSA-like SEWGS system with various interfering parameters, the definition of ideal operating conditions of the overall setup with multiple reactors can be challenging (Choi et al., 2003; Zheng et al., 2014). Modeling and simulation tools provide a time- and resource-efficient way to investigate a variety of influencing parameters that might be difficult to observe on a purely experimental basis in complex reaction systems. Therefore, advanced system scale models are needed to determine optimum (cyclic) operating strategies and ensure enhanced overall process performance and efficiency. System scale models are based on reactor and particle scale models to simulate reactive adsorption and subsequent regeneration.

Concerning reactor and particle scale models, significant effort was put on modeling the sorption behavior on K-HDMO under real working conditions, e.g., elevated temperature and pressure or in the presence of steam. Reactor as well as kinetic models are available in great depth. Recently, Martins et al. successfully modelled CO₂ capture from flue gas on K-HDMO at 623 K and 134 kPa in dry and wet conditions (Martins et al., 2022). They applied a bi-Langmuir equilibrium expression to consider CO₂ adsorption on two different sites and Elovich-type equations accounting for the heterogeneous adsorption/desorption activation energy. Coenen et al. (2019) intensively investigated the sorption mechanisms and kinetics of H₂O and CO₂ as well as the interactions of both components on K-HDMO. Their model includes three adsorption sites: two weaker chemisorption sites for H₂O and CO₂, respectively, and one exchange site for both gases. They concluded that the presence of steam remarkably influences the desorption behavior by means of exchanging CO₂ on the exchange site. Karagöz et al. (2019) developed a multi-scale process model with a Langmuir adsorption isotherm to quantify the catalyst and adsorbent effectiveness factors and stated a rapid convergence to a long-term cyclic solution. Likewise, a variety of kinetic expressions is given in literature for the WGS reaction rate on low-temperature Cu-based catalysts. Some suggestions include mechanistic aspects derived from redox (Uchida et al., 1967; Ovesen et al., 1996) or Langmuir-Hinshelwood-type models (Amadeo and Laborde, 1995), while others are purely

empiric (Ovesen et al., 1996; Choi and Stenger, 2003; Koryabkina et al., 2003). A comprehensive overview of WGS reaction models and proposed mechanisms is given by Smirniotis (2015).

Concerning system scale models, interesting concepts for multi-column PSA systems were published. For example, Boon et al. (2014) and Boon et al. (2015) presented the simulation of a complete SEWGS cycle consisting of eleven steps in a nine-column system. The simulation is based on their single column model and was used to establish an enhanced cycle design (Boon et al., 2014; Boon et al., 2015). Another multi-train model was developed by Najmi et al. (2016). Their system consists of eight parallel reactors and shows the influence of rinse and purge steam loads on CO₂ purity for predefined cycle times. The authors concluded that cycle times should be adjusted depending on the feed gas composition to maintain the target performance. More recently, Sebastiani et al. (2021) demonstrated a six reactor SEWGS model and validated it with single column and multi-column experiments with simulated blast furnace gas. Here, always one column is calculated, while the interacting column states are stored in a database for use upon requirement (Sebastiani et al., 2021).

So far, less attention has been paid to overall SEWGS modeling and practical operational concepts in small-sized apparatus under intensified process conditions. Therefore, we herein present the complete dynamic simulation of our compact pilot plant SEWGS reactor which was manufactured in the frame of the Kerogreen project. This diffusion-bonded reactor was designed for decentralized plant installation. It enables continuous cyclic operation in six packed bed reaction chambers, each with a separate in- and outlet. Due to space constraints that arise from the modular container-sized setup, the amount of available sorbent for CO₂ separation is very limited. For that reason, a carefully chosen operating strategy derived from simulation-driven process design is of utmost importance to increase the process' overall efficiency. A simplified mathematical description with experimentally determined kinetic parameters was used to model combined reaction and adsorption as well as consecutive desorption. The model accounts for mass transfer limited sorption kinetics, nonlinear adsorption equilibrium (Freundlich model), and empirical WGS reaction kinetics. It was extended for simulating the full pilot plant reactor on system scale. An elaborated graphical simulation approach in MATLAB Simulink was established to enable automated switching between reactive adsorption and regeneration in all six reaction chambers simultaneously. The hybrid system consisting of continuous states (reaction chamber conditions) and discrete states (valve positions) is controlled with a finite state machine in MATLAB Stateflow. This novel approach is capable to work without predefined switching times: switches from, e.g., reactive adsorption to regeneration occur



automatically based on the outlet CO_2 concentration to ensure constant product purity. A case study including different design configurations and process conditions was performed to identify optimum operating strategies regarding sorbent loading and process efficiency.

2 Materials and methods

2.1 Catalyst and sorbent

Commercial $\text{Cu}/\text{ZnO}/\text{Al}_2\text{O}_3$ WGS catalyst pellets were crushed and sieved to obtain particles with diameters from $100\ \mu\text{m}$ to $300\ \mu\text{m}$. Catalyst reduction took place *in-situ* under 3% H_2 in N_2 flow (up to 240°C), followed by pure H_2 flow from 240°C to 250°C .

K-HDMO served as CO_2 sorbent under WGS conditions. It was obtained through impregnation and calcination of Pural MG70 (Sasol GmbH, Germany), a HTC with $\text{Al}_2\text{O}_3:\text{MgO} = 30:70$. Pural MG70 was loaded with 20 wt% potassium to form potassium-impregnated HTC (K-HTC) by means of incipient wetness impregnation with potassium carbonate (K_2CO_3 , $\geq 99\%$, Sigma-Aldrich, United States). K-HTC was calcined *ex-situ* at 400°C in N_2 atmosphere for 10 h to K-HDMO. K-HDMO particles were crushed and sieved to keep the diameter range between $100\ \mu\text{m}$ and $300\ \mu\text{m}$.

2.2 CO_2 sorption isotherm

The physico-chemical characterization of K-HDMO in terms of a CO_2 sorption equilibrium isotherm was performed under

dry conditions with a 3Flex Surface Characterization instrument (Micromeritics Instrument Corporation, United States). Calcined and outgassed samples (~0.2 g) were exposed to pulses of analysis gas (CO₂) at 250°C (equilibration interval 20 s).

2.3 Experimental setup

Catalyst activity as well as breakthrough experiments were performed in the laboratory setup depicted in Figure 1. The results were used to estimate the model parameters introduced in Section 2.6. The gases N₂, CO, CO₂ and H₂ were fed into the system by calibrated mass flow controllers (Brooks Instrument, United States). Precise and pulsation-free steam supply was realized with a liquid flow controller (Brooks Instrument, United States) in combination with an electrically heated micro nozzle evaporator (manufactured inhouse). Unwanted condensation in the tubes was prevented by electrical heatings. All gases entered the stainless steel two-slit packed bed microchannel reactor (PBMR, manufactured inhouse), which was filled with catalyst and/ or sorbent particles, respectively. Isothermal reaction conditions in both reaction slits (each 2 mm × 50 mm × 100 mm) were ensured by five programmable electrical heating cartridges controlled by type K thermocouples, and tempering air-flow in adjacent microchannels. The reaction temperature was monitored continuously by additional type K thermocouples in the packed bed. The PBMR could optionally be bypassed for feed gas analysis. An automated valve (Flowserve, United States) regulated the system pressure. The steady-state wet gas composition was analyzed in a gas chromatograph (GC, Agilent 7890A, Agilent Technologies, United States) equipped with two columns (HP-Plot/Q and HP-Molsieve/5A, Agilent Technologies, United States) and two detectors (TCD and FID). N₂ served as internal standard and Ar as carrier gas. The CO, CO₂ and H₂ volume fractions in the dry effluent were continuously recorded in a process gas analyzer (PGA, X-STREAM Enhanced, Emerson, United States). CO and CO₂ were monitored by infrared-based detectors, and H₂ by a TCD. H₂O was removed from the gas flow in a micro heat exchanger (manufactured inhouse) in countercurrent flow with a cooling liquid (0°C). Both analyzers, GC and PGA, measured the respective gases within 1% of accuracy between each other. Further information related to the experimental setup can be found in (Stadler et al., 2021).

2.4 Water-gas shift catalyst activity experiments

For the catalyst activity tests, Cu/ZnO/Al₂O₃ particles were sufficiently diluted with silicon carbide (SiC, 100 μm–300 μm, ESK-SIC GmbH, Germany) and filled in the first quarter of the

PBMR reactor slits. The catalyst mass accounted for 0.50 g. The remaining space of the reactor slits was filled with pure SiC. This arrangement was chosen due to comparability with subsequent experiments and resulted from preliminary studies (Stadler et al., 2021). The feed gas flow rate was kept constant at 2,000 ml min⁻¹. The CO volume fraction was 0.1 and the steam content was varied to achieve Steam-to-Gas ratios between 0.5 and 4.5 (Eq. 2) balanced in N₂.

$$S/G = \frac{\dot{n}_{\text{H}_2\text{O,feed}}}{\dot{n}_{\text{CO,feed}}} \quad (2)$$

The reaction pressure was kept constant at 8 bar. The reaction temperatures were set to 225°C, 250°C, and 275°C, respectively. The temperature gradient in the catalyst bed was always kept below 1 K, hence isothermal conditions could be assumed.

GC measurements of feed and product gas compositions revealed carbon balances within 2% of closure, and no byproduct formation was detected. Preliminary tests with SiC filling without catalyst did not reveal blank activity. The steady-state conversion of CO was determined according to Eq. 3.

$$X_{\text{CO}} = \frac{\dot{n}_{\text{CO,feed}} - \dot{n}_{\text{CO}}}{\dot{n}_{\text{CO,feed}}} \quad (3)$$

2.5 CO₂ breakthrough experiments

The K-HDMO stability and cyclic working capacity was tested in typical breakthrough experiments with and without WGS catalyst under PSA conditions. Blank experiments with inert SiC particles of identical size (100 μm–300 μm, ESK-SIC GmbH, Germany) were used to determine the residence time distribution in the reactor, tubes, fittings and components. Preliminary tests without catalyst (K-HDMO sorbent only) ensured that the sorbent was not catalytically active for the WGS reaction at 8 bar and 250°C, as neither products nor byproducts of any kind were detected in the effluent.

In the first series of experiments, a pure K-HDMO filling (9.70 g) was packed into the PBMR for PSA breakthrough experiments. The adsorption step was investigated with a feed flow consisting of various compositions of CO, CO₂, H₂, and H₂O balanced in N₂. The step duration was 15 min at 8 bar and 250°C. CO and H₂ were fed for comparison with CO₂.

The second series of experiments was performed with a catalyst-sorbent-mixture PBMR filling. The first quarter of the reaction slits was packed with a homogeneous mixture of 0.51 g Cu/ZnO/Al₂O₃ catalyst and K-HDMO sorbent. The remaining space of the slits was packed with pure K-HDMO. The total sorbent mass was 9.35 g. Experimental reasons were responsible for minor deviations in the total packed bed filling weight of the two series. The reactive adsorption feed flow was varied regarding the compositions of CO and H₂O balanced in N₂. The duration of

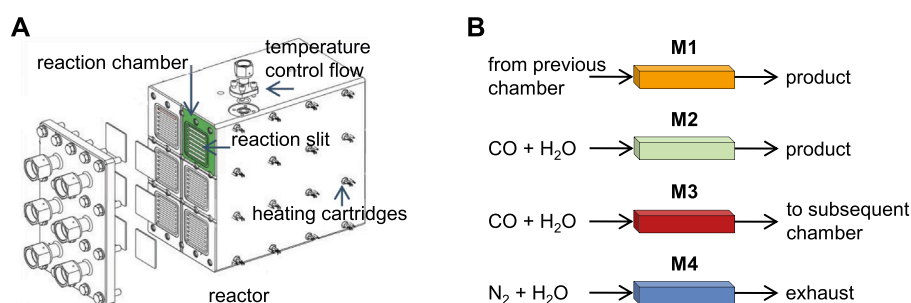


FIGURE 2

(A) Compact SEWGS pilot plant reactor with six individually fed reaction chambers, each consisting of seven rectangular slits. Microchannels and heating cartridges enable advanced temperature control for isothermal operation in the slits. Uniform gas distribution in the slits is realized by means of sintered metal plates. (B) Pilot plant reactor operation modes. M2 stands for reactive adsorption with fresh feed, and M4 for regeneration with purge flow. M1 and M3 (both reactive adsorption) occur only in serial configuration, when the outlet of one reaction chamber is optionally connected to the inlet of the subsequent reaction chamber Stadler et al. (2022b).

the reactive adsorption step was always 15 min at 8 bar and 250°C.

In both experimental series, the regeneration step was performed at 1 bar, 250°C, and lasted for 40 min. The regeneration purge gas consisted always of 40% H₂O and 60% N₂.

A LabVIEW process control program (National Instruments, United States) enabled fully automated reproducible PSA operation. All experiments were repeated with at least five and maximum 70 cycles.

2.6 Sorption-enhanced water-gas shift process model

A hybrid dynamic reactor model was developed to describe simultaneous reaction and adsorption, as well as consecutive desorption on a homogeneous catalyst-sorbent-mixture. The model is capable to automatically compute and adjust cyclic PSA switching times during runtime according to a defined threshold. This threshold can, for example, be a defined CO₂ concentration in the product flow.

The model aims to predict and plan the operation of the pilot plant reactor depicted in Figure 2A. The pilot plant reactor is basically an extended version of the laboratory-scale two-slit PBMR. It consists of six parallel reaction chambers, each with a separate in- and outlet, merged in one diffusion-bonded apparatus (manufactured inhouse). For continuous H₂ production in cyclic operation, at least one reaction chamber must be in reactive adsorption mode. Subsequent chambers can optionally be interconnected in series to maximize sorbent loading, hence, increase the time span of reactive adsorption. An overview of operation modes for the pilot plant reactor is given in Figure 2B. In serial configuration, M1-4 take place, while in single stage configuration (without interconnected chambers) only

M2 and M4 occur. In the real pilot plant as well as in the model, the switch between different modes is realized by means of discrete valve positions.

2.6.1 Conservation equations in bulk and particle phase

A simplified set of differential algebraic equations was used to describe WGS reaction and CO₂ adsorption as well as desorption in a packed bed reactor model. The homogeneous mixture of identically sized catalyst and sorbent particles was assumed as one phase. Time- and space (axially) resolved mole balances for bulk and particle phase are given in Table 1.

Internal mass transfer limitations were considered (according to Weisz-Prater-criterion) with a linear driving force (LDF) model (in line with Glueckauf-criterion), while external limitations could be neglected (proven by Maers-criterion). The initial conditions for the first step represented a fresh sorbent, while all subsequent PSA steps based on the conditions at the end of the previous step. Dirichlet boundary conditions arising from the feed flow were applied at the inlet, and Neumann boundary conditions at the outlet of each reaction chamber. Negligible pressure drop as well as the absence of gradients rectangular to flow direction could be assumed owing to the technical properties of the reactor. Isothermal conditions in the slits were realized by an advanced temperature control system: electrical heating cartridges in combination with adjacent tempering channels, where purge gas is fed through, enable excellent heat transfer.

2.6.2 Reaction and adsorption kinetics

A power law kinetic expression in combination with Arrhenius' equation (Eq. 4) was used to describe the experimental observations for the WGS reaction rate. This type of empirical expression is frequently found in literature for resembling catalysts (Smirniotis, 2015). The reaction

equilibrium constant is a function of temperature and was calculated with the well-established correlation given in Eq. 5 (Moe, 1962).

$$r_{WGS} = k_{co} \cdot \exp\left(-\frac{E_a}{R \cdot T}\right) \cdot \left(p_{CO} \cdot p_{H_2O} - \frac{p_{CO_2} \cdot p_{H_2}}{K_{eq}}\right) \quad (4)$$

$$K_{eq} = \exp\left(\frac{4577.8}{T} - 4.33\right) \quad (5)$$

The equilibrium-based ad- and desorption of CO₂ on K-HDMO surface was modelled with Eqs 6, 7, respectively (Zhu et al., 2017; Coenen et al., 2019; Martins et al., 2022).

$$a_{ads,CO_2} = k_{ads} \cdot (q_{CO_2}^{eq} - q_{CO_2}) \quad (6)$$

$$a_{des,CO_2} = k_{des} \cdot (q_{CO_2}^{eq} - q_{CO_2}) \quad (7)$$

The adsorption rate coefficient was assumed to be a function of temperature and can therefore be fitted directly. The desorption rate coefficient was described by an Arrhenius-type expression (Eq. 8). Due to the heterogeneity of the surface, an Elovich-type equation was employed to describe the activation energy of desorption (Eq. 9) (Ho, 2006). The number of fitted parameters was reduced by simplifying Eqs 8–10 (Coenen et al., 2019).

$$k_{des} = k_{des}^0 \cdot \exp\left(-\frac{E_{a,des}}{R \cdot T}\right) \quad (8)$$

$$E_{a,des} = E_{a,des}^0 - \beta_{des} \cdot \left(\frac{q_{CO_2}}{q_{max}}\right) \quad (9)$$

$$k_{des} = k_{des}^1 \cdot \exp\left(-\frac{\left(-\beta_{des} \cdot \frac{q_{CO_2}}{q_{max}}\right)}{R \cdot T}\right) \quad (10)$$

The equilibrium isotherm for CO₂ adsorption on K-HDMO was modelled with the empirical Freundlich equation for heterogeneous surfaces (Eq. 11).

$$q_{CO_2}^{eq} = k_{Fr} \cdot p_{CO_2}^{\frac{1}{n}} \quad (11)$$

2.7 Model parameters

The SEWGS model comprises a set of various parameters and properties, which have to be defined,

measured or calculated: Axial dispersion coefficients were determined according to Eq. 12 (Guffanti et al., 2021). Linear driving force approximation coefficients resulted from Eq. 13 (Yang, 1987). Gas mixture diffusion coefficients and effective diffusion coefficients were taken from (Poling et al., 2020).

$$D_{ax,i} = D_{mix,i} \cdot \sqrt{\varepsilon_b} + u \cdot r_p \quad (12)$$

$$k_{LDF,i} = \frac{15 \cdot D_{eff,i}}{r_p^2} \quad (13)$$

Kinetic and sorption isotherm parameters were obtained through nonlinear least-squares regression by minimization of the objective function (Eq. 14). Optimized parameters contained in ϕ were computed in MATLAB by the optimization solver `lsqnonlin`.

$$F(\phi) = \sum \left(\frac{y_{sim}(\phi) - y_{exp}}{y_{sim}(\phi)} \right)^2 \quad (14)$$

Table 2 gives an overview of all required information concerning the operating conditions in the simulation base case.

2.8 Numerical solution

A novel graphical implementation approach was applied for solving the set of partial differential and algebraic equations simultaneously in all six reaction chambers in the MATLAB Simulink programming environment (Figure 3). The implementation is based on the Method-of-Lines with uniform spatial discretization in up to 100 finite differences. It employs the built-in solver `ode23t` for moderately stiff ordinary differential equations. The cyclic PSA operation was performed by a state-machine created in the Simulink add-on Stateflow. This state-machine switches the PSA modes by leveraging discrete valve positions just like in the real plant. Switches from reactive adsorption to regeneration during runtime can, for example, be triggered by a predefined threshold of CO₂ in the product gas. Detailed information on the implementation method and numerical solution of the hybrid model can be found in our recent publication (Stadler et al., 2022b).

TABLE 1 Reactor model equations for bulk and particle phase.

Bulk gas phase	$\varepsilon_b \frac{\partial c_i}{\partial t} = -u \frac{\partial c_i}{\partial z} + \varepsilon_b D_{ax,i} \frac{\partial^2 c_i}{\partial z^2} + (1 - \varepsilon_b) k_{LDF,i} (\bar{c}_i - c_i)$	(15)
Particle void phase	$\varepsilon_p \frac{\partial \bar{c}_i}{\partial t} = \varepsilon_p k_{LDF,i} (c_i - \bar{c}_i) + w_{cat} \rho \nu_i r_{WGS} - (1 - w_{cat}) \rho a_{ads/des,i}$	(16)
Particle solid phase	$\frac{\partial q_{CO_2}}{\partial t} = a_{ads/des,CO_2}$	(17)

$i = CO, H_2O, CO_2, H_2, N_2$. $\nu_i = -1$ for $i = CO, H_2O$; $\nu_i = 1$ for $i = CO_2, H_2$; $\nu_i = 0$ for $i = N_2$. $a_{ads/des,i} = 0$ for $i = CO, H_2O, H_2, N_2$; $a_{ads/des,i} = \text{Eq. 6/Eq. 7}$ for $i = CO_2$.

TABLE 2 Parameters and operating conditions used in the pilot plant base case simulation.

Reactor dimensions		
Number of chambers		6
Number of slits per chamber		7
Rectangular slit dimensions		4 mm × 50 mm × 300 mm
General parameters		
Bed void fraction	ϵ_b	0.4
Particle void fraction	ϵ_p	0.5
Bulk density	ρ	1,096 kg m ⁻³
Particle radius	r_p	100 μm
Catalyst weight fraction ^a	w_{cat}	0.05
Adsorption parameters		
Pressure	p	8 bar
Temperature	T	250°C
Flow rate	F_{STP}	1,000 ml min ⁻¹
CO volume fraction	$y_{CO,feed}$	0.3
H ₂ O volume fraction	$y_{H_2O,feed}$	0.6
N ₂ volume fraction	$y_{N_2,feed}$	0.1
Desorption parameters		
Pressure	p	1 bar
Temperature	T	250°C
Flow rate	F_{STP}	500 ml min ⁻¹
H ₂ O volume fraction	$y_{H_2O,feed}$	0.4
N ₂ volume fraction	$y_{N_2,feed}$	0.6

^aCatalyst is homogeneously mixed with sorbent in the first quarter of the reactor length.

3 Results and discussion

3.1 Water-gas shift catalyst activity

The empirical WGS reaction rate expression (Eq. 4) adequately described the catalyst's behavior under the prevailing conditions in the SEWGS system. Experimental CO conversion rates for three different temperatures are shown together with fitted model data in Figure 4. The fitted kinetic parameters are listed in Table 3. The values for the frequency factor as well as the activation energy are comparable to those presented in literature for resembling catalysts, albeit, slightly lower conversions were obtained (Choi and Stenger, 2003; Smirniotis, 2015).

3.2 CO₂ sorption on K-HDMO

The Freundlich adsorption equation (Eq. 11) provided a good fit for the measured CO₂ equilibrium isotherm on K-HDMO at 250°C under dry conditions (Figure 5). The empirical correlation

was capable to account for the heterogeneity of the sorbent's surface (Al-Ghouti and Da'ana, 2020). It required the definition of the temperature-dependent adsorption intensity, which is an indicator for the adsorption strength, and the Freundlich coefficient, which is related to the adsorption capacity (Dada et al., 2012). As $1/n_{Fr}$ is smaller than one, normal adsorption can be assumed. The fitted parameters are listed in Table 3. The CO₂ uptake of the self-prepared sorbent was relatively low compared to resembling sorbents reported in literature, where adsorption capacities ranging from 0.1 mmol g⁻¹ to 1 mmol g⁻¹ can be found (Iruetagoiena Ferrer, 2016).

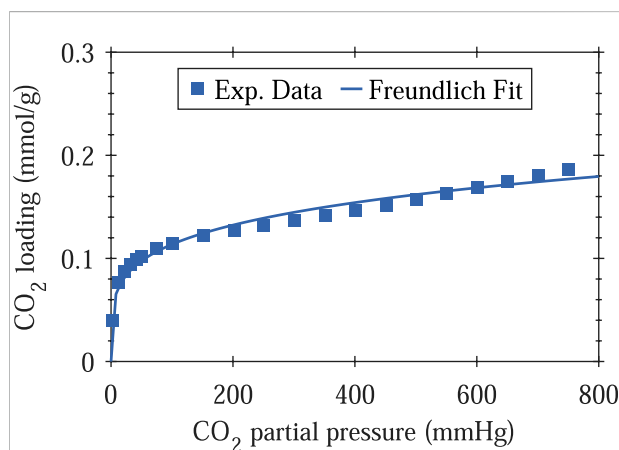
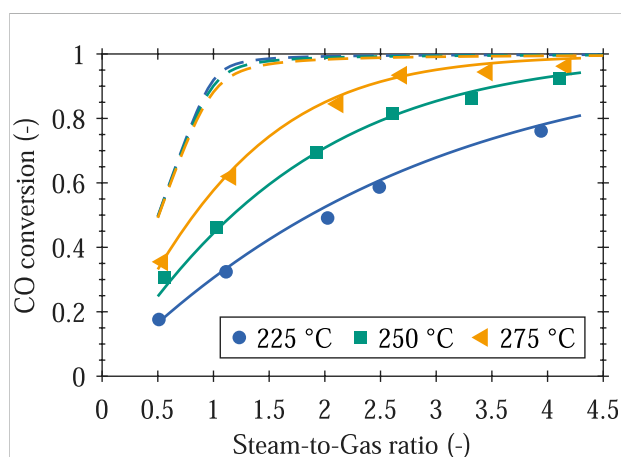
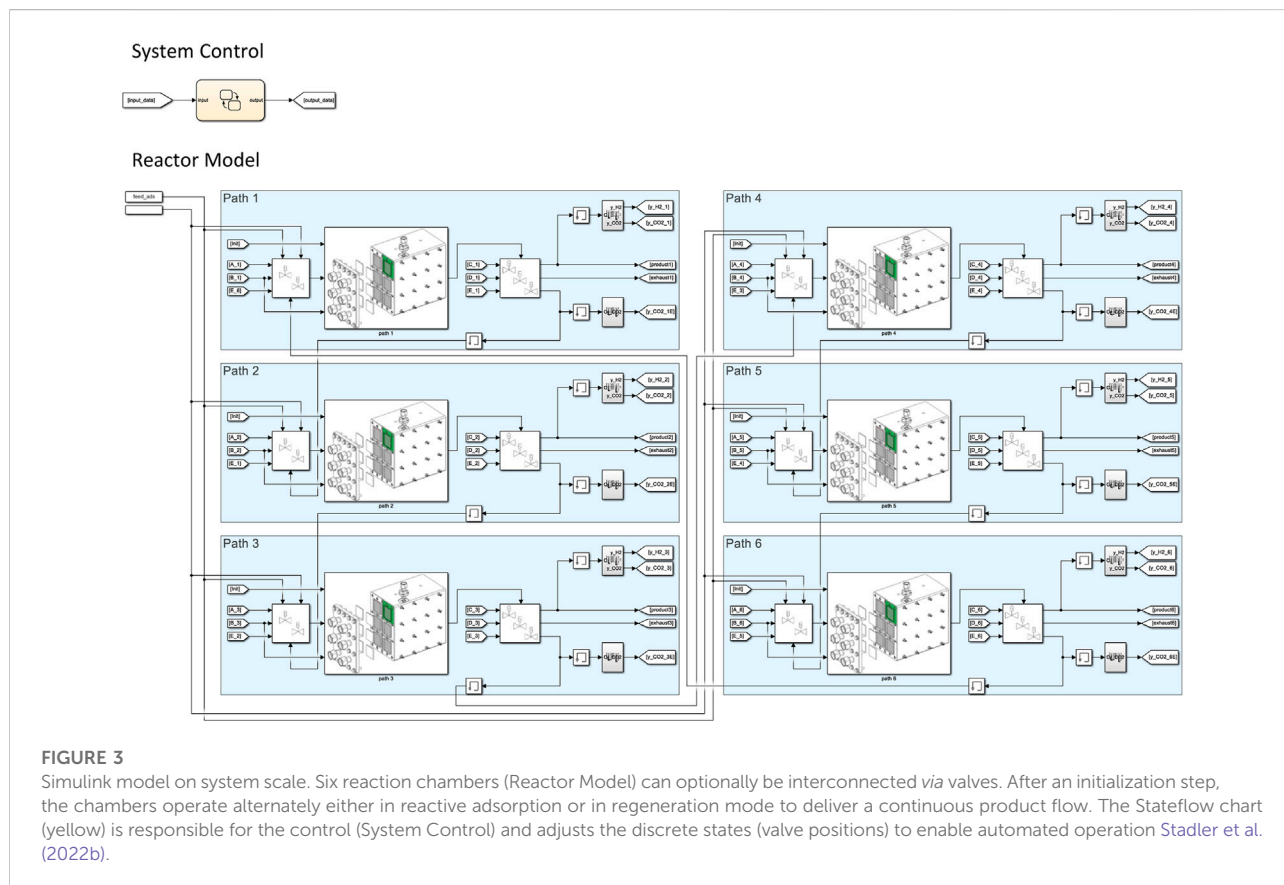
3.3 Breakthrough experiments

The breakthrough experiments in the single reaction chamber PBMR revealed an appropriate stability and cyclic working capacity for the tested PSA conditions.

In Figure 6, the first five cycles of an experimental run with pure K-HDMO filling are shown. Non-adsorbing CO was co-fed for comparison with adsorbing CO₂, and the time shift between the evolution of the gases indicated CO₂ adsorption on K-HDMO. After the first cycle, a significant loss of sorption capacity was observed. Due to severe back-mixing in the tubes and in other parts downstream the reactor, no sharp ramp, as expected for ideal plug-flow behavior, was detectable. Therefore, the residence time distribution for the employed reactor had to be considered for quantitative claims.

Experimental results for a long-term run with catalyst-sorbent-mixture filling are presented in Figure 7. Back-mixing and residence time distribution also had an apparent effect on the breakthrough curves here. It has been proven that long-term operation up to at least 70 cycles was possible (depicted are the curves for cycle 1, 3, 13, 43, 63). A constant steady-state CO conversion of 89.6% was reached, and the time shift between H₂ and CO₂ changed less than 20% over 70 cycles. During desorption (cycle 2 to cycle 70), a relatively constant value of (0.011 ± 0.002) mmol_{CO₂} g⁻¹ was released from the sorbent.

A computational approach was applied to estimate the kinetic parameters proposed in the model in Section 2.6. Blank experiments were implemented to account for the residence time distribution of the gas flow in the overall setup to get a set of appropriate parameters which best fit the experimental data for the tested process conditions. To account for the significant drop in sorption capacity due to irreversible bulk carbonate formation, the first cycle was not considered for the parameter estimation. The maximum sorbent loading was required to express the dependence of the desorption rate from the surface coverage (Eq. 10) and was calculated for a pressure of 20 bar, as also done by others (Coenen et al., 2019). Experimental and modelled curves are shown together in Figure 8 for the third cycle on K-HDMO without (Figure 8A) and with catalyst (Figure 8B) for a feed consisting of 5% CO and



20% H₂O, balanced in N₂. It can be seen that the initial increase is fitted quite well, while the experimental and simulated CO curves in the upper part deviate when approaching the final state.

TABLE 3 Kinetic and equilibrium parameters obtained by nonlinear regression from experimental data.

WGS reaction rate parameters	
k_{CO}	$2.01 \times 10^5 \text{ mol bar}^{-2} \text{ g}^{-1} \text{ h}^{-1}$
E_a	$51.845 \text{ kJ mol}^{-1}$
Isotherm parameters	
k_{Fr}	$0.177 \text{ mmol g}^{-1} \text{ bar}^{-n_{\text{Fr}}}$
$1/n_{\text{Fr}}$	0.220
Sorption kinetic parameters	
k_{ads}	0.1125 s^{-1}
k_{des}^1	$5.38 \times 10^{-4} \text{ s}^{-1}$
β_{des}	$74,000 \text{ J mol}^{-1}$

The set of kinetic parameters obtained by non-linear regression over a series of experiments is listed in Table 3. This model calibration can be used for simplified SEWGS simulation and is only valid for the tested conditions and materials. Simplifying assumptions had to be made due to experimental limitations. More elaborated models should additionally account for the highly important interactions of steam with the sorbent to describe the competitive adsorption of CO_2 and H_2O on K-HDMO (Coenen et al., 2019; Sebastiani et al., 2021). Therefore, an enhanced multi-component isotherm, as suggested by Boon et al. (2014) is required. Furthermore, a smaller setup with less pronounced influence of residence time distribution could lead to more precise data. Further experiments at different temperatures may be performed to further validate and refine the estimated model parameters.

However, the simplified parameterized model presented here served as a sufficient base considering setup and simulation times. The dynamic simulations on system scale can be used to determine real plant operating conditions.

3.4 Dynamic simulation

The dynamic MATLAB Simulink model on system scale enabled insights into every axial position of every reaction chamber of the pilot plant reactor at every time step. Due to automated switching between different modes during runtime, the influence of key operating parameters and design configurations on the overall process performance could be investigated.

Figure 9 presents MATLAB Simulink results for the pilot plant base case simulation in single stage configuration (Figures 9A,C,E) and serial (Figures 9B,D,F) configuration. The switch from M2 to M4 (single stage configuration) or M3 (serial configuration), respectively, was triggered as soon as the CO_2 fraction at the outlet of the reaction chamber exceeded $y_{\text{CO}_2} > 0.05$. Thus, the product purity in both cases was comparable. The switch from M3 to M4 in serial configuration occurred when $y_{\text{CO}_2} > 0.15$ for the gas being fed to the subsequent chamber. The operating schedules depicted in Figures 9A,B demonstrate that both configurations enabled the generation of high pressure H_2 in a single unit operation. As always at least one reaction chamber was in M2, continuous H_2 production was realized while the CO_2 content in the product was always kept below 5%. Cyclic studies exhibited that the process reached cyclic steady-state behavior within the first four operating cycles, what is well in line with previously published observations (Karagöz et al., 2019). The time spans of each operation mode (in Figures 9C,D

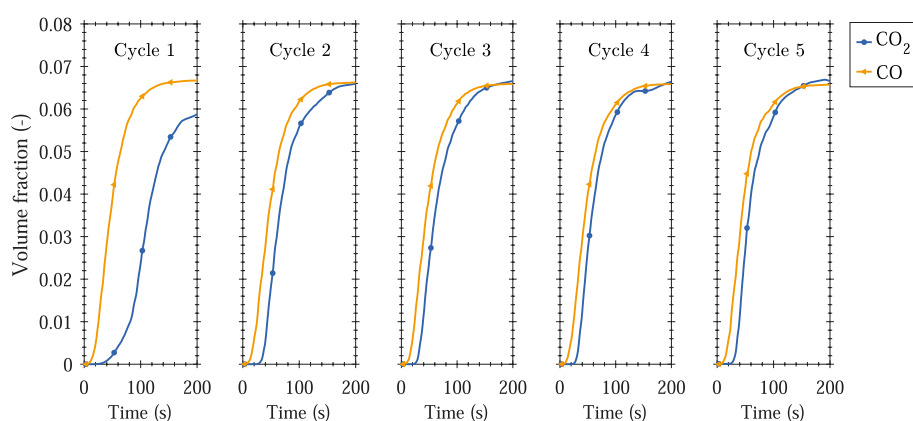


FIGURE 6

Experimental breakthrough curves (dry volume fraction) of CO_2 and CO for the first five adsorption cycles on pure K-HDMO sorbent (no catalyst). CO is shown for comparison. Sorbent mass: 9.70 g, temperature: 250°C , pressure: 8 bar, feed composition: 0.05/0.05/0.05/0.2/0.65 $\text{CO}_2/\text{H}_2/\text{H}_2\text{O}/\text{N}_2$. Regeneration pressure: 1 bar, regeneration feed composition: 0.4/0.6 $\text{H}_2\text{O}/\text{N}_2$.

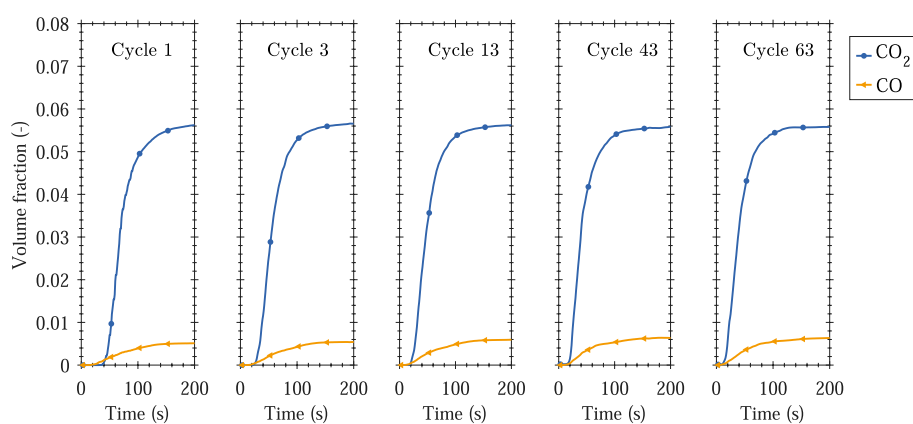


FIGURE 7

Experimental breakthrough curves (dry volume fraction) of CO₂ and CO for adsorption cycles 1, 3, 13, 43, and 63 on K-HDMO sorbent and Cu/ZnO/Al₂O₃ catalyst. Sorbent mass: 9.35 g, catalyst mass: 0.51 g, temperature: 250°C, pressure: 8 bar, feed composition: 0.05/0.2/0.75 CO/H₂O/N₂. Regeneration pressure: 1 bar, regeneration feed composition: 0.4/0.6 H₂O/N₂. Catalyst is homogeneously mixed with sorbent material in the first quarter of the reactor.

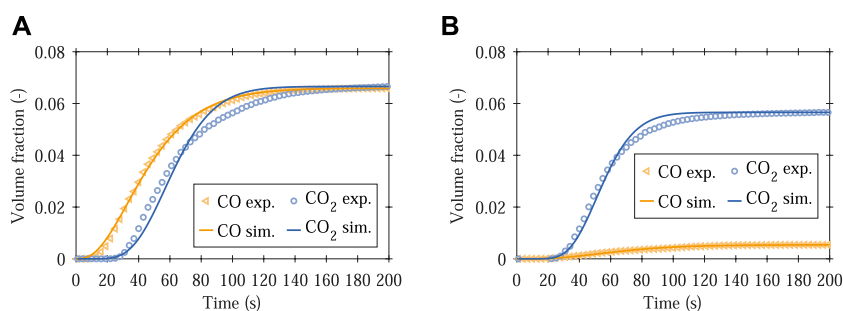


FIGURE 8

Exemplary experimental and simulated breakthrough curves. (A) third cycle on pure K-HDMO sorbent (see Figure 6), (B) third cycle on K-HDMO sorbent and Cu/ZnO/Al₂O₃ catalyst (see Figure 7).

shown for the first five cycles in chamber 1) did not change anymore after cycle 4. The relative sorbent loadings at the end of each operation mode based on the maximum loading (determined after 600 s reactive adsorption) are depicted in Figures 9E,F for the first five cycles in chamber 1. Owing to the serial configuration, the sorbent loading in each cycle could be increased by 7% compared to single stage configuration. Thus, interconnected reactor chambers in serial configuration can improve the overall performance of the process operation.

Figure 10 illustrates the CO₂ loading at the end of each reactive adsorption mode in serial configuration for the fifth cycle in chamber 1 over the reactor chamber length. Cycle 5 has an exemplary significance as the system already attained its long-term behavior by then. Chamber 1 was arbitrarily chosen and could be replaced by every other chamber, too. In both cases,

Figures 10A,B, the switch from M2 to M3 was triggered as soon as the CO₂ fraction in the product gas at the outlet of the reaction chamber reached $y_{\text{CO}_2} > 0.05$. The switch from M3 to M4 occurred when the CO₂ volume fraction to the subsequent chamber was $y_{\text{CO}_2} > 0.10$ (Figure 10A), or $y_{\text{CO}_2} > 0.15$ (Figure 10B). The larger area at the end of M3 in Figure 10B compared to Figure 10A shows that the K-HDMO loading could notably be improved with increasing M3-M4 threshold. Consequently, higher sorbent loadings could be realized resulting in longer cycle time spans and better efficiencies.

The influence of the M2-M4 threshold (in single stage configuration) is depicted in Figure 11. This key operating parameter controlled the switch from reactive adsorption to desorption and thereby, the purity of the product gas. The

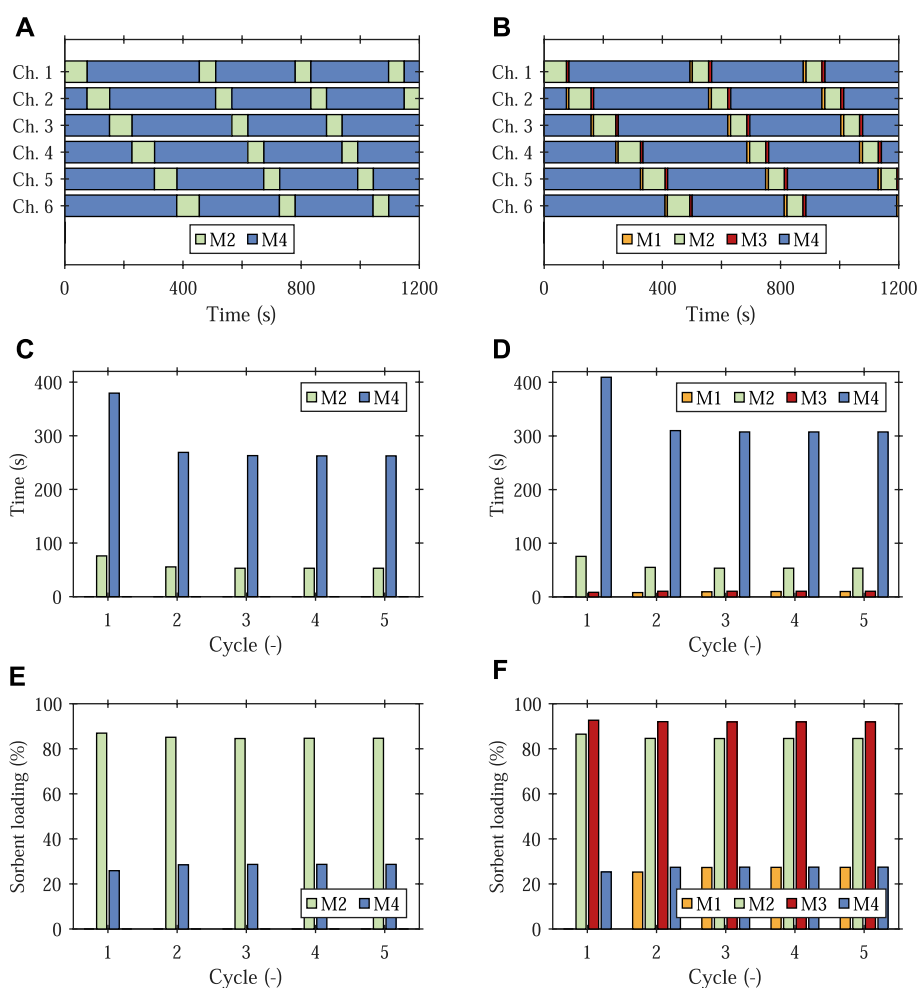


FIGURE 9

MATLAB Simulink results for the pilot plant base case simulation in single stage configuration (A,C,E) and serial configuration (B,D,F). The switch from M2 to M4 (single stage configuration) or M3 (serial configuration), respectively, is triggered as soon as $y_{(\text{CO}_2)} > 0.05$ in the outlet of the reaction chamber. The switch from M3 to M4 in serial configuration occurs when the CO_2 volume fraction to the subsequent chamber is $y_{(\text{CO}_2)} > 0.15$. (A,B) Operating schedule for all six reaction chambers, (C,D) Time span of each operation mode for the first five cycles in chamber 1, (E,F) Relative sorbent loading at the end of each operation mode for the first five cycles in chamber 1.

time span of M2 as well as the relative sorbent loading at the end of M2 increased with increasing M2-M4 threshold (Figure 11A). The latter observation is illustrated in terms of the CO_2 loading over the reactor length for various M2-M4 thresholds in Figure 11B. Here, it becomes apparent that the highest potential for intensified sorbent loading is given in the last third of the reactor length.

Another key operating parameter was found to be the adsorption-to-desorption flow ratio. With increasing adsorption flow, the time span of M2 as well as the sorbent loading at the end of M2 decreased (Figure 12A). However, the fraction of H_2 in the product gas remained constant and the product flow increased linearly with increasing feed. The sorbent loading over the whole reactor length was remarkably influenced

by the flow ratio (Figure 12B). Thus, a trade-off between reasonably high product flows and adequate sorbent loadings must be made to achieve acceptable switching times and process efficiencies. A less pronounced influence on the system behavior has been detected for the catalyst weight fraction. This parameter was varied from 0.02 to 0.08 and no remarkable effect on neither time span, sorbent loading nor H_2 production was observed.

Based on this case study performed with the novel simulation approach, important insights regarding the planned pilot plant operation and control could be gained by simulation-driven process design. Fast switching times and low sorbent loadings should be avoided in the compact pilot plant reactor to increase the process' efficiency and improve its overall performance.

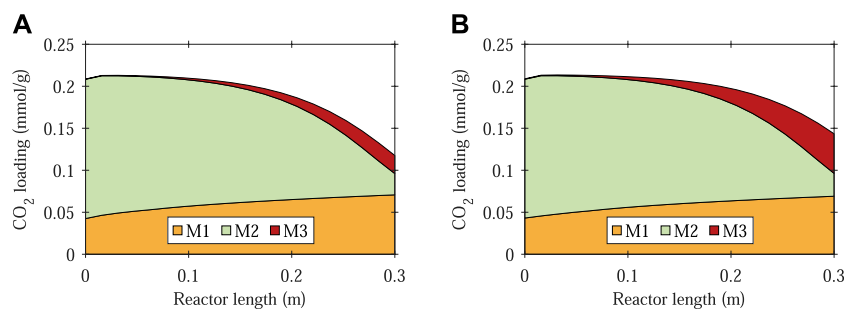


FIGURE 10
 MATLAB Simulink results for the pilot plant base case simulation in serial configuration. CO₂ loading at the end of each reactive adsorption mode for cycle 5 in chamber 1 over the reactor length. The switch from M2 to M3 is triggered as soon as $y_{(CO_2)} > 0.05$ at the outlet of the reaction chamber. The switch from M3 to M4 occurs when the CO₂ volume fraction to the subsequent chamber is (A) $y_{(CO_2)} > 0.10$, (B) $y_{(CO_2)} > 0.15$.

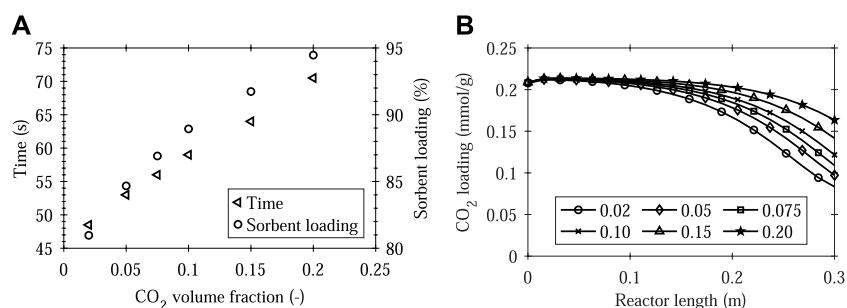


FIGURE 11
 MATLAB Simulink results for the pilot plant base case simulation with various $y_{(CO_2)}$ thresholds (switch M2 to M4) in single stage configuration. (A) Time span of M2, and relative sorbent loading at the end of M2 as a function of the threshold CO₂ volume fraction (cycle 5 in chamber 1), (B) CO₂ loading at the end of M2 over the reactor length for various CO₂ volume fraction thresholds (cycle 5 in chamber 1).

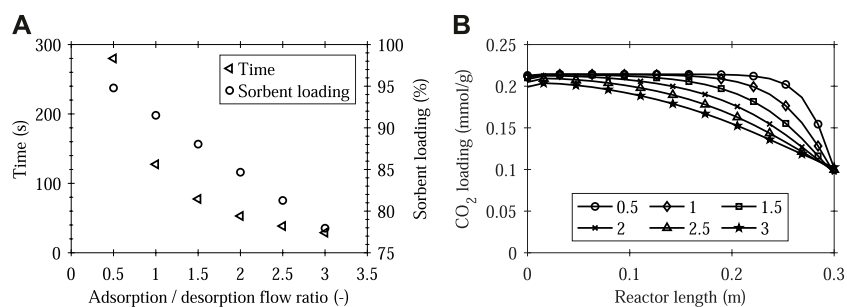


FIGURE 12
 MATLAB Simulink results for the pilot plant base case simulation with various adsorption-to-desorption flow ratios in single stage configuration. The switch from M2 to M4 is triggered as soon as $y_{(CO_2)} > 0.05$ in the outlet of the reaction chamber. (A) Time span of M2, and relative sorbent loading at the end of M2 as a function of the adsorption-to-desorption flow ratio (cycle 5 in chamber 1), (B) CO₂ loading at the end of M2 over the reactor length for various adsorption-to-desorption ratios (cycle 5 in chamber 1).

4 Conclusion

A novel compact SEWGS reactor has been designed and built. It produces synthesis gas ($\text{CO} + \text{H}_2$) from pure CO in an advanced e-fuels process route. The overall process is currently demonstrated in a pilot plant. Simulation-driven process design was applied to determine optimized operation procedures for the intended reactor operation. Therefore, a comprehensive MATLAB Simulink model on system scale was developed. It is based on a reactor scale model accounting for simultaneous WGS reaction and CO_2 adsorption as well as consecutive desorption. It employs an empirical rate expression for the WGS reaction rate and the Freundlich isotherm model for CO_2 adsorption equilibrium. The kinetic and equilibrium parameters were fitted to experimental data obtained in laboratory-scale experiments and adequately described the process. The dynamic system scale model was used to quantify the influence of design configurations and key operating process parameters. The simulation case study revealed rapid convergence to a final periodic solution after the fourth cycle and continuous product generation. It was shown that the serial configuration with interconnected reaction chambers lead to intensified sorbent loading compared to simple single stage operation by 7%. Hence, better efficiencies could be realized due to longer cycle times. Investigations in single stage configuration exhibited a trade-off between high throughput (high adsorption flow) and high product purity (low M2-M4 threshold) which considerably determined the length of the switching times and the degree of the sorbent loading. Consequently, the dynamic simulation provided process guidelines for practical application to maximize switching time spans and sorbent loadings. It enabled valuable insights on how to operate the compact pilot plant reactor as efficient as possible with improved overall performance.

Data availability statement

The original contributions presented in the study are included in the article, further inquiries can be directed to the corresponding author.

References

- Al-Ghouti, M. A., and Da'ana, D. A. (2020). Guidelines for the use and interpretation of adsorption isotherm models: A review. *J. Hazard. Mater.* 393, 122383. doi:10.1016/j.jhazmat.2020.122383
- Amadeo, N., and Laborde, M. (1995). Hydrogen production from the low-temperature water-gas shift reaction: Kinetics and simulation of the industrial reactor. *Int. J. Hydrogen Energy* 20, 949–956. doi:10.1016/0360-3199(94)00130-R
- Beaver, M. G., Caram, H. S., and Sircar, S. (2009). Selection of CO_2 chemisorbent for fuel-cell grade H_2 production by sorption-enhanced water

Author contributions

TS conducted the conception and design of the study, performed the simulations and data analysis, and wrote the first draft of the manuscript. LB and TS carried out the experiments. PP was responsible for the conceptual design of the research project. All authors contributed to manuscript revision, read, and approved the submitted version.

Funding

The work presented in this paper is part of the European project Kerogreen, which has received funding from the European Union's Horizon 2020 research and innovation programme under grant agreement No. 763909.

Acknowledgments

The authors kindly acknowledge the donation of sorbent material from Sasol GmbH, Germany. The authors would like to thank Kerstin Albers (Institut für Chemieingenieurwesen, Universität Ulm) for conducting CO_2 chemisorption measurements. TS kindly acknowledges financial support from the Joint Programme on Energy Storage of the European Energy Research Alliance for this publication.

Conflict of interest

The authors declare that the research was conducted in the absence of any commercial or financial relationships that could be construed as a potential conflict of interest.

Publisher's note

All claims expressed in this article are solely those of the authors and do not necessarily represent those of their affiliated organizations, or those of the publisher, the editors and the reviewers. Any product that may be evaluated in this article, or claim that may be made by its manufacturer, is not guaranteed or endorsed by the publisher.

gas shift reaction. *Int. J. Hydrogen Energy* 34, 2972–2978. doi:10.1016/j.ijhydene.2009.01.065

Bhagiyalakshmi, M., Lee, J. Y., and Jang, H. T. (2010). Synthesis of mesoporous magnesium oxide: Its application to CO_2 chemisorption. *Int. J. Greenh. Gas Control* 4, 51–56. doi:10.1016/j.ijggc.2009.08.001

Boon, J., Cobden, P. D., van Dijk, H., Hoogland, C., van Selow, E. R., and van Sint Annaland, M. (2014). Isotherm model for high-temperature, high-pressure adsorption of and on K-promoted hydrotalcite. *Chem. Eng. J.* 248, 406–414. doi:10.1016/j.cej.2014.03.056

- Boon, J., Cobden, P. D., van Dijk, H., and van Sint Annaland, M. (2015). High-temperature pressure swing adsorption cycle design for sorption-enhanced water-gas shift. *Chem. Eng. Sci.* 122, 219–231. doi:10.1016/j.ces.2014.09.034
- Choi, W. K., Kwon, T. I., Yeo, Y. K., Lee, H., Song, H. K., and Na, B. K. (2003). Optimal operation of the pressure swing adsorption (PSA) process for CO₂ recovery. *Korean J. Chem. Eng.* 20, 617–623. doi:10.1007/BF02706897
- Choi, Y., and Stenger, H. G. (2003). Water gas shift reaction kinetics and reactor modeling for fuel cell grade hydrogen. *J. Power Sources* 124, 432–439. doi:10.1016/S0378-7753(03)00614-1
- Coenen, K., Gallucci, F., Hensen, E., and van Sint Annaland, M. (2019). Kinetic model for adsorption and desorption of H₂O and CO₂ on hydrotalcite-based adsorbents. *Chem. Eng. J.* 355, 520–531. doi:10.1016/j.cej.2018.08.175
- Cunha, A. F., Moreira, M. N., Mafalda Ribeiro, A., Ferreira, A. P., Loureiro, J. M., and Rodrigues, A. E. (2015). How to overcome the water-gas-shift equilibrium using a conventional nickel reformer catalyst. *Energy Technol.* 3, 1205–1216. doi:10.1002/ente.201500175
- Cunha, A. F., Moreira, M. N., Ribeiro, A. M., Loureiro, J. M., Rodrigues, A. E., Terzan, J., et al. (2017). Synthesis gas adjustment by low temperature sorption enhanced water-gas shift reaction through a copper-zeolite 13X hybrid material. *Chem. Eng. Process. Process Intensif.* 121, 97–110. doi:10.1016/j.cep.2017.07.023
- Dada, A., Olalekan, A., Olatunya, A., and Dada, O. (2012). Langmuir, Freundlich, temkin and dubinin–radushkevich isotherms studies of equilibrium sorption of Zn 2+ unto phosphoric acid modified rice husk. *IOSR J. Appl. Chem.* 3, 38–45. doi:10.9790/5736-0313845
- Du, H., Williams, C. T., Ebner, A. D., and Ritter, J. A. (2010). *In situ* FTIR spectroscopic analysis of carbonate transformations during adsorption and desorption of CO₂ in K-promoted HTLc. *Chem. Mat.* 22, 3519–3526. doi:10.1021/cm100703e
- Faria, A. C., Trujillano, R., Rives, V., Miguel, C. V., Rodrigues, A. E., and Madeira, L. M. (2022). Alkali metal (Na, Cs and K) promoted hydrotalcites for high temperature CO₂ capture from flue gas in cyclic adsorption processes. *Chem. Eng. J.* 427, 131502. doi:10.1016/j.cej.2021.131502
- Fleming, G., and de Lépinay, I. (2019). *Environmental trends in aviation to 2050. ICAO Environmental Report* Chapter 1.
- Glud, W., Keller, K., Schönfelder, R., and Klemm, W. (1931). *Production of hydrogen*. US Patent US1816523.
- Goede, A. P. H. (2018). CO₂ neutral fuels. *EPJ Web Conf.* 189, 00010. doi:10.1051/epjconf/201818900010
- Guffanti, S., Visconti, C. G., van Kampen, J., Boon, J., and Groppi, G. (2021). Reactor modelling and design for sorption enhanced dimethyl ether synthesis. *Chem. Eng. J.* 404, 126573. doi:10.1016/j.cej.2020.126573
- Halabi, M. H., de Croon, M., van der Schaaf, J., Cobden, P. D., and Schouten, J. C. (2012). High capacity potassium-promoted hydrotalcite for CO₂ capture in H₂ production. *Int. J. Hydrogen Energy* 37, 4516–4525. doi:10.1016/j.ijhydene.2011.12.003
- Ho, Y. S. (2006). Review of second-order models for adsorption systems. *J. Hazard. Mater.* 136, 681–689. doi:10.1016/j.jhazmat.2005.12.043
- Hu, Y., Liu, W., Yang, Y., Qu, M., and Li, H. (2019). CO₂ capture by Li₄SiO₄ sorbents and their applications: Current developments and new trends. *Chem. Eng. J.* 359, 604–625. doi:10.1016/j.cej.2018.11.128
- IATA (2020). Recovery delayed as international travel remains locked down. Available at: <https://www.iata.org/en/pressroom/pr/2020-07-28-02/> (Accessed June 14, 2022).
- IPCC (2018). *Global Warming of 1.5°C. An IPCC Special Report on the impacts of global warming of 1.5°C above pre-industrial levels and related global greenhouse gas emission pathways, in the context of strengthening the global response to the threat of climate change, sustainable development, and efforts to eradicate poverty*. Cambridge, UK and New York, NY, USA: Cambridge University Press. doi:10.1017/9781009157940
- Iruetagoiena Ferrer, D. (2016). *Supported layered double hydroxides as CO₂ adsorbents for sorption-enhanced H₂ production*. Cham: Springer International Publishing. doi:10.1007/978-3-319-41276-4
- Iwan, A., Stephenson, H., Ketchie, W. C., and Lapkin, A. A. (2009). High temperature sequestration of CO₂ using lithium zirconates. *Chem. Eng. J.* 146, 249–258. doi:10.1016/j.cej.2008.06.006
- Jansen, D., van Selow, E., Cobden, P., Manzolini, G., Macchi, E., Gazzani, M., et al. (2013). SEWGS technology is now ready for scale-up! *Energy Procedia* 37, 2265–2273. doi:10.1016/j.egypro.2013.06.107
- Karagöz, S., Chen, H., Cao, M., Tsotsis, T. T., and Manousiouthakis, V. I. (2019). Multiscale model based design of an energy-intensified novel adsorptive reactor process for the water gas shift reaction. *AIChE J.* 65, e16608. doi:10.1002/aic.16608
- Kerogreen (2022). KEROGREEN – towards sustainable and green aviation fuel production. Available at: <https://www.kerogreen.eu/> (Accessed June 14, 2022).
- Kirsch, H., Brübach, L., Loewert, M., Riedinger, M., Gräfenhahn, A., Böltken, T., et al. (2020). CO₂-neutrale Fischer–Tropsch–Kraftstoffe aus dezentralen modularen Anlagen: Status und Perspektiven. *Chem. Ing. Tech.* 92, 91–99. doi:10.1002/cite.201900120
- Koryabkina, N., Phatak, A., Ruettinger, W., and Farrauto, R. R. F. (2003). Determination of kinetic parameters for the water-gas shift reaction on copper catalysts under realistic conditions for fuel cell applications. *J. Catal.* 217, 233. doi:10.1016/S0021-9517(03)00050-2
- Lee, D. S., Fahey, D. W., Skowron, A., Allen, M. R., Burkhardt, U., Chen, Q., et al. (2021). The contribution of global aviation to anthropogenic climate forcing for 2000 to 2018. *Atmos. Environ.* 244, 117834. doi:10.1016/j.atmosenv.2020.117834
- Lee, J. M., Min, Y. J., Lee, K. B., Jeon, S. G., Na, J. G., and Ryu, H. J. (2010). Enhancement of CO₂ sorption uptake on hydrotalcite by impregnation with K₂CO₃. *Langmuir* 26, 18788–18797. doi:10.1021/la102974s
- Lee, K. B., Beaver, M. G., Caram, H. S., and Sircar, S. (2008). Effect of reaction temperature on the performance of thermal swing sorption-enhanced reaction process for simultaneous production of fuel-cell-grade H₂ and compressed CO₂ from synthesis gas. *Ind. Eng. Chem. Res.* 47, 6759–6764. doi:10.1021/ie071372k
- León, M., Díaz, E., Bennici, S., Vega, A., Ordóñez, S., and Auroux, A. (2010). Adsorption of CO₂ on hydrotalcite-derived mixed oxides: Sorption mechanisms and consequences for adsorption irreversibility. *Ind. Eng. Chem. Res.* 49, 3663–3671. doi:10.1021/ie902072a
- Li, Z., Liu, Y., and Cai, N. (2012). Effect of CaO hydration and carbonation on the hydrogen production from sorption enhanced water gas shift reaction. *Int. J. Hydrogen Energy* 37, 11227–11236. doi:10.1016/j.ijhydene.2012.04.160
- Martins, V., Miguel, C. V., Gonçalves, J. C., Rodrigues, A. E., and Madeira, L. M. (2022). Modeling of a cyclic sorption-desorption unit for continuous high temperature CO₂ capture from flue gas. *Chem. Eng. J.* 434, 134704. doi:10.1016/j.cej.2022.134704
- Millward, A. R., and Yaghi, O. M. (2005). Metal-organic frameworks with exceptionally high capacity for storage of carbon dioxide at room temperature. *J. Am. Chem. Soc.* 127, 17998–17999. doi:10.1021/ja057003z
- Moe, J. M. (1962). Design of water-gas shift reactors. *Chem. Eng. Prog.* 58, 3.
- Moreira, M. N., Ribeiro, A. M., Cunha, A. F., Rodrigues, A. E., Zabitskiy, M., Djinović, P., et al. (2016). Copper based materials for water-gas shift equilibrium displacement. *Appl. Catal. B Environ.* 189, 199–209. doi:10.1016/j.apcatb.2016.02.046
- Mulloth, L. M., and Finn, J. E. (1998). *Carbon dioxide adsorption on a 5A zeolite designed for CO₂ removal in spacecraft cabins*. Washington, DC, USA: National Aeronautics and Space Administration.
- Najmi, B., Bolland, O., and Colombo, K. E. (2016). A systematic approach to the modeling and simulation of a Sorption Enhanced Water Gas Shift (SEWGS) process for CO₂ capture. *Sep. Purif. Technol.* 157, 80–92. doi:10.1016/j.seppur.2015.11.013
- Oliveira, E. L., Grande, C. A., and Rodrigues, A. E. (2008). CO₂ sorption on hydrotalcite and alkali-modified (K and Cs) hydrotalcites at high temperatures. *Sep. Purif. Technol.* 62, 137–147. doi:10.1016/j.seppur.2008.01.011
- Ovesen, C. V., Clausen, B. S., Hammershøi, B. S., Steffensen, G., Askgaard, T., Chorkendorff, I., et al. (1996). A microkinetic analysis of the water-gas shift reaction under industrial conditions. *J. Catal.* 158, 170–180. doi:10.1006/jcat.1996.0016
- Petrescu, L., Chisalita, D. A., Cormos, C. C., Manzolini, G., Cobden, P., and van Dijk, H. (2019). Life cycle assessment of SEWGS technology applied to integrated steel plants. *Sustainability* 11, 1825. doi:10.3390/su11071825
- Poling, B. E., Prausnitz, J. M., and O'Connell, J. P. (2020). *Properties of gases and liquids*. Fifth Edition. New York, N.Y.: McGraw-Hill Education and McGraw Hill.
- Rives, V. (2002). Characterisation of layered double hydroxides and their decomposition products. *Mater. Chem. Phys.* 75, 19–25. doi:10.1016/S0254-0584(02)00024-X
- Salomé Macedo, M., Soria, M. A., and Madeira, L. M. (2021). High temperature CO₂ sorption using mixed oxides with different Mg/Al molar ratios and synthesis pH. *Chem. Eng. J.* 420, 129731. doi:10.1016/j.cej.2021.129731
- Sebastiani, F., James, J., van Dijk, H., Pieterse, J. A., Boon, J., Cobden, P. D., et al. (2021). Modelling of CO₂ and H₂O interaction during adsorption cycles on hydrotalcite for SEWGS applications. *SSRN J.* doi:10.2139/ssrn.3811608
- Sebastiani, F., Lucking, L., Sarić, M., James, J., Boon, J., van Dijk, H. J. A., et al. (2022). Steam and pressure management for the conversion of steelworks arising

- gases to H₂ with CO₂ capture by stepwise technology. *Separations* 9, 20. doi:10.3390/separations9010020
- Siriwardane, R. V., Shen, M. S., Fisher, E. P., and Poston, J. A. (2001). Adsorption of CO₂ on molecular sieves and activated carbon. *Energy Fuels* 15, 279–284. doi:10.1021/ef000241s
- Smirniotis, P. (2015). *Water gas shift reaction: Research developments and applications*. Burlington: Elsevier Science.
- Soria, M. A., Rocha, C., Tosti, S., Mendes, A., and Madeira, L. M. (2019). CO_x free hydrogen production through water-gas shift reaction in different hybrid multifunctional reactors. *Chem. Eng. J.* 356, 727–736. doi:10.1016/j.cej.2018.09.044
- Soria, M. A., Tosti, S., Mendes, A., and Madeira, L. M. (2015). Enhancing the low temperature water-gas shift reaction through a hybrid sorption-enhanced membrane reactor for high-purity hydrogen production. *Fuel* 159, 854–863. doi:10.1016/j.fuel.2015.07.035
- Stadler, T. J., Barbig, P., Kiehl, J., Schulz, R., Klövekorn, T., and Pfeifer, P. (2021). Sorption-enhanced water-gas shift reaction for synthesis gas production from pure CO: Investigation of sorption parameters and reactor configurations. *Energies* 14, 355. doi:10.3390/en14020355
- Stadler, T. J., Bertin-Mente, B., Dittmeyer, R., Brübach, L. T., Böltken, T., and Pfeifer, P. (2022a). Influence of CO₂-rich syngas on the selectivity to C10–C14 in a coupled Fischer–Tropsch/hydrocracking process. *Chem. Ing. Tech.* 94, 289–298. doi:10.1002/cite.202100172
- Stadler, T. J., Knoop, J. H., Decker, S., and Pfeifer, P. (2022b). Numerical simulation approach for a dynamically operated sorption-enhanced water-gas shift reactor. *Processes* 10, 1160. doi:10.3390/pr10061160
- Uchida, H., Isogai, N., Oba, M., and Hasegawa, T. (1967). The zinc oxide-copper catalyst for carbon monoxide-shift conversion. I. The dependency of the catalytic activity on the chemical composition of the catalyst. *Bull. Chem. Soc. Jpn.* 40, 1981–1986. doi:10.1246/bcsj.40.1981
- UNEP (2021). *Emissions Gap Report 2021: The Heat Is on - a world of climate promises not yet delivered*. Nairobi, Kenya: UNEP.
- van Selow, E. R., Cobden, P. D., van Dijk, H., Walspurger, S., Verbraeken, P. A., and Jansen, D. (2013). Qualification of the ALKASORB sorbent for the sorption-enhanced water-gas shift process. *Energy Procedia* 37, 180–189. doi:10.1016/j.egypro.2013.05.100
- van Selow, E. R., Cobden, P. D., Wright, A. D., van den Brink, R. W., and Jansen, D. (2011). Improved sorbent for the sorption-enhanced water-gas shift process. *Energy Procedia* 4, 1090–1095. doi:10.1016/j.egypro.2011.01.159
- Wang, S., Shen, H., Fan, S., Zhao, Y., Ma, X., and Gong, J. (2013). Enhanced CO₂ adsorption capacity and stability using CaO-based adsorbents treated by hydration. *AIChE J.* 59, 3586–3593. doi:10.1002/aic.14126
- Yang, R. T. (1987). “Gas separation by adsorption processes,” in *Butterworths series in chemical engineering* (Boston: Butterworths).
- Yin, G., Liu, Z., Liu, Q., and Wu, W. (2013). The role of different properties of activated carbon in CO₂ adsorption. *Chem. Eng. J.* 230, 133–140. doi:10.1016/j.cej.2013.06.085
- Yong, Z., Mata, V., and Rodrigues, A. E. (2001). Adsorption of carbon dioxide onto hydrotalcite-like compounds (HTLcs) at high temperatures. *Ind. Eng. Chem. Res.* 40, 204–209. doi:10.1021/ie000238w
- Zheng, Y., Shi, Y., Li, S., Yang, Y., and Cai, N. (2014). Elevated temperature hydrogen/carbon dioxide separation process simulation by integrating elementary reaction model of hydrotalcite adsorbent. *Int. J. Hydrogen Energy* 39, 3771–3779. doi:10.1016/j.ijhydene.2013.12.167
- Zhu, X., Li, S., Shi, Y., and Cai, N. (2019). Recent advances in elevated-temperature pressure swing adsorption for carbon capture and hydrogen production. *Prog. Energy Combust. Sci.* 75, 100784. doi:10.1016/j.peccs.2019.100784
- Zhu, X., Shi, Y., and Cai, N. (2017). High-pressure carbon dioxide adsorption kinetics of potassium-modified hydrotalcite at elevated temperature. *Fuel* 207, 579–590. doi:10.1016/j.fuel.2017.06.137

Nomenclature

Abbreviations

Ch. Chamber
FID Flame ionization detector
GC Gas chromatograph
HDMO Hydrotalcite-derived mixed oxide
HTC Hydrotalcite
K-HDMO Potassium-impregnated hydrotalcite-derived mixed oxide
K-HTC Potassium-impregnated hydrotalcite
LDF Linear driving force
M1-M4 Operation mode 1-4
PBMR Packed bed microchannel reactor
PGA Process gas analyzer
PSA Pressure swing adsorption
SAF Sustainable aviation fuel
SEWGS Sorption-enhanced water-gas shift
TCD Thermal conductivity detector
WGS Water-gas shift

Symbols

β_{des} activation energy change (J mol^{-1})
$\Delta H_{\text{R}}^{\ominus}$ standard reaction enthalpy (kJ mol^{-1})
ϵ_{b} bed void fraction (–)
ϵ_{p} particle void fraction (–)
ν_i stoichiometric reaction coefficient (–)
ρ bulk density (kg m^{-3})
$a_{\text{ads,des},i}$ adsorption/ desorption rate ($\text{mol kg}^{-1} \text{s}^{-1}$)
\bar{c}_i particle void phase concentration (mol m^{-3})
c_i bulk phase concentration (mol m^{-3})
$D_{\text{ax},i}$ axial dispersion coefficient ($\text{m}^2 \text{s}^{-1}$)

$D_{\text{eff},i}$ effective diffusion coefficient ($\text{m}^2 \text{s}^{-1}$)
$D_{\text{mix},i}$ gas mixture diffusion coefficient ($\text{m}^2 \text{s}^{-1}$)
E_{a} activation energy (J mol^{-1})
$E_{\text{a,des}}$ activation energy for desorption (J mol^{-1})
$E_{\text{a,des}}^0$ activation energy for desorption (J mol^{-1})
eq equilibrium (–)
exp experimental (–)
F objective function (–)
F_{STP} flow rate (ml min^{-1})
i species CO, H ₂ O, CO ₂ , H ₂ , N ₂ (–)
k_{∞} frequency factor ($\text{mol bar}^{-2} \text{g}^{-1} \text{h}^{-1}$)
$k_{\text{ads/des}}$ adsorption/ desorption coefficient (s^{-1})
$k_{\text{des}}^{0/1}$ desorption coefficient (s^{-1})
K_{eq} WGS equilibrium constant (–)
k_{Fr} Freundlich constant ($\text{mmol g}^{-1} \text{bar}^{-n_{\text{Fr}}}$)
$k_{\text{LDF},i}$ linear driving force coefficient (s^{-1})
\dot{n}_i molar flow (mol s^{-1})
n_{Fr} Freundlich adsorption intensity (–)
$p_{(i)}$ (partial) pressure (bar)
$q_{\text{CO}_{2\{i\}}}$ CO ₂ sorbent loading (mol kg^{-1})
q_{max} maximum CO ₂ sorbent loading (mol kg^{-1})
R gas constant ($\text{J mol}^{-1} \text{K}^{-1}$)
r_{p} particle radius (m)
r_{WGS} WGS reaction rate ($\text{mol g}^{-1} \text{h}^{-1}$)
S/G steam-to-gas ratio (–)
sim simulation (–)
T temperature (K)
t time (s)
u gas velocity (m s^{-1})
w_{cat} catalyst weight fraction (–)
X_{CO} CO conversion (–)
y volume fraction (–)
z axial coordinate (m)

P IV Impact on subsequent Process Steps

Influence of CO₂-Rich Syngas on the Selectivity to C₁₀–C₁₄ in a Coupled Fischer-Tropsch/Hydrocracking Process

Published in Chemie Ingenieur Technik 2022, 94, 3


Publishing Date 20 January 2022

DOI <https://doi.org/10.1002/cite.202100172>

Influence of CO₂-Rich Syngas on the Selectivity to C₁₀–C₁₄ in a Coupled Fischer-Tropsch/Hydrocracking Process

Tabea J. Stadler¹, Barbara Bertin-Mente¹, Roland Dittmeyer¹, Lucas T. Brübach¹, Tim Böltken², and Peter Pfeifer^{1,2,*}

DOI: 10.1002/cite.202100172

 This is an open access article under the terms of the Creative Commons Attribution-NonCommercial License, which permits use, distribution and reproduction in any medium, provided the original work is properly cited and is not used for commercial purposes.

Dedicated to Prof. Dr. Thomas Hirth on the occasion of his 60th birthday

Synthesis gas (syngas) used for the production of synthetic fuels may contain significant amounts of CO₂, depending on its source. For Fischer-Tropsch synthesis on cobalt, CO₂ can be considered as inert diluent. However, in the specific case of a coupled Fischer-Tropsch-hydrocracking (FT-HC) process, CO₂ could interact with the catalyst in the HC step. In this experimental study, HC product distributions obtained for FT-syngas compositions with and without CO₂ and N₂ are presented. The selected feed gas compositions result from an advanced syngas production route via plasma splitting of CO₂. Main target product was kerosene, here being defined as C₁₀–C₁₄. It was found that the CO₂ presence is negligible with regard to adsorption or reaction on the HC catalyst. Further insights into possible impacts of CO₂ could be obtained from the analysis of alcohols in the aqueous phase.

Keywords: CO₂-rich syngas, Fischer-Tropsch synthesis, Hydrocracking, Plasma splitting of CO₂, Power-to-fuels

Received: September 10, 2021; *revised:* October 14, 2021; *accepted:* December 13, 2021

1 Introduction

Carbon neutral synthetic fuels are among the most promising alternatives for the successful defossilization of the transport sector [1]. Since not all means of transport can manage without liquid fuels due to gravimetric or volumetric restrictions, so-called Power-to-Liquid (PtL) processes are emerging technologies. The Kerogreen project aims to investigate a compact PtL conversion route from water and captured CO₂ to carbon neutral aviation fuel powered by renewable energy sources [2]. Here, CO₂ is activated to CO in a plasma splitting reactor combined with O₂ separation in a solid oxide electrolyte cell [3]. CO is partly converted back to CO₂ with steam in order to produce synthesis gas, a mixture of CO + H₂ (syngas), via the water-gas shift reaction. The by-product CO₂ is removed and recovered in situ through a sorption-enhanced process (SEWGS) [4]. Syngas reacts subsequently in a Fischer-Tropsch (FT) reactor followed by a hydrocracking (HC) reactor to produce primarily hydrocarbons in the middle distillate range. Therefore, it is important to know if certain concentrations of CO₂ in the syngas influence the product composition in this process, since also further upgrading steps are necessary with the hydrotreated crude to meet the fuel quality regulations for direct use as synthetic kerosene [5–7].

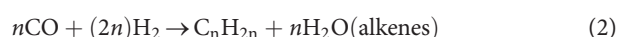
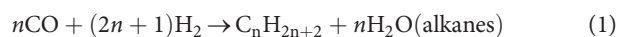
Compact, decentralized PtL concepts, such as the Kero-green process but also others in general, do not only require a modification of the FT process but also of the product upgrading steps in terms of simplicity and conditions. Commercial HC processes are firstly not applicable in a compact coupled FT-HC process layout due to pure H₂ requirement and, secondly, they cannot be economically scaled down so far [8]. One possibility to overcome this issue is the direct coupling of the HC reactor into the synthesis gas loop of the FT. The HC reaction is then conducted under FT conditions, i.e., in presence of CO. In any case of CO₂ in the syngas, also the CO₂ contribution towards process performance gains interest. Advantages and disadvantages of the direct coupling are discussed in the subsequent paragraphs.

¹Tabea J. Stadler, Barbara Bertin-Mente, Prof. Dr.-Ing. Roland Dittmeyer, Lucas T. Brübach, Prof. Dr.-Ing. Peter Pfeifer
peter.pfeifer@kit.edu

Karlsruhe Institute of Technology (KIT), Institute for Micro Process Engineering (IMVT), Hermann-von-Helmholtz-Platz 1, 76344 Eggenstein-Leopoldshafen, Germany.

²Dr.-Ing. Tim Böltken, Prof. Dr.-Ing. Peter Pfeifer
INERATEC – Innovative Chemical Reactor Technologies GmbH, Siemensallee 84, 76187 Karlsruhe, Germany.

The FT synthesis is a heterogeneously catalyzed, polymerization-like exothermic hydrogenation reaction and converts syngas to a hydrocarbon mixture and water [9]. The hydrocarbon product consists of a variety of species with up to 100 carbon atoms and can be denoted as synthetic crude (syncrude). FT carried out with cobalt-based catalysts at low temperatures (200–250 °C, Co-LTFT) produces mainly linear alkanes (Eq. (1)), but also alkenes (Eq. (2)) and minor quantities of oxygenates, such as alcohols (Eq. (3)) [10].



The product distribution on a weight basis can be approximated by means of the Anderson-Schulz-Flory distribution (ASF, Eq. (4)) [11, 12].

$$w_{\text{ASF},n_{\text{Ci}}} = n_{\text{Ci}}(1 - \alpha)^2 \alpha^{(n_{\text{Ci}}-1)} \quad (4)$$

A graphical illustration of the ASF product distribution is depicted in Fig. 1. The chain growth probability α is defined as the ratio of propagation to the sum of propagation and termination and depends on the reaction conditions and catalyst. Typical Co-LTFT α values range from 0.88 to 0.95 [13]. According to Eq. (4), the primary selectivity towards kerosene (here being defined as C_{10} – C_{14}) is limited to a theoretical maximum of 23 % for $\alpha = 0.84$. To overcome this limitation, the product distribution must be narrowed with adequate upgrading processes. Assuming complex refining technologies at large scale, an industrial LTFT jet fuel refinery can yield up to 57 % jet fuel from syncrude [14].

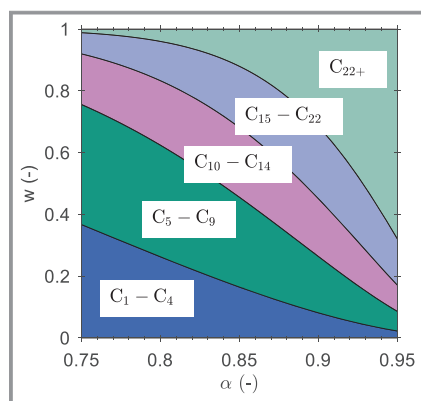


Figure 1. ASF syncrude composition for lumped product groups: C_1 – C_4 , gases; C_5 – C_9 , naphtha; C_{10} – C_{14} , kerosene; C_{15} – C_{22} , gas oil; C_{22+} , waxes.

HC is among the most relevant refinery processes for the conversion of long-chain hydrocarbons to mainly middle distillates with naphtha as by-product. It promotes skeletal

isomerization of n -alkanes to isoalkanes to enhance the cold flow properties of the resulting synthetic fuel. HC is carried out on bifunctional catalysts with de/hydrogenation and cracking functionality. On the metal sites of the catalyst, alkanes are dehydrogenated to alkenes. On the Brønsted acid sites, these alkenes are protonated to form alkylcarbenium ions and undergo isomerization and scission reactions of the carbon-carbon bonds. The products desorb from the acid sites and unsaturated alkenes can further be hydrogenated on the metal sites. Ideal hydrocracking (Eq. (5)) occurs if the de/hydrogenation and the cracking functionality are properly balanced so that secondary cracking becomes negligible [15]. HC is typically performed under elevated pressure (35 to 70 bar) and temperature (325 to 375 °C). In direct combination with FT, “mild” HC with lower pressure and temperature can be applied [16, 17]. On the one hand, this lower pressure and lower temperature is beneficial with regard to the process efficiency since no compression or considerable heating-up of the product gas and liquid flow are required. On the other hand, noble metals are required for the carbenium ion formation and hydrogenation steps, which are partly blocked due to competitive adsorption of CO. This may lead to secondary cracking and, thus, to a potential negative impact on middle distillate yield.



Many studies reported on the influence of CO_2 -rich feeds in Co-LTFT [18–21]. The majority concluded that CO_2 , which is, e.g., contained in significant amounts in biomass-derived syngas, acts mainly as diluent on Co catalysts. However, the influence of CO_2 on coupled FT-HC processes has received less attention in literature although it may be a serious parameter in a case of process integration.

Therefore, this experimental study aims to understand the impact of a possible slip of CO_2 . CO_2 could originate from incomplete separation in the SEWGS reactor (for a detailed process description, see [4]), and thus, influence the subsequent process steps and product quality in the Kerogreen process chain. Various syngas compositions were fed to an FT reactor coupled with an HC reactor cascade. The weight hourly space velocity ($WHSV_{\text{FT}}$, Eq. (12)) as well as the CO conversion (X_{CO} , Eq. (6)) in the FT were kept constant. The following cases were investigated: syngas with low CO_2 dilution (incomplete CO_2 removal in the SEWGS reactor) and with high CO_2 dilution (no CO_2 removal in the SEWGS reactor), and for comparative purposes: syngas with equivalent N_2 dilution and without dilution.

2 Materials and Methods

2.1 Reactors and Catalysts

The experiments were conducted in a micro-structured FT reactor coupled with an HC reactor cascade consisting of three identical tubular reactors in sequence, see also [22].

A commercial Co-based catalyst was used for low-temperature FT (spheres with a diameter of 50–200 μm). In the HC reactor cascade, bifunctional Pt/H-ZSM-5 (0.5 wt % Pt) catalyst extrudates (1/16" \times 3 mm) were employed.

2.2 Experimental Setup

Fig. 2 shows a simplified process scheme of the experimental setup used in this study. The feed gases H_2 , CO , CO_2 , and N_2 were provided by a central gas supply and fed into the system by calibrated mass flow controllers (Brooks Instrument, USA). 5 vol % of the total flow passed through a permanent bypass to enable continuous feed control in the online gas chromatograph (GC). The electrically preheated gases entered the reaction channels of the evaporation-cooled FT reactor (INERATEC GmbH, Germany) [22–24].

The reaction channels of the FT reactor were filled with catalyst and adjacent cooling channels ensure precise temperature control. Preheated water entered the cooling channels, evaporated by consuming the reaction heat, and left the reactor as two-phase flow. Temperature adjustment in the reactor was realized by means of the boiling point, which could be adjusted by the pressure in the water cycle. This technology results in nearly isothermal reaction conditions. Electrical heating cartridges alongside the reactor provided additional heat for the start-up of the reaction and compensated heat losses at the outer walls. The reactor itself was placed in a box filled with insulation material to reduce heat losses. Type K thermocouples in the water cycle as well as in the reactor inlet and outlet, and at various positions between the channels were used to monitor the temperatures. An automated shutdown routine implemented in the process control system (LabView, National Instruments, USA) ensured safe operation conditions.

The product flow leaving the FT reactor could either be directed to the product separation unit (hot and cold trap) for analysis or to the HC reactor cascade for further pro-

cessing. Due to their interconnections, the number of operating HC reactors could be adjusted manually. Additional gas could optionally be dosed into the HC section. The temperature of each tubular HC reactor (inner diameter: 14 mm, length: 102 mm) was regulated by a heating jacket and monitored internally by a K-type thermocouple located inside the catalyst bed. The whole reactor cascade was placed in a box filled with insulation material to reduce heat losses.

Products from FT or coupled FT-HC were fed into the hot trap under pressure. The hot trap was electrically heated to a constant temperature of 180 $^{\circ}\text{C}$. Long-chain hydrocarbons (the wax fraction) condense and accumulate here. The remaining parts of the product moved on to the cold trap which was cooled to 10 $^{\circ}\text{C}$. Here, the oil and water fraction condensed. To ensure that no water condensation occurred in the hot trap, thus leading to under-estimation of alcohols in the water phase of the cold trap, the hot trap temperature was set sufficiently high [23]. Wax, oil, and water fraction were analyzed in offline GCs. The non-condensed gases were analyzed in an online GC and left the system through an exhaust line.

A back-pressure regulator (BSH series, Swagelok, USA) controlled the system pressure. Unwanted condensation and wax plugging in the tubes was prevented by electrical heating coils.

2.3 Product Analysis and Data Evaluation

The feed and gaseous product flows were analyzed online in a GC (7890B, Agilent Technologies, customized by Teckso GmbH, Germany) equipped with two thermal conductivity detectors (TCD1, TCD3) and one flame ionization detector (FID). H_2 , CH_4 , CO , and N_2 were detected by TCD1 after being separated on a micropacked HayeSep Q and a mole sieve 5A column. CO_2 and hydrocarbons (up to C_7) were separated on a HP-Plot/Q column (all columns: Agilent Technologies, USA) and detected by TCD3 and the FID, respectively. Ar was used as carrier gas and N_2 as internal standard.

Water and oil phase gathered in the cold trap were separated in a separation funnel. Both phases were analyzed offline in a GC (7820A, Agilent Technologies, USA) equipped with an Rtx-1 column (60 m, 0.32 mm, 1 μm , Restek, USA) and an FID. Acetonitrile was added as internal standard to the water phase for the quantification of alcohols (C_1 – C_5). The oil phase (hydrocarbons: $\sim\text{C}_4$ – C_{27}) was injected without a solvent by an auto-

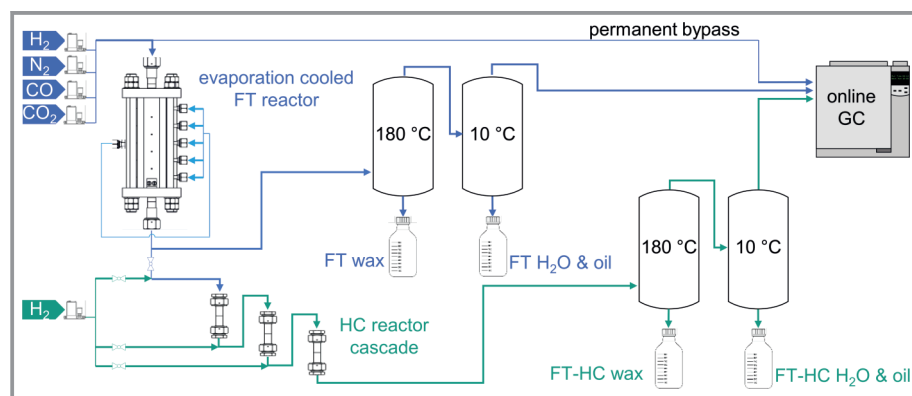


Figure 2. Simplified flow scheme of the experimental setup. Feed gases enter the micro-structured FT reactor and can optionally be fed to the HC reactor cascade. Products are separated in a wax phase (hot trap), liquid (oil and water) phase (cold trap), and remaining gases.

matic liquid sampler. It was analyzed quantitatively with a 100-% method under the assumption of a constant relative response factor. This is usually justified for aliphatic hydrocarbon mixtures without heteroatoms [25].

The composition of the long-chain hydrocarbons in the wax fraction ($\sim C_{10}-C_{60}$) was determined offline in a high-temperature GC (7890B, Agilent Technologies, USA) equipped with a MXT-1 column (30 m, 0.53 mm, 0.25 μ m, Restek, USA) and a high temperature FID. The dissolved wax sample (200 mg wax dissolved in 20 mL cyclohexane, ultrasound bath at 40 °C) was directly injected into the temperature programmable inlet (Da Vinci Laboratory Solutions B.V., The Netherlands) to avoid discrimination of high-boiling components.

The conversion of CO X_{CO} was calculated according to Eq. (6).

$$X_{CO} = \frac{\dot{n}_{CO,in} - \dot{n}_{CO,out}}{\dot{n}_{CO,in}} \quad (6)$$

Wax, water, and oil samples collected under steady-state conditions were weighted for integral mass flow \dot{m} determination. Mass fraction w of hydrocarbon i and carbon monoxide related selectivity S towards hydrocarbon i were calculated according to Eqs. (7) and (8), respectively. The average chain length \bar{n}_C was derived from Eq. (9). As far as analytically feasible, it was further distinguished between n -alkanes and 1-alkenes [26]. The n -alkane fraction a of hydrocarbon i is calculated according to Eq. (10). The conversion of long-chained hydrocarbons ($n_C > 22$) $X_{C_{22+}}$ in the HC reactor resulted from Eq. (11).

$$w_i = \frac{\dot{m}_{i,out}}{\sum \dot{m}_{i,out}} \quad (7)$$

$$S_{i,CO} = \frac{\dot{n}_{i,out}}{\dot{n}_{CO,in} - \dot{n}_{CO,out}} n_{C,i} \quad (8)$$

$$\bar{n}_C = \sum (w_i n_{C,i}) \quad (9)$$

$$a_i = \frac{\dot{n}_{i,n-alkane}}{\dot{n}_i} \quad (10)$$

$$X_{C_{22+}} = \frac{\frac{X_{CO,FT-HC}}{X_{CO,FT}} \sum (\dot{n}_{C_{22+,FT,out}} n_{C,i}) - \sum (\dot{n}_{C_{22+,FT-HC,out}} n_{C,i})}{\frac{X_{CO,FT-HC}}{X_{CO,FT}} \sum (\dot{n}_{C_{22+,FT,out}} n_{C,i})} \quad (11)$$

2.4 Experimental Procedure

2.4.1 Reduction and Pre-Conditioning

Prior to the experiments, both catalysts were reduced in situ in H_2 atmosphere (FT: 100 % H_2 , 320 °C, 16 h; HC: 10 % H_2 in N_2 , 300 °C, 5 h). A run-in phase of 500 h ensured stable catalyst activity. Typical initial degradation due to wax formation in the catalyst pores requires ~ 70 h according to preliminary studies. To observe possible catalyst deactivation, a reference point was repeatedly analyzed during the measurement campaign; the conversion remained constant within the noise of analytics of ± 2 %.

2.4.2 FT and FT-HC Coupling Experiments

The system pressure was set to 20 bar for all experiments. The reaction temperature in the FT reactor was adjusted to maintain a constant CO conversion in all experiments between 195 and 200 °C. The reaction temperature in the HC reactor cascade was set to 230 °C.

The experimental nomenclature was chosen in the following order: "Dil" for dilution of the syngas with "N2" or "CO2" followed by a numbering with the concentration level "1" or "2" followed by "A" or "B" for variation of other parameters (number of HC stages and hydrogen addition to the HC feed) used in the experiment. "FT" and "HC" at the end indicate whether the product is derived from FT or from the coupled FT-HC process. An exception from the nomenclature is the experiment "Ref_A" which indicates an undiluted syngas for "FT" or coupled process "HC". The specific conditions are provided in the following tables and paragraphs.

Fig. 3 shows the ramp-up of an individual experimental point with regard to reaction temperatures in FT and HC stages and conversion in the FT reactor. The process conditions for every experimental point were kept constant for about 24 h in the FT reactor to accomplish steady state in

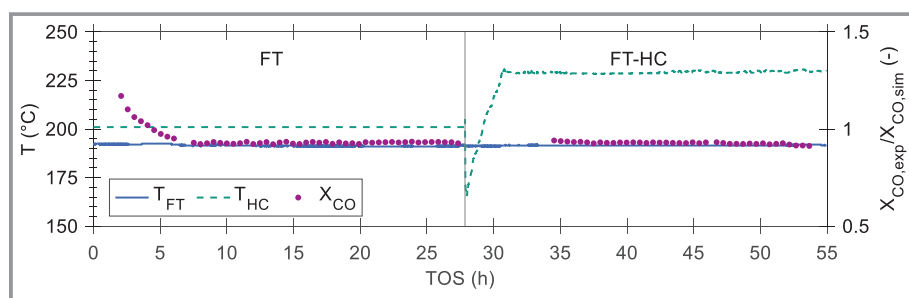


Figure 3. Exemplary experimental curve for FT-HC coupling experiment (Dil_CO2_1).

the individual run, and FT reference samples were collected for at least 3 h at the end of that period in the traps. For the FT-HC coupling, the FT effluent was slowly redirected to the pressurized and preheated HC reactor cascade. The cascade was flushed for at least 30 min to ensure the build-up of a wax layer on the catalyst pellets. Then, the HC reactors were heated to target temperature (230 °C). After about 24 h, steady-state HC samples were taken out of the traps (collection time ~3 h). The graph in Fig. 3 indicates that the FT reactor has reached steady-state reaction conditions in the run-in phase and also during ramp-up. During the FT reference measurement, the HC reactor cascade was flushed with an H₂/N₂ mixture to avoid possible catalyst oxidation and pressure surge.

The CO conversion plotted in Fig. 3 is normalized to simulated CO conversion. Simulated values were derived from an INERATEC in-house MATLAB® program, which was fitted to a simplified version of the Visconti model [27] with data points obtained in a smaller oil-cooled reactor as used elsewhere [28] and which has been approved by many data points before. The activation energies in the model parameter set are slightly lower and the rate constants are in the order of 7–10 higher than in the original publication of Visconti et al. due to the applied highly active catalyst.

FT inlet conditions for all experiments are summarized in Tab. 1. Nitrogen was used as diluent and (partly) replaced in two runs with CO₂ while the reference run was performed with only 3 % N₂ as internal standard. Typically, the weight hourly space velocity in the FT reactor $WHSV_{FT}$ was kept constant (Eq. (12)).

$$WHSV_{FT} = \frac{\dot{m}_{in}}{m_{cat,FT}} \quad (12)$$

Table 1. FT feed in the FT-HC coupling experiments. System pressure: 20 bar; H₂/CO ratio: 2; FT catalyst mass/HC catalyst mass: 7.4; temperature in FT: 195–200 °C (adjusted to maintain constant CO conversion); no additional gas feed to HC; temperature in HC: 230 °C.

	H ₂ [%]	CO [%]	CO ₂ [%]	N ₂ [%]	$WHSV_{FT}$ [h ⁻¹]
Dil_N2	38.8	19.4	0	41.8	4.5
Dil_CO2_1	38.8	19.4	38.8	3.0	4.5
Dil_CO2_2	38.8	19.4	5.0	36.8	4.5
Ref_A	64.7	32.3	0	3	3.5 ^{a)}

a) The desired value of 4.5 was not reachable due to experimental restrictions.

2.4.3 Variation of HC Reaction Conditions

To further investigate the influence of CO₂ on HC, two modifications in the HC were tested with identical FT product as feed: 1) additional H₂ feed in the HC, and 2) reduction of HC catalyst mass (Tab. 2).

Table 2. Variation of HC conditions. FT feed equal to Dil_CO2_1 (Tab. 1). Temperature in HC: 230 °C.

	H ₂ HC [mL _N min ⁻¹]	$m_{cat,FT}/m_{cat,HC}$ [-]
Dil_CO2_1	0	7.4
Dil_CO2_1A	500	7.4
Dil_CO2_1B	500	11.1

3 Results and Discussion

In this section, hydrocarbons were classified according to their carbon number and grouped into lumps: C₁–C₄: gases, C₅–C₉: naphtha, C₁₀–C₁₄: kerosene, C₁₅–C₂₂: gas oil, C₂₂₊: waxes. The main target product was kerosene, here being defined as C₁₀–C₁₄ [14]. Further insights into possible impacts of CO₂ could be obtained from the analysis of alcohols in the aqueous phase.

Concluding from the high reproducibility of the reference point in both reactors, FT and HC, no significant catalyst deactivation occurred during the measurement campaign after the run-in phase. The total mass balance deviation was well below 3.5 % in all experiments. It was determined from the integral mass flow of the liquid and wax phase collected under steady-state conditions and continuous gas phase analysis.

3.1 FT Reference Measurements

Fig. 4 shows the carbon-based mass fractions for all FT reference measurements in form of an Anderson-Schulz-Flory (ASF) plot, i.e., the logarithmic of the weight fraction of the C-species divided by the respective C-number. For the C₁₀–C₅₀ species, a product distribution, characterized by an averaged chain-growth probability of 0.91, is obtained. The

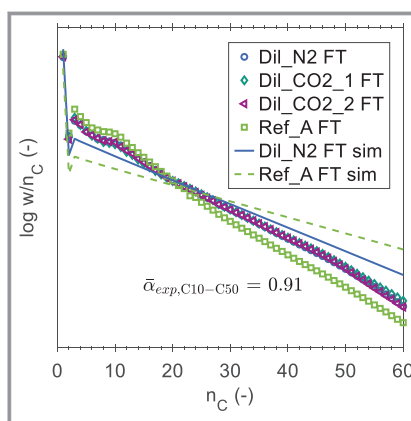


Figure 4. Experimental carbon-related mass fractions of hydrocarbons for FT reference measurements (Tab. 1) versus model prediction with the in-house MATLAB® code. Fitted average ASF chain growth probability for C₁₀–C₅₀ (Eq. (4)).

chain growth probability was fitted according to Eq. (4) with R^2 values above 0.99 for all individual fits. The modeling results are also plotted for the two reference points as lines.

For short-chain hydrocarbons ($< C_{10}$), saddle-like deviations from the ideal ASF distribution emerge. These deviations might rather be explained by experimental artefacts than mechanistic effects [29]. One possible explanation might be found in the sampling procedure. The sampling of the liquid and wax phase included a release to ambient temperature and pressure. Hence, short chain hydrocarbons dissolved in the liquid and wax phase under reaction conditions could be irrecoverably lost to air due to a phase change into gas state. This flash loss could result in a dip as observed in the ASF plot [30]. This fact can lead to a deviation of the detected chain-growth probability in the range of 1–2 % despite high quality fits and explain deviations from the modeling results. Nevertheless, the long-chain product fractions of interest do not seem to be influenced by the loss during liquid sampling.

Detailed information on the FT reference measurements is given in Tab. 3. The mass fractions for hydrocarbon lumps agree well with literature data for Co-LTFT [10]. Unfortunately, it was not possible to reach equal CO conversion in all experiments due to technical restrictions of the setup. The reference measurement without dilution (Ref_A) exhibited significantly higher heat production and was run under less than half the desired conversion. This could explain the different product distribution for Ref_A. The results show that no significant difference is observed between the product distribution obtained from syngas enriched with N_2 and CO_2 . As known from previous studies, N_2 has no influence on the FT kinetics and serves as inert gas [31]. Thus, also CO_2 does not play an influencing role in FT with the employed Co catalyst and acts mainly as diluent in the presence of CO. This observation is in line with various studies which stated that CO_2 removal from raw syngas is not necessary for FT on Co catalysts [19–21, 32]. Visconti et al. attributed the inert behavior of CO_2 in the presence of CO to competitive adsorption on the catalyst free sites [18]. An increase in methane selectivity due to CO_2 was not expected for the investigated CO conversion range under constant H_2/CO feed ratio [33–35].

3.2 Coupled FT-HC Measurements

In all FT-HC coupling experiments, a shift in the product distribution towards shorter hydrocarbons is clearly identified compared to the corresponding FT reference. The product distribution of one experimental point (Dil_CO2_1) is exemplarily shown in Fig. 5 in terms of the weight fractions of the C-species as function of the corresponding C-numbers. The net production of hydrocarbon species through the hydrocracking process is strictly limited to C_{14} in all experiments. Considering preliminary studies, this effect is mainly attributed to the shape selectivity of the employed H-ZSM-5 and gives rise to the occurrence of pore mouth cracking. Primarily produced long-chain hydrocarbons undergo secondary cracking reactions due to mass transfer limitations in the narrow pores of the zeolite.

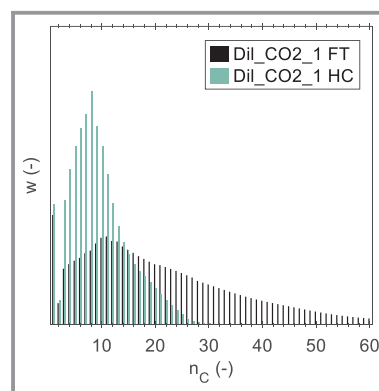


Figure 5. Hydrocarbon mass fractions for FT and coupled FT-HC measurement (Dil_CO2_1). FT feed: 38.8 % H_2 , 19.4 % CO , 38.8 % CO_2 , 3.0 % N_2 , $WHSV_{FT} = 4.5 h^{-1}$.

Minor deviations ($< 2\%$) between the CO conversion of the FT reference measurement and the coupled FT-HC point were considered for the determination of the wax conversion (Eq. (11)). The results summarized in Tab. 4 do not indicate a correlation between the wax conversion and the ratio of gas velocity and FT product. All wax conversion rates are well above 75 % and therefore quite high. However, the corresponding changes in boundary conditions for phase equilibrium influence the reaction conditions on the

Table 3. Experimental conversion and mass fractions of hydrocarbon product lumps for FT reference measurements (Tab. 1), fitted ASF chain growth probability, and calculated kerosene (C_{10} – C_{14}) mass fraction.

	$X_{CO,exp,FT}/X_{CO,sim}$ [-]	w_{C5-C9} [-]	$w_{C10-C14}$ [-]	$w_{C15-C22}$ [-]	w_{C22+} [-]	$\alpha_{C10-C50}$ [-] ^{a)}	$w_{ASF,C10-C14}$ [-] ^{b)}
Dil_N2 FT	0.85	0.15	0.17	0.22	0.39	0.92	0.16
Dil_CO2_1 FT	0.93	0.14	0.17	0.21	0.40	0.92	0.16
Dil_CO2_2 FT	0.96	0.15	0.18	0.21	0.39	0.92	0.16
Ref_A FT	0.39	0.19	0.22	0.22	0.28	0.90	0.19

a) Fitted value: $R^2 > 0.99$; b) Eq. (4) with determined chain growth probability.

Table 4. Experimental wax (C_{22+}) conversion in coupled FT-HC measurements and average chain length for FT and FT-HC measurements (Tabs. 1 and 2).

	$X_{C_{22+,HC}}$ [%]	$\bar{n}_{C,FT}$ [-]	$\bar{n}_{C,HC}$ [-]
Dil_N2	86.0	20	11
Dil_CO2_1	94.8	20	9
Dil_CO2_2	81.7	20	11
Ref_A	77.0	17	11

HC catalyst surface. More gas phase means that more heavy molecules may evaporate, and the probability of drying out of the liquid film on the catalyst increases. This would allow further secondary cracking, i.e., loss of the gas oil fraction. The average chain length decreased in the HC by 9 and 11 with diluted syngas feed (N_2 and CO_2), and by only 6 in the pure syngas feed experiment.

The integral product selectivity of the FT and FT-HC hydrocarbon product lumps is depicted in Fig. 6 for C_6 – C_9 (naphtha), C_{10} – C_{14} (kerosene), C_{15} – C_{21} (gas oil), and C_{22+} (wax) to identify decrease and increase of these fractions. It is apparent that the wax fraction together with small parts of the gas oil fraction is selectively converted to kerosene and naphtha range hydrocarbons in the HC. A more detailed look at the product composition with respect to the n -alkane content in C_6 – C_9 (naphtha), C_{10} – C_{14} (kerosene), and C_{15} – C_{21} (gas oil) is given in Fig. 7. Even though it is not possible to distinguish with normal GC analysis between isoalkanes and different molecules of alkenes and isoalkenes, it can be concluded that the n -alkane fraction in gas oil and kerosene is remarkably lower for all FT-HC products compared to the corresponding FT product, whereas the reverse effect occurs slightly for the waxes. These results indicate that linear FT alkanes were either successfully isomerized or dehydrogenated in the HC.

A high content of isoalkanes in the synthetic fuel is desirable as it enhances its cold flow properties, but any type of alkene is lowering the thermal stability and is therefore not allowed in the synthetic kerosene substitute. As the presence of CO and water in the HC feed heavily influences the catalyst behavior [36,37], the formation of mainly isoalkenes is nevertheless highly likely and a subsequent hydrogenation is required. The pure syngas feed (Ref_A) showed similar trends as the diluted feed. No significant difference between the syngas feed with N_2 (Dil_N2) and CO_2 (Dil_CO2_1 and Dil_CO2_2) could be deduced. Thus, the effects of dilution on the product distribution obtained in the coupled FT-HC process are negligible within the limited variations of parameters (i.e., upfront dilution and FT conver-

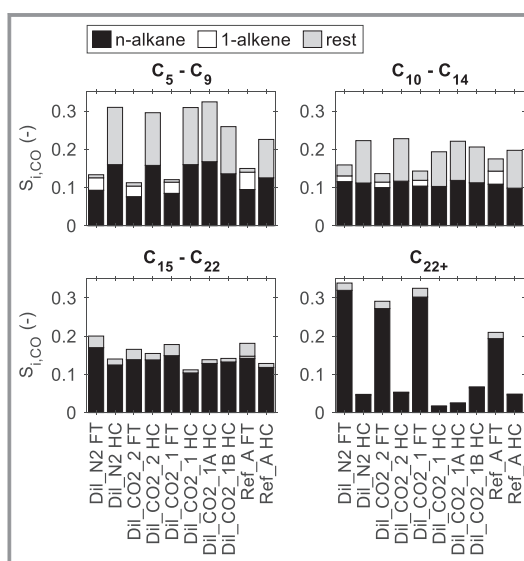


Figure 6. Integral CO-related hydrocarbon selectivity of product lumps for FT and FT-HC measurements (Tab. 1, Tab. 2). In FT products, n -alkanes and 1-alkenes could be distinguished; in FT-HC products, only n -alkanes could be distinguished with the GC analysis at hand.

sion effect on wax/gas ratio) and the analysis at hand. A more detailed analysis of the HC products would require GC×GC analysis.

3.3 Variation of HC Conditions

To enhance the kerosene selectivity at the expense of naphtha production, the conditions in the HC were varied. Additional H_2 feed (Dil_CO2_1A compared to Dil_CO2_1) as suggested by Freitez et al. [38] did neither exhibit a remarkable influence on kerosene and naphtha selectivity nor on mass distribution or average chain length (Fig. 6, Fig. 8, Tab. 5). The wax conversion decreased slightly under H_2 addition. Due to the higher H_2 partial pressure, the dehydrogenation/hydrogenation equilibrium shifts towards hydro-

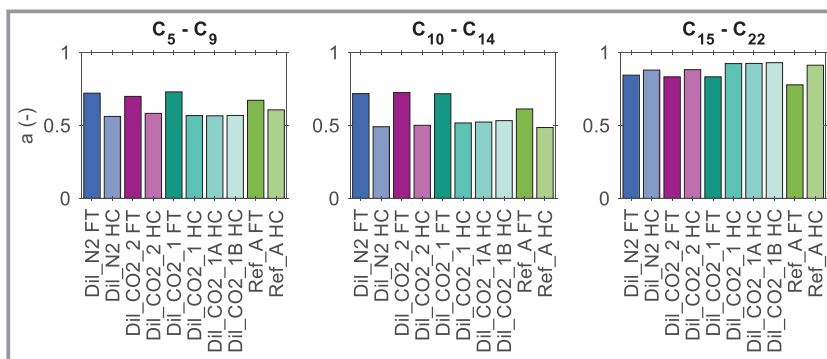


Figure 7. Integral n -alkane fraction (Eq. (10)) of product lumps for FT and FT-HC measurements (Tab. 1, Tab. 2).

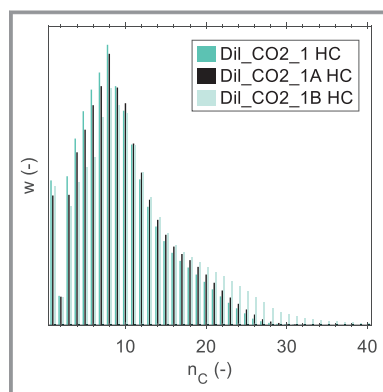


Figure 8. Hydrocarbon mass fractions for coupled FT-HC measurements with varying HC conditions (Tab. 2). FT feed: 38.8 % H₂, 19.4 % CO, 38.8 % CO₂, 3.0 % N₂, $WHSV_{FT} = 4.5 \text{ h}^{-1}$.

genation. This gives rise to the assumption that less dehydrogenation of long-chain alkanes as cracking initiation step occurred, and higher hydrogen partial pressure is inhibiting this step. The hydrogenation functionality is further influenced by the considerably high CO content.

Table 5. Experimental wax (C₂₂₊) conversion in coupled FT-HC measurements and average chain length for FT and FT-HC measurements with varying HC conditions (Tabs. 1 and 2).

	$X_{C_{22+}}$ [%]	$\bar{n}_{C,FT}$ [-]	$\bar{n}_{C,HC}$ [-]
Dil_CO2_1	94.8	20	9
Dil_CO2_1A	92.6	20	10
Dil_CO2_1B	79.0	20	11

To further decrease the wax conversion in the HC, the catalyst mass was reduced from Dil_CO2_1A to Dil_CO2_1B. Fig. 8 shows the weight distribution of the C-species as function of the C-number while varying the HC conditions only. The figure indicates that the fractions of hydrocarbons with more than 11 carbon atoms are higher with decreasing catalyst mass. A lower wax conversion seems to be beneficial to avoid over-cracking.

The investigated variations of the HC operating conditions did not lead to any change in the *n*-alkane fraction (Fig. 7). A more complex process design including wax recycling is therefore commissioned in the Kerogreen process chain to reduce the consumption of the gas oil fraction and to improve the kerosene selectivity. The proof of the beneficial conditions in a liquid-rich HC step is nevertheless pending by future work.

3.4 Carbonaceous Species in the Water Phase

Besides hydrocarbons, also oxygenates, mainly alcohols and traces of carboxylic acids, are produced in Co-LTFT. Primary alcohols with up to five carbon atoms dissolve selectively in the aqueous phase, whereas long-chain alcohols aggregate in the oil fraction [10].

Fig. 9a displays the alcohol mass fractions of methanol, ethanol, 1-propanol up to 1-pentanol in the water phase collected in the cold trap at 10 °C for FT reference measurements. The values range from 0.5 wt% (methanol) to less than 0.1 wt% (1-pentanol). In coupled FT-HC operation mode, oxygenates of the FT product reacted further on the bifunctional HC catalyst. Fig. 9b shows the conversion of alcohols in the HC stage. From this graph, it can be seen that the decrease of mass fraction after HC was more pronounced for long-chain alcohols and accounted for around 25 to 50 % for methanol, and more than 80 % for 1-pentanol.

To the best of the authors' knowledge, no research has been published on the aqueous phase oxygenates reactions of FT products directly converted on HC catalysts. Depending on the hydrogen partial pressure and prevailing reaction conditions, potential reactions could involve dehydroxylation and hydrogenation steps. The former being catalyzed on Brønstedt-active acidic sites, the latter on the Pt sites of the catalyst.

In Fig. 9b, no clear relation between alcohol conversion and CO₂ content in the syngas feed is observed. Reasonable trends for the variation of HC conditions could be distinguished: first, additional H₂ feed in the HC resulted in smaller alcohol conversion. This effect could either be attributed to the lower residence time or indicate that hydrogenation is not solely responsible for oxygenate reactions on the bifunctional catalyst. Second, as expected, less catalyst mass led to smaller conversion of alcohols. These results show that FT syncrude upgrading by means of directly coupled HC reduces the loss of carbonaceous species to the water phase.

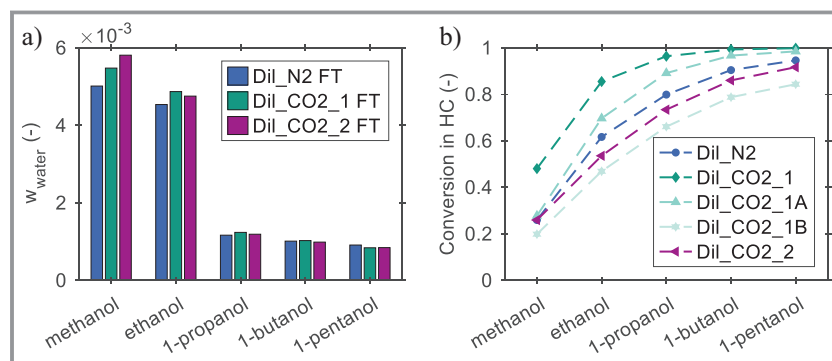


Figure 9. C₁–C₅ alcohols in the water phase collected in the cold trap at 10 °C. a) Mass fractions in water phase for FT reference measurements. b) Conversion of alcohols in the HC for FT-HC measurements.

4 Conclusions

This experimental study investigated the influence of CO₂-rich syngas feeds on the product distribution of combined FT-HC operation. Therefore, syngas with and without CO₂ was used as feed for solely FT and coupled FT-HC experiments. Commercial catalysts were employed: cobalt-based in the FT, and Pt/H-ZSM in the HC. The product distribution was obtained from gas, oil (collected at 10 °C), and wax (collected at 180 °C) phase analysis. Additionally, the oxygenates dissolved in the water phase were analyzed.

The FT reference measurements (without HC) confirmed that CO₂ does not influence the FT product distribution and can be treated as an inert gas. The product distribution for C₁₀–C₅₀ could be well described according to the ASF model with an average chain growth probability of 0.91.

The coupled FT-HC experiments showed that mainly the wax fraction and parts of the gas oil fraction were selectively converted to kerosene and naphtha range hydrocarbons during HC. Linear FT alkanes were either isomerized or dehydrogenated and a limited hydrocarbon net production of C₁₄ was revealed. As no significant difference between the syngas with N₂ and CO₂ was detected, the effects of CO₂ in the coupled FT-HC process seem to be negligible. Although the FT-HC product is rich in kerosene substitute starting material, the loss of gas oil should be lowered in a compact FT-HC process. A recycling of wax may be straightforward to lower the wax conversion per pass, thus, keeping CO away from the catalyst surface and lowering conversion. This will be tested in the future in the Kerogreen plant.

Interestingly, it was found that alcohols (C₁–C₅) dissolved in the FT water phase reacted further on the bifunctional HC catalyst. Although no clear relation between the CO₂ content in the syngas and the alcohol conversion could be deduced, a clear trend was visible for the alcohol conversion in dependence of the alcohol chain length.

The experimental results show that FT syncrude upgrading by means of direct HC is not remarkably influenced by the CO₂ content in the syngas feed. Nevertheless, the diluting effect has to be considered for the reactor design. Therefore, the investigated Kerogreen process route seems to be an interesting case study in the PtL framework.

The authors would like to thank Florian Mian for experimental and Daniel Hodonj for experimental and analytical support. The work presented in this paper is part of the European project Kerogreen, which has received funding from the European Union's Horizon 2020 research and innovation programme under grant agreement no. 763909. Open access funding enabled and organized by Projekt DEAL.

Symbols

a	[-]	n -alkane fraction
m	[g]	mass
\dot{m}	[g h ⁻¹]	mass flow rate
\dot{n}	[mol h ⁻¹]	molar flow rate
n_C	[-]	carbon number
\bar{n}_C	[-]	average chain length
S	[-]	selectivity
w	[-]	mass fraction
$WHSV$	[h ⁻¹]	weight hourly space velocity
X	[-]	conversion
α	[-]	chain growth probability

Sub- and superscripts

cat	catalyst
CO	carbon monoxide
exp	experimental value
FT	Fischer-Tropsch
HC	hydrocracking
i	hydrocarbon chain length
in	reactor inlet
out	reactor outlet
sim	simulated value

Abbreviations

ASF	Anderson-Schulz-Flory distribution
Co-LTFT	low temperature Fischer-Tropsch on cobalt catalyst
FID	flame ionization detector
FT	Fischer-Tropsch
FT-HC	Fischer-Tropsch coupled with hydrocracking
GC	gas chromatograph
HC	hydrocracking
PtL	Power-to-Liquid
SEWGS	sorption-enhanced water-gas shift
syncrude	Fischer-Tropsch crude product
syngas	synthesis gas (CO + H ₂)
TCD	thermal conductivity detector
TOS	time-on-stream

References

- [1] *A European Strategy for Low-Emission Mobility*, European Commission, Brussels 2016. <https://eur-lex.europa.eu/legal-content/en/TXT/?uri=CELEX:52016DC0501>
- [2] A. P. H. Goede, *EPJ Web Conf.* **2018**, 189, 00010. DOI: <https://doi.org/10.1051/epjconf/201818900010>
- [3] P. Viegas, L. Vialetto, A. J. Wolf, F. J. J. Peeters, P. W. C. Groen, T. W. H. Righart, W. A. Bongers, M. C. M. van de Sanden, P. Diomedea, *Plasma Sources Sci. Technol.* **2020**, 29 (10), 105014. DOI: <https://doi.org/10.1088/1361-6595/abb41c>

- [4] T. J. Stadler, P. Barbig, J. Kiehl, R. Schulz, T. Klövekorn, P. Pfeifer, *Energies* **2021**, *14* (2), 355. DOI: <https://doi.org/10.3390/en14020355>
- [5] A. Ramirez, S. M. Sarathy, J. Gascon, *Trends Chem.* **2020**, *2* (9), 785–795. DOI: <https://doi.org/10.1016/j.trechm.2020.07.005>
- [6] H. Kirsch, N. Lochmahr, C. Staudt, P. Pfeifer, R. Dittmeyer, *Chem. Eng. J.* **2020**, *393*, 124553. DOI: <https://doi.org/10.1016/j.cej.2020.124553>
- [7] S. Jürgens, P. Oßwald, M. Selinsek, P. Piermartini, J. Schwab, P. Pfeifer, U. Bauder, S. Ruoff, B. Rauch, M. Köhler, *Fuel Process. Technol.* **2019**, *193*, 232–243. DOI: <https://doi.org/10.1016/j.fuproc.2019.05.015>
- [8] A. de Klerk, in *Fischer-Tropsch Synthesis, Catalysts, and Catalysis: Advances and Applications* (Eds: B. H. Davis, M. L. Occelli), Chemical Industries, Vol. 142, CRC Press, Boca Raton, FL **2016**.
- [9] D. Chakrabarti, V. Prasad, A. de Klerk, in *Fischer-Tropsch Synthesis, Catalysts, and Catalysis: Advances and Applications* (Eds: B. H. Davis, M. L. Occelli), Chemical Industries, Vol. 142, CRC Press, Boca Raton, FL **2016**.
- [10] A. de Klerk, *Fischer-Tropsch Refining*, Wiley-VCH, Weinheim **2011**.
- [11] R. B. Anderson, R. A. Friedel, H. H. Storch, *J. Chem. Phys.* **1951**, *19* (3), 313–319. DOI: <https://doi.org/10.1063/1.1748201>
- [12] P. J. Flory, *J. Am. Chem. Soc.* **1936**, *58* (10), 1877–1885. DOI: <https://doi.org/10.1021/ja01301a016>
- [13] F. G. Botes, L. P. Dancuart, H. G. Nel, A. P. Steynberg, A. P. Vogel, B. B. Breman, J. Font Freide, in *Advances in Clean Hydrocarbon Fuel Processing*, Woodhead Publishing, Cambridge **2011**.
- [14] A. de Klerk, *Energy Environ. Sci.* **2011**, *4* (4), 1177. DOI: <https://doi.org/10.1039/c0ee00692k>
- [15] J. Weitkamp, *ChemCatChem* **2012**, *4* (3), 292–306. DOI: <https://doi.org/10.1002/cctc.201100315>
- [16] C. Sun, T. Zhan, P. Pfeifer, R. Dittmeyer, *Chem. Eng. J.* **2017**, *310*, 272–281. DOI: <https://doi.org/10.1016/j.cej.2016.10.118>
- [17] T. Hanaoka, T. Miyazawa, K. Shimura, S. Hirata, *Chem. Eng. J.* **2015**, *263*, 178–185. DOI: <https://doi.org/10.1016/j.cej.2014.11.042>
- [18] C. G. Visconti, L. Lietti, E. Tronconi, P. Forzatti, R. Zennaro, E. Finocchio, *Appl. Catal., A* **2009**, *355* (1–2), 61–68. DOI: <https://doi.org/10.1016/j.apcata.2008.11.027>
- [19] M. K. Gnanamani, W. D. Shafer, D. E. Sparks, B. H. Davis, *Catal. Commun.* **2011**, *12* (11), 936–939. DOI: <https://doi.org/10.1016/j.catcom.2011.03.002>
- [20] Y. Yao, X. Liu, D. Hildebrandt, D. Glasser, *Chem. Eng. J.* **2012**, *193–194*, 318–327. DOI: <https://doi.org/10.1016/j.cej.2012.04.045>
- [21] A. H. Lillebø, A. Holmen, B. C. Enger, E. A. Blekkan, *Wiley Interdiscip. Rev.: Energy Environ.* **2013**, *2* (5), 507–524. DOI: <https://doi.org/10.1002/wene.69>
- [22] H. Kirsch, L. Brübach, M. Loewert, M. Riedinger, A. Gräfenhahn, T. Böltken, M. Klumpp, P. Pfeifer, R. Dittmeyer, *Chem. Ing. Tech.* **2020**, *92* (1–2), 91–99. DOI: <https://doi.org/10.1002/cite.201900120>
- [23] R. Dittmeyer, P. Pfeifer, K. Schubert, *EP2617487 (A1)*, **2013**.
- [24] P. Pfeifer, P. Piermartini, A. Wenka, *DE102015111614 (A1)*, **2015**.
- [25] K. Dettmer-Wilde, W. Engewald, *Practical Gas Chromatography*, Springer, Berlin **2014**.
- [26] W. Shafer, M. Gnanamani, U. Graham, J. Yang, C. Masuku, G. Jacobs, B. Davis, *Catalysts* **2019**, *9* (3), 259. DOI: <https://doi.org/10.3390/catal9030259>
- [27] C. G. Visconti, E. Tronconi, L. Lietti, R. Zennaro, P. Forzatti, *Chem. Eng. Sci.* **2007**, *62* (18–20), 5338–5343. DOI: <https://doi.org/10.1016/j.ces.2006.12.064>
- [28] P. Piermartini, T. Boeltken, M. Selinsek, P. Pfeifer, *Chem. Eng. J.* **2017**, *313*, 328–335. DOI: <https://doi.org/10.1016/j.cej.2016.12.076>
- [29] R. Yang, L. Zhou, J. Gao, X. Hao, B. Wu, Y. Yang, Y. Li, *Catal. Today* **2017**, *298*, 77–88. DOI: <https://doi.org/10.1016/j.cattod.2017.05.056>
- [30] J. Gao, B. Wu, L. Zhou, Y. Yang, X. Hao, J. Xu, Y. Xu, Y. Li, *Ind. Eng. Chem. Res.* **2012**, *51* (36), 11618–11628. DOI: <https://doi.org/10.1021/ie201671g>
- [31] Y. Lu, T. Lee, *J. Nat. Gas Chem.* **2007**, *16* (4), 329–341. DOI: [https://doi.org/10.1016/S1003-9953\(08\)60001-8](https://doi.org/10.1016/S1003-9953(08)60001-8)
- [32] T. Riedel, M. Claeys, H. Schulz, G. Schaub, S.-S. Nam, K.-W. Jun, M.-J. Choi, G. Kishan, K.-W. Lee, *Appl. Catal., A* **1999**, *186* (1–2), 201–213. DOI: [https://doi.org/10.1016/S0926-860X\(99\)00173-8](https://doi.org/10.1016/S0926-860X(99)00173-8)
- [33] C. L. Tucker, E. van Steen, *Catal. Today* **2020**, *342*, 115–123. DOI: <https://doi.org/10.1016/j.cattod.2018.12.049>
- [34] C. G. Visconti, M. Martinelli, L. Falbo, L. Fratolocchi, L. Lietti, *Catal. Today* **2016**, *277*, 161–170. DOI: <https://doi.org/10.1016/j.cattod.2016.04.010>
- [35] Y. Zhang, G. Jacobs, D. E. Sparks, M. E. Dry, B. H. Davis, *Catal. Today* **2002**, *71* (3–4), 411–418. DOI: [https://doi.org/10.1016/S0920-5861\(01\)00468-0](https://doi.org/10.1016/S0920-5861(01)00468-0)
- [36] R. Brosius, J. C. Fletcher, *J. Catal.* **2014**, *317*, 318–325. DOI: <https://doi.org/10.1016/j.jcat.2014.07.004>
- [37] R. Brosius, P. J. Kooyman, J. C. Q. Fletcher, *ACS Catal.* **2016**, *6* (11), 7710–7715. DOI: <https://doi.org/10.1021/acscatal.6b02223>
- [38] A. Freitez, K. Pabst, B. Kraushaar-Czarnetzki, G. Schaub, *Ind. Eng. Chem. Res.* **2011**, *50* (24), 13732–13741. DOI: <https://doi.org/10.1021/ie201913s>